DEVELOPMENT OF RAMAN INSTRUMENTATION AND METHODOLOGIES FOR PEPTIDE AND PROTEIN INVESTIGATIONS

by

Sergei V. Bykov

B.S., Kiev National University, 1997

Submitted to the Graduate Faculty of

University of Pittsburg in partial fulfillment

of the requirements for the degree of

Doctor of Philosophy

University of Pittsburgh

2010

UNIVERSITY OF PITTSBURGH

FACULTY OF ART AND SCIENCES

This dissertation was presented

by

Sergei V. Bykov

It was defended on

December 14, 2009

and approved by

Lillian Chong, Professor, Department of Chemistry

Sunil Saxena, Professor, Department of Chemistry

Ronald Wetzel, Professor, Department of Structural Biology

Dissertation Advisor: Sanford A. Asher, Distinguished Professor, Department of Chemistry

DEVELOPMENT OF RAMAN INSTRUMENTATION AND METHODOLOGIES FOR PEPTIDE AND PROTEIN INVESTIGATIONS

Sergei V. Bykov, PhD

University of Pittsburgh, 2010

Raman spectroscopy is a tool which offers numerous advantages for investigating biological macromolecules and complex systems. The advantages include but are not limited to: ultrahigh sensitivity to changes in molecular bond lengths (better then pm resolution); time-resolved measurements down to picoseconds time intervals; high selectivity offered by resonance enhancement; high adaptivity for investigation of objects of various sizes in different physical state.

This thesis is focused on the development of UV resonance Raman spectroscopy as a sensitive and incisive technique for polypeptide secondary structure determinations. We built a state-of-the-art tunable UV Raman spectrometer for the 193 – 270 nm spectral region. This instrument allows for steady state and transient UV Raman measurements of the conformational transitions of polypeptides and other macromolecules. We also continued our search for new polypeptide backbone conformational markers. For the first time we investigated the dependence of the $C_\alpha H_2$ stretching vibrations frequencies on Ramachandran φ and ψ angles in glycine-based peptides and showed their potential for polypeptide conformational analysis.

We investigated the conformational preferences of polyglycine, poly-L-lysine and poly-L-glutamic acid in aqueous solutions in their unfolded states. Our studies indicate that polyglycine in solution assumes a broad ensemble of conformations centered around the

Ramachandran angles of the 3_1-helix. We explained this polyglycine conformational preference by favorable electrostatic interactions between adjacent peptide bond carbonyl dipoles. Poly-L-lysine and poly-L-glutamic acid in non-α-helical states in solution show a preference for a left-handed 3_1-helix conformation with some contribution from a left-handed 2.5_1-helical conformation which is likely stabilized due to electrostatic repulsion between charged side chains. In addition, we find that a poly-L-lysine and poly-L-glutamic acid mixture at neutral pH is ~60% β-sheet.

We used time-resolved UV resonance Raman spectroscopy to characterize the spatially resolved (termini vs. center) kinetics of thermal unfolding of a 21 amino acid isotopically labeled, mainly alanine, peptide. We found that the relaxation rates are significantly different for the middle and terminal peptide bonds and strongly depend on T-jump temperatures. We explain the observed kinetics in terms of different relative contributions of different α-helix-like motifs such as pure α-helices, π-bulges and 3_{10}-helices to the observed melting kinetics.

TABLE OF CONTENTS

LIST OF TABLES

LIST OF FIGURES

ACKNOWLEDGMENTS

I would like to express my gratitude to my research advisor Distinguished Professor Sanford Asher for the opportunity to work in his excellent scientific group and for his guidance during my graduate school years at the University of Pittsburgh.

I am very grateful to former Asher group members who guided me through the spectroscopy basics at the beginning of my work at Pitt: Prof. Igor Lednev, Prof. Anatoli Ianoul, Dr. Anton Karnaup and Dr. Mary Boyden.

I am indebted to my colleagues who were directly involved in work presented in this thesis: Dr. Nataliya Myshakina for theoretical insight, Dr. Alex Mikhonin and Bhavya Sharma for mutual experimental work, discussion and publications preparation. Without their contribution and help this work would not be possible.

I am deeply grateful to Fran Nagy and Sharon Mansfield for support and guiding me through administrative matters.

I would like to appreciate former and present Asher group members: Dr. John Jackovitz, Dr. Vladimir Alexeev, Dr. Zeeshan Ahmed, Konstantin Pimenov, Zhenmin Hong, Lu Ma and Kan Xiong for support and friendly environment.

I want to express special thanks to my parents for their support and encouragement.

LIST OF ABBREVIATIONS

AmI (II, III)	**Amide I (II, III)**
CD	**Circular dichroism**
CCD	**Charge-coupled device**
CW	**Continuous wave**
DUV	**Deep ultra violet**
HB	**Hydrogen bond(ing)**
PB	**Peptide bond**
PGA	**Poly-L-Glutamic acid**
PGI (II)	**Polyglycine I (II)**
PLL	**Poly-L-Lysine**
PPII	**Polyproline II**
SNR	**Signal-to-noise ratio**
TGS	**Triglycine sulphate**
UVRRS	**Ultra Violet Resonance Raman Spectrum**

1.0 INTRODUCTION

1.1 BRIEF HISTORICAL OUTLINE OF RAMAN SPECTROSCOPY

Raman spectroscopy is among the most widely used techniques in science today. The Raman effect was discovered in India in 1928 by C. V. Raman,[1] and almost simultaneously by G. Landsberg and L. Mandelstam[2] in the Soviet Union. Soon after that C. V. Raman was awarded the Nobel Prize in 1930. After the initial burst of interest and activity, the use of Raman spectroscopy declined because of the intrinsic weakness of the Raman scattering and interference from fluorescence. During the period from 1940-1960, Raman spectroscopy was suppressed by rapid progress in IR instrumentation which made obtaining IR vibrational data quick and easy.

Raman spectroscopy is intrinsically more exacting to the instrumentation since only very small fraction of incident light scatters inelastically, about 10^{-8}, giving rise to the Raman spectrum. The history of Raman spectroscopy has been greatly influenced by developments of spectroscopic instrumentation. First Raman instruments utilized mercury discharge lamps as a source of monochromatic light, glass prism or diffraction grating as a dispersing element and photographic film as a detector.[3] The first significant upgrade of spectroscopic instrumentation which improved Raman spectroscopy was introduction of electronic rather than photographic recording of Raman spectra. First the photomultiplier-based Raman spectrometer was introduced in mid-1940s. The introduction of lasers as an excitation radiation sources gave Raman

spectroscopy a second life in the 1960s. Lasers are powerful sources of monochromatic radiation which makes them ideal tools for exciting Raman spectra. Introduction of tunable dye lasers in the 1970s significantly increased interest in resonance Raman spectroscopy (RRS) which provides great and selective enhancement of the Raman bands when the exciting line falls within the electronic absorption band. Tunable lasers make selecting the optimal excitation wavelength easy. Today dye lasers are almost completely substituted by much more convenient tunable solid state systems based on Ti-sapphire oscillators coupled with harmonics doubling/quadrupling or mixing packages. Significant progress has also been made in light detecting systems. Today's high quantum yield back-thinned CCD-based cameras significantly improve signal-to-noise of Raman spectra and shorten accumulation times. Other advances in commercially available optics together with improved monochromator design resulted in the situation that today it is often easier to obtain the Raman spectrum of a sample then it is IR spectrum because of much simpler sample preparation and handling.

More details on developments of the UV resonance Raman instrumentation at the University of Pittsburgh during past several years is given in Chapter 2 of this thesis.

1.2 THE RAMAN SCATTERING PHENOMENA

When light falls on matter it may be reflected at the surface or alternatively it may be absorbed or scattered. Scattering is a two-photon phenomenon which includes interaction of the incident electromagnetic wave with the electron cloud of the molecule forcing it to oscillate, creating an oscillating induced dipole which, in turn, emits electromagnetic radiation. Most of

the emitted radiation has a frequency identical to that of the incident light. But a small fraction of the scattered light has different frequency due to the exchange of energy between molecule and incident light. The scattering without change of frequency is called Rayleigh scattering, and that with change of frequency is called Raman scattering. In case of Raman scattering, the frequency difference between incident and scattered light contains information about energy states of the scattering molecule. Raman phenomena are often explained in terms of an energy diagram as shown in Fig. 1.1.

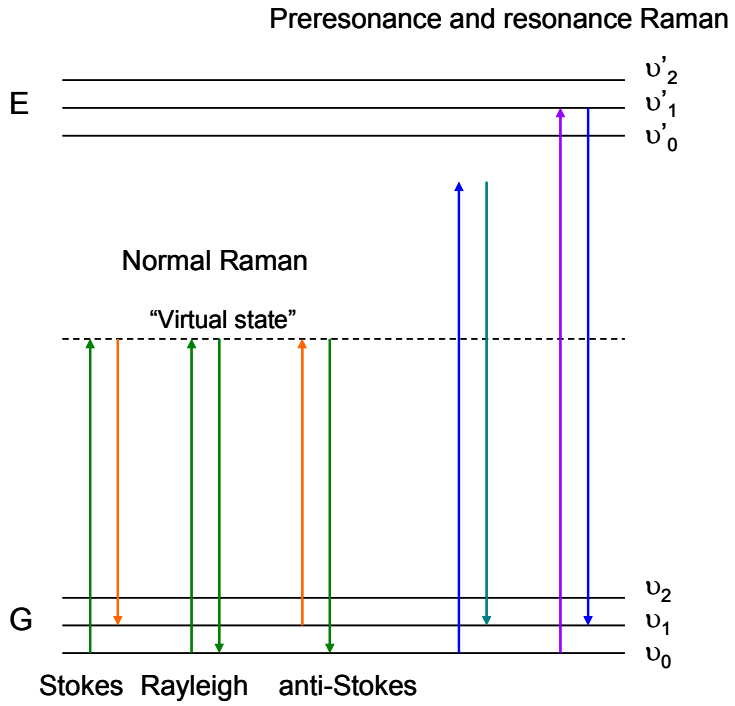

Figure 1.1: Energy diagram for the normal Raman (Stokes, Rayleigh and anti-Stokes), preresonance Raman and resonance Raman (only Stokes are shown). G and E are the ground and excited electronic states of the molecule. υ_n are vibrational sublevels.

In Rayleigh scattering a photon interacts with a molecule in the ground vibrational state (υ_0) raising it to a "virtual" energy state and almost immediately (~10^{-14} sec) the molecule drops back down to ground state, releasing a photon. This photon can be released in any direction,

resulting in a random scattering. Since the molecule is dropping back to the same state, the energy of the initial and released photons is identical. Therefore the Rayleigh scattering occurs without a change in photon energy. It is also called elastic scattering.

Raman scattering is inelastic since photons lose or gain energy during interactions with the molecule. If the molecule is promoted from a ground (υ_0) to a virtual state back down to a higher energy vibrational state (υ_1) then the scattered photon has less energy and this process is called Stokes scattering. If the molecule is initially at υ_1 and after ends up in a lower energy state υ_0 then the scattered photon has more energy and this process is called anti-Stokes scattering.

It should be noted that under normal conditions Stokes scattering is much stronger than anti-Stokes scattering, due to the significantly higher population of molecules in the ground state. This is why the Stokes scattering is used in Raman spectroscopy more frequently.

1.2.1 Theory of the Raman Scattering

A basic description of the Raman effect can be developed using classic theory but a more detailed description requires a quantum-mechanical approach. Although this thesis is solely focused on the development of Raman methodology as an empirical method it is useful to give a brief overview of basic theory underlining the methodology. In the next two paragraphs a brief overview of classical and quantum-mechanical approaches is given. It is based on the D. A. Long monographs.[4,5]

1.2.2 Classical Description of the Raman Effect

The scattered light is brought about by oscillating electric dipoles induced by the oscillating electric field of incident (exciting) radiation. The electric field of incident radiation oscillates at frequency ω_o with the amplitude E:

$$E = E_o \cos(\omega_o t) \tag{1.3-1}$$

This electric field interacts with molecule electrons and nuclei, shifts them from equilibrium positions creating induced dipole moment which can be presented in a form of power series

$$\mu_I = \alpha E + \frac{1}{2}\beta EE + \frac{1}{6}\gamma EEE + \ldots \tag{1.3-2}$$

Where α is a polarizability, β is hyperpolarizability, γ is a second hyperpolarizability and so on. The polarizability can be thought of as a responsiveness of the molecular electron cloud to perturbation by the external electric field. We can neglect the hyperpolarizability terms since their contributions are usually small, unless E is very high. The induced dipole moment becomes:

$$\mu_I = \alpha E \tag{1.3-3}$$

where α is averaged over all coordinates. α is a second order tensor which for the most cases can be represented as following matrix:

$$\alpha = \begin{bmatrix} \alpha_{xx} & 0 & 0 \\ 0 & \alpha_{yy} & 0 \\ 0 & 0 & \alpha_{zz} \end{bmatrix} \tag{1.3-4}$$

In vibrating molecule the polarizability is affected by the change in the molecule shape. Assuming linear dependence of the polarizability on vibrational coordinates, each component of

the polarizability tensor can be written in a form of a Taylor series with respect to the normal coordinates of vibration:

$$\alpha_{\rho\sigma} = \left(\alpha_{\rho\sigma}\right)_o + \left(\frac{\partial \alpha_{\rho\sigma}}{\partial Q_k}\right)_o Q_k = \alpha_o + \alpha'_k Q_k \qquad (1.3\text{-}5)$$

Where α_0 is Equilibrium polarizability which is associated with elastic Rayleigh scattering while α'_k stands for the change in polarizability with the *k*-th normal coordinate which is responsible for inelastic Raman scattering.

Assuming harmonic vibration the molecular normal coordinate varies with time as:

$$Q_k = Q_{ko} \cos(\omega_k t + \delta_k) \qquad (1.3\text{-}6)$$

where Q_{ko} is the amplitude of a vibration, ω its frequency, and δ_k its phase. Combining (1.3-6) with (1.3-3) gives:

$$\mu_I = \alpha_o E_o \cos(\omega_o t) + \left(\frac{\partial \alpha_{\rho\sigma}}{\partial Q_k}\right)_o E_o Q_{ko} \cos(\omega_k t + \delta_k) \cos(\omega_o t) \qquad (1.3\text{-}7)$$

Now we rearrange (1.3-7) equation for the induced dipole moment for the k^{th} vibration as:

$$\mu_I = \alpha_o E_o \cos(\omega_o t) + \frac{1}{2}\alpha'_k E_o Q_{ko} \cos[(\omega_o + \omega_k)t + \delta_k)] + \frac{1}{2}\alpha'_k E_o Q_{ko} \cos[(\omega_o - \omega_k)t - \delta_k)] \qquad (1.3\text{-}8)$$

Thus, the interaction of electromagnetic radiation of frequency ω_o with a molecule results in induced dipole moments oscillating and emitting electromagnetic radiation at three different frequencies. The first term describes elastic Rayleigh scattering oscillating at initial frequency ω_o. The second term characterized by $(\omega_o+\omega_k)$ accounts for anti-Stokes Raman scattering. The last term stands for Stokes Raman scattering of frequency $(\omega_o-\omega_k)$. The $\omega_o \pm \omega_k$ are so called beat

frequencies which result from the exchange of energy between incident electromagnetic radiation and the molecule

The cross-section of the Raman scattering is proportional to the square of polarizability tensor:

$$\sigma_R = \frac{2^7 \pi^5}{3^2 c^4} (\nu_o \pm \nu_{mn})^4 \sum \left| \alpha_{\rho\sigma} \right|^2 \qquad (1.3\text{-}9)$$

(Where c stands for the velocity of light, ν_o is the incident light frequency, and ν_{mn} is the frequency of the transition between vibrational levels in the electronic ground state)

Classical description of Raman scattering shows the origin of the Stokes and anti-Stokes scattering as well as gives some insight into polarization properties and Raman selection rules. But it does not explain the Raman band intensities and the resonance enhancement effect.

1.2.3 Quantum-mechanical description of the Raman Effect

In the quantum-mechanical description or, more exactly semi-quantum-mechanical treatment, the molecule is treated quantum mechanically while the electromagnetic field is still treated classically. According quantum mechanical principles the molecule can absorb or emit only quantized amounts of energy which correspond to the difference between discrete energy states of the molecule. Incident electromagnetic radiation is now treated as a source of perturbation of the molecule. The induced electric dipole of classic theory is substituted by the transition electric dipole associated with a transition of the molecule from state *m*, to state *n*, due to the perturbation of the incident electromagnetic wave of frequency ν_0. The expression for the induced transition moment is:

$$M_{mn} = \int \psi_n^* \cdot \mu \cdot \psi_m \cdot d\tau \qquad (1.3\text{-}10)$$

Where ψ_n and ψ_m are the time independent wavefunctions of final and initial states while μ is the electric dipole moment operator.

Similar to classical treatment, the semi-quantum mechanical approach results in expressions for transition polarizability $(\alpha_{\rho\sigma})_{mn}$ and for the total scattered light intensity (I_{mn}) due to transition between molecular quantum states (vibrational sublevels within the ground electronic state) $|m\rangle$ and $|n\rangle$:

$$(\alpha_{\rho\sigma})_{mn} = \frac{1}{h}\sum_r \left(\frac{\langle m|\mu_\sigma|r\rangle\langle r|\mu_\rho|n\rangle}{\nu_{rm} - \nu_o - i\Gamma_e} + \frac{\langle m|\mu_\rho|r\rangle\langle r|\mu_\sigma|n\rangle}{\nu_{rn} + \nu_o - i\Gamma_e} \right) \qquad (1.3\text{-}11)$$

$$I_{mn} \sim (\nu_o \pm \nu_{mn})^4 I_o \sum \left| (\alpha_{\rho\sigma})_{mn} \right|^2 \qquad (1.3\text{-}12)$$

h is Planck's constant; m, r and n are initial, intermediate and final states respectively and sum is over all intermediate states r; I_o is the intensity of incident light of frequency ν_o; ν_{rm} and ν_{rn} are frequencies corresponding to the energy differences between states denoted by the subscripts; ν_{mn} is a frequency of the transition between initial and final states $|m\rangle$ and $|n\rangle$; μ_ρ and μ_σ are components of the electronic transition dipole moments along the ρ and σ directions; Γ_e is a damping constant related to lifetime of the intermediate state $|r\rangle$, $\tau_r = (h/4\pi\Gamma_e)^{-1}$.

Equation for the transient polarizability (1.3-11) shows that if Γ_e is omitted and frequency of excitation radiation (ν_o) approaches frequency necessary for an electronic transition (ν_{rm}), the first term approaches infinity (resonance Raman conditions). The damping term Γ_e keeps the intensity finite. Dumping factor can be omitted in off-resonance conditions since its contribution is very small.

After applying the Herzberg-Teller expansion under adiabatic approximation (separates electronic and vibrational parts of the molecular wavefunction) the polarizability tensor can be expressed as a sum of three Albrecht terms *A*, *B*, and *C*:

$$\left(\alpha_{\rho\sigma}\right)_{gi,gf} = A + B + C \tag{1.3-13}$$

where

$$\mathrm{A} = \frac{1}{h}\sum_{ev}\left(\frac{\left(M_\sigma\right)_{ge}\left(M_\rho\right)_{eg}}{\nu_{ev,gi} - \nu_o - i\Gamma_e} + \frac{\left(M_\rho\right)_{ge}\left(M_\sigma\right)_{eg}}{\nu_{ev,gf} + \nu_o - i\Gamma_e}\right)\langle i|v\rangle\langle v|f\rangle \tag{1.3-14}$$

$$B = \frac{1}{h}\sum_{ev}\sum_{sk}\left\{\left(\frac{\left(M_\sigma\right)_{ge}\left(h_k\right)_{es}\left(M_\rho\right)_{sg}}{\nu_{ev,gi} - \nu_o - i\Gamma_e} + \frac{\left(M_\rho\right)_{ge}\left(h_k\right)_{es}\left(M_\sigma\right)_{sg}}{\nu_{ev,gf} + \nu_o - i\Gamma_e}\right)\frac{\langle i|v\rangle\langle v|Q_k|f\rangle}{\Delta E^o_{es}} + \right.$$
$$\left. + \left(\frac{\left(M_\sigma\right)_{gs}\left(h_k\right)_{se}\left(M_\rho\right)_{eg}}{\nu_{ev,gi} - \nu_o - i\Gamma_e} + \frac{\left(M_\rho\right)_{gs}\left(h_k\right)_{se}\left(M_\sigma\right)_{eg}}{\nu_{ev,gf} + \nu_o - i\Gamma_e}\right)\frac{\langle i|Q_k|v\rangle\langle v|f\rangle}{\Delta E^o_{es}}\right\} \tag{1.3-15}$$

$$C = \frac{1}{h}\sum_{ev}\sum_{tk}\left\{\left(\frac{\left(h_k\right)_{gt}\left(M_\sigma\right)_{te}\left(M_\rho\right)_{eg}}{\nu_{ev,gi} - \nu_o - i\Gamma_e} + \frac{\left(h_k\right)_{gt}\left(M_\rho\right)_{te}\left(M_\sigma\right)_{eg}}{\nu_{ev,gf} + \nu_o - i\Gamma_e}\right)\frac{\langle i|v\rangle\langle v|Q_k|f\rangle}{\Delta E^o_{et}} + \right.$$
$$\left. + \left(\frac{\left(M_\sigma\right)_{ge}\left(M_\rho\right)_{et}\left(h_k\right)_{tg}}{\nu_{ev,gi} - \nu_o - i\Gamma_e} + \frac{\left(M_\rho\right)_{ge}\left(M_\sigma\right)_{et}\left(h_k\right)_{tg}}{\nu_{ev,gf} + \nu_o - i\Gamma_e}\right)\frac{\langle i|Q_k|v\rangle\langle v|f\rangle}{\Delta E^o_{gt}}\right\} \tag{1.3-16}$$

$\nu_{ev,gi}$ and $\nu_{ev,gf}$ are frequencies corresponding to the differences between energy lavels (E_{ev} - E_{gi}) and (E_{ev} - E_{gf}). $(M_\sigma)_{ge}$ and $(M_\rho)_{eg}$ are electronic transition moments for corresponding transitions. $(h_k)_{xy}$ are vibronic coupling parameters which reflect the electronic wavefunction perturbations due to k^{th} normal mode vibration.

The resonance denominator ($\nu_{ev,gi}$ - ν_o) makes terms A and B large when ν_o is near the absorption frequency. For normal Raman, far from the resonance, A-term contributes only to the

Rayleigh scattering.[15] In case of the resonance Raman, in contrast, term A dominates enhancement of totally symmetric modes via strongly allowed electronic transitions. Non-totally symmetric modes are enhanced mostly via B term due to vibrational coupling of excited states. Enhancement via C term is usually weak and related to the forbidden electronic transitions.[16]

The quantum mechanical treatment, in contrast to the classical, provide quantitative insight as well as selection rules. It predicts the Raman intensities in normal, pre-resonance and resonance cases.

1.3 RAMAN SPECTROSCOPY FOR BIOLOGICAL APPLICATIONS

For a long time application of Raman spectroscopy was restricted to studying small molecules and to qualitative analysis of unknown compounds using characteristic frequencies of chemical groups. After quite a long period of time in the mid-1960s, due to the progress in spectroscopic instrumentation and in molecular biophysics, Raman spectroscopy was introduced into biology related research.[6]

The most important tasks in molecular biophysics today are the elucidation of the structure-function relationships and reaction mechanisms of biological macromolecules. This requires structural information beyond the resolution of classical methods used in structural biology. Full understanding of biomolecule reaction mechanisms is only possible if time-resolved structural information is available. In all these respects, Raman spectroscopy offers a variety of advantages.

1.3.1 Motivation for Using UV resonance Raman spectroscopy

Raman spectroscopy is an atomic scale analytical tool which allows determination of the separate bond lengths to a better than pm resolution. These changes are too small to be detected by other methods common in protein structure research such as NMR and x-ray crystallography. In addition, unlike NMR spectroscopy, Raman spectroscopy is not restricted by the size of the sample and can be used for investigations of small biomolecules, as well as complex biological systems.[7]

One of the most important advantages of Raman spectroscopy in comparison with other spectroscopic methods is in the relative ease in observing the vibrational spectra of the sample in different states at different conditions including physiological conditions. The Raman scattering of water is weak and generally does not interfere. This is increasingly important for investigation of conformational preferences and conformational dynamics of biomolecules because water is their natural environment. Since, it is always possible to modify the Raman technique according to the specific requirements of the investigated system, measurements can be done with samples in any state - solid, liquid, monocrystalline, or in thin monolayers.[3]

The second important advantage of Raman spectroscopy for studying complex macromolecules is the possibility of resonance enhancement. When the excitation wavelength of Raman scattering falls within electronic transition band of a molecule, molecular vibrations which distort ground state geometry towards its excited state gain strong enhancement, up to 10^6. This resonance Raman effect gives high selectivity and allows investigation of enhanced species in diluted solutions in the presence of high concentrations of other species. It also significantly simplifies the spectral analysis.[3]

A classical example of the utility of resonance Raman spectroscopy for investigation of biomolecules is the globular protein hemoglobin. By changing the excitation wavelength we can choose the segment of the complex macromolecule to be studied. If the Raman spectrum of this protein is excited with visible excitation ~ 415 nm this would bring about enhancement of the normal modes associated with heme group vibrations. If the spectrum is excited with ~ 230 nm UV light near the maxima of absorption of aromatic amino acids side chains, the spectrum will be dominated by vibrations of the aromatic rings of tyrosine, tryptophan and phenylalanine which allows for selective monitoring of their environment. Excitation with deep UV ~ 200 nm radiation within the $\pi \rightarrow \pi^*$ electronic transition of the peptide bond selectively enhances vibrations of the polypeptide backbone which allows for the quantitative determination of the peptides and proteins secondary structure. It should be also noted that UV Raman measurements of condensed phase samples do not show interference from background fluorescence.[8]

The third and likely the most important advantage of Raman spectroscopy is the possibility of fast time resolved measurements.[9,10] Detailed information regarding the dynamics of biological systems can be obtained, down to picosecond time intervals. In Asher group at Pitt we used a laser induced T-jump technique to probe the spatially (termini vs. central residues) resolved α-helix peptide melting which occurred in nanosecond time intervals. This work is described in the Chapter 6.

1.3.2 Polypeptide secondary structure determination using UV resonance Raman spectroscopy

One of the well established applications of UVRR spectroscopy with respect to biological systems is determination of the polypeptide backbone secondary structure. Multiple studies have

shown that UV resonance Raman spectroscopy provides a convenient method for quantitative analyses of polypeptide secondary structure in solution.[11-13]

Time resolved UV resonance Raman spectroscopy gives a detailed kinetic of different protein folding events from fast melting of isolated α-helices to long timescale refolding of large proteins.[9,10,14]

Excitation with the deep ultraviolet radiation within the $\pi \rightarrow \pi^*$ transition of the peptide bond brings about resonance enhancement of the Raman bands associated with vibrations which distort the peptide bonds (PB) ground state towards their excited states. These amide band vibrations involve polypeptide backbone heavy atom stretches coupled to amide N-H and $C_\alpha H$ bending. These amide bands are sensitive and convenient markers for a peptide and protein secondary structure.

Figure 1.2 illustrates typical UVRR spectrum of a polypeptide in solution and the main normal modes of a polypeptide backbone.

The Amide I band which is mainly C=O stretch with some admixture of N-H banding is typically found between 1620–1670 cm-1 depends on polypeptide secondary structure and hydrogen bonding to the peptide bond carbonyl. The Amide II band at 1540–1560 cm-1, which is mainly an out-of-phase combination of CN stretch and NH bending shows frequency dependence on polypeptide secondary structure and a hydrogen bonding to PB N-H. The Cα-H bending band appears at 1360–1400 cm-1. This band is resonantly enhanced due to mechanical coupling with the N-H bending vibration. As a result its cross section shows strong dependence on mutual orientation of Cα-H and N-H bonds. The Cα-H bending bands are enhanced only in extended conformations where Cα-H and N-H bonds are in the cis conformation. The Amide III band at 1200 – 1350 cm-1 is an in-phase combination of CN stretch and NH bending. This band

show strong frequency correlation with the Ramachandran ψ-angle because of the coupling with CαH bending vibration which depends on the peptide bond ψ-angle. Mikhonin et. al. recently in detail investigated the dependence of the amide III3 frequency from Ramachandran ψ angle and hydrogen bonding. This allows for development of a family of relationships to directly estimate the Ψ Ramachandran angle from measured UVR AmIII3 frequencies for peptide bonds with known hydrogen bonding. Figure 1.3 demonstrates these dependencies.

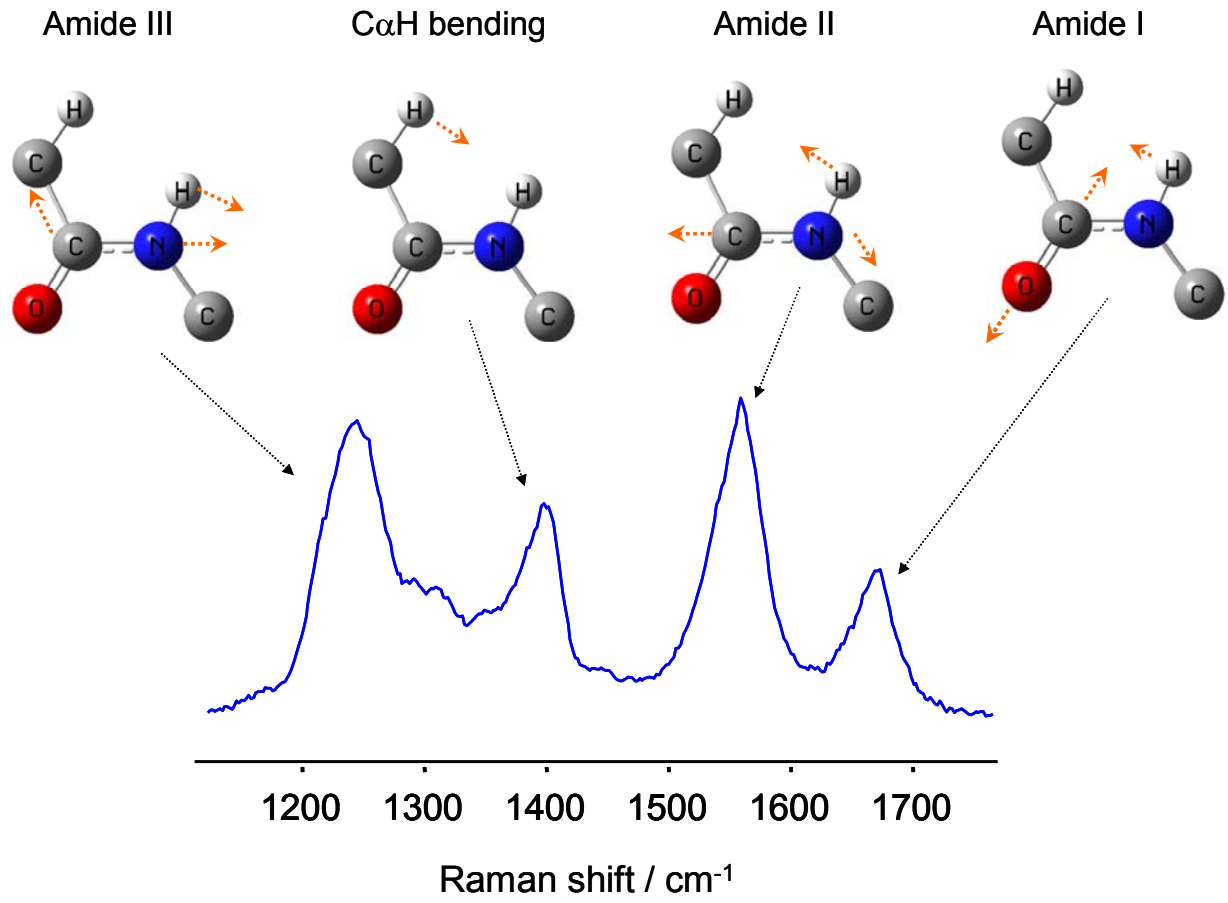

Figure 1.2: UVRR spectrum (204 nm excitation) of a 50% / 50% mixture of polyglutamic acid and polylycine in aqueous solution. Molecular models above the spectrum shows normal modes of polypeptide secondary structure sensitive amide bands in 1000 – 1800 cm^{-1} spectral region.

The amide III band is a good example of an extensively studied and well understood polypeptide backbone conformational marker which now allows quantitative polypeptide secondary structure analysis. In this work we continue the search for new polypeptide backbone conformational markers using both experimental data and theoretical modeling. Our detailed investigation of the conformational sensitivity of $C_\alpha H_2$ stretching vibrations in glycine-based peptides is presented in the chapter 2 of this thesis.

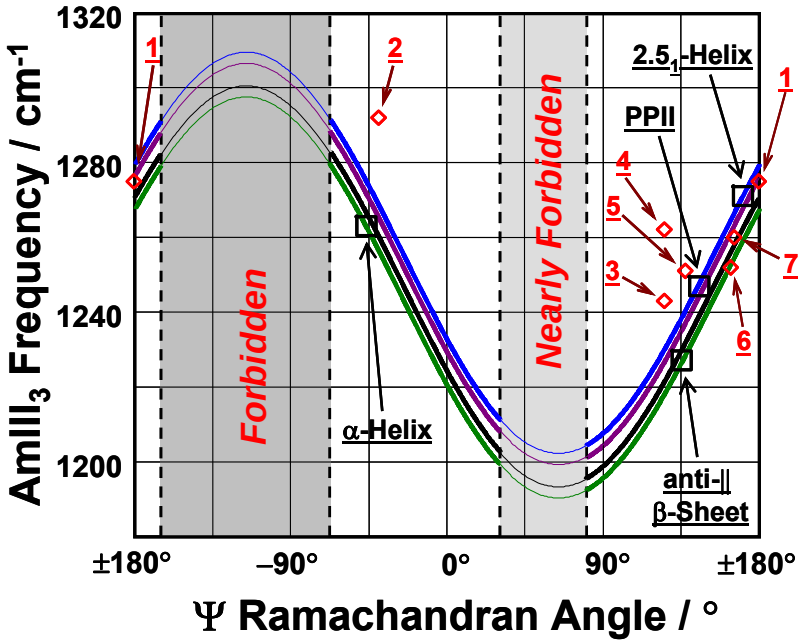

Figure 1.3 Correlation between $AmIII_3$ frequency, HB pattern, and Ψ Ramachandran angle. (□) measured $AmIII_3$ frequencies of α-helix, antiparallel β-sheet, PPII and 2.5_1 helix in aqueous solutions; (◊) measured $AmIII_3$ frequencies of peptide crystals, plotted against their Ψ Ramachandran angles: 1–Ala-Asp; 2–Gly-Ala-Leu•3H_2O; 3–Val-Glu; 4–Ala-Ser; 5–Val-Lys; 6–Ser-Ala; 7–Ala-Ala; the blue curve theoretically predicted correlation for PB, which are fully exposed and fully HB to water (PPII, 2.5_1-Helix, extended β-strand); the green curve theoretically predicted correlation for PB, for two end-on PB-PB HB (infinite α-helix, interior strands of β-sheet); the magenta curve theoretically predicted correlation for PB where only the C=O group has a PB-PB HB (example: three α-helix N-terminal PB, half of PB of the exterior strands of a β-sheet; the black curve theoretically predicted correlation for PB with just their N-H group PB-PB HB (example: three α-helix C-terminal PB, the other half of PB of exterior strands of β-sheet). (Mikhonin, A. V.; Bykov, S. V.; Myshakina, N. S.; Asher, S. A. *Journal of Physical Chemistry B* 2006, *110*, 1928-1943.)

1.4 THESIS OUTLINE

The first introductory chapter of this thesis gives brief outline of the Raman spectroscopy history, brief overview of Raman scattering theory and the utility of Raman spectroscopy for investigation of biology related problems.

Instrumentation is often the major limiting factor of the Raman data quality and informational content. The second chapter of this thesis in details describes a state-of-the-art tunable UV Raman spectrometer. We combined the best available excitation sources, optics and detectors in order to obtain the leading performance in the UV Raman spectroscopy field.

The third chapter describes our search for new polypeptide conformational markers, Raman bands whose frequencies of which show a quantitative, dependence on the polypeptide backbone secondary structure. A detailed investigation of the φ, ψ-sensitivity of $C_\alpha H_2$ stretching vibrations in glycine and diglycine is discussed in this chapter.

In chapter 4 we discuss the utility UVRR spectroscopy for investigation of the conformational preferences of unfolded polypeptides in water solution - polyglycine, poly-L-lysine and poly-L-glutamic. The polyglycine can be thought of as a polypeptide backbone whose conformational preferences are not affected by steric and electrostatic interactions between side-chain groups. In contrast, the conformations of poly-L-lysine and poly-L-glutamic are significantly affected by side chain interaction.

Chapter 5 describes the utility of the UV resonance Raman spectroscopy for time-resolved studies of fast conformational dynamics of polypeptides. We investigated the spatially

resolved (terminal residues vs. central residues), laser T-jump induced conformational transitions in 21-residue mainly alanine model peptide in the nanosecond to microsecond time frame.

1.5 BIBLIOGRAPHY

(1) Raman, C. V. *Nature (London, U. K.)* **1928**, *121*, 619.

(2) Landsberg, G.; Mandelstam, L. *Naturwissenschaften* **1928**, *16*, 557-558.

(3) Chalmers, J. M.; Griffiths, P. R. **2002**.

(4) Long, D. A. *Raman Spectroscopy*, 1976.

(5) Long, D. A. *The Raman Effect: A Unified Treatment of the Theory of Raman Scattering by Molecules*, 2001.

(6) Siebert, F.; Hildebrandt, P. *Handbook of vibrational spectroscopy* **2008**.

(7) Hamaguchi, H.-o. *Curr. Sci.* **2009**, *97*, 186-191.

(8) Asher, S. A.; Johnson, C. R. *Science (Washington, DC, United States)* **1984**, *225*, 311-313.

(9) Lednev, I. K.; Karnoup, A. S.; Sparrow, M. C.; Asher, S. A. *Journal of the American Chemical Society* **1999**, *121*, 8074-8086.

(10) Lednev, I. K.; Karnoup, A. S.; Sparrow, M. C.; Asher, S. A. *Journal of the American Chemical Society* **2001**, *123*, 2388-2392.

(11) Copeland, R. A.; Spiro, T. G. *Biochemistry* **1987**, *26*, 2134-2139.

(12) Chi, Z.; Chen, X. G.; Holtz, J. S. W.; Asher, S. A. *Biochemistry* **1998**, *37*, 2854-2864.

(13) Mikhonin, A. V.; Bykov, S. V.; Myshakina, N. S.; Asher, S. A. *Journal of Physical Chemistry B* **2006**, *110*, 1928-1943.

(14) Mikhonin, A. V.; Asher, S. A.; Bykov, S. V.; Murza, A. *Journal of Physical Chemistry B* **2007**, *111*, 3280-3292.

(15) Albrecht, A. C.: *The Journal of Chemical Physics* **1960**, *34*, 1467-1484.

(16) Tang J; Albrecht A. C, *in Raman Spectroscopy Theory and Practice*, H. A. Szymanski, ed., vol. 2 (Plenum Press, New York, 1970), pp. 33-68

2.0 DEVELOPMENT OF THE UV RAMAN INSTRUMENTATION

This chapter was published in *Applied Spectroscopy* **2005**, *59*, 1541-1552. The coathors are Sergei Bykov, Igor Lednev, Anatoli Ianoul, Aleksandr Mikhonin, Calum Munro and Sanford Asher.

2.1 STEADY STATE AND TRANSIENT UV RESONANCE RAMAN SPECTROMETER FOR THE 193-270 NM SPECTRAL REGION

We describe a state-of-the-art tunable UV Raman spectrometer for the 193 – 270 nm spectral region. This instrument allows for steady state and transient UV Raman measurements. We utilize a 5 KHz Ti-sapphire continuously tunable laser (~20 nsec pulse width) between 193 nm and 240 nm for steady state measurements. For transient Raman measurements we utilize one Coherent Infinity YAG laser to generate nsec IR pump laser pulses to generate a T-jump and a second Coherent Infinity YAG laser which is frequency tripled and Raman shifted into the deep UV (204 nm) for transient UV Raman excitation. Numerous other UV excitation frequencies can be utilized for selective excitation of chomophoric groups for transient Raman measurements. We constructed a subtractive dispersion double monochromator to minimize stray light. We utilize a new CCD camera which responds efficiently to UV light, as opposed to the previous CCD and photodiode detectors which required intensifiers for detecting UV-light.

For the T-jump measurements we use a second camera to simultaneously acquire the Raman spectra of the water stretching bands (2500 – 4000 cm^{-1}) whose band-shape and frequency reports the sample temperature.

2.2 INTRODUCTION

Raman spectroscopy is a routine technique in analytical chemistry, physical chemistry, materials science and biological areas of research.[1-3] New inexpensive instruments have recently been commercialized for near IR spectral region excitation by utilizing inexpensive diode lasers. This follows the development of FTIR Raman spectrometers which utilized 1.06 μm continuous wave (CW) Nd:YAG laser sources. Numerous applications using near IR excitation have been demonstrated over the last decade.[4-8] A major advantage of IR excitation, compared to the previously more common visible wavelength excitation is that the IR laser excitation minimizes sample fluorescence.[9]

Excitation in the near IR normally occurs far from any electronic transitions. In this case, the magnitudes of the Raman cross sections are proportional to the square of the Raman polarizability, the derivative of the molecular polarizability for motion along the normal mode coordinate.[10] Most vibrations have similar Raman polarizabilities and thus give rise to similar intensities. Thus, all Raman allowed vibrations contribute similarly and complex samples give rise to congested complex spectra. The spectra are also weak, and thus require relatively high sample concentrations.

The use of resonance excitation, where the excitation wavelength occurs within an electronic transition of the sample, can give rise to dramatic increases in the intensity of those

vibrational normal modes whose nuclei are localized at the chromophoric segment.[10] The Raman intensity can increase by orders of magnitude (as high as ~10^8) for favorable cases. This leads to great selectivity and simple spectra which only display vibrations localized within the chromophore. Only molecules containing the resonant chromophore show resonance enhancement. This may be a particular analyte, or it may be a chromophoric segment of a macromolecule. For example, numerous studies of heme proteins and visual pigments utilized excitation in the visible spectral region to excite resonance Raman spectra of the heme and the polyene.[11-16]

More recently a number of groups have been working to extend Raman into the deep UV spectral region where all molecules show electronic transitions. Many of these groups are targeting UV resonance Raman excitation to excite within the UV chromophores of biological molecules, such as the aromatic amino acid ring $\pi \rightarrow \pi^*$ transitions[17-29] and the peptide bond $\pi \rightarrow \pi^*$ transitions.[30-33] In addition to the generally large resonance excitation enhancement, UV excitation has the further advantage that the light scattering efficiency scales with the fourth power of frequency; 200 nm excitation shows a 600-fold greater efficiency than would near IR excitation at 1000 μm. In addition, UV excitation avoids fluorescence interference; relaxed emission in condensed phase samples does not occur below 250 nm with excitation below 250 nm.[34]

We, as well as other groups have been pioneering the development of UV Raman spectroscopy.[35-46] This work has demonstrated that UV Raman secondary structure determination methodologies are the most sensitive methods for elucidating secondary structure of low concentrations of proteins in solution.[47] Moreover, this method can be used kinetically to investigate fast structural changes in proteins and peptides.[48-58] The methodology allows the

convenient study of aromatic molecules at low concentrations. Species such as aromatic amino acids and nucleic acids are easily monitored and the spectra give information on hydrogen bonding and environment.[17-20,23-29,59]

The instrumentation for UV Raman studies has rapidly evolved over time. The earliest prelaser instruments utilized mercury arc excitation.[60,61] The first modern instruments built in the mid 1980's utilized low duty cycle Nd:YAG lasers which were frequency tripled, quadrupled and Raman shifted, and/or utilized frequency doubled Nd:YAG to excite a dye laser which was frequency doubled and/or mixed with the 1.06 μm fundamental to achieve tunable excitation down to 212 nm.[35,36] These laser sources caused nonlinear photochemistry and depletion of the ground state populations of samples which led to Raman saturation phenomena.[62] These were useful phenomena for excited state studies but were a nuisance in measurements which attempted to measure ground state resonance Raman spectra.

More recent spectrometers utilized high repetition rate (300 Hz, 20 nsec pulse width) XeCl excimer lasers to pump dye lasers, which were frequency doubled down to 206 nm excitation. These higher duty cycle lasers helped to avoid nonlinear phenomena.[63,64] Unfortunately, UV Raman measurements using these lasers were labor intensive due to the low stability of the laser dyes and the gallons of dye solutions required.

Dramatic improvements in laser excitation sources occurred with the development of intracavity doubled argon and krypton-ion lasers using β-Barium Borate (BBO) nonlinear crystals. This allows the generation of CW radiation with wavelengths of 206.5 and 234 nm for krypton[65] and 228.9, 238, 244, 248 and 257 nm for argon-ion lasers.[38] Such excitation sources were reliable, with low peak powers which eliminated nonlinear, saturation and thermal

degradation problems. The main disadvantage of these lasers was that they only offered a limited number of wavelengths.

In the work here we describe a state-of-the-art UV Raman spectrometer which for steady state measurements utilizes a continuously tunable laser source between 193 - 240 nm which is based on a Ti:Sapphire laser. This quasi-continuous wave 5 KHz laser has a ~ 20 nsec pulsewidth that for many samples avoids nonlinear phenomena. It should be noted that our Ti:Sapphire laser source is somewhat similar to the Ti:Sapphire UV laser recently reported by the Spiro group.[66]

Our UV Raman spectrometer is also designed for kinetic measurements (nsec-msec) by utilizing two high repetition rate Nd:YAG lasers. One laser generates nsec pump pulses in the IR, visible or UV spectral region, while the other generates the nsec UV probe pulses to excite the UV Raman spectra at the appropriate delay time.[52]

2.3 EXPERIMENTAL

2.3.1 Samples

Penta-alanine $(Ala)_5$, acetonitrile and sodium perchloride were purchased from Sigma-Aldrich (St. Louis, MO) and were used as received. Sodium perchlorate is used as an internal standard. Munsell color white reflectance standard, which is a highly purified powder of barium sulfate, was purchased from GretagMacbeth LLC (New Windsor, NY).

Horse heart metmyoglobin (holo-Mb) was purchased from Sigma Chemical (St. Louis, MO). The heme group was removed by 2-butanone extraction as described by Teale.[67] The

apomyoglobin (apo-Mb) was then purified by Sephedax-25 gel chromatography, lyophilized and stored at -20°C. We used about 40 μM solutions for steady state and kinetic Raman measurements in D_2O. We use D_2O rather than H_2O due to a lower deuterium oxide extinction coefficient at 1.9 μm. This allowed us to use less concentrated protein solutions. Concentrations were determined from the absorption spectra by using a Perkin-Elmer Lambda 9 UV-VIS absorption spectrometer. We used a molar absorption coefficient value of 14260 $M^{-1}cm^{-1}$ at 280 nm.

2.3.2 Spectrometer efficiency measurements

The spectrometer throughput efficiency was measured by recording the transmittance of UV light from a standard of ultraviolet spectral irradiance deuterium lamp (UV-40) manufactured by Optronic Laboratories Inc (Orlando, FL). This lamp was scattered from the surface of the barium sulfate powder pressed into a holder which was used as a Lambert surface. $BaSO_4$ works well as a reflectance standard in the UV because of its high stability and low absorbance.[68-70] The ~ 5 mm thick pressed $BaSO_4$ powder scattered all of the incident light. It was placed in the normal sample position. The normal to the $BaSO_4$ reflectance surface was oriented to lie along the spectrometer optic axis. The standard intensity lamp illuminated the barium sulfate surface at an angle of ~ 45° to this normal.

2.4 INSTRUMENTATION

2.4.1 Continiously Tunable UV Laser

To cover the 193 - 240 nm spectral region we use two different Positive Light Co. (Los Gatos, CA) Indigo-S tunable UV laser systems. These two systems contain Evolution-15 pump lasers, tunable Ti:Sapphire oscillators and the appropriate nonlinear crystals and optics to generate the fourth harmonic of the Ti:Sapphire output. One system uses two successive frequency doublers to generate tunable light from 210 to 240 nm. Because crystals are not available to frequency double below 206 nm we obtain shorter wavelengths by mixing the third harmonic with the fundamental to generate continuously tunable fourth harmonic UV radiation between 193 and 210 nm. Longer wavelengths from 240 to 270 nm are also available as the output of the third-harmonic generator.

The Ti:Sapphire oscillator layouts for generating the fundamental or for generating the frequency doubled output are shown in Fig. 2.1 A and 2.1 C. The optical diagram of the nonlinear optics for converting the fundamental to the third harmonic and for mixing with the fundamental is shown in Fig. 2.1 B. Figure 2.1 D shows the optical diagram for the frequency doubled system.

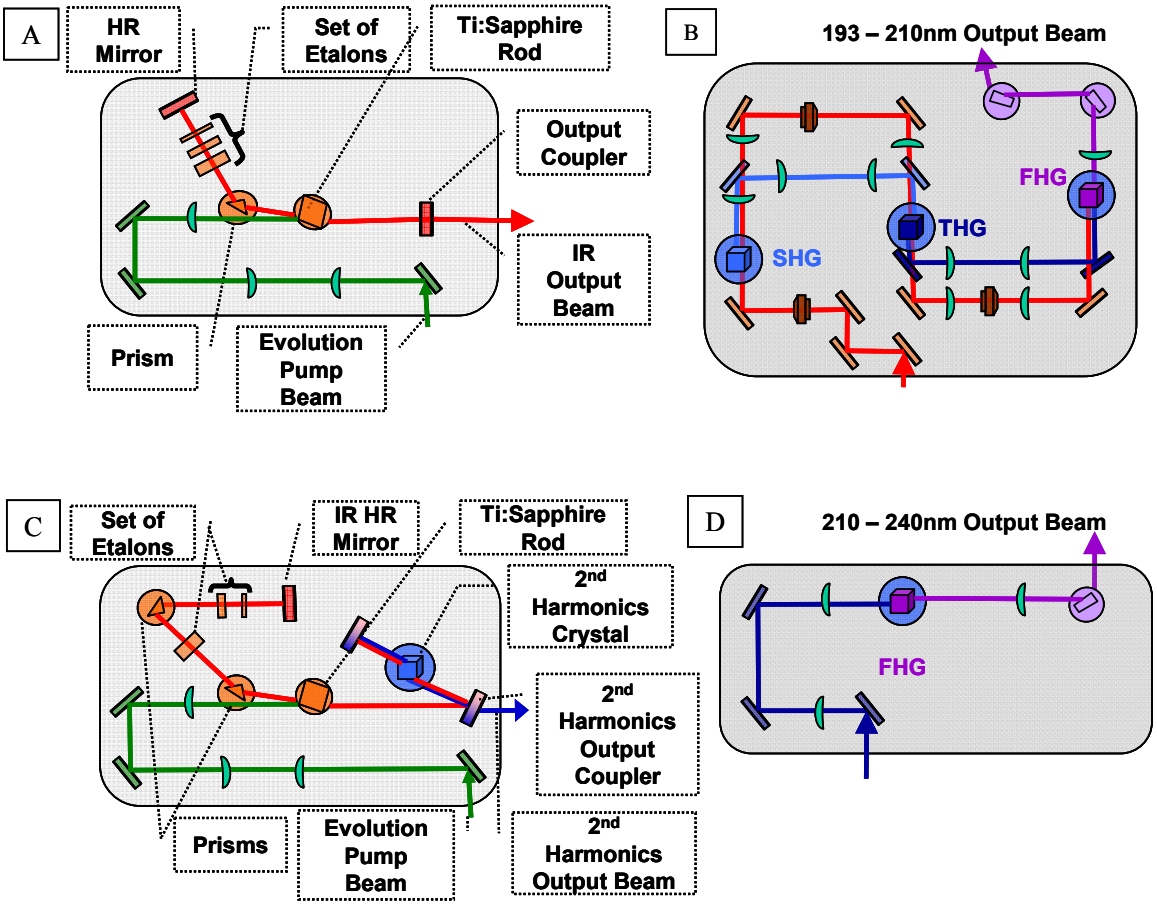

Figure 2.1 Optical layouts for fundamental Ti:Sapphire output (A) and intra-cavity doubled Ti:Sapphire oscillators (C). Optical configuration for the 193 – 210 nm frequency doubling and mixing package (B) and the 210 – 240 nm frequency doubling (D).

The Evolution-15 pump laser is an acousto-optically Q-switched Nd:YLF system which operates at 5 kHz frequency to generate a 1053 nm wavelength fundamental with a 100 to 350 ns pulse duration depending on the pulse energy. This laser is intra-cavity frequency doubled using

a Lithium Tri-Borate (LBO) crystal which is noncritically* phased matched by heating to ~ 320° F to generate 527 nm light which is used to pump the Ti:Sapphire oscillator. The wavelength tunable Ti:Sapphire oscillator utilizes etalons to generate narrow-linewidth near IR radiation which is converted to UV radiation by the nonlinear optics harmonics packages.

The 193-210 nm laser harmonics package consists of a second-harmonic generator (SHG) which converts the 772 - 820 nm Ti:Sapphire IR fundamental to 386 – 410 nm light with ~ 20% efficiency. The THG crystals mix the 386 – 410 nm light with the IR fundamental to produce the 257 - 273 nm 3rd harmonic with an efficiency of up to 10%. The final stage mixes the third harmonic with the residual fundamental to produce 193 – 210 nm light with a somewhat lower efficiency of about 5%. The deep UV output power depends on the wavelength and varies from ~ 9 mW at ~ 200 nm to ~ 3 mW at the edges of the 193 – 210 nm spectral region. Typical output powers for the 193 nm system are shown in Fig. 2.2.

In the 210 - 240 nm system IR light generated by the Ti:Sapphire oscillator is intracavity frequency doubled. This second harmonic light (420 – 480 nm) is directly converted to the UV by further frequency doubling. The overall efficiency is ~ 20% which results in 10 - 40 mW of 210 nm to 240 nm UV radiation. Typical output powers are shown in Fig. 2.3.

---

* Birefringence of the BBO crystal can be adjusted by using its temperature dependence. This is called noncritical phase matching or temperature phase matching.

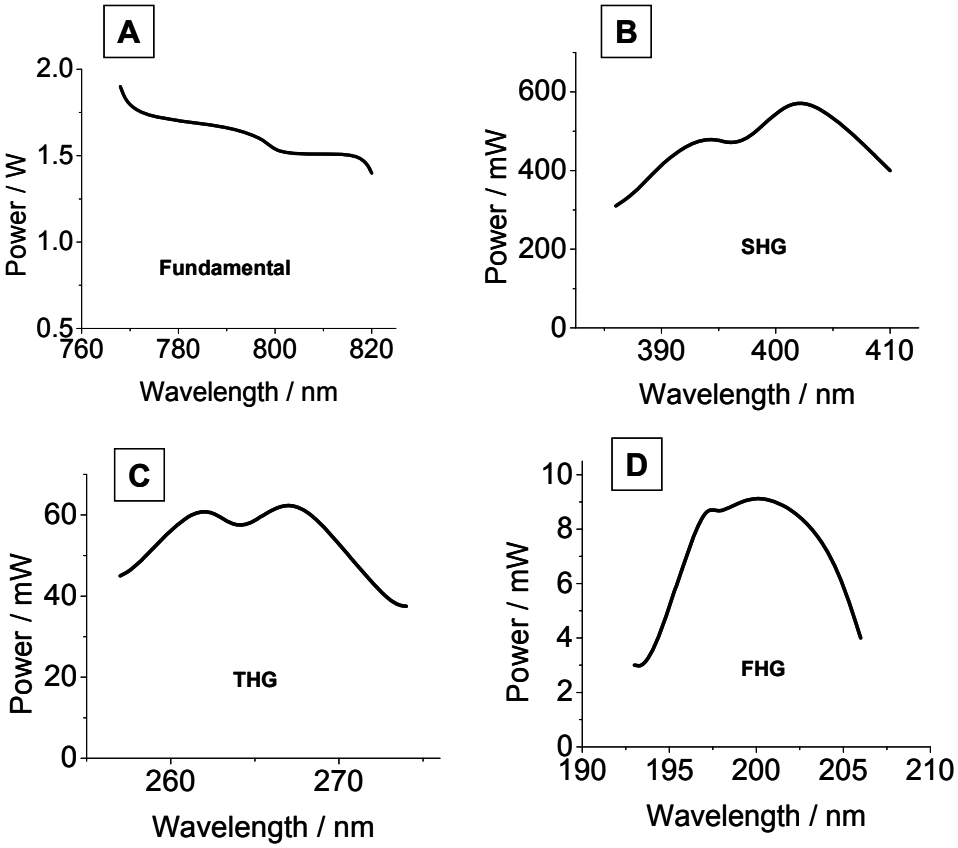

Figure 2.2: Typical output average powers for the 193 – 210 nm Indigo-S DUV tunable laser. A – oscillator IR power, B – second harmonic, C – third harmonic, D – fourth harmonic.

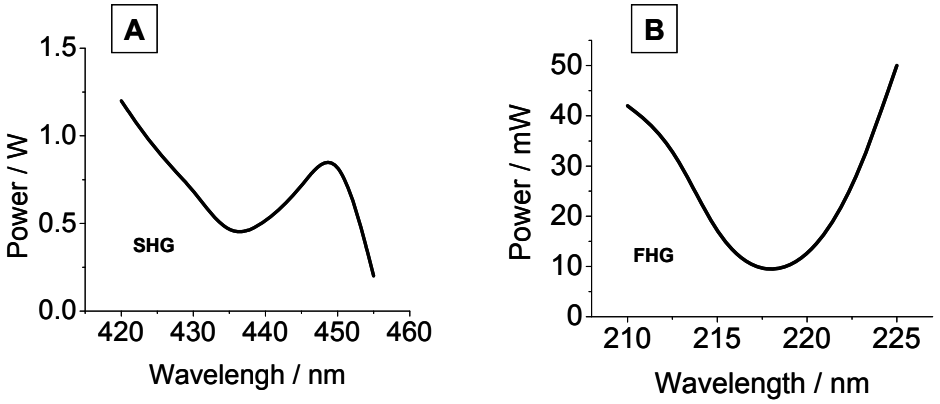

Figure 2.3: Typical output powers for 210 – 240 nm Indigo-S DUV tunable laser. A intracavity doubled oscillator SHG power. B fourth harmonic UV power.

2.4.2 Pulsed IR, Visible and UV Laser

The transient Raman instrument utilizes two Coherent Inc. (Santa Clara, CA) Infinity Nd:YAG lasers (Fig. 2.4).

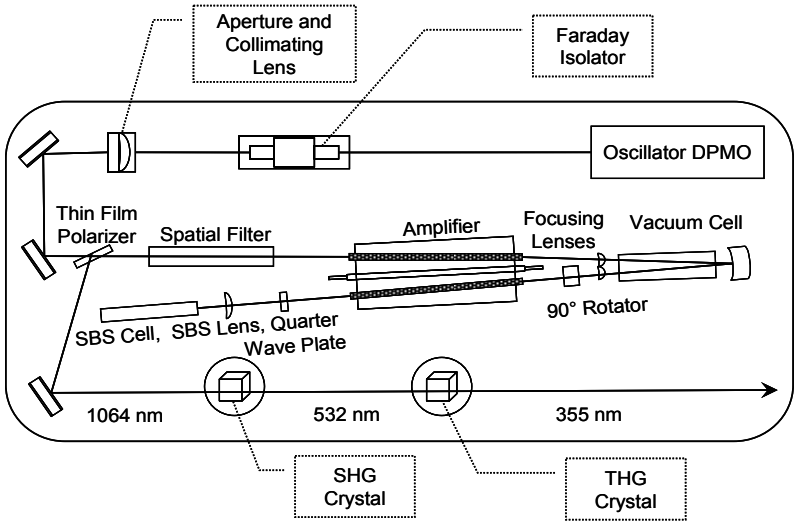

Figure 2.4: Optical layout of the Coherent Infinity Nd:YAG laser with 2nd and 3rd harmonic crystals.

These lasers have the exceptionally high quality temporal and spatial beam profiles, essential for efficient frequency conversion by Raman shifting multiple harmonics in hydrogen or other gases.[35,71-73] The Infinity Nd:YAG laser consists of an internal diode pump and Q-switched master oscillator which provides the initiating pulse for the dual rod, single lamp amplifier stage. This laser is equipped with a feedback system. A phase conjugate mirror (SBS cell) is utilized to correct for wave front distortions created by the thermal and stress induced effects in the Nd:YAG rods. As a result the Infinity system can produce superior quality laser pulses independently of repetition rate and output power. We also recently acquired an XPO

optical parametric oscillator system to continuously change the wavelength of the heating IR pulse.

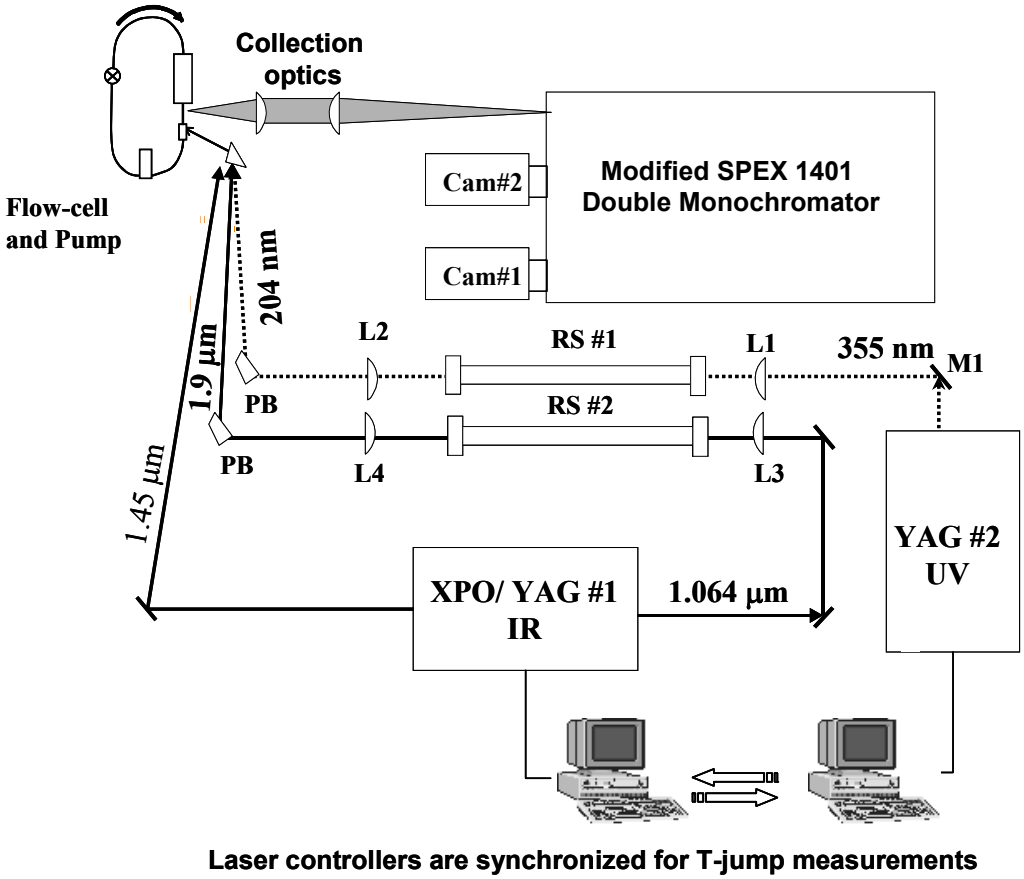

Figure 2.5: Schematic diagram of the spectrometer for UV resonance Raman transient (T-jump) measurements.

The layout of the T-jump instrument is shown in Fig. 2.5. Our transient Raman spectrometer consists of two electronically synchronized Coherent Nd:YAG Infinity lasers. The first laser generates an IR heating pulse or a visble or UV pulse to excite the system. The other Coherent Nd:YAG Infinity laser generates a delayed UV pulse to excite the resonance Raman scattering. The lasers operate at 100 Hz and generate 3.5 nsec UV pulses.

In the original design[52] the heating beam was obtained by Raman shifting the YAG fundamental in H_2 to 1.9 μm (1st Stokes) as described in earlier publications.[74] The Nd:YAG fundamental is focused by lens L3 into the Raman shifter RS#2 filled with H_2 at a high pressure of ~ 1000 psi. The 1st Stokes beam at 1.9 μm is separated by a Pellin-Broca prism and directed to the sample by a few gold-coated mirrors.

This setup allows us to generate a T-jump as high as 65 °C when the 1.5 mJ, 1.9 μm laser pulses are focused to a ~ 200 - 300 μm diameter spot in the flow-stream.[51] However, this very high water absorbance of ~ 40/cm at 1.9 μm requires us to use highly concentrated protein/peptide solutions. This is because our experiment requires us to collect Raman scattering from the same sample depth that we heat; the UV Raman exciting light must experience similar sample absorbance as the IR T-jump pulse. Since we use a recirculating sample stream which generally utilizes ~10 ml of solution we require large amounts of sample which can be very expensive. In addition, high concentrations are often undesirable because many biological macromolecules aggregate at high concentrations.

We have partially solved this problem by using a Coherent Infinity-XPO tunable optical parametric oscillator (OPO). This allows for IR tuning from ~1 μm to ~2.2 μm. Our desired wavelength is 1.45 μm, where the water absorption is reduced to ~12/cm which allows us to decrease the peptide/protein concentration. The main disadvantage of this approach is a lower T-jump due to lower IR absorption. Further, the Infinity XPO laser is less efficient than the Stokes Raman scattering process that generates 1.9 μm light.

The laser used to generate 204 nm radiation (YAG #2) is frequency tripled. ~3 W of this 355 nm UV radiation is directed onto the dichroic mirror M1 which filters out most of the 2nd harmonic. This light is then focused by lens L1 into the Raman shifter RS #1 which is filled with

60 psi hydrogen (Fig. 2.5). The resulting polychromic radiation is focused by lens L2 onto a Pellin-Broca prism which disperses the light and separates out the 204 nm 5th anti-Stokes beam. This light (~3 mW) is focused into the volume element of the sample heated by the IR pulse in order to excite the UV resonance Raman spectra. The delay time between heating and probing pulses can be varied between ~5 nsec and 6 msec with ~ 0.5 nsec accuracy in the nsec and μsec regions, and with ~ 100 nsec accuracy in the msec region.

2.4.3 Multichannel Detectors

As discussed for transient Raman measurements we separately and simultaneously measure the high frequency (2500 to 4000 cm^{-1}) and low frequency (800 to 1800 cm^{-1}) Raman spectra by optically selecting the high frequency portion of the Raman scattering in the first stage of the monochromator. Thus, we use two separate multichannel detectors.

We utilize a liquid nitrogen cooled Princeton Instruments Spec-10:400B digital CCD detector as the high S/N detector for accumulation of highly resolved spectra in the 800 -1800 cm^{-1} region. It has a 1340 x 400 array of 20 x 20 μm pixels (26.8 mm x 8.0 mm image area). It is a cryogenically cooled back thinned CCD with a reported > 30% quantum efficiency in the deep UV region.

We have utilized ever improving detectors over the years as we refine our Raman instrument. It turns out that we could only determine the utility of a detector by actually testing it in our laboratory side-by-side with detectors we were already successfully using. Manufacturer' spectral efficiency specifications were repeatedly found to be completely unreliable.

The present camera is the first CCD which we found capable of detecting UV light with significant efficiency. This CCD camera gives us ~ 3-fold better spectral S/N than did our Princeton Instruments solar blind intensified CCD ICCD-Max-1024-E, which in turn, had ~ 3-fold better S/N than the non-solar blind intensified Princeton Instruments detector, ICCD 1024 MS-E we previously utilized, which had a ~ 10-fold improved S/N compared to our earliest EG&G Princeton Applied Research 1420 and 1456 intensified photodiode arrays.

Over the last decade we have tested multiple back-thinned CCD cameras from numerous manufacturers in our laboratory which we found were unable to detect UV photons in spite of their quoted high UV quantum yields. The manufacturers were quite confused by these results.

2.4.4 UV Raman Spectrograph

The scattered light was dispersed by a SPEX 1401 0.75 m Czerny-Turner (originally additive) double monochromator, f/6.8 (Fig. 2.6). Spectrometer stray light is the major interference that limits the Raman spectral S/N ratios. This stray light results from the lack of complete rejection of the Rayleigh scattering. Some fraction of light at this wavelength finds itself in the spectrograph image plane situated on the detector overlapping the actual Raman inelastically scattered light. Thus, it is detected as if it were Raman scattered light. This light which underlies the Raman spectrum is known as instrumental stray light.[75,76] It originates from blemishes in dispersive and reflective elements of the monochromator, dust particles, etc., and from unintentional light reflections and scattering which can derive, for example, from retrodiffraction from the CCD detector or from the pincushion intensifier.[77] This stray light can introduce artifacts and can decrease the Raman spectral S/N. It can also contribute features

which interfere, and in the worst cases can confound the Raman spectral measurements. Good monochromator design attempts to substantially reduce unwanted reflections and scattering.

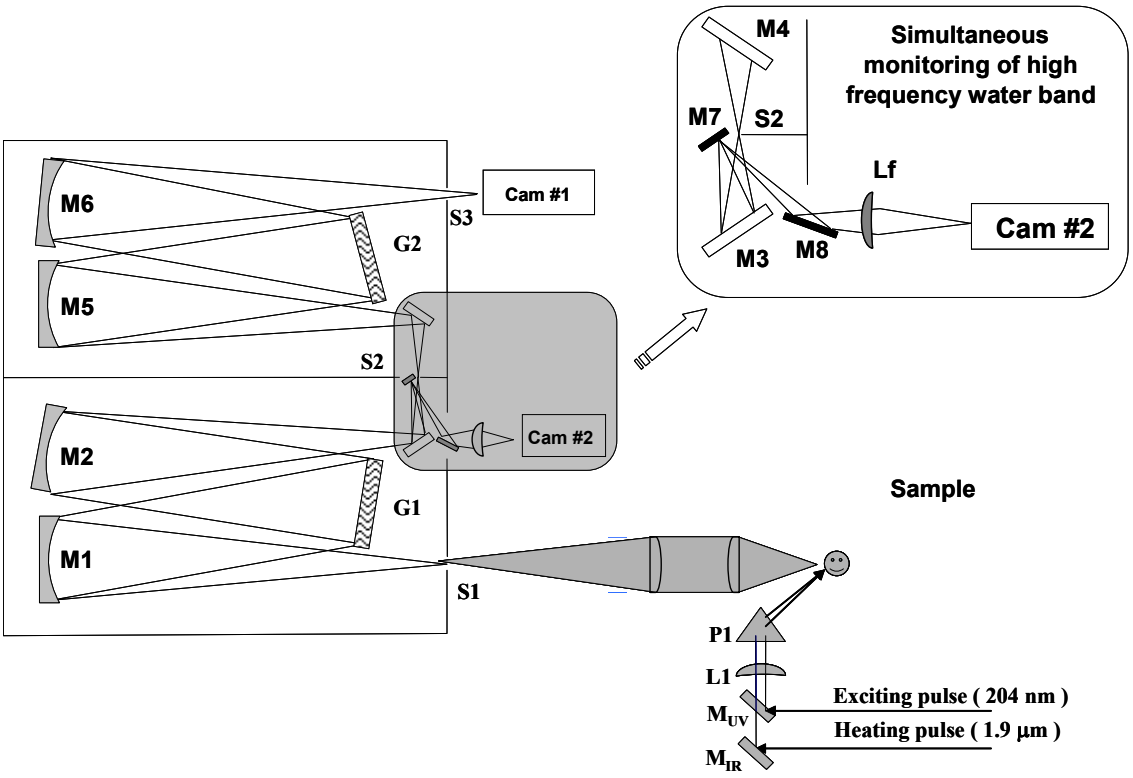

Figure 2.6: Modified SPEX 1401 double monochromator and collection optics. The insert shows the optics used to direct the ~2500-3500 cm^{-1} Raman scattered light dispersed by grating G1 to a second detector (Cam #2)

We significantly modified the spectrometer to minimize the stray light, to optimize its efficiency for deep UV measurements and to permit simultaneous monitoring of the high frequency and mid frequency Raman spectra at high resolution. We minimized stray light by using the double monochromator in partial subtractive dispersion. Subtractive dispersion double monochromators were originally described by van Cittert[78] as well as others.[79-83] In contrast to the additive configuration, when both gratings of the monochromator disperse light in the same

direction, subtractive dispersion uses the second grating to partially or completely undisperse the light.

This is a method often used in triple monochromators, where the first stage disperses the spectrum, and the edge of a slit blocks the Rayleigh scattering. This dispersed light, without the Rayleigh scattering is then sent to a second completely subtractive stage that recombines the light onto the entrance slit of a spectrograph. This "pink light" is then dispersed by the spectrograph stage onto a multichannel detector, where the stray light is significantly reduced.

We wish to optimize the throughput efficiency of the spectrometer and, thus, only utilize two stages by using a double monochromator in subtractive dispersion in a manner similar to that reported by Mathies.[84] The originally linked gratings of our vintage 1960 SPEX 1401 double monochromator G1 and G2 were decoupled by removing the mechanical connection. Both gratings were then controlled by two separate micrometer screw drives threaded through holes in the faceplate of the spectrometer. This allowed us to use these gratings in a subtractive dispersion configuration. As discussed below, this significantly reduces the stray light which occurs at the Rayleigh frequency.

Figure 2.7 compares the performances of double spectrometers which operate in additive and subtractive dispersion. In both cases the 1^{st} stage utilizes a 600 groove/mm grating in the +1 order. In order to achieve identical linear dispersions at the final second stage image plane, the 2^{nd} stage additive dispersion utilizes a 2400 groove/mm grating used in $+1^{st}$ order (case I). For subtractive dispersion we use a second stage 1800 groove/mm grating in -2^{nd} order (case II).

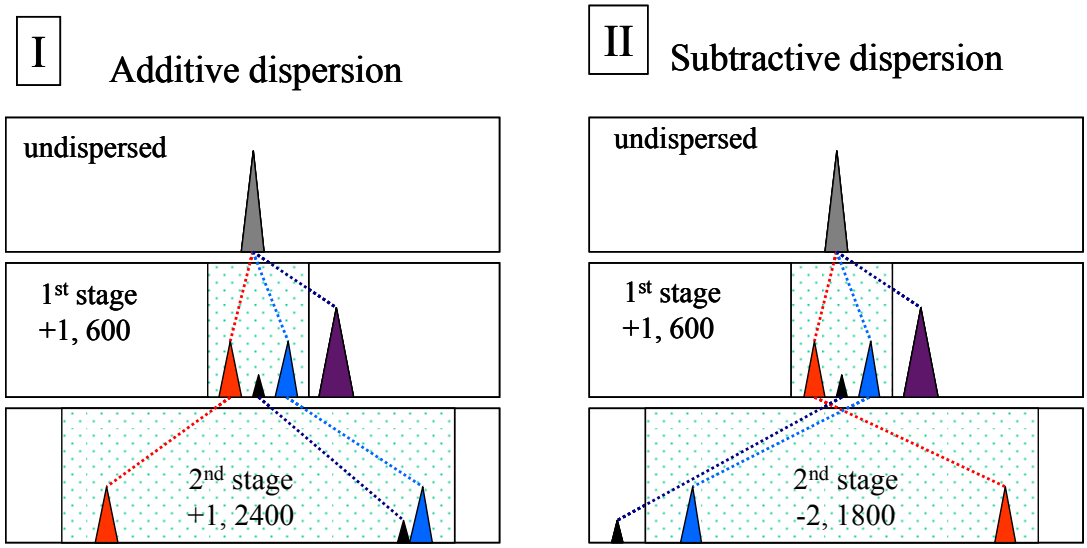

Figure 2.7: Reduction of stray light by the use of subtractive (II) rather than additive (I) dispersion. Raman spectral intensities are shown at the spectrograph image planes after the first and second spectrograph stages. A small black peak represents a portion of a stray light at the excitation frequency but situated at the centre of the detector, the large purple peak is the Rayleigh line, while the red and blue peaks are the low frequency and the high frequency Raman bands respectively.

The first stage disperses both the Rayleigh light (purple triangle) and the Raman spectrum. The red and blue triangles indicate Raman bands at the extreme edges of the measured Raman spectra. The small black triangle indicates a spacially defined portion of the stray light at the Rayleigh wavelength, which is localized on the image plane at an artifactual location at an apparent intermediate Raman wavelength. In additive dispersion, the second monochromator increases the linear dispersion to increase the distance between the "red" and "blue" bands. The Rayleigh stray light band is also further dispersed, but given the desired linear dispersion, remains within the Raman spectral interval in the image plane. The Raman lines are equivalently dispersed as if a single 3000 groove/mm grating dispersed the light. The stray light was dispersed by only the second stage and was dispersed by a single 2400 groove/mm grating. Thus, the stray light remains in the Raman spectral region but is blue shifted by the dispersion in

the second stage to the high frequency side of the spectrum (to the low frequency spectral portion).

In subtractive dispersion (II), our second grating has six times the dispersion of the first grating. Thus, after the second stage the light ends up with four times the dispersion of the first stage. However, the spectrum is spatially dispersed backwards, with the red band on the left and the blue on the right compared to additive dispersion. The stray light is dispersed far towards the blue (the low frequency portion of the Raman spectrum). There is more dispersion to reject the stray light in the subtractive dispersion situation. The Raman light is dispersed by the equivalent of a single 3000 groove/mm grating, the same as in additive dispersion. In contrast, the stray light is dispersed by the equivalent of a 3600 groove/mm grating.

To increase the spectrometer efficiency all of the original evaporated aluminum mirrors in the spectrometer (M1-M6) were dielectrically coated by CVI Laser LLC. (Albuquerque, NM) mirrors to give a ~ 95 % reflectance efficiency for the 200 - 215 nm and 229 - 244 nm spectral regions. This contrasts with a ~90 % reflectance for the MgF_2 coated UV enhanced Al mirrors, which degrades over a year to only a 70 % reflectance. This increased reflection efficiency has a significant impact since the double monochromator has a minimum of six mirrors. For convenience we utilize the monochromator backwards by placing the entrance slit on the exit image plane and by placing the detector at the normal entrance slit plane.

The total throughput of the spectrometer is shown in Fig. 2.8. The spectrometer efficiency varies between 15% to 20% in the 200 - 230 nm spectral region. The spectrometer efficiency drops rapidly for wavelengths shorter then 195 nm, becoming zero at ~ 191 nm. We are unsure of the phenomenon that limits the efficiency at the shortest wavelengths since we do not have reliable data on the barium sulfate powder reflectance, or on the CCD camera quantum

efficiency below 200 nm. In addition, our spectrometer efficiency was measured in air which can strongly absorb UV radiation at wavelengths shorter than 200 nm. The throughput profile below 200 nm shows a series of narrow troughs due to the well known Schumann-Runge molecular oxygen absorption bands.[85] These bands also show up in the UVRR spectra (see below).

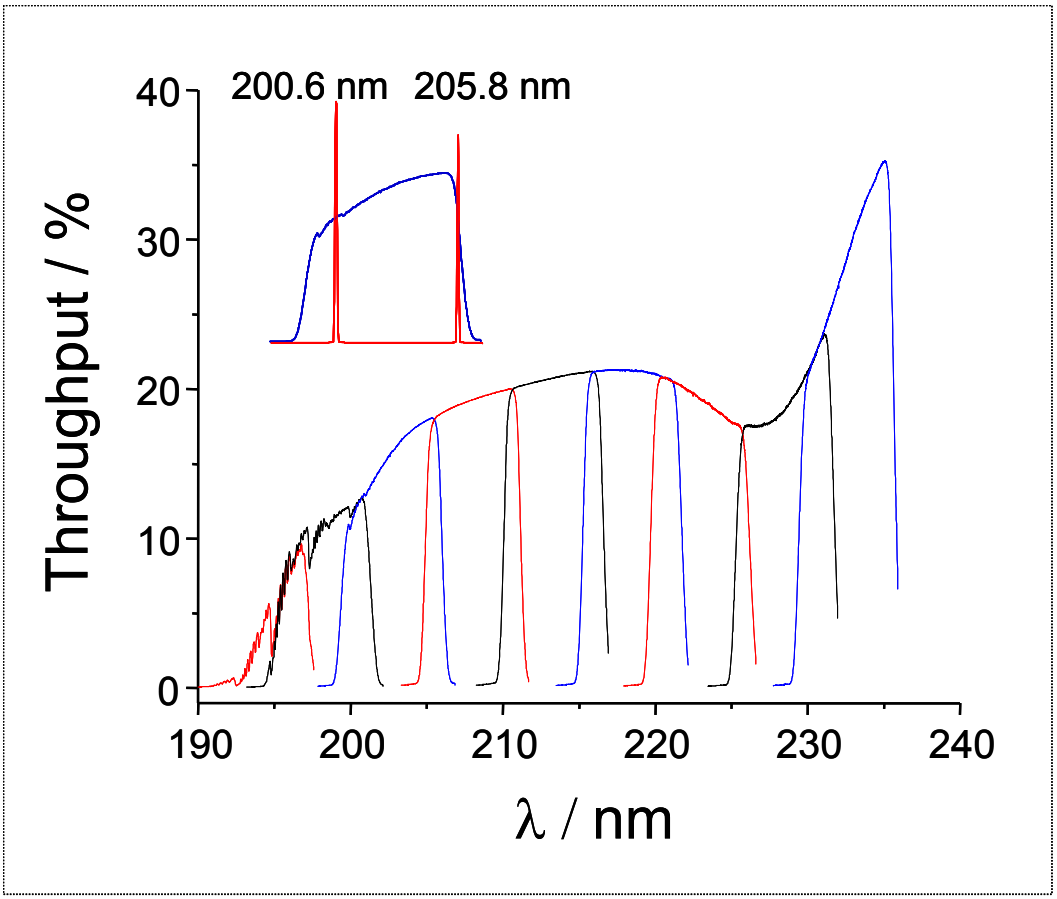

Figure 2.8: Spectrometer efficiency (collection optics, monochromator and detector) for the 193 – 235 nm region. The total curve is composed of 9 separately measured ~ 6 nm segments at different grating positions. Each segment was wavelength calibrated by using the output of the Indigo-S tunable DUV lasers described above. The inset shows how the separate segments were wavelength calibrated by using the Rayleigh light scattered by the barium sulfate powder Lambert surface. The total throughput was normalized to the standard D_2-lamp irradiance. The absolute throughput of the standard lamp was determined by measuring the transmission of a 220 nm laser beam through the spectrometer.

A small plane mirror M7 was attached onto the edge of the middle slit S2 in order to deflect the high frequency part of the Raman spectrum to mirror M8 which focuses it onto a second camera attached to the first stage of the monochromator. We utilized an EG&G Princeton Applied Research 1456 intensified photo diode array with 1024 25 μm x 2.5 mm active elements (Fig. 2.6). The second detector detects the ~ 2500 cm^{-1} to ~ 4000 cm^{-1} Raman spectral region which for aqueous solutions is dominated by the water OH stretching band, which changes band shape with the solution temperature.[86]

This detector has a S/N approximately 90-fold below that of the CCD camera. However, the intensity of the Raman water stretching band is very high and the S/N of the high frequency spectra are sufficiently high to accurately determine the T-jump temperature.

2.4.5 Spectral Resolution

The Spectral Resolution (SR), is usually defined as the minimum frequency separation between two peaks in the spectra that the instrument can resolve. SR is mainly determined by the resolving power of a monochromator given the size of a single light sensitive element (here a CCD pixel) in the detector system. For two peaks to be resolved at the CCD detector their maxima should be separated by at least one pixel with a decreased intensity between them. In the best case, two resolved peaks at the CCD sensor would span 3 pixels.

The reciprocal linear dispersion, R_d of the SPEX 1401 monochromator can be written as in Eq. 2.1 by considering a single stage Czerny-Turner spectrograph with an equivalent grating.[†]

$$R_d = d\frac{\cos\beta}{f|m|} \qquad (2.1)$$

where d is the distance between grooves of the equivalent grating, β is the angle between the grating normal and diffracted ray for an equivalent single monochromator, f is the focal length of the last mirror focusing the spectrum on the CCD detector, m is the order of diffraction of the equivalent grating. At λ_{exc} = 204 nm, R_d = ~ 0.32 nm/mm or ~ 75 cm^{-1}/mm. The limiting spectral resolution, SR_{lim} of our spectrograph consisting of a SPEX 1401 monochromator and Spec-10:400B digital camera can be calculated using the Eq. 2.2:

$$SR_{\lim} = R_d[cm^{-1}/mm] \times P_w[mm/pix] \times 3[pix] \qquad (2.2)$$

where R_d is a reciprocal linear dispersion of the monochromator, P_w is the detector pixel width and 3 is a minimum number of pixels to record two resolved bands. The pixel width of the Spec-10:400B digital camera is 20 μm giving us a limiting spectral resolution of ~ 4.5 cm^{-1}.

Figure 2.9 shows the experimentally determined dependence of the full width at half maximum (FWHM) of a mercury atomic emission line upon the spectrometer entrance slitwidth. Atomic emission bands of low pressure lamps have < 1 cm^{-1} linewidths. Thus, our observed linewidth is limited by our spectrograph resolution. A 100 micrometers slit projected onto CCD imaging plane covers ~5.1 pixels which is close to the value expected, given our Spec-10:400B

[†] In our case equivalent grating has a groove density of (1800 × 2) – 600 = 3000 groove/mm.

CCD camera pixel size of 20 micrometers. At a ~204 nm excitation wavelength and 100 micrometers slitwidth the FWHM of the Stokes Raman band in the protein amide region (~ 800 – 1800 cm^{-1}) would be 5 pixels × 1.5 cm^{-1}/pixel = 7.5 cm^{-1}.

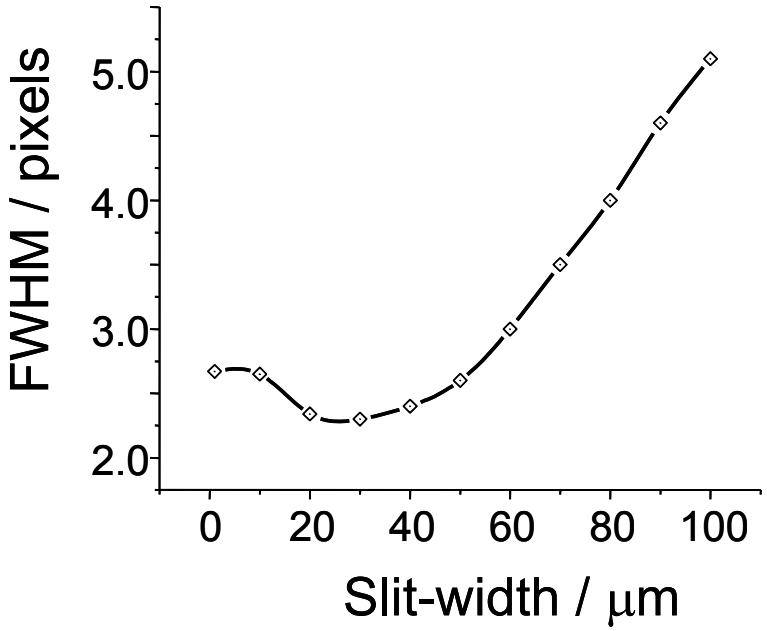

Figure 2.9: Dependence of width (FWHM) of the low pressure atomic Hg lamp line at (265.204 nm) upon slit width of the SPEX 1401 monochromator.

The width of the mercury line decreases with decreasing slitwidth down to ~ 50 micrometers, after which the slope flattens reaching its minimum of ~ 2 pixels or ~ 3 cm^{-1} at a monochromator slitwidth of ~ 20 micrometers. The increase in linewidth at small slitwidths presumably is due to diffraction at the slit aperture.

The resolution of the spectra accumulated by the second camera is significantly lower because light is dispersed only by the 1st, low groove density grating in the first stage. R_d calculated from experimental data at λ_{exc} = 204 nm is ~ 400 cm^{-1}/mm in the water stretch region,

which gives us the limiting spectral resolution of ~ 30 cm^{-1}. However, this resolution is adequate for the broad OH stretching bands of liquid water as shown by Fig. 2.10 A which show the Raman spectra of acetonitrile and water. The water band at ~ 3200 cm^{-1} is due to OH stretching while the acetonitrile bands at ~ 2943 cm^{-1} and ~ 2253 cm^{-1} derive from CH and CN stretching, respectively.

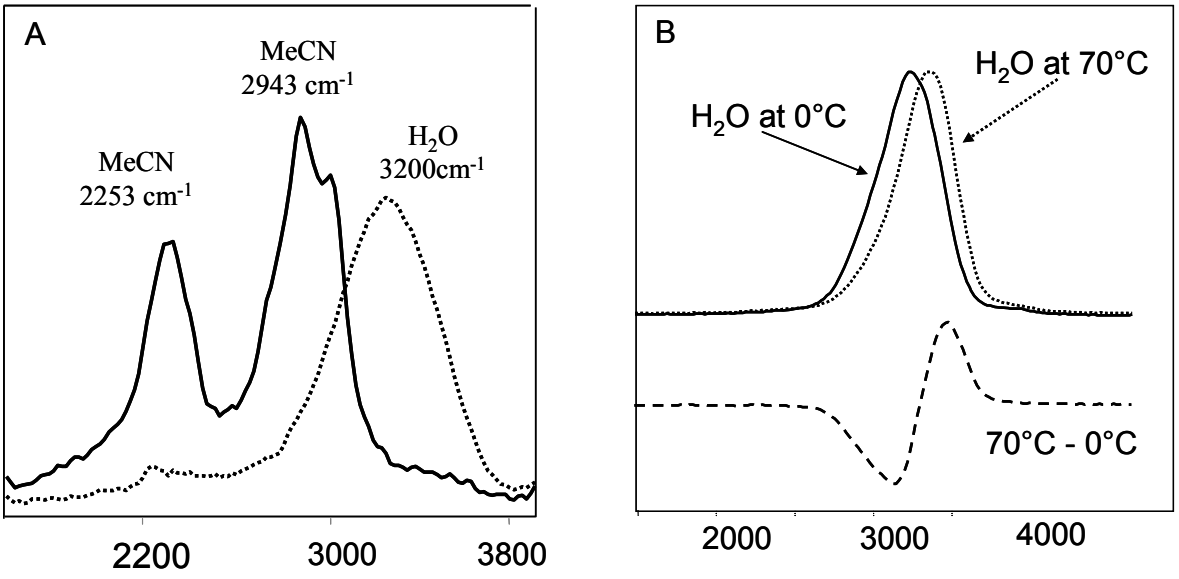

Figure 2.10: A UVRR spectra of acetonitrile and water excited at 204 nm detected by the second EG&G 1456 Princeton Applied Research Intensified Diode Array detector. B Water OH stretching band temperature dependence at 0 and 70 ºC.

Fig. 2.10 B shows two water spectra measured by the second detector at two different temperatures (70 °C and 0 °C) and the difference between them. The OH stretching band shows the shift to higher frequency which is associated with hydrogen bonding strength decrease as the temperature increases. This is a complex band which can be fitted with four Gaussian components. Each component is assigned to water molecules in different hydrogen bonding

states.[87] Much of the overall band shape change occurs due to redistribution of the water molecules among those states as the temperature changes. The measured value of $\Delta I/I_0$ can be used to calculate the solution temperature change.[51] Thus, we use these Raman spectra as an internal thermometer for determining the temperature of the small spot (~ 200 μm in diameter) heated by the IR pulse during the T-jump experiment.

2.4.6 Sample Handling

UV Raman measurements require constant exchange of the illuminated sample volume during the experiment. This is especially important if pulsed lasers with high peak powers are used for Raman excitation. These pulsed sources may cause sample heating and photochemical degradation. For liquid samples our temperature controlled open stream system produces the highest signal/noise ratios (Fig. 2.11). However, this sample cell requires a relatively large sample volume (~ 10 ml), and cannot be used with highly volatile liquids.

We use a thin quartz capillary for smaller 50 μL volumes of solution.[88] Temperature controlled quartz cells[19] with a magnetic stirrer are utilized when the sample may not be exposed to the air. Other types of quartz cells are commercially available from manufacturers such as Starna Cells Inc. (Atascadero, CA) or Uvonic Instruments Inc. (Plainview, NY). We also utilize rotating quartz NMR tubes to contain sample solutions for backscattering Raman measurements. The main disadvantage of quartz cells is the interference of SiO_2 Raman bands. The data reported here utilized the open stream system.

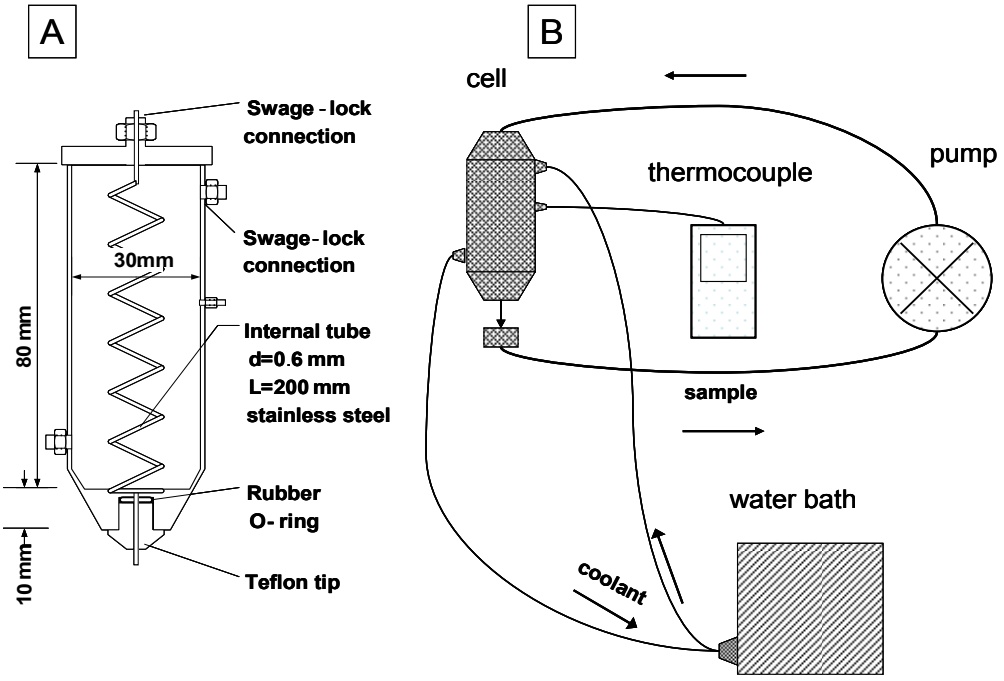

Figure 2.11: A. Temperature controlled flow-cell used for liquid samples. The sample cell was constructed from stainless steel and brass. A glass cell was used for samples sensitive to metal ions. The 0.6 mm diameter internal tube is ~ 200 mm long to allow efficient heat exchange with the thermally controlled reservoir. B. Temperature controlled flow system connections. The Micropump Inc model 120 pump obtained from Cole-Parmer Instrument Co. (Vernon Hills, IL) was controlled by a Model 75225 Pump Drive Controller which circulates the sample at a ~ 0.15 – 1.5 ml/sec flow rate. The flow rate is adjusted to minimize stream instabilities to avoid laser reflections and light scattering. This is especially important for the time resolved T-jump measurements where heating and probing pulses must be precisely superimposed on the stream surface. This system requires 10 ml of solution for normal operation. The temperature of the sample solution is controlled by a circulating thermostated water-thylene glycol solution whose temperature is controlled by a thermostated water bath.

Dielectric coated mirrors and fused silica prisms are used to direct the laser beam onto the sample. The back-scattered Raman light is collected and focused onto the spectrometer slit using a 50 mm diameter fused silica plano-convex lens matched to the spectrometer f/number. We have used the transient T-jump spectrometer to examine the earliest events in protein folding.[51,52]

2.4.7 Steady State and Transient Measurements

Figure 2.12 shows UVR Raman spectra of penta-alanine (Ala_5) in water solution taken with 193 and 204 nm excitation. Both excitation wavelengths are within the $\pi \rightarrow \pi^*$ transition of the peptide bond[89] which results in selective enhancement of the amide Raman bands. Since the Raman amide band frequencies and cross sections are sensitive to backbone geometry[90,91,81] they provide direct quantitative information about peptide/protein secondary structure.[30,47,92,93] Penta-alanine in water shows the typical UV resonance Raman spectra of a polypeptide chain in a PPII conformation[90] ($\psi \approx 145°$, $\varphi \approx -75°$) with the Amide I band at ~1663 cm^{-1}, the Amide II band at ~1560 cm^{-1}, the Amide III band at ~1254 cm^{-1}, $C_\alpha H$ bending bands at ~1371 cm^{-1} and at ~1401 cm^{-1}. The sharp and intense band at ~ 932 cm^{-1} is due to ClO_4^- that we use as an internal standard.

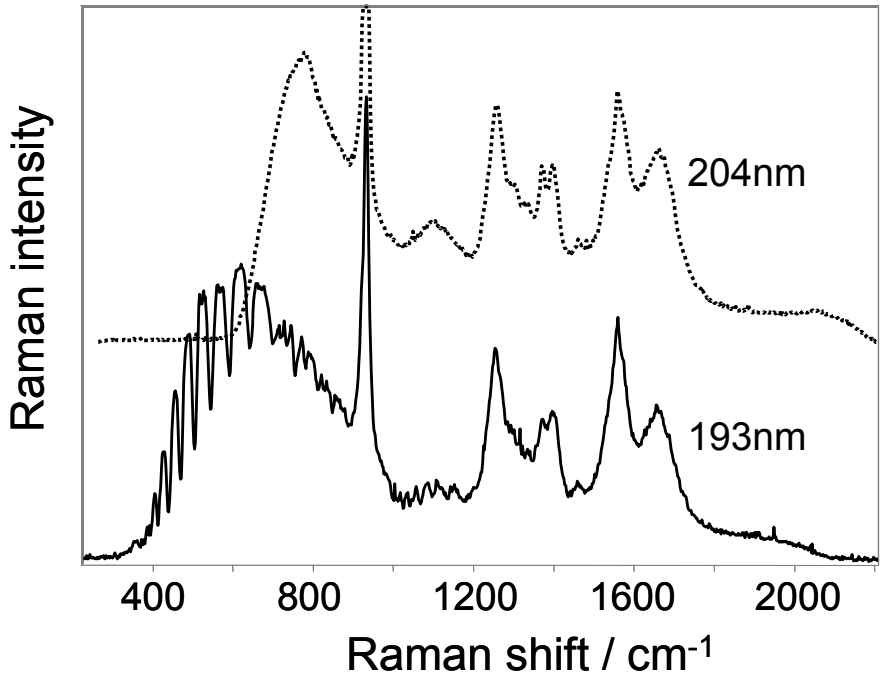

Figure 2.12: UVRR spectra of $(Ala)_5$ in water (C = 0.2 mg/ml) at room temperature. Accumulation time for each spectrum is 5 min with a slitwidth of 100 μm.

The broad and intense band at low frequencies is mainly due to H_2O bending with some contribution from stray light. In the spectrum excited with ~193 nm light a series of narrow troughs appears on the broad OH bending band of water at frequencies below 700 cm^{-1} that are due to molecular oxygen absorption by the Schumann-Runge bands of O_2, which arise from the transition $B^3\sum_u^- \leftarrow X^3\sum_g^-$ in the 175 - 205 nm region.[85] The UV light oxygen absorption does not significantly affect the 193 nm higher frequency amide region, but shorter excitation wavelengths would require an oxygen-free atmosphere.

The absorption frequencies and cross sections of the Schumann-Runge bands are well known.[94,95] Thus, the troughs in the UVRR spectra caused by Schumann-Runge bands can serve as internal frequency standards for Raman spectral calibration. In fact they could be used to independently determine the level of stray light present in the spectra.

Another possible application of the Schumann-Runge bands is to use them as very narrow frequency range absorption filters for suppressing Rayleigh lines in deep UV Raman spectroscopy. If the frequency of light used for UV Raman excitation coincides with that of strong oxygen absorption band, the Rayleigh light scattering could be significantly attenuated, given the large oxygen absorption cross sections which are as high as ~10^{-19} cm^2 at wavelengths close to 180 nm.

To demonstrate the utility of our setup for fast transient measurements we studied the kinetics of apo-Mb folding. We utilized a T-jump from -3 to 10 °C in D_2O at pD ≈ 6. Between these temperatures apoMb undergoes refolding from a cold denaturated state to a more compact native state. Figure 2.13 shows the steady state UVRR spectra of apo-Mb at -3 and 10 °C in D_2O. The amide backbone N-deuteration dramatically impacts the protein UVRR spectra, which is in D_2O dominated by an amide II' band which is almost a pure C-N stretch.[96] The hydrophobic core

of apo-Mb is mostly α-helical.[97] Upon a temperature increase from -3 to 10 °C we observe that the intensity of the amide II' band decreases due to the α-helix fraction increase and the resulting hypochromism present in the intact α-helix folded conformations.

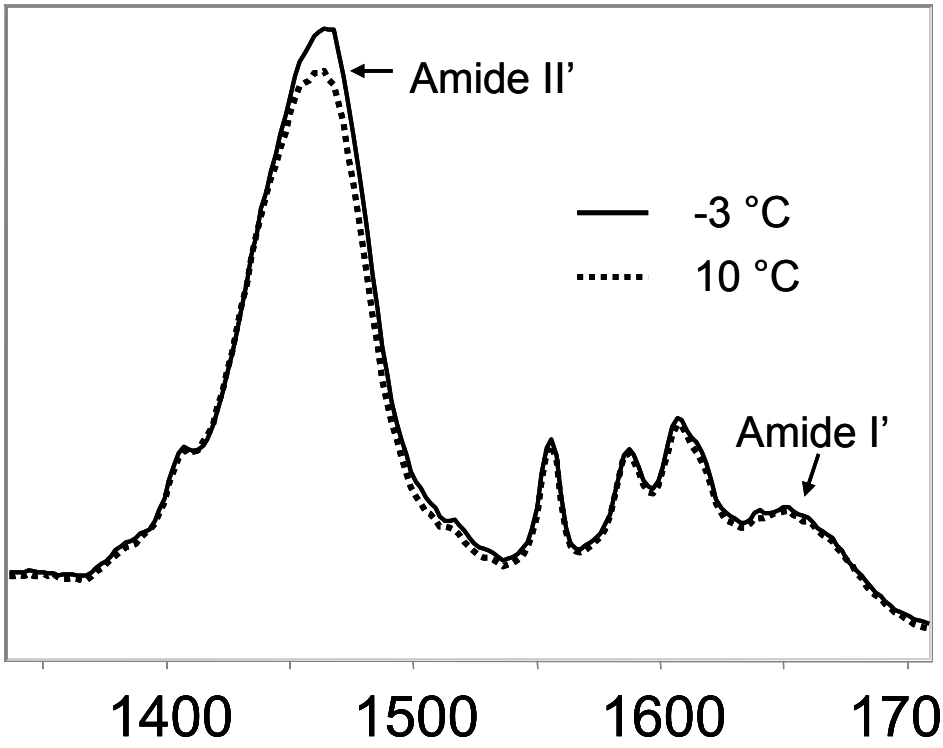

Figure 2.13: Steady state UVRR spectra of apo-Mb at -3 amd +10 °C in D_2O, pD ~ 6, concentration is 40 μM. The amide II' intensity decrease indicates apo-Mb refolding.

Figure 2.14 A shows the transient difference spectra obtained by subtracting steady state apo-Mb UVRR spectra at -3 °C from transient spectra measured at delays of 400 ns, 20 μs and 300 μs subsequent to a T-jump from -3 to 10 °C. The major transient change observed is the amide II' intensity decrease observed in the steady state measurement of Fig. 2.13. Transient difference spectra measured with delays shorter than 400 ns do not show significant spectral

changes. Thus, the refolding process requires at least 400 nsec to begin. Transient difference spectra at delays longer than 300 μs (not shown) are essentially identical to the steady state difference spectrum indicating that apo-Mb refolding is essentially complete within a few hundred microseconds.

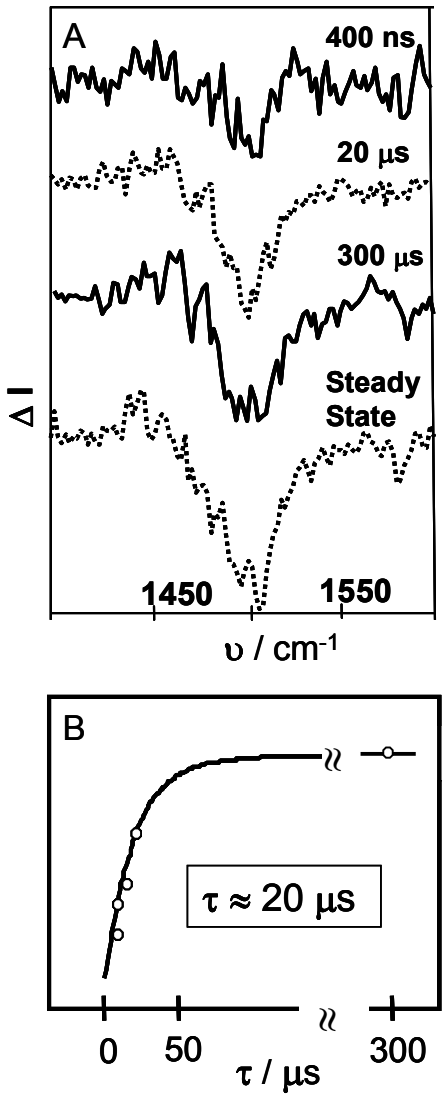

Figure 2.14: A apo-Mb difference spectra obtained by subtracting steady state spectra at -3 °C from transient spectra measured at time delays of 400 ns, 20 μs, 300 μs and at an infinite time delay (steady state). B – Relaxation curve for apo-Mb refolding after T-jump from -3 to 10 °C. Refolding is monitored by a change in the amide II' intensity. The data is best fit by single exponential decay with a relaxation time of ~ 20 μs**.**

The relaxation kinetics curve for apo-Mb is shown in Fig. 2.14 B fits well to a mono-exponential decay with a relaxation time of ~ 20 μs. This relaxation time is significantly longer than the typical ~200 nsec delay times observed for short helical monomeric peptides[51,98,99]. This indicates an increase in constraints for α-helix folding in apo-Mb due to the tertiary interactions present for this protein. These kinetic results agree well with apo-Mb cold denaturation kinetic studies using methods such as fluorescence[100], IR.[101]

2.5 CONCLUSIONS

We built a novel UV Raman spectrometer for steady state and kinetic spectral measurements. Steady state measurements can now be made with any excitation wavelengths between 193 - 270 nm, and with discrete Nd:YAG harmonics and Raman shifted lines at discrete frequencies from the UV through the visible spectral region. High average powers together with low peak powers allow accumulation of high signal-to-noise UVRR spectra within short periods of time.

We constructed a novel high efficiency subtractive double spectrograph which is efficient in the deep UV region down to excitation wavelengths as short as 193 nm. We used two detectors to simultaneously measure high resolution spectra in the amide band region of proteins (~ 800 - 1800 cm^{-1}) and low resolution spectra in the water OH stretching band region (~ 2500 - 4000 cm^{-1}). This spectrometer can also be used with nsec Nd:YAG excitation for transient pump probe methods which permit T-jumps as well as electronic excitation by nsec pulses from the IR through the visible into the UV excitation region.

ACKNOWLEDGEMENT. The authors thank Bhavya Sharma, Konstantin Pimenov, Jonathan Scaffidi and Zeeshan Ahmed for the help in preparing of this manuscript. This work was supported by NIH grant 8RO1 EB002053021.

2.6 BIBLIOGRAPHY

1. P. J. Hendra, The Raman Spectroscopy of Polymers (Wiley, New York, 1993).

2. I. R. Lewis and H. G. M. E. Edwards, Handbook of Raman Spectroscopy (Marcel Dekker, Inc., New York, 2001).

3. J. M. Chalmers and G. Dent, Instrumental Analysis with Raman Spectroscopy (Royal Society of Chemistry, Cambridge, 1997).

4. Z. Huang, A. McWilliams, H. Lui, D. I. McLean, S. Lam, and H. Zeng, International Journal of Cancer **107,** 1047 (2003).

5. B. Schrader, B. Dippel, I. Erb, S. Keller, T. Lochte, H. Schulz, E. Tatsch, and S. Wessel, Journal of Molecular Structure **480-481,** 21 (1999).

6. C. Krafft, Analytical and Bioanalytical Chemistry **378,** 60 (2004).

7. N. S. Eikje, Y. Ozaki, K. Aizawa, and S. Arase, Journal of Biomedical Optics **10,** 014013/1 (2005).

8. H. Schulz, M. Baranska, and R. Baranski, Biopolymers **77,** 212 (2005).

9. T. Hirschfeld and B. Chase, Applied Spectroscopy **40,** 133 (1986).

10. D. A. Long, The Raman Effect (John Wiley & Sons Ltd, Baffins Lane, Chichester, West Sussex PO19 1UD, England, 2002).

11. T. G. Spiro, Advances in Protein Chemistry **37,** 111 (1985).

12. T. G. Spiro, G. Smulevich, and C. Su, Biochemistry **29,** 4497 (1990).

13. T. Kitagawa and T. Ogura, Advances in Spectroscopy (Chichester, United Kingdom) **21,** 139 (1993).

14. V. Palaniappan and D. F. Bocian, Biochemistry **33,** 14264 (1994).

15. K. Nakamoto, Coordination Chemistry Reviews **226,** 153 (2002).

16. P. R. Carey, Biochemical Applications of Raman and Resonance Raman Spectroscopies (Academic Press, New York, 1982), Chap. 8, p. 100.

17. T. G. Spiro and C. A. Grygon, Journal of Molecular Structure **173,** 79 (1988).

18. J. A. Sweeney and S. A. Asher, Journal of Physical Chemistry **94,** 4784 (1990).

19. P. J. Larkin, W. G. Gustafson, and S. A. Asher, Journal of Chemical Physics **94,** 5324 (1991).

20. G. G. Kochendoerfer, S. Kaminaka, and R. A. Mathies, Biochemistry **36,** 13153 (1997).

21. L. Mayne and B. Hudson, Journal of Physical Chemistry **91,** 4438 (1987).

22. Z. Chi and S. A. Asher, Journal of Physical Chemistry B **102,** 9595 (1998).

23. V. W. Couling, P. Fischer, D. Klenerman, and W. Huber, Biophysical Journal **75,** 1097 (1998).

24. L. Sokolov and I. Mukerji, Journal of Physical Chemistry B **104,** 10835 (2000).

25. Z. Q. Wen, S. A. Overman, P. Bondre, and G. J. Thomas, Jr., Biochemistry **40,** 449 (2001).

26. N. Haruta, M. Aki, S.-i. Ozaki, Y. Watanabe, and T. Kitagawa, Biochemistry **40,** 6956 (2001).

27. S. Hashimoto, M. Sasaki, H. Takeuchi, R. Needleman, and J. K. Lanyi, Biochemistry **41,** 6495 (2002).

28. A. Toyama, Y. Takahashi, and H. Takeuchi, Biochemistry **43,** 4670 (2004).

29. I. R. Rodriguez-Mendieta, G. R. Spence, C. Gell, S. E. Radford, and D. A. Smith, Biochemistry **44,** 3306 (2005).

30. R. A. Copeland and T. G. Spiro, Biochemistry **26,** 2134 (1987).

31. S. Song, S. A. Asher, S. Krimm, and J. Bandekar, Journal of the American Chemical Society **110,** 8547 (1988).

32. S. A. Asher, Z. Chi, and P. Li, Journal of Raman Spectroscopy **29,** 927 (1998).

33. M. Xu, V. V. Ermolenkov, W. He, and I. K. Lednev, Abstracts of Papers, 229th ACS National Meeting, San Diego, CA, United States, March 13-17, 2005**,** PHYS (2005).

34. S. A. Asher and C. R. Johnson, Science (Washington, DC, United States) **225,** 311 (1984).

35. L. D. Ziegler and B. Hudson, Journal of Chemical Physics **74,** 982 (1981).

36. S. A. Asher, C. R. Johnson, and J. Murtaugh, Review of Scientific Instruments **54,** 1657 (1983).

37. R. P. Rava and T. G. Spiro, Journal of Physical Chemistry **89,** 1856 (1985).

38. S. A. Asher, R. W. Bormett, X. G. Chen, D. H. Lemmon, N. Cho, P. Peterson, M. Arrigoni, L. Spinelli, and J. Cannon, Applied Spectroscopy **47,** 628 (1993).

39. S. Hashimoto, T. Ikeda, H. Takeuchi, and I. Harada, Applied Spectroscopy **47,** 1283 (1993).

40. M. P. Russell, S. Vohnik, and G. J. Thomas, Jr., Biophysical Journal **68,** 1607 (1995).

41. V. Pajcini, C. H. Munro, R. W. Bormett, R. E. Witkowski, and S. A. Asher, Applied Spectroscopy **51,** 81 (1997).

42. X. Zhao, C. Tengroth, R. Chen, W. R. Simpson, and T. G. Spiro, Journal of Raman Spectroscopy **30,** 773 (1999).

43. X. Zhao, R. Chen, C. Tengroth, and T. G. Spiro, Applied Spectroscopy **53,** 1200 (1999).

44. M. C. Sparrow, J. F. Jackovitz, C. H. Munro, W. F. Hug, and S. A. Asher, Applied Spectroscopy **55,** 66 (2001).

45. H. S. Sands, F. Demangeot, E. Bonera, S. Webster, R. Bennett, I. P. Hayward, F. Marchi, D. A. Smith, and D. N. Batchelder, Journal of Raman Spectroscopy **33,** 730 (2002).

46. I. K. Lednev, V. V. Ermolenkov, W. He, and M. Xu, Analytical and Bioanalytical Chemistry **381,** 431 (2005).

47. Z. Chi, X. G. Chen, J. S. W. Holtz, and S. A. Asher, Biochemistry **37,** 2854 (1998).

48. S. Kaminaka, T. Ogura, and T. Kitagawa, Journal of the American Chemical Society **112,** 23 (1990).

49. P. J. Reid, S. J. Doig, S. D. Wickham, and R. A. Mathies, Journal of the American Chemical Society **115,** 4754 (1993).

50. V. Jayaraman, K. R. Rodgers, I. Mukerji, and T. G. Spiro, Science (Washington, D. C.) **269,** 1843 (1995).

51. I. K. Lednev, A. S. Karnoup, M. C. Sparrow, and S. A. Asher, Journal of the American Chemical Society **121,** 8074 (1999).

52. I. K. Lednev, A. S. Karnoup, M. C. Sparrow, and S. A. Asher, Journal of the American Chemical Society **123,** 2388 (2001).

53. X. Zhao, G. Balakrishnan, E. G. Moore, and T. G. Spiro, Journal of Raman Spectroscopy **31,** 349 (2000).

54. D. Wang, X. Zhao, and T. G. Spiro, Journal of Physical Chemistry A **104,** 4149 (2000).

55. N. Haruta and T. Kitagawa, Biochemistry **41,** 6595 (2002).

56. T. Kitagawa, N. Haruta, and Y. Mizutani, Biopolymers **61,** 207 (2002).

57. J. E. Kim, D. Pan, and R. A. Mathies, Biochemistry **42,** 5169 (2003).

58. J. Kneipp, G. Balakrishnan, and T. G. Spiro, Journal of Physical Chemistry B **108,** 15919 (2004).

59. S. A. Asher, Annual Review of Physical Chemistry **39,** 537 (1988).

60. R. W. Wood, Nature (London, United Kingdom) **125,** 464 (1930).

61. M. Werth, Physical Review **39,** 299 (1932).

62. J. Teraoka, P. A. Harmon, and S. A. Asher, Journal of the American Chemical Society **112,** 2892 (1990).

63. C. M. Jones, V. L. Devito, P. A. Harmon, and S. A. Asher, Applied Spectroscopy **41,** 1268 (1987).

64. C. Su, Y. Wang, and T. G. Spiro, Journal of Raman Spectroscopy **21,** 435 (1990).

65. J. S. W. Holtz, R. W. Bormett, Z. Chi, N. Cho, X. G. Chen, V. Pajcini, S. A. Asher, L. Spinelli, P. Owen, and M. Arrigoni, Applied Spectroscopy **50,** 1459 (1996).

66. G. Balakrishnan, Y. Hu, S. B. Nielsen, and T. G. Spiro, Applied Spectroscopy **59,** 776 (2005).

67. F. W. J. Teale, Biochimica et Biophysica Acta **35,** 543 (1959).

68. F. Grum and a. G. W. Luckey, Applied Optics **7,** 2289 (1968).

69. W. Erb, Applied Optics **14,** 493 (1975).

70. E. R. Young, K. C. Clark, R. B. Bennett, and a. T. L. Houk, Applied Optics **19,** 3500 (1980).

71. V. Wilke and W. Schmidt, Applied Physics (Berlin) **16,** 151 (1978).

72. D. P. Gerrity, L. D. Ziegler, P. B. Kelly, R. A. Desiderio, and B. Hudson, Journal of Chemical Physics **83,** 3209 (1985).

73. A. D. Papayannis, G. N. Tsikrikas, and A. A. Serafetinides, Applied Physics B: Lasers and Optics **B67,** 563 (1998).

74. S. Ameen, Review of Scientific Instruments **46,** 1209 (1975).

75. M. A. Donaldson, Journal of Scientific Instruments **29,** 150 (1952).

76. V. Deckert, C. Fickert, D. Gernet, P. Vogt, T. Michelis, and W. Kiefer, Applied Spectroscopy **49,** 253 (1995).

77. R. W. Bormett and S. A. Asher, Applied Spectroscopy **48,** 1 (1994).

78. P. H. v. Cittert, Physica **3,** 181 (1923).

79. C. Leiss, Z. Phys **77,** 412 (1932).

80. G. A. Boutry, Instrumental Optics (Interscience, NY)**,** 532 (1961).

81. F. R. Lipsett, G. Oblinsky, and S. Johnson, Applied Optics **12** (1973).

82. R. E. Siemon, Applied Optics **13,** 697 (1974).

83. D. J. Dunstan and M. D. Frogley, Review of Scientific Instruments **73,** 3742 (2002).

84. R. Mathies, Chemical and biochemical applications of lasers, New York, Academic Press. (Moor, C.B. ed.) **v.4,** 55 (1979).

85. B. R. Lewis, S. T. Gibson, L. W. Torop, and D. G. McCoy, Geophysical Research Letters **25,** 2457 (1998).

86. G. E. Walrafen, M. R. Fisher, M. S. Hokmabadi, and W. H. Yang, Journal of Chemical Physics **85,** 6970 (1986).

87. N. Nishi, T. Nakabayashi, and K. Kosugi, Journal of Physical Chemistry A **103,** 10851 (1999).

88. X. G. Chen, D. H. Lemmon, R. W. Bormett, and S. A. Asher, Applied Spectroscopy **47,** 248 (1993).

89. A. P. Demchenko, *Ultraviolet Spectroscopy of Proteins* (Spring-Verlag, New York, 1986).

90. S. A. Asher, A. V. Mikhonin, and S. Bykov, Journal of the American Chemical Society **126,** 8433 (2004).

91. A. Ianoul, M. N. Boyden, and S. A. Asher, Journal of the American Chemical Society **123,** 7433 (2001).

92. J. C. Austin, K. R. Rodgers, and T. G. Sprio, Methods in enzymology **226,** 374 (1993).

93. S. A. Asher, A. Ianoul, G. Mix, M. N. Boyden, A. Karnoup, M. Diem, and R. Schweitzer-Stenner, Journal of the American Chemical Society **123,** 11775 (2001).

94. K. Yoshino, D. E. Freeman, J. R. Esmond, and W. H. Parkinson, Planetary and Space Science **31,** 339 (1983).

95. T. Matsui, A. S. C. Cheung, K. W. S. Leung, K. Yoshino, W. H. Parkinson, A. P. Thorne, J. E. Murray, K. Ito, and T. Imajo, Journal of Molecular Spectroscopy **219,** 45 (2003).

96. X. G. Chen, S. A. Asher, R. Schweitzer-Stenner, N. G. Mirkin, and S. Krimm, Journal of the American Chemical Society **117,** 2884 (1995).

97. H. C. Shin, G. Merutka, J. P. Waltho, L. L. Tennant, H. J. Dyson, and P. E. Wright, Biochemistry **32,** 6356 (1993).

98. C.-Y. Huang, Z. Getahun, Y. Zhu, J. W. Klemke, W. F. DeGrado, and F. Gai, Proceedings of the National Academy of Sciences of the United States of America **99,** 2788 (2002).

99. T. Wang, Y. Zhu, Z. Getahun, D. Du, C.-Y. Huang, W. F. DeGrado, and F. Gai, Journal of Physical Chemistry B **108,** 15301 (2004).

100. R. M. Ballew, J. Sabelko, and M. Gruebele, Proceedings of the National Academy of Sciences of the United States of America **93,** 5759 (1996).

101. R. Gilmanshin, R. H. Callender, and R. B. Dyer, Nature Structural Biology **5,** 363 (1998).

3.0 INVESTIGATION OF NEW CONFORMATIONAL MARKERS

This chapter was published in *Journal of Physical Chemistry B* **2008**, *112*, 5803-5812. The coathors are Sergei V. Bykov, Nataliya S. Myshakina and Sanford A. Asher

3.1 DEPENDENCE OF GLYCINE CH_2 STRETCHING FREQUENCIES ON CONFORMATION, IONIZATION STATE, AND HYDROGEN BONDING

We experimentally and theoretically examined the conformation, pH and temperature dependence of the CH_2 stretching frequencies of glycine (gly) in solution and in the crystalline state. To separate the effects of the amine and carboxyl groups on the CH_2 stretching frequencies we examined the Raman spectra of 2,2,2-d_3-ethylamine (CD_3-CH_2-NH_2) and 3,3,3-d_3-propionic acid (CD_3-CH_2-COOH) in D_2O. The symmetric ($\nu_s CH_2$) and asymmetric ($\nu_{as} CH_2$) stretching frequencies show a significant dependence on gly conformation. We quantified the relation between the frequency splitting ($\Delta = \nu_{as} CH_2 - \nu_s CH_2$) and the ξ angle which determines the gly conformational geometry. This relation allows us to determine the conformation of gly directly from the Raman spectral frequencies. We observe a large dependence of the $\nu_s CH_2$ and $\nu_{as} CH_2$ frequencies on the ionization state of the amine group, which we demonstrate theoretically results from a negative hyperconjugation between the nitrogen lone pair and the C-H anti-bonding orbitals. The magnitude of this effect is maximized for C-H bonds trans to the nitrogen

lone pair. In contrast, a small dependence of the CH_2 stretching frequencies on the carboxyl group ionization state arises from delocalization of electron density from carboxyl oxygen to C-H bonding orbitals. According to our experimental observations and theoretical calculations the temperature dependence of the $\nu_s CH_2$ and $\nu_{as} CH_2$ of gly is due to the change in the hydrogen bonding strength of the amine/carboxyl groups to water.

3.1.1 Introduction

Vibrational spectroscopy is a powerful technique to study the conformations of peptides and proteins. Vibrational spectroscopy provides a unique opportunities to study fast protein folding dynamics[1-5] and unordered states of polypeptides chains.[6] Vibrational spectra are highly informative on molecular structure due to the extreme sensitivity of certain vibrational bands or so-called "conformational markers", to the small structural alterations such as bond lengths, dihedral angles, and hydrogen bonding patterns.

The most commonly used markers for the polypeptide backbone conformation analysis are the amide bands. The Amide I band (primarily C=O stretching of the peptide bond) is used for the IR spectroscopy secondary structure elucidation.[1,5] The Amide II, Amide III and $C_\alpha H$ bending vibrations, observed in Raman spectra, have been shown to be even more valuable for peptide secondary structure analysis.[3,4,7,8] There should be other conformationally sensitive vibrations which can be used to expand the informational context of vibrational spectroscopy.

The CH (or deuterated CD) stretch is a potential candidate for use as a conformational marker to study the secondary structure of polypeptide chains. It has recently been shown theoretically[9,10] that the $C_\alpha H$ ($C_\alpha D$) bond stretching frequency depends on the ψ and φ Ramachandran angles.

CH stretching vibrations have previously been used to determine the structure of small organic molecules. Isolated C-D stretching frequencies have also been used in the conformational analysis of alkylamino chains,[11] and monosaccharides.[12] Good correlations have been experimentally found between isolated methyl CH stretching frequencies and HCH angles.[13]

The origin of the CH conformational sensitivity is not well understood. It is generally agreed that the CH stretching frequencies depend almost solely on the C-H bond lengths because these vibrations are essentially decoupled from other vibrations. Previous work has quantified the relationship between CH stretching frequencies and C-H bond lengths in various organic compounds[14,15] This work includes McKean, Bellamy and others[16,17] extensive IR spectroscopy studies in 60's and 70's which examined the factors influencing CH stretching frequencies

In the present study we focus our attention on gly, the smallest amino acid, which has a hydrogen atom instead of a side chain. There is no coupling of the gly CH_2 stretches in proteins and peptides with the CH stretches of the adjacent amino acid residue side chains. In addition, the CH_2 stretches of gly are unaffected by Fermi resonances because of the significant downshift of the CH_2 scissoring vibration. The two CH stretches of the gly CH_2 group couple with each other to form a high-frequency asymmetric and a low-frequency symmetric CH_2 stretching components, which appear as a doublet in the Raman spectra. The magnitude of the frequency splitting of this doublet depends on the extent of vibrational coupling which in turn is determined by the C-H bond length difference.

The unique flexibility of gly makes it an essential structural element of many proteins, determining protein folding pathways, tertiary structure and biological function. Gly is frequently found in the turn and loop structures, which play an important role in polypeptide

chain collapse during the early stages of folding. Gly accelerates loop formation compared to other amino acids.[18] Gly rich flexible motifs are often impossible to characterize by x-ray crystallography and 2D NMR.[19] Thus, there is a great need to develop new structural methods to determine the gly residue conformations.

In this paper we investigate the gly CH_2 stretching frequency dependence on amino acid conformation and ionization state in order to develop methodologies for the conformational analysis of gly residues in polypeptides and proteins.

3.1.2 Experimental methods

3.1.2.1 Sample Preparation

For the pD measurements anhydrous gly (Sigma Chemicals) was dissolved in D_2O (Cambride Isotope Laboratories Inc). Low and high pD samples were prepared by addition of DCl or NaOD solutions (Sigma Chemicals). 2,2,2-d_3-ethylamine hydrochloride was obtained from Medical Isotopes Inc. and 3,3,3-d_3-propionic acid from Cambride Isotope Laboratories Inc. Crystals of Gly•HCl, Gly•HNO_3, 3Gly•H_2SO_4 (TGS) were obtained by slow evaporation of water solutions of stoichiometric mixtures of gly and the corresponding acid. All acids were purchased from J. T. Baker Inc. Crystal structures were determined by using x-ray crystallography.

3.1.2.2 Raman measurements

All Raman measurements were performed using 488 nm Ar-ion Laser (Coherent Inc.) excitation. Scattered light was collected using a back-scattering geometry, dispersed by a single monochromator and collected using a Princeton Instruments Spec-10:400B CCD camera (Roper

Scientific). A 488 nm holographic notch filter (Kaiser Optical Systems Inc.) was used for Raleigh rejection. Typical accumulation times were ~ 2 min. A temperature controlled fused silica cell (20 mm path length, Starna Cell Inc.) was used for solutions. A custom made, rotating metal cell was used for solid powder samples to avoid light-induced degradation under continuous irradiation. The powder was pressed into a circular groove cut in the rotating metal cylinder.

3.1.3 Computational methods

We optimized the geometries and calculated the vibrational frequencies, normal mode compositions, molecular orbital analysis, and charge distributions of a series of gly conformers in neutral and zwitterionic forms. We also performed the calculations for zwitterionic gly hydrogen bonded to one or two water molecules (Fig. 3.1).

All calculations were carried out at the DFT level of theory[20-22] employing the B3LYP exchange functional[23-25] and 6-311+G(d,p) basis set. All frequencies were calculated at the harmonic approximation and scaled by 0.98.[26,27] The presence of the solvent water was modeled using the Polarizable Continuum Model (PCM) initially devised by Tomasi and coworkers.[28-30] The PCM calculations were performed using the integral equation formalism model[30] (IEFPCM) and the Bondii's atomic radii. Atomic charges were calculated using the Atoms in Molecule (AIM) algorithm[31-33] as implemented in Gaussian'98. Orbital occupancies and hybridization analysis of Natural Local Molecular Orbitals were obtained through the Natural Bond Orbital (NBO) Analysis. All calculations except the AIM charge calculations were performed with the Gaussian'03 calculational package.[34] Normal mode compositions for the calculated vibrational frequencies were obtained from the Gaussian output files employing the GAR2PED program.[35]

Since the primary interest of our study is the conformational dependence of the CH_2 stretching frequencies we constrained the geometry of gly to conformations of interest. We fixed the dihedral angle N1-C3-C6-O9 (defined as ξ) at 0° in the anti and gauche rotamers of neutral gly (Fig. 3.1a) and eclipsed-gly$^{\pm}$ (Fig. 3.1b). We fixed ξ at -60° in twisted-gly$^{\pm}$. In staggered-gly$^{\pm}$ in addition to ξ=0° we fixed H8-N1-C3-C6 at -60° to prevent its relaxation to more stable eclipsed-gly$^{\pm}$. We also studied a series of conformers of neutral glycine with the ξ angle fixed at values 80° from -80°.

3.1.4 Experimental Results

3.1.4.1 The conformational dependence of the CH_2 stretching frequencies on carboxyl group orientation of gly in the solid state

We investigated the structures of gly found in the Cambridge Structural Database:

1) Gly hydrochloride (Gly•HCl). In this crystal all heavy atoms lie almost in the same plane.[36]

2) Gly nitrate (Gly•HNO_3). Here gly is bent.[37]

3) Triglycine sulphate (3Gly•H_2SO_4), TGS. In this crystal structure two gly molecules have geometries close to planar while one gly molecule is bent.[38]

In these structures the amine groups are protonated (-NH_3^+). Thus, rotation about the N-C bond should not significantly affect the CH_2 stretching frequencies.

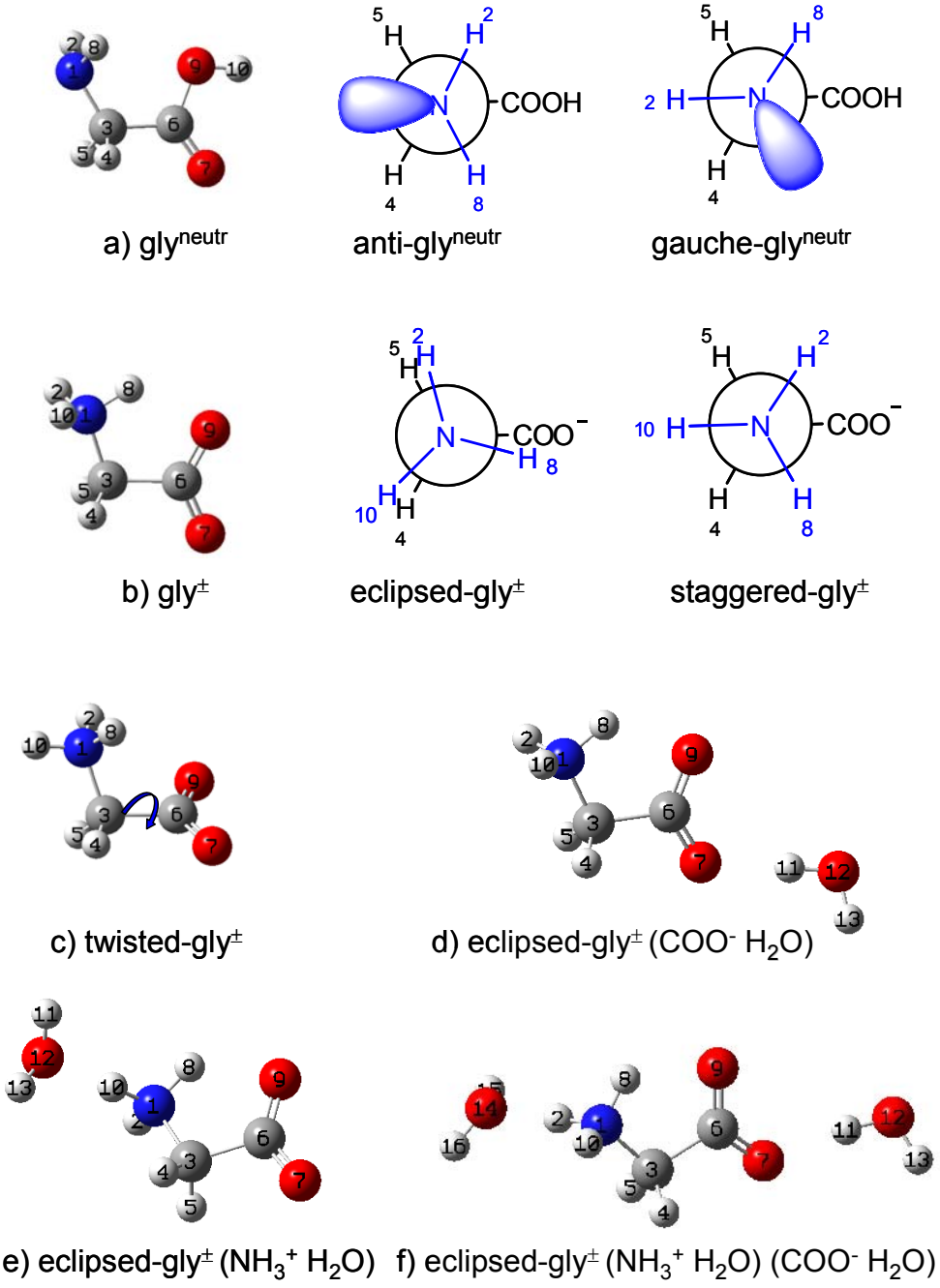

Figure 3.1: Calculated conformers of gly: a) anti and gauche rotamers of neutral gly; b) eclipsed and staggered rotamers of zwitterionic gly; c) non-planar conformer (ξ = -60°) of zwitterionic gly; d) eclipsed zwitterionic gly hydrogen bonded to the acceptor water molecule, e) eclipsed zwitterionic gly hydrogen bonded to the donor water molecule, f) eclipsed zwitterionic gly hydrogen bonded simultaneously to the acceptor and donor water molecules. All conformers except c) are planar ξ = 0°.

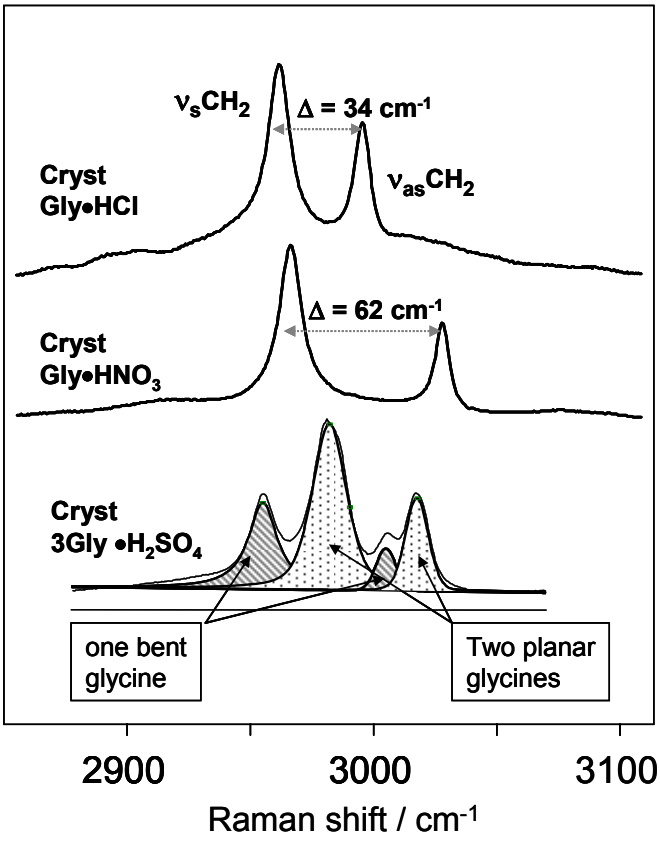

Figure 3.2: Raman spectra of the CH stretching region of the crystalline gly hydrochloride (Gly•HCl), crystalline gly nitrate (Gly•HNO_3), crystalline trigly sulphate or TGS (3Gly•H_2SO_4).

There is a remarkable difference in the frequencies and the frequency splitting between the CH_2 symmetric ($\nu_s CH_2$) and asymmetric ($\nu_{as} CH_2$) stretching frequencies for these three samples. The Raman spectrum of crystalline Gly•HCl shows the symmetric and asymmetric stretching bands at $\nu_s CH_2$ = 2962 cm^{-1} and $\nu_{as} CH_2$ = 2996 cm^{-1}, with a splitting Δ of ~ 34 cm^{-1}. Crystalline Gly•HNO_3 has a much larger splitting, Δ ~ 62 cm^{-1} between the $\nu_s CH_2$ = 2966 cm^{-1} and $\nu_{as} CH_2$ = 3028 cm^{-1} bands, mainly due to the upshift of the $\nu_{as} CH_2$. TGS has 3 nonequivalent gly in the crystal unit cell. In TGS we observe two different doublets of $\nu_s CH_2$ and $\nu_{as} CH_2$.

X-ray crystallographic data shows (Fig. 3.3) that in Gly•HCl crystals all heavy atoms (N-C-COO) lie almost in the same plane and the two C-H bonds are symmetrically disposed about this plane. The dihedral angel ξ, defined by atoms N-C-C-$O_{cis\ to\ N}$ (since carboxyl group has two oxygens, ξ is defined by the one which is the closest (cis) to the nitrogen). The ξ angle indicates the deviation of gly from the planar conformation through rotation around the C-C bond. When ξ = 0˚ all heavy atoms in the gly molecule lie in the same plane (Figure 3.3). In contrast, the -COOH group of the Gly•HNO_3 crystal is rotated such that ξ ~ 21°. In this case the C-H bonds are not symmetrically disposed on both sides of the COO plane, which results in greater splitting between the $\nu_s CH_2$ and $\nu_{as} CH_2$ frequencies.

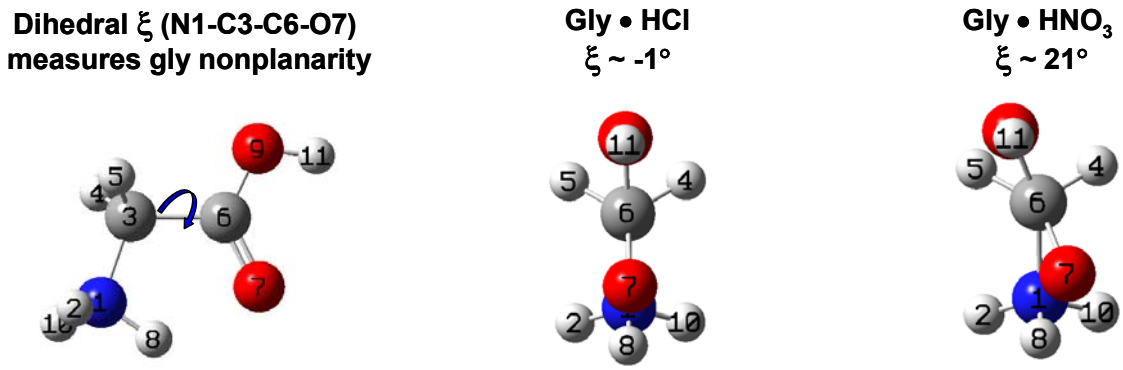

Figure 3.3: Dihedral angle ξ measures planarity of gly molecule. If ξ ~ 0°, the molecule is planar and the C-H bonds are symmetric with respect to the carboxyl group plane, as in case of Gly•HCl. In Gly•HNO_3 the carboxyl is rotated ~ 21° with respect to the N1-C3 bond making the C-H bonds nonequivalent.

In TGS crystals, two of the gly molecules are almost planar (ξ = 4° and = 5°), while the third one is bent ξ ~ 21°. Thus, we assign the more intense, less split doublet (2982 cm^{-1} and 3017 cm^{-1}) to the two planar gly molecules and the less intense more split doublet (2956 cm^{-1} and 3005 cm^{-1}) to the third gly.

3.1.4.2 pD and temperature dependences of the CH_2 stretching frequencies of gly in solution

We investigated the influence of the ionization state of the carboxyl and amine groups on the CH_2 stretching vibrations. Deuteration of the amine in gly molecule significantly downshifts the N-D stretches which removes overlap or coupling between C-H and N-D stretches and simplifies the interpretation of the Raman spectra.

Figure 3.4 shows the 488 nm Raman spectra of gly in D_2O at various pD values at 5°C and 60°C. At low pD values gly is cationic D_3N^+-CH_2-COOD (gly^+), while at pD values close to neutral gly is zwitterionic D_3N^+-CH_2-COO^- ($gly^\pm$), and at high pD values gly is anionic D_2N-CH_2-COO^- (gly^-).

pD Dependence. For the low pD (gly^+) and neutral pD values ($gly^\pm$) the CH_2 stretching region Raman spectra are very similar, indicating that the ionization state of the carboxyl group has little effect on the CH_2 group stretching frequencies. The CH_2 symmetric stretch is at ~ 2970 cm^{-1} and is ~ 4 times more intense than the CH_2 asymmetric stretch at ~ 3010 cm^{-1}.

For pD values close to or above the pK_a value of the gly amine group (pD = 9.8) a peak appears at lower frequency ~ 2920 cm^{-1}, which must be due to C-H bond weakening due to interaction with the lone pair of the unprotonated amine group ($-ND_2$), as discussed in detail below.

The frequency splitting between ν_sCH_2 and $\nu_{as}CH_2$ is ~ 41 cm^{-1} for gly^+ and $gly^\pm$, while for gly^- it is smaller (Δ ~ 34 cm^{-1}).

Thus, the C-H bonds stretching frequencies depend only on the ionization state of the terminal amine with a little influence of the ionization state of the carboxyl.

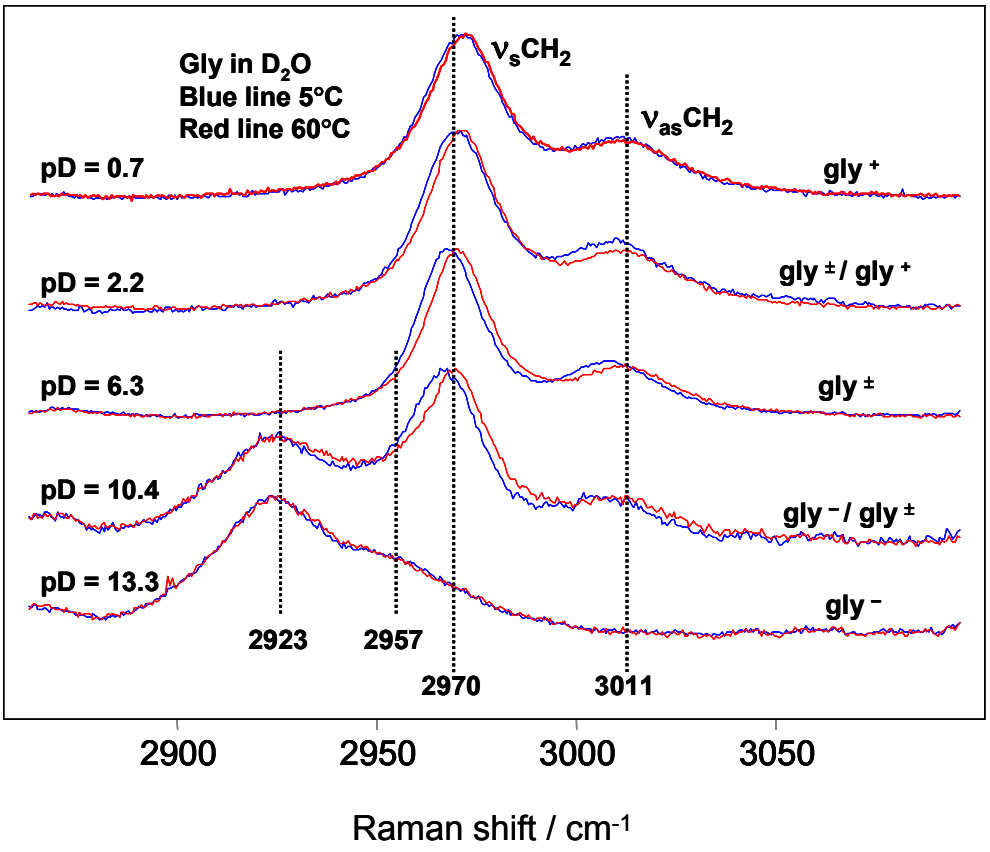

Figure 3.4: 488 nm excitation Raman spectra of gly solution in D_2O at pD = 0.7, 2.2, 6.3, 10.4, 13.3. For each solution spectra were accumulated at two temperatures 5°C and 60°C.

Temperature dependence. Figure 3.4 and Table 3.1 indicate the temperature dependence of the CH_2 stretching frequencies of gly in D_2O.

There is a significant temperature dependence of the symmetric and asymmetric CH_2 stretching frequencies on pD. Temperature induced frequency shifts are larger at neutral pD than at high or low pD values. At pD = 13.3 the broad low frequency doublet is essentially temperature independent.

Table 3.1: Temperature dependence of the Raman CH_2 stretching frequencies of gly in D_2O

Solution	*T℃*	*$\nu_s CH_2$ / cm^{-1}*	*$\Delta\nu/\Delta T$ sym*	*$\nu_{as} CH_2$ / cm^{-1}*	*$\Delta\nu/\Delta T$ asym*
D_2O	5	2971.2	0.016	3011.2	0.025
pD = 0.7	60	2972.1		3012.6	
D_2O	5	2969.9	0.027	3009.3	0.055
pD = 2.2	60	2971.4		3012.3	
D_2O	5	2968.1	0.038	3008.6	0.064
pD = 6.3	60	2970.2		3012.1	
D_2O	5	2923.1	0	2956.8	0
pD = 13.3	60				

The stretching frequencies of gly methylene are affected by both the amine and carboxyl groups. In order to characterize the impact of the amine and carboxylic groups separately we investigated the CH_2 stretching frequencies of 2,2,2-d_3-ethylamine (CD_3-CH_2-NH_2) and 3,3,3-d_3-propionic acid (CD_3-CH_2-COOH) in D_2O at different pD values and temperatures.

3.1.4.3 pD And temperature dependence of the CH_2 stretching vibrations of CD_3-CH_2-COOD and CD_3-CH_2-ND_2

pD Dependence. In CD_3-CH_2-ND_2 and CD_3-CH_2-COOD, the CH_2 is affected by changes in the ionization state of either the amine or carboxylic groups.

Figure 3.5 shows the CH_2 stretching region of the Raman spectra of CD_3-CH_2-ND_2 and CD_3-CH_2-COOD in D_2O. At low and neutral pD values 2,2,2-d_3-ethylamine is in its cationic form (CD_3-CH_2-ND_3+). The $\nu_s CH_2$ and $\nu_{as} CH_2$ frequencies are 2987 cm^{-1} and 3008 cm^{-1}, respectively. At high pD values 2,2,2-d_3-ethylamine is in its neutral form (CD_3-CH_2-ND_2) where

the nitrogen possesses a lone pair of electrons. As in gly, the adjacent ND_2 group significantly downshifts the CH_2 stretching vibrations.

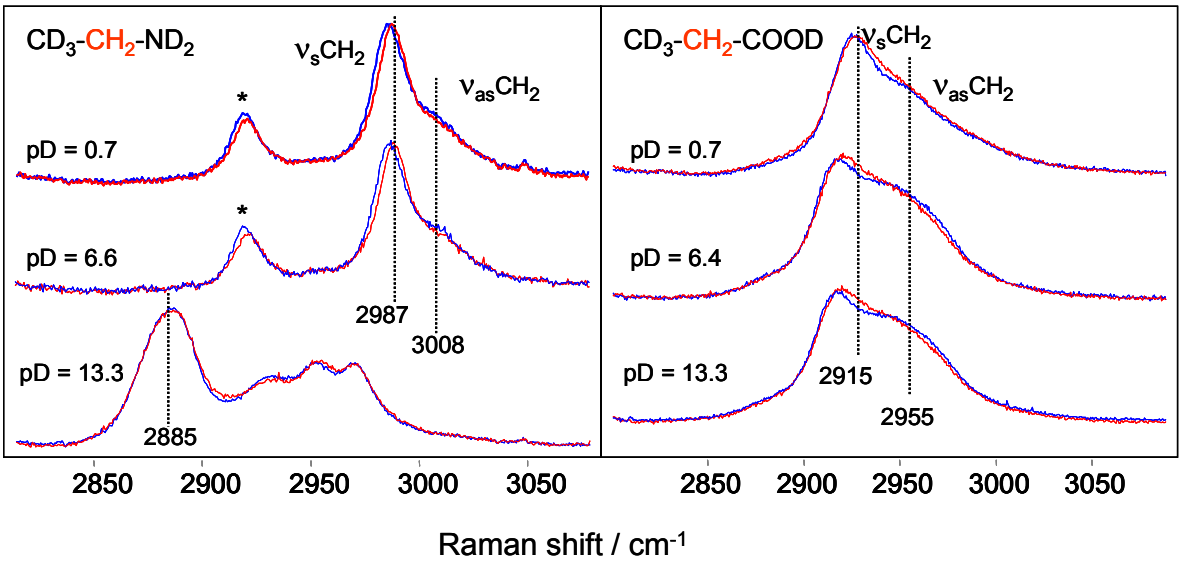

Figure 3.5: CH_2 stretching region of the Raman spectra of the 2,2,2-d_3-ethyl amine and 3,3,3-d_3-propionic acid in D_2O at different pD values at 5°C (blue curve) and 60°C (red curve). Band marked with (*) at 2918 cm^{-1} in 2,2,2-d_3-ethylamine is most likely due to Fermi resonance of the $\nu_s CH_2$ with the overtone of the CH_2 scissoring. The splitting between symmetric and asymmetric CH_2 stretches in CD_3-CH_2-ND_3^+ at pD = 0.7 and 6.6 is unusually small, ~ 19 cm^{-1} (an additional indication that $\nu_s CH_2$ is up-shifted due to Fermi resonance) In gly and propionic acid CH_2 scissoring is at a significantly lower frequency than in ethylamine which removes the condition for Fermi resonance.

The Raman spectrum of the 2,2,2-d_3-ethylamine at pD = 13.3 consists of four bands in the CH_2 stretching region which are due to the free rotation about the C-N bond and presence of both gauche- and anti- rotamers. The gauche form is slightly more stable (~ 0.3 kcal/mol) and gauche-anti rotational barrier is about 2 kcal/mol for the vapor phase.[39] The assignment of the high pD spectrum will be given late in the discussion after getting additional information from theoretical calculations.

The 3,3,3-d_3-propionic acid CH_2 stretching vibrations ($\nu_s CH_2 \sim 2915\ cm^{-1}$ and $\nu_{as} CH_2 \sim 2955\ cm^{-1}$) show a weak frequency dependence on solution pD. At neutral and high pD, the anionic CD_3-CH_2-COO^- CH_2 stretching bands are somewhat broader than are those of the protonated species at low pD.

Temperature dependence. High pD neutral 2,2,2-d3-ethylamine (CD_3-CH_2-ND_2) shows no CH_2 stretching temperature dependence (figure 3.5). In the cationic form (at low and neutral pD values) the CH_2 symmetric stretches upshift with temperature similar to that of the CH_2 symmetric stretch of $gly^{\pm}$, while the temperature shift of the CH_2 asymmetric stretch is 2-fold smaller. Table 3.2 shows the CH_2 stretching frequencies and their temperature dependence.

The temperature induced CH_2 stretching frequency shifts in 2,2,2-d_3-ethylamine are similar to those of zwitterionic gly (compare Table 3.1 and Table 3.2). 3,3,3-d_3-propionic acid, in contrast, shows little temperature dependence of the CH_2 stretching frequencies for any solution pD values. Thus, we can conclude that the amine group dominates the temperature dependence of the CH_2 stretching frequencies in gly.

Table 3.2: Temperature dependence of the CH_2 ν_s and ν_{as} of 2,2,2-d_3-ethylamine in D_2O

pD	*T℃*	$\nu_s CH_2 / cm^{-1}$	$\Delta\nu/\Delta T$ *sym*	$\nu_{as} CH_2 / cm^{-1}$	$d\nu/dT$ *asym*
0.7	5	2985.7	0.033	3006.3	0.033
	60	2987.5		3008.3	
6.6	5	2986.1	0.033	3007.5	0.022
	60	2987.9		3008.7	

3.1.4.4 pD and temperature dependence of the CD_3 stretching frequency in CD_3-CH_2-COOD and CD_3-CH_2-ND_2

Deuteration of the methyl group in CD_3-CH_2-ND_2 and CD_3-CH_2-COOD separates the originally overlapping methylene and methyl stretching vibrations, allowing us to unambiguously observe these vibrations in different solution conditions.

Figure 3.6 shows the CD_3 stretching region for 2,2,2-d_3-ethylamine and 3,3,3-d_3-propionic acid at different pD values and temperatures. For both compounds, the CD_3 stretching frequencies depend on the carboxyl or amine ionization states.

At pD = 0.7 and pD = 6.6 the 2,2,2-d_3-ethylamine cation (CD_3-CH_2-ND_3^+) shows $\nu_s CD_3$ frequencies of 2135 cm^{-1} and $\nu_{as} CD_3$ frequencies of 2250 cm^{-1} (Fig. 3.6). In contrast, at pD = 13.3 the $\nu_s CD_3$ vibration of neutral CD_3-CH_2-ND_2 splits in two bands. One remains near ~ 2135 cm^{-1} while the other downshifts 52 cm^{-1} to 2083 cm^{-1}. The $\nu_{as} CD_3$ of the neutral form downshifts ~ 14 cm^{-1} to 2236 cm^{-1} and broadens. For 3,3,3-d_3-propionic acid the $\nu_{as} CD_3$ downshifts ~ 8 cm^{-1} (from 2245 cm^{-1} to 2237 cm^{-1}) as the carboxylic acid (pD = 0.7) becomes a carboxylate anion (pD = 6.4 and 13.3).

From these data we conclude that the CD_3 stretches in CD_3-CH_2-ND_2 and CD_3-CH_2-COOD show the pD-induced frequency shifts of about the same magnitude as do the CH_2 stretches, despite the fact that the CD_3 group is not directly attached to the ND_2 or COOD groups. It should be noted, however, that although the CD_3 group is not directly bound to the amine or carboxyl group, it is very close to them; in their equilibrium conformations. The CD_3 deuterium atoms are closer to the carbonyl oxygen or nitrogen lone pairs than are the CH_2 group hydrogens.

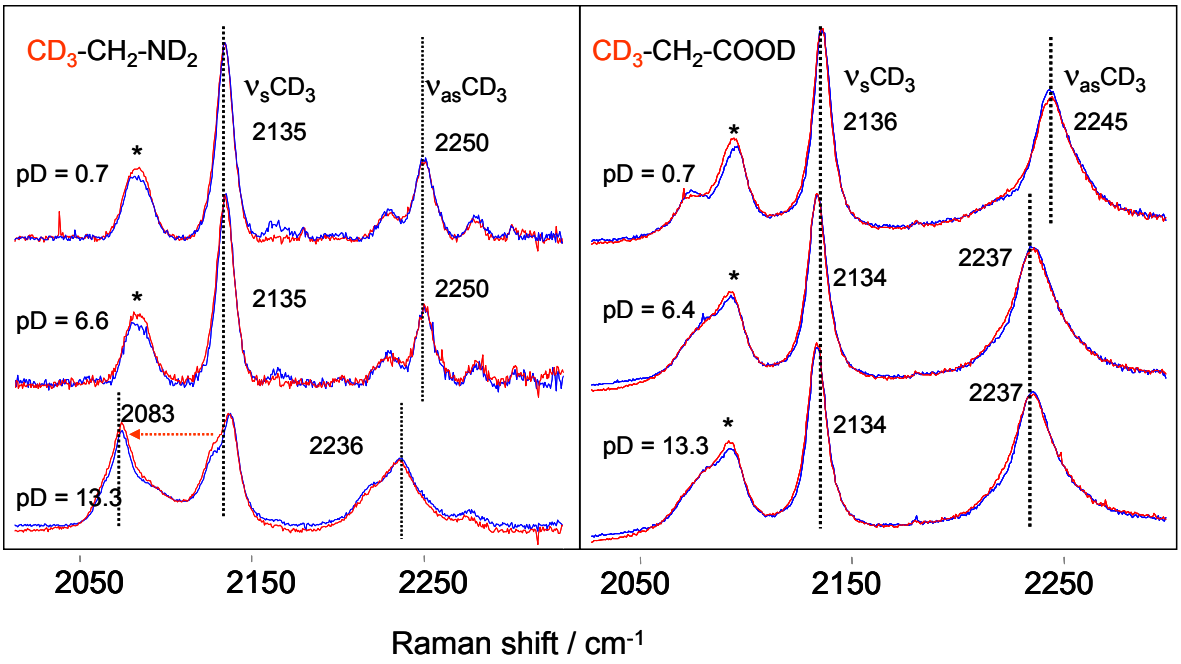

Figure 3.6: CD_3 stretching region of the 2,2,2-d_3-ethyl amine and 3,3,3-d_3-propionic acid in D_2O at different pD values at 5°C (blue curve) and 60°C (red curve). CD_3 stretches show a clear dependence on the ionization state of the amine and carboxylic group even though the CD_3 group is not directly linked to the carboxyl or amine groups. Frequencies of the ν_sCD_3 and $\nu_{as}CD_3$ for both 2,2,2-d_3-ethylamine and 3,3,3-d_3-propionic acid do not show any temperature dependence at any pD values. Band marked by (*) is an overtone of CD_3 asymmetric bending ($2\delta_{asym}$ CD_3) enhanced due to Fermi resonance with intense CD_3 symmetric stretch.[40]

In contrast to CH_2 stretching vibrations the CD_3 stretches show no temperature dependence for any pD value for both 2,2,2-d_3-ethylamine and 3,3,3-d_3-propionic acid. In both these compounds the CH_2 group is directly linked to amine or carboxyl groups by a σ-bond while the CD_3 group is only spatially close. This indicates that in order to show a CH_2 stretching frequency temperature dependence the CH_2 group must be directly linked to the amine or carboxyl group.

3.1.5 Theoretical calculations

3.1.5.1 The effect of carboxyl group orientation on the CH_2 stretching frequencies

The experimental results indicate a dependence of the CH_2 stretching frequencies on carboxyl group orientations. Although in real crystals the range of available conformations is limited because gly prefer to be in planar conformations where ξ is small,[41] theoretical calculations allow us to explore a much broader range of conformations. Thus, we theoretically modeled the conformational dependence of CH_2 vibrations frequencies upon the ξ angle for neutral gly. We fixed the orientation of $-NH_2$ group with respect to the CH_2 group to rule out any possible impact of nitrogen lone pair orientation.

As expected from experiments, our theoretical results show that the $\nu_{as}CH_2$ and ν_sCH_2 frequencies significantly depend on ξ (Fig. 3.7A), and these frequencies correlate with the C-H bond lengths (Fig. 3.7B).

For $\xi = 0^\circ$the C-H bonds symmetrically arrange with respect to the carboxyl group plane and have identical bond lengths (Fig. 3.7B). This results in the minimum calculated frequency splitting between the $\nu_{as}CH_2$ and ν_sCH_2 coordinates ($\Delta_{0^\circ, calc} = 33\ cm^{-1}$). At $\xi = \pm 31^\circ$ one of the C-H bonds is almost perpendicular to the carboxyl plane, while the other lies within the COO plane. These conformations have the maximal frequency splitting between the ν_s and ν_{as} CH_2 stretching frequencies and the largest differences in C-H bond lengths. At $\xi = \pm 81^\circ$ the ν_sCH_2 and $\nu_{as}CH_2$ frequencies are at their maximum values, both C3-H4 and C3-H5 bonds have their shortest bond lengths and both lie almost within the COO plane (Fig. 3.7, top). It should also be noted that calculated CH_2 stretching frequencies and frequency splitting in gly rotamers with OH group in cis and trans position to amine group are essentially identical.

The normal mode composition indicates that the extent of coupling between the two C-H stretching vibrations depends on the difference in C-H bond lengths. For planar gly ($\xi = 0^{\circ}$) with equivalent C-H bonds, both C-H stretching vibrations contribute equally to symmetrical and asymmetrical components of CH_2 stretching (Fig. 3.7C). At $\xi = \pm 31^{\circ}$, where the C-H bond length difference is the largest, the coupling is smallest, and each calculated C-H stretching mode is an almost local vibration. The longer the C-H bond length, the more it contributes to the low-frequency symmetric vibration and vice versa.

Our experimental data and our theoretical modeling show that the proximity of the C-H bond to the carboxyl group oxygen results in significant upshift of the corresponding CH stretching frequencies due to C-H bond shortening.

Table 3.3: AIM charge distributions for selected ξ conformations

	$\xi = 0^{\circ}$	$\xi = 81^{\circ}$	$\xi = 31^{\circ}$
N1	-1.014	-1.001	-1.012
H2	0.366	0.368	0.369
C3	0.365	0.367	0.366
H4	0.052	0.044	0.047
H5	0.052	0.041	0.051
C6	1.503	1.493	1.501
O7	-1.208	-1.199	-1.203
H8	0.366	0.370	0.365
O9	-1.122	-1.121	-1.124
H10	0.641	0.064	0.641

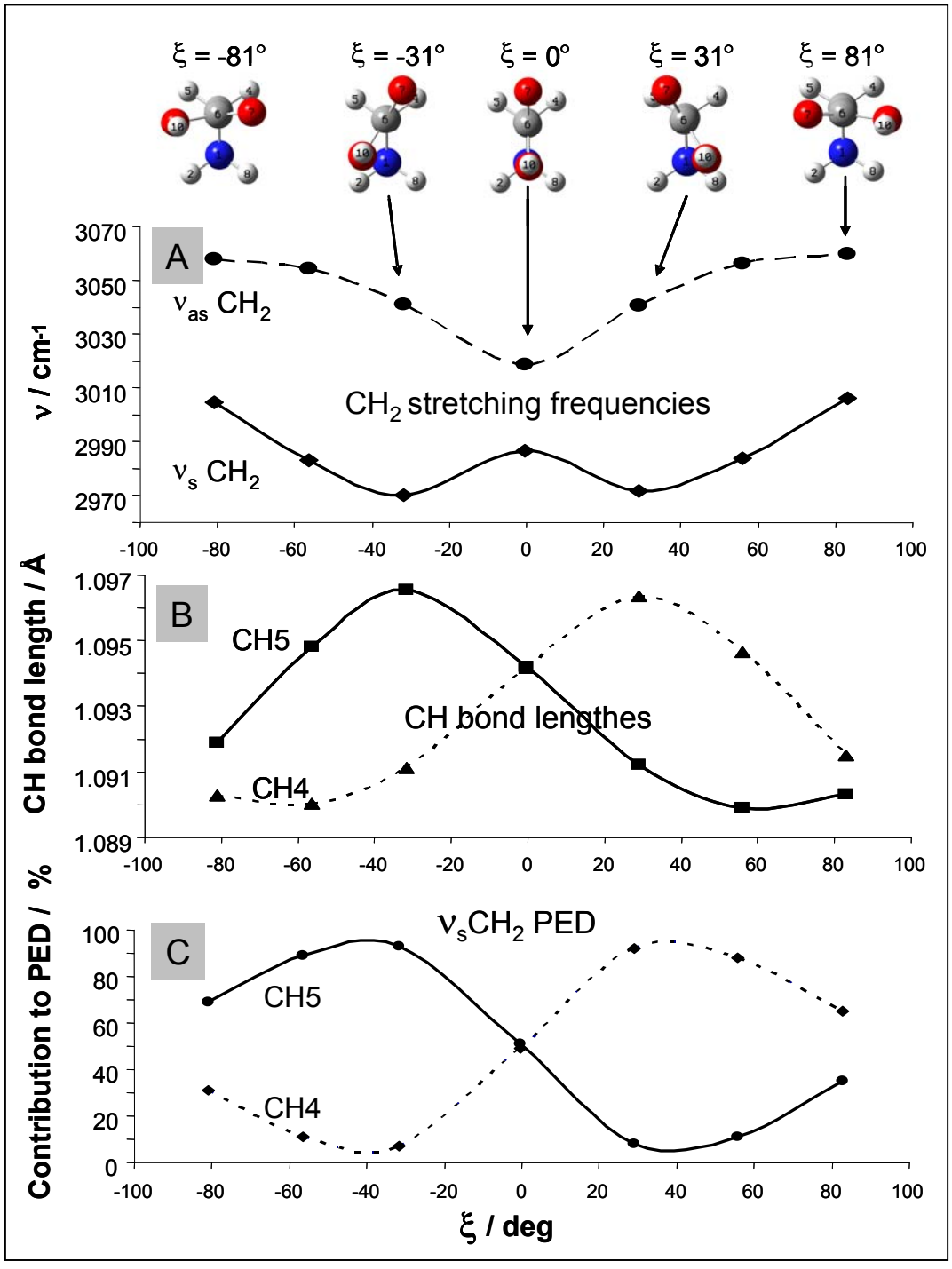

Figure 3.7: Calculated ξ angular dependence of (A) gly CH_2 stretching frequencies, (B) C-H bond lengths, and (C) normal mode composition (%) of CH_2 symmetric stretch. Frequencies are scaled to 0.98.

As shown above, the carboxyl group orientation affects the C-H bond length. To study the carboxyl group orientation effect on the gly electronic structure, we calculated the AIM charge distributions for the $\xi = 0^{\circ}$, $\xi = 31^{\circ}$, $\xi = 81^{\circ}$ gly conformers. The calculated charge distributions indicate that the C-H bond length decrease results from transfer of electronic density from the carboxyl group oxygen to the nearest methylene hydrogen which decreases the oxygen negative charge and decreases the hydrogen positive charge. The magnitude of this effect depends on the distance between the C=O and C-H bonds. At $\xi = 0^{\circ}$, where both hydrogens are equidistant from the COOH plane, the two methylene hydrogens have equal charge (Table 3.3). At $\xi = 81^{\circ}$ both hydrogens are closer to the COOH plane than in the $\xi = 0^{\circ}$ conformer.

Consequently, the hydrogens will have similar, less positive charges than for the $\xi = 0^{\circ}$ conformer. In addition, the negative charges on both oxygens are decreased compared to the $\xi = 0^{\circ}$ conformer. In the $\xi = 31^{\circ}$ conformer, the hydrogen atom of the C-H bond closest to the COOH plane has less positive charge than does the other, while the negative charge on the oxygen decreases.

3.1.5.2 Theoretical modeling of the pD dependence of CH_2 stretching frequency. Effect of the amine and carboxyl ionization states and orientations

We calculated the geometry, electronic structure properties, vibrational frequencies and normal mode compositions for a series of gly conformers in neutral and zwitterionic forms in solution. Both neutral and zwitterionic forms were calculated in an implicit solvent with the dielectric constant of water modeled by PCM. PCM was employed to both stabilize the zwitterion which is unstable in gas phase calculations, and to account for the macroscopic effects of water. We calculated neutral gly.

Amine group effect. The nitrogen lone pair impact on the C-H stretching frequencies of organic compounds has been referred to as either the "trans effect of lone pair", “negative hyperconjugation” or “the Bohlmann effect”.[16,42] C-H bonds within the same CH_3 or CH_2 linked to an atom carrying a lone pair of electrons often have different lengths.[43] Some C-H bonds are substantially longer which results in large frequency downshifts (up to 150 cm^{-1}). This phenomenon is especially prominent in cases with nitrogen or oxygen lone pair electrons. The specific influence of the lone pair is confirmed by the disappearance of C-H bond lengthening when the lone pair was removed.

It is generally agreed that the trans-C-H bond weakening occurs because of partial transfer of the lone pair electrons to the vacant σ* orbital of the C-H bond.[44] The stretching frequency of the C-H bond trans to the lone pair is significantly decreased compared to that of the gauche C-H bond.[45,46] It should be noted that “lone pair trans effect” is quite general, also occurring for OH, NH, etc.[46]

Transfer of electronic density to a σ^* orbital is expected to be particularly favored when the acceptor orbital presents a smooth, nodeless character in the region of the donor orbital as do σ^*C-H orbitals. The best donor orbital for such interaction would be a diffuse lone pair nonbonding orbital, such as the nitrogen lone pair. From the shapes of these orbitals, simple consideration suggests that the n-σ^* interaction is optimized in a linear “end-on” arrangement. Thus, the strongest n-σ^* interactions would occur for the C-H bond trans to the lone pair, since this particular orientation gives a linear arrangement of the nitrogen lone pair relative to the C-H antibonding orbital (Fig. 3.1).

We examined the effect of the nitrogen lone pair on two conformations of neutral gly with different orientations of the CH_2 group relative to the NH_2 group (Fig. 3.1a). In anti-gly^{neut}

the nitrogen lone pair is gauche to both C-H bonds, where both C-H bonds are approximately equidistant from the lone pair. In contrast, in gauche-gly^{neut} one of C-H bond (C3-H4) is gauche to the nitrogen lone pair, while the other (C3-H5) is trans. In zwitterionic gly such orientations are not differentiated because of the lack of the nitrogen lone pair.

For neutral gly our calculations show that anti-gly^{neut} has equivalent C-H bonds, while in gauche-gly^{neut} the C3-H5 bond trans to the nitrogen sp^3 lone pair orbital is significantly elongated, while the other bond is slightly contracted compared to anti-gly^{neut} (Table 3.4). In zwitterionic gly both C-H bonds have equal length. The zwitterionic C-H bonds shorten because of the proximity of the positively charged NH_3^+ group.

The C-H stretching frequencies differ between anti-gly^{neut} and gauche-gly^{neut}. In anti-gly^{neut} the $\nu_s CH_2$ is calculated at 2962 cm^{-1}, while in gauche-gly^{neut} this vibration downshifts by 60 cm^{-1} compared to that in anti-gly^{neut}. The frequency splitting between the symmetrical and asymmetrical components of CH_2 also differs in these structures. In anti-gly^{neut}, where both C-H bonds are equal, the split is 33 cm^{-1}, while in gauche-gly^{neut} the split is a much larger 81 cm^{-1} (Table 3.4). Our Raman spectra of gly at pD = 13.3 shows a 34 cm^{-1} spliting between the two CH_2 stretching peaks which agrees well with the frequencies calculated for anti-gly^{neut}. This suggests that at high pH gly exists mainly in the anti-gly^{neut} conformation. However, the breadth of both CH_2 stretching bands indicates the existence of additional conformations in solution.

C-H bond length changes impact the coupling between the CH_2 stretching vibrations (Table 3.4). In anti-gly^{neut} both C-H bonds contribute equally to the asymmetric and symmetric components. In contrast, in gauche-gly^{neut} the two C-H vibrations are uncoupled. The high frequency vibration is almost a pure stretch of the shorter C-H bond, while the low-frequency band is almost a pure stretch of the longer C-H bond.

In zwitterion gly the C-H bonds have the same length, but are shorter than in anti-gly^{neut}. Consequently, both symmetric and asymmetric stretches of CH_2 occur at higher frequencies (Table 3.4) The zwitterion calculated CH_2 54 cm^{-1} frequency splitting is larger than for the anti-gly^{neut} conformer. We also observe a larger frequency splitting of the CH_2 stretching vibrations at lower pD than at higher pD.

The charge distribution on the CH_2 group (Table 3.4) indicates that in the zwitterion each C-H bond is more polar than in the neutral form. This increased bond polarity results from the nitrogen negative inductive effect, which shortens the zwitterionic C-H bonds. In anti-gly^{neut}, the C-H bond lengths and charges on both methylene hydrogens are equal. In gauche-gly^{neut}, different bond lengths and charge distributions occur. The longest C-H bond hydrogen atom is less positive than the other, whereas the positive charge is almost equal to that in anti-gly^{neut}. In gauche-gly^{neut} the decreased hydrogen positive charge indicates an increased electronic density transferred from the nitrogen lone pair, since the nitrogen negative charge is decreased compared to that in anti-gly^{neut}. The correlation of an increased electronic density with a bond length elongation indicates that the electronic density was accepted by an orbital with non- or anti-bonding character; the NBO analysis shows an increased occupancy of the C-H σ^* MO (Table 3.5). This interaction elongates the corresponding C-H bond resulting in a downshift of the C-H stretching frequency in the gly anion compared to the zwitterion or cation, where the lone pair is removed by protonation. This explains the strong dependence of C-H stretching frequencies on the ionization state of the gly amino group.

The effect of carboxyl group in zwitterionic gly. Comparison of the solution gly Raman spectra measured at pD = 0.7 (cationic form) and pD = 6.3 (zwitterionic form) show that the carboxyl group ionization does not significantly affect the CH stretching vibrations. The

frequency shift of both C-H stretching vibrations does not exceed 3 cm^{-1} (see Table 3.1). The charge distribution calculated for the $\xi = 0^{\circ}$ (staggered) and $\xi = -60^{\circ}$ (twisted) conformations of gly zwitterion (Table 3.4) indicates that the C-H bond length decrease is caused by redistribution of electronic density from the C=O bond lying in the same plane with the C-H bond. Analysis of the molecular orbital occupancy (Table 3.5) shows a significantly increased occupancy of the bonding orbital of the short C3-H4 bond and a decreased O7 lone pair molecular orbital occupancy. The 0.002 Å bond length difference between the C-H bonds of twisted-$gly^{\pm}$ prevents coupling between the two CH stretches. PED indicates that two CH stretching frequencies calculated for twisted-$gly^{\pm}$ result from almost pure vibrations of the individual C-H bonds, while in staggered-$gly^{\pm}$ the CH stretching motions are coupled into symmetric and asymmetric vibrations (Table 3.4). In twisted-$gly^{\pm}$ the C-H bond contraction results in an 11 cm^{-1} upshift of the high-frequency CH stretch, while the low-frequency CH stretch is equal to that in staggered-$gly^{\pm}$.

Table 3.4: Calculated C-H bond lengths, C-H stretching frequencies[c], normal mode compositions, and AIM charge distributions for neutral, zwitterionic gly conformer, and the hydrogen bonded zwitterionic gly-water conformers

		gly^{neut}		*gly$^{\pm}$*			*gly$^{\pm}$-Water Complexes*		
		anti-glyneut	*gauche-glyneut*	*eclipsed-gly±*	*staggered-gly±*	*twisted-gly± (ξ=-60°)*	*eclipsed-gly± NH_3 H_2O*	*eclipsed-gly$^{\pm}$ COO^- H_2O*	*eclipsed-gly$^{\pm}$ NH_3 H_2O, COO^- H_2O*
l(C-H) / Å	C3-H4	1.096	1.095	1.090	1.091	1.089	1.091	1.090	1.090
	C3-H5	1.096	1.101	1.090	1.091	1.091	1.090	1.090	1.091
Freq / cm^{-1}*	$\nu_s CH_2$	2962	2902	3015	3007	3008	3011	3017	3012
	$\nu_{as} CH_2$	2995	2983	3069	3063	3074	3063	3073	3065
PED / %	$\nu_s CH_2$	C-H5 s (51) C-H4 s (48)	C-H5 s (97) C-H4 s (3)	C-H4 s (50) C-H5 s (48)	C-H5 s (50) C-H4 s (49)	C-H5 s (67) C-H4 s (33)	C-H4 s (55) C-H5 s (44)	C-H4 s (52) C-H5 s (47)	C-H4 s (56) C-H5 s (44)
	$\nu_{as} CH_2$	C-H4 s (51) C-H5 s (48)	C-H4 s (97) C-H5 s (3)	C-H5 s (51) C-H4 s (49)	C-H4 s (50) C-H5 s (49)	C-H4 s (66) C-H5 s (33)	C-H5 s(55) C-H4 s (44)	C-H5 s(52) C-H4 s (48)	C-H5 s(56) C-H4 s (44)
AIM Charges	N1	-1.013	-1.003	-0.980	-0.962	-0.959	-1.010	-0.979	-1.010
	H2	0.364	0.364	0.468	0.473	0.473	0.455	0.469	0.504
	C3	0.359	0.348	0.244	0.249	0.261	0.250	0.247	0.253
	H4	0.052	0.055	0.083	0.080	0.070	0.073	0.086	0.079
	H5	0.052	0.034	0.083	0.080	0.076	0.076	0.086	0.076
	C6	1.508	1.523	1.654	1.660	1.647	1.648	1.655	1.649
	O7	-1.204	-1.204	-1.257	-1.263	-1.254	-1.261	-1.235	-1.239
	H8	0.364	0.361	0.482	0.472	0.473	0.469	0.481	0.468
	O9	-1.134	-1.128	-1.241	-1.256	-1.257	-1.246	-1.231	-1.236
	H10	0.642	0.641	0.468	0.469	0.473	0.502	0.470	0.456

* Frequencies are scaled by 0.98

Table 3.5: NBO calculated occupancies of selected molecular orbitals of methylene, amino, and carboxyl groups in neutral and zwitterionic gly conformers

			gly^{neut}		$gly^{\pm}$			$gly^{\pm}$-Water Complexes		
			anti-glyneut	gauche-glyneut	eclipsed-$gly^{\pm}$	staggered-$gly^{\pm}$	twisted-$gly^{\pm}$ $\xi = 60^{\circ}$	eclipsed-$gly^{\pm}$ NH_3 H_2O	eclipsed-$gly^{\pm}$ COO^- H_2O	eclipsed $gly^{\pm}$ NH_3 H_2O, COO^- H_2O
MO Occupancy	σ	C-H4	1.964	1.963	1.978	1.976	1.985	1.978	1.978	1.978
		C-H5	1.964	1.969	1.978	1.976	1.979	1.978	1.978	1.978
	σ^*	C-H4	0.0157	0.0139	0.0083	0.0096	0.0107	0.0094	0.0083	0.0084
		C-H5	0.0157	0.0287	0.0083	0.0096	0.0096	0.0085	0.0083	0.0094
	LP N		1.950	1.958	N/A					
	COO^-	LP_2 O7	1.863	1.864	1.884	1.885	1.897	1.886	1.874	1.875
		LP_3 O9	N/A		1.631	1.616	1.613	1.629	1.825	1.612
		LP_2 O9	1.799	1.797	1.872	1.892	1.893	1.876	1.869	1.873
		BD CO7	1.996	1.996	1.996	1.996	1.988	1.996	1.832	1.993
	NH_3^+	BD N-H2	N/A		1.994	1.993	1.993	1.994	1.994	1.993
		BD N-H8	N/A		1.993	1.994	1.994	1.993	1.993	1.993
		BD N-H10	N/A		1.994	1.994	1.993	1.993	1.994	1.994

Effect of hydrogen bonding to amine and carboxyl groups on the CH (CD) stretching frequencies of glycine, deuterated ethylamine and propionic acid. As shown above the electronic configuration of the nitrogen atom and spatial orientation of the carboxyl group have a large impact on the neighboring CH_2 bond lengths and stretching frequencies. Hydrogen bonding to $-NH_3^+$/$-NH_2$ and -COOH/$-COO^-$ of gly affects the electronic configurations of these groups which, in turn, change the CH_2 bond strengths, which shift the CH_2 stretching frequencies.

To examine the effect of water hydrogen bonding on the C-H frequencies, we calculated the geometries and electronic properties of gly zwitterion ($\xi = 0°$), the zwitterion with water attached to the NH_3^+ group and the zwitterion with water attached to the COO^- site. We also examined gly zwitterion with waters attached to both NH_3^+ and COO^-.

Water hydrogen bonding to the gly $-COO^-$ terminus does not change the C-H bond lengths significantly. However, it does result in a slight frequency increase of both the symmetric (2 cm^{-1}) and asymmetric (4 cm^{-1}) C-H stretching vibrations (Table 3.4). Hydrogen bonding to the NH_3^+ site elongates both C-H bonds more significantly. As a result, the frequencies of the symmetric and asymmetric C-H stretching vibrations downshift by 4 and 6 cm^{-1} respectively. Two waters added to COO^- and NH_3^+ groups results in an increase in C-H bond lengths and frequency downshifts of the symmetric (4 cm^{-1}) and asymmetric (6 cm^{-1}) stretches.

The MO occupancy listed in Table 3.5 shows that the water hydrogen bonded to $-NH_3^+$ decreases the electronic density of the N-H bonding orbitals and increases the electronic density of the C-H σ^* orbitals. In contrast, water hydrogen bonding to COO^- did not significantly change the C-H bond electronic density.

An additional important insight into the origin of the CH_2 stretching temperature induced frequency shifts is evident from the CD_3 stretching frequencies of CD_3-CH_2-ND_2 and CD_3-CH_2-COOD. As shown above, the CD_3 group, which is not directly connected to the amine or carboxyl, does not show any temperature induced frequency shifts but does show a significant dependence on the amine and carboxyl group ionization state. Thus, we conclude that the temperature dependence results from some inductive interaction through σ-bonds.

Our calculations show that water hydrogen bonding to the donor ($-NH_3^+$) group downshifts CH_2 stretching frequencies while water hydrogen bonding to the acceptor group ($-COO^-$) upshifts CH_2 stretches. The deprotonated amine ($-NH_2$) and the protonated carboxyl (-COOH) can serve as both hydrogen bond donors and acceptors. Thus, the temperature induced frequency shift of the CH_2 stretches of gly in solution depends on interplay of different hydrogen bonding patterns. However, our experimental and theoretical results show that at the pH values close to neutral, hydrogen bonding to the gly $-NH_3^+$ group has dominant effect on the CH_2 stretching frequencies.

3.1.5.3 CH_2 stretching frequency splitting monitors gly non-planarity

The splitting between $\nu_s CH_2$ and $\nu_{as} CH_2$ stretching vibrational frequencies should depend less on environment than the frequencies themselves because the splitting depends mostly on C-H bond nonequivalence which depends upon the gly conformation. The actual doublet frequency can depend on the dielectric constant of the medium, hydrogen bonding to the amine/carboxyl groups etc. Such environmental factors will likely shift the frequencies of the symmetric and asymmetric stretches in the same direction without significantly changing the splitting between them. This makes the splitting a more reliable criterion for gly conformational analysis.

For the planar Gly•HCl molecules the calculated and observed splittings between the $\nu_{as}CH_2$ and ν_sCH_2 vibrations are essentially identical at $\Delta \sim 33$ cm^{-1}. For gly nitrate, Gly•HNO_3, the $\xi \sim 21°$ deviation from planarity results in $\Delta_{Gly•HNO3\ cryst} = 62$ cm^{-1} (Fig. 3.3), while the calculated $\xi = 21°$ splitting is $\Delta_{21°,\ calc} \sim 56$ cm^{-1}. For TGS, the splitting between $\nu_{as}CH_2$ and ν_sCH_2 of the more intense doublet (2982 cm^{-1} and 3017 cm^{-1}) corresponding to almost planar gly pair is $\Delta_{TGS,\ planar} \sim 35$ cm^{-1}, which again is very close to the calculated value. In contrast for bent gly the observed value is $\Delta_{TGS,\ bent} \sim 45$ cm^{-1} compared to a calculated $\Delta_{\xi = 19°,\ calculated} = 53$ cm^{-1}. Thus, the splitting between the $\nu_{as}CH_2$ and ν_sCH_2 stretching frequencies definitely depends upon the relative orientations of the CH_2 and carboxylic groups. The small deviations between calculated and measured CH_2 frequency splitting values in crystals may result from crystal packing forces which distort the gly molecules.

As we have shown both experimentally (Fig. 3.2) and theoretically (Fig. 3.7A), the frequency splitting between symmetrical and asymmetrical components of CH_2 stretching depends on the value of ξ angle. Therefore, the frequency splitting (Δ) measured experimentally can be used to determine the ξ angle defined by the gly conformation. Figure 3.8 shows the frequency splitting calculated for gly conformers versus the ξ angle.

This correlation describes the frequency splitting change which results from the non-planarity of gly molecule, when the amide group is protonated and the nitrogen lone pair does not affect the CH_2 stretching frequencies.

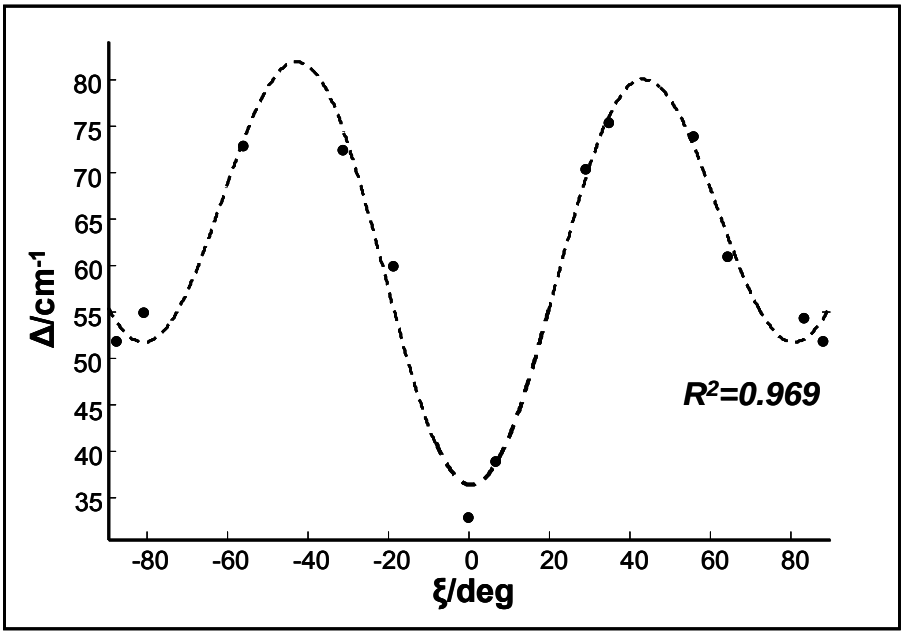

Figure 3.8: Calculated ξ angular dependence of frequency splitting of the gly CH_2 stretching. The dots represent calculated data points, the dashed line is the Fourier fit to the calculated results. $\Delta(\xi) = 60 - 10.6\cos(0.04\xi) - 4.3\sin(0.04\xi) - 21.3\cos(0.08\xi) - 3.6\sin(0.08\xi)$

Conformational preferences of gly in solution. Figure 3.9 shows Raman spectra of 2,2,2-d_3-ethylamine and gly in solution at pD = 13.3. Two staggered conformations – gauche and anti are populated in solution at room temperature which differ by a rotation about the C-N bond in ethylamine. In the gauche conformation the nitrogen lone pair is trans to a C-H bond which results in elongation of the trans C-H bond due to electron delocalization from the nitrogen lone pair to the C-H anti-bonding σ* orbital which significantly downshifts the C-H stretching frequency by ~ 100 cm^{-1} to ~2885 cm^{-1}. The other C-H bond is slightly upshifted. Thus, the two most intense, most separated bands at ~2885 cm^{-1} and ~2971 cm^{-1} correspond to the uncoupled CH stretches of the gauche conformation of ethylamine. Interaction of the C-H bonds with the lone pair in the anti conformer modestly downshifts both CH stretching vibrations without increasing the frequency splitting between the symmetric and asymmetric components at ~ 2930

cm^{-1} and 2952 cm^{-1} are $\nu_s CH_2$ and $\nu_{as} CH_2$ of anti-ethylamine. Assuming that the areas of the bands are proportional to the population of the ethylamine rotamers in D_2O allows us to calculate that the population of gauche conformers is ~ 71 % and the anti conformer is ~ 29 %. This distribution agrees well with that for n-propylamine in the gas phase as determined from the NH_2 wagging and torsion bands in the IR spectra.[47]

In contrast to ethylamine, gly^- shows only two bands at ~ 2923 cm^{-1} ($\nu_s CH_2$) and 2957 cm^{-1} ($\nu_{as} CH_2$), with frequencies similar to those for the anti conformation of 2,2,2-d_3-ethylamine. This indicates that the anti-gly^- conformer dominates high pD solutions. This anti-conformational preference of gly^- in solution may result from bifurcated intramolecular hydrogen bonding between the amine group hydrogens and the carboxylic group oxygen (Fig. 3.9) Such a hydrogen bond was shown to stabilize gas phase gly conformations[48,49] and gly molecules in inert gas matrices at low temperatures.[50] Hyperconjugation could also contribute to the increased stability of the gly anti- conformation.[51]

3.1.6 Conclusions

We examined the dependence of the CH_2 stretching frequencies of glycine, 2,2,2-d_3-ethylamine and 3,3,3-d_3-propionic acid on conformation, pD and temperature by means of Raman spectroscopy (488 nm excitation) and DFT calculations.

Experimental data show a large dependence of the CH_2 stretching frequencies on the ionization state of the amine group. We theoretically demonstrate that the high sensitivity of the $\nu_s CH_2$ and $\nu_{as} CH_2$ frequencies on the orientation and ionization state of the amine group results

from a negative hyperconjugation between the nitrogen lone pair and anti-bonding C-H orbitals. This effect is maximal when a C-H bond is trans to the lone pair.

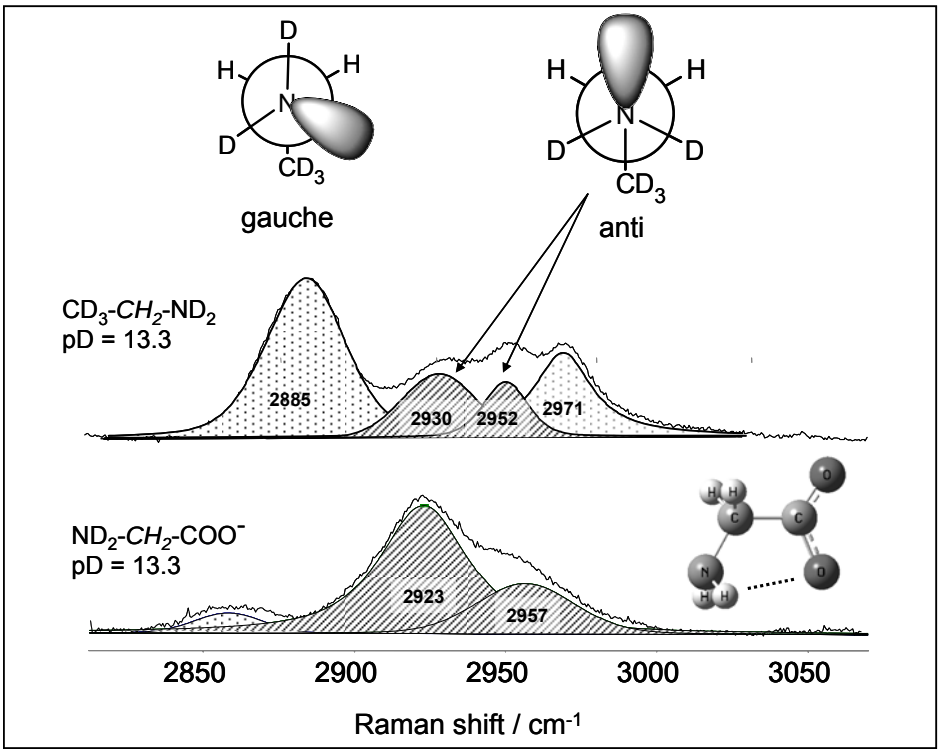

Figure 3.9: Fitted Raman spectrum (CH_2 stretching region) of the CD_3-CH_2-ND_2 and ND_2-CH_2-COO^- solutions in D_2O at pD = 13.3. Also shown are the two conformations of the ethylamine and for gly^- in solution

The C-H stretching frequency dependence on the carboxyl group ionization state is small, however carboxyl group orientation affects the CH_2 symmetric and asymmetric stretching frequencies as well as their frequency splitting. The magnitude of frequency splitting between the $\nu_s CH_2$ and $\nu_{as} CH_2$ depends on the relative orientation of the CH_2 and $COOH/COO^-$ groups. The calculated conformational dependence of the CH_2 stretches frequency splitting ($\nu_{as} CH_2$ - $\nu_s CH_2$) agrees well with the experimental data obtained from gly crystals.

According to our experimental observations and theoretical calculations, the temperature dependence of the $\nu_s CH_2$ and $\nu_{as} CH_2$ of gly in solution is due to the change in hydrogen bonding strength of the amine and carboxyl groups to water. This effect has an inductive mechanism and occurs only for the CH_2 directly connected to amine/carboxyl groups by a σ-bond. The magnitude of the frequency shifts varies with the ionization states of amine/carboxyl groups. At pD values close to neutral, hydrogen bonding to the protonated amine group ($-NH_3^+$) is likely to dominate temperature dependence of the CH_2 stretches of gly.

CD_3 stretching of the deuterated methyl of 2,2,2-d_3-ethylamine and 3,3,3-d_3-propionic acid show a significant dependence on the ionization state of the amine and carboxylic groups even though the CD_3 group is separated by a CH_2 group. It appears that the delocalization of the electron density from the amine and carboxyl groups to the CH/CD bonds occurs "through space" and requires interacting groups to be spatially close, but not necessarily linked by a covalent bond. Our results indicate that in D_2O at high pD gly is predominantly in an anti conformation in contrast to 2,2,2-d_3-ethylamine which exists in both anti and gauche conformers.

ACKNOWLEDGMENT This work was supported by NIH Grant GM8RO1EB002053.

3.1.7 BIBLIOGRAPHY

(1) Huang, C.-Y.; Getahun, Z.; Wang, T.; DeGrado, W. F.; Gai, F. *Journal of the American Chemical Society* **2001**, *123*, 12111-12112.

(2) Hamm, P.; Hochstrasser, R. M. *Practical Spectroscopy* **2001**, *26*, 273-347.

(3) Lednev, I. K.; Karnoup, A. S.; Sparrow, M. C.; Asher, S. A. *Journal of the American Chemical Society* **2001**, *123*, 2388-2392.

(4) Mikhonin, A. V.; Asher, S. A.; Bykov, S. V.; Murza, A. *Journal of Physical Chemistry B* **2007**, *111*, 3280-3292.

(5) Brewer, S. H.; Song, B.; Raleigh, D. P.; Dyer, R. B. *Biochemistry* **2007**, *46*, 3279-3285.

(6) Shi, Z.; Chen, K.; Liu, Z.; Kallenbach, N. R. *Chemical Reviews (Washington, DC, United States)* **2006**, *106*, 1877-1897.

(7) Chi, Z.; Chen, X. G.; Holtz, J. S. W.; Asher, S. A. *Biochemistry* **1998**, *37*, 2854-2864.

(8) Mikhonin, A. V.; Bykov, S. V.; Myshakina, N. S.; Asher, S. A. *Journal of Physical Chemistry B* **2006**, *110*, 1928-1943.

(9) Mirkin, N. G.; Krimm, S. *Journal of Physical Chemistry A* **2004**, *108*, 10923-10924.

(10) Mirkin, N. G.; Krimm, S. *Journal of Physical Chemistry A* **2007**, *111*, 5300-5303.

(11) Ohno, K.; Nomura, S.-I.; Yoshida, H.; Matsuura, H. *Spectrochimica Acta, Part A: Molecular and Biomolecular Spectroscopy* **1999**, *55A*, 2231-2246.

(12) Longhi, G.; Zerbi, G.; Paterlini, G.; Ricard, L.; Abbate, S. *Carbohydrate Research* **1987**, *161*, 1-22.

(13) McKean, D. C. *Journal of Molecular Structure* **1976**, *34*, 181-185.

(14) McKean, D. C.; Duncan, J. L.; Batt, L. *Spectrochimica Acta, Part A: Molecular and Biomolecular Spectroscopy* **1973**, *29*, 1037-1049.

(15) Thomas, H. D.; Chen, K.; Allinger, N. L. *Journal of the American Chemical Society* **1994**, *116*, 5887-5897.

(16) McKean, D. C. *Chemical Society Reviews* **1978**, *7*, 399-422.

(17) Bellamy, L. J. *Advances in Infrared Group Frequencies, Vol. 2: The Infrared Spectra of Complex Molecules. 2nd Ed*, 1980.

(18) Krieger, F.; Moeglich, A.; Kiefhaber, T. *Journal of the American Chemical Society* **2005**, *127*, 3346-3352.

(19) Vertessy, B. G. *Proteins: Structure, Function, and Genetics* **1997**, *28*, 568-579.

(20) Kohn, W.; Sham, L. J. *Physical Review* **1965**, *137*, 1697-1705.

(21) Parr, R. G.; W. Yang *Density-functional theory of atoms and molecules*; Oxford Univ. Press: Oxford, 1989.

(22) Hohenberg, P.; Kohn, W. *Phys. Rev.* **1964**, *136*, B864.

(23) Becke, A. D. *Journal of Chemical Physics* **1993**, *98*, 5648-5652.

(24) Lee, C.; Yang, W.; Parr, R. G. *Physical Review B: Condensed Matter and Materials Physics* **1988**, *37*, 785-789.

(25) Miehlich, B.; Savin, A.; Stoll, H.; Preuss, H. *Chemical Physics Letters* **1989**, *157*, 200-206.

(26) Irikura, K. K.; Johnson, R. D., III; Kacker, R. N. *Journal of Physical Chemistry A* **2005**, *109*, 8430-8437.

(27) Halls, M. D.; Velkovski, J.; Schlegel, H. B. *Theoretical Chemistry Accounts* **2001**, *105*, 413-421.

(28) Miertus, S.; Scrocco, E.; Tomasi, J. *Chemical Physics* **1981**, *55*, 117-129.

(29) Cossi, M.; Barone, V.; Mennucci, B.; Tomasi, J. *Chemical Physics Letters* **1998**, *286*, 253-260.

(30) Mennucci, B.; Tomasi, J. *Journal of Chemical Physics* **1997**, *106*, 5151-5158.

(31) Bader, R. F. W. *Atoms in Molecules: A Quantum Theory*; Oxford Univ. Press: Oxford, 1990.

(32) Cioslowski, J.; Mixon, S. T. *Journal of the American Chemical Society* **1991**, *113*, 4142-4145.

(33) Cioslowski, J. *Chemical Physics Letters* **1992**, *194*, 73-78.

(34) Frisch, M. J. T., G. W.; Schlegel, H. B.; Scuseria, G. E.; Robb, M. A.; Cheeseman, J. R.; Montgomery, Jr., J. A.; Vreven, T.; Kudin, K. N.; Burant, J. C.; Millam, J. M.; Iyengar, S. S.; Tomasi, J.; Barone, V.; Mennucci, B.; Cossi, M.; Scalmani, G.; Rega, N.; Petersson, G. A.; Nakatsuji, H.; Hada, M.; Ehara, M.; Toyota, K.; Fukuda, R.; Hasegawa, J.; Ishida, M.; Nakajima, T.; Honda, Y.; Kitao, O.; Nakai, H.; Klene, M.; Li, X.; Knox, J. E.; Hratchian, H. P.; Cross, J. B.; Bakken, V.; Adamo, C.; Jaramillo, J.; Gomperts, R.; Stratmann, R. E.; Yazyev, O.; Austin, A. J.; Cammi, R.; Pomelli, C.; Ochterski, J. W.; Ayala, P. Y.; Morokuma, K.; Voth, G. A.; Salvador, P.; Dannenberg, J. J.; Zakrzewski, V. G.; Dapprich, S.; Daniels, A. D.; Strain, M. C.; Farkas, O.; Malick, D. K.; Rabuck, A. D.; Raghavachari, K.; Foresman, J. B.; Ortiz, J. V.; Cui, Q.; Baboul, A. G.; Clifford, S.;

Cioslowski, J.; Stefanov, B. B.; Liu, G.; Liashenko, A.; Piskorz, P.; Komaromi, I.; Martin, R. L.; Fox, D. J.; Keith, T.; Al-Laham, M. A.; Peng, C. Y.; Nanayakkara, A.; Challacombe, M.; Gill, P. M. W.; Johnson, B.; Chen, W.; Wong, M. W.; Gonzalez, C.; and Pople, J. A.; Revision C.01 ed.; Gaussian, Inc.: Wallingford CT., 2004.

(35) J.M.L.Martin; Alsenoy, C. V.; University of Antwerpen: Antwerpen, 1995.

(36) Al-Karaghouli, A. R.; Cole, F. E.; Lehmann, M. S.; Miskell, C. F.; Verbist, J. J.; Koetzle, T. F. *Journal of Chemical Physics* **1975**, *63*, 1360-1366.

(37) Narayanan, P.; Venkataraman, S. *Journal of Crystal and Molecular Structure* **1975**, *5*, 15-26.

(38) Itoh, K.; Mitsui, T. *Ferroelectrics* **1973**, *5*, 235-251.

(39) Manocha, A. S.; Tuazon, E. C.; Fateley, W. G. *Journal of Physical Chemistry* **1974**, *78*, 803-807.

(40) Robertson, A. H. J.; McQuillan, G. P.; McKean, D. C. *Journal of the Chemical Society, Dalton Transactions: Inorganic Chemistry* **1995**, 3941-3954.

(41) Ho, B. K.; Brasseur, R. *BMC Structural Biology* **2005**, *5*, No pp. given.

(42) Lii, J.-H.; Chen, K.-H.; Allinger, N. L. *Journal of Physical Chemistry A* **2004**, *108*, 3006-3015.

(43) Henbest, H. B.; Meakins, G. D.; Nicholls, B.; Wagland, A. A. *J. Chem. Soc.* **1957**, 1462-1464.

(44) Hamlow, H. P.; Okuda, S.; Nakagawa, N. *Tetrahedron Letters* **1964**, 2553-2559.

(45) McKean, D. C.; Ellis, I. A. *Journal of Molecular Structure* **1975**, *29*, 81-96.

(46) Bellamy, L. J.; Mayo, D. W. *Journal of Physical Chemistry* **1976**, *80*, 1217-1220.

(47) Sato, N.; Hamada, Y.; Tsuboi, M. *Spectrochimica Acta, Part A: Molecular and Biomolecular Spectroscopy* **1987**, *43A*, 943-954.

(48) Hu, C. H.; Shen, M.; Schaefer, H. F., III *Journal of the American Chemical Society* **1993**, *115*, 2923-2929.

(49) Jensen, J. H.; Gordon, M. S. *Journal of the American Chemical Society* **1991**, *113*, 7917-7924.

(50) Ivanov, A. Y.; Sheina, G.; Blagoi, Y. P. *Spectrochimica Acta, Part A: Molecular and Biomolecular Spectroscopy* **1999**, *55A*, 219-228.

(51) Wang, W.; Pu, X.; Zheng, W.; Wong, N.-B.; Tian, A. *Chemical Physics Letters* **2003**, *370*, 147-153.

3.2 CONFORMATIONAL DEPENDENCE OF DIGLYCINE CH_2 STRETCHING VIBRATIONS

3.2.1 Introduction

In this study we continue our search for new spectroscopic markers to investigate polypeptide backbone conformations. Our previous studies of glycine show a significant dependence of CH_2 stretching frequencies on the amino acid conformation.[1] Here we focus our attention on the CH_2 stretching frequency conformational dependence in diglycine (glygly). We experimentally show a strong dependence of the CH_2 stretching frequencies on the peptide conformation using crystalline glygly derivatives of known structure, and theoretically modeled the CH_2 stretching frequencies φ and ψ dependences to gain insight into their origin.

3.2.2 Experimental Details

Crystals of diglycine hydrochloride (GlyGly∗HCl∗H_2O) and diglycine lithium chloride (GlyGly∗LiCl) were obtained by slow evaporation of water solutions of equimolar mixtures of glygly (Sigma Chemicals) and HCl (J. T. Baker Inc) or LiCl (J. T. Baker Inc). Crystal structures were determined by using x-ray crystallography.

All Raman measurements were performed using 488 nm Ar-ion Laser (Coherent Inc.) excitation. Scattered light was collected using a back-scattering geometry, dispersed by a single monochromator and collected using a Princeton Instruments Spec-10:400B CCD camera (Roper

Scientific). A 488 nm holographic notch filter (Kaiser Optical Systems Inc.) was used for Raleigh rejection. Typical accumulation times were ~ 2 min. A custom made, rotating metal cell was used for solid powder samples to avoid light-induced degradation under continuous irradiation. The powder was pressed into a circular groove cut in the rotating metal cylinder.

3.2.3 Computational Details

We optimized the geometries and then calculated the vibrational frequencies and normal mode compositions of following conformers of neutral diglycine (glygly):

All calculations were carried out at the DFT level of theory[2,3] employing the B3LYP exchange functional[4,5] and 6-311+G(d,p) basis set. All frequencies were calculated at the harmonic approximation and scaled by 0.98.[6,7] All calculations were performed with the Gaussian'03 calculation package.

3.2.4 Raman Spectra of Diglycine in Two Crystalline Forms

The CH_2 stretch Raman bands appear as a doublet due to coupling of the two C-H stretches which results in two vibrations – a lower frequency symmetric stretching band ($\nu_s CH_2$) and a higher frequency asymmetric stretching band ($\nu_{as} CH_2$). For diglycine crystals GlyGly∗HCl∗H_2O and GlyGly∗LiCl we observe two doublets in the C-H stretching region of the Raman spectra from the two CH_2 groups (Fig. 3.10). The conformations of these diglycine (GlyGly∗HCl∗H_2O and GlyGly∗LiCl) crystals differ. Both crystals have similar ψ angles (166°

and 162°) but significantly different φ angles (-152° and -80° Fig. 3.10).** Our previous work demonstrated a large dependence of the CH_2 stretching frequencies on glycine conformation, where the C-H bond lengths depends on the orientation of the C-H bonds relative to carboxyl and amine group.[1] In peptides, the CH_2 group vibrations may be affected by orientation of neighboring peptide bonds (PB).

In these diglycine crystals the CH_2 groups adjacent to PB carbonyls have similar orientations since the ψ angles are similar. These CH_2 groups should show similar frequencies. In contrast, the stretching frequencies of the CH_2 groups adjacent to peptide bond N-H are expected to significantly differ because of their different φ angle values. Accordingly, the doublet at 2946 and 2991 cm^{-1} in the spectrum of Gly_2*LiCl is similar in frequencies to the 2958 and 3008 cm^{-1} doublet in Gly_2*HCl spectrum. Thus, we assign the doublets with similar frequencies to the CH_2 groups adjacent to PB with similar ψ torsion angles. The, doublets where frequencies differ (2913 and 2962 cm^{-1} in GlyGly∗LiCl spectrum and 2945 and 2984 cm^{-1} in GlyGly∗HCl∗H_2O spectrum) are assigned to the CH_2 groups adjacent to PB N-H.

Thus, there is a large dependence of the CH_2 stretching frequencies on the Ramachandran φ-angle. To elucidate the origin of the CH_2 stretching frequency conformational dependence we theoretically modeled the φ and ψ dependences.

** Note that here and further in the text we always discuss φ and ψ angles adjacent to the peptide bond as shown in Fig. 1.

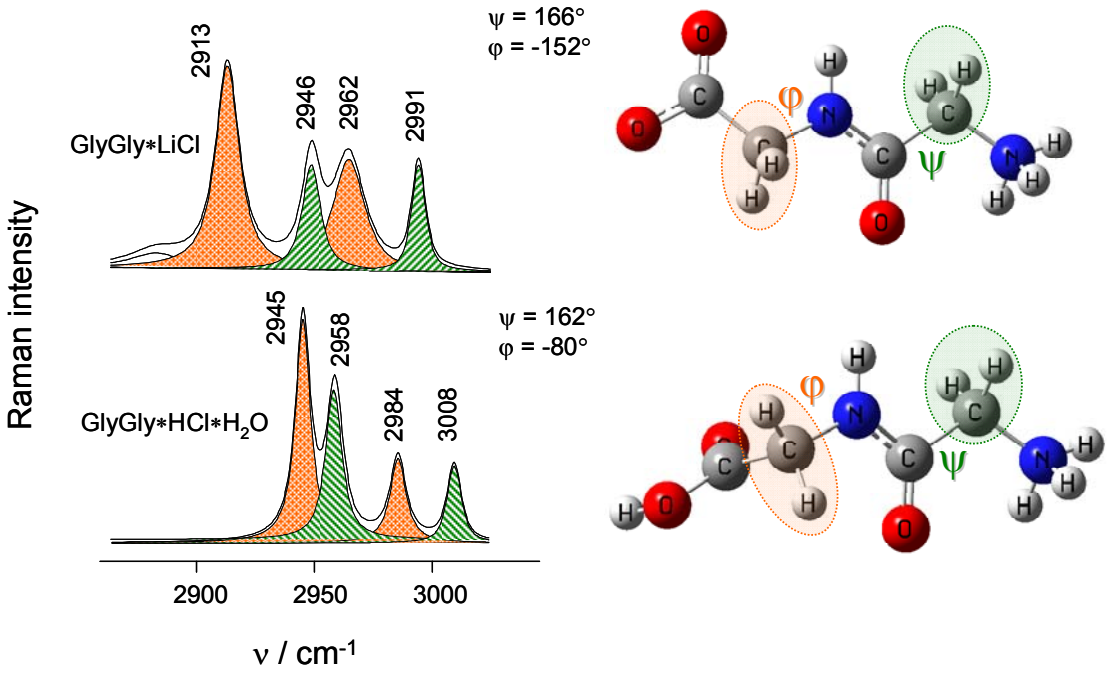

Figure 3.10: The CH_2 stretching region of the Raman spectra (488 nm exitation) of crystalline Gly_2*LiCl and Gly_2*HCl. Raman bands assigned to the CH_2 group adjacent to PB N-H with φ angle marked with orange, bands assigned to the CH_2 group adjacent to PB carbonyl with ψ angle marked with green. Right side shows models of the diglycine molecules geometry in crystals.

3.2.5 Calculated φ-dependence of the CH_2 stretching frequencies and the C-H bond lengths in diglycine

We optimized the geometry and calculated the vibrational frequencies of series of glygly conformers with ψ = 145° where the φ angle varied from 77˚ to 177˚. Figure 3.11A shows the φ angle dependence of the CH_2 symmetrical and the asymmetrical stretches frequencies. As the φ angle increases from 77˚ to 177˚ the $\nu_{as}CH_2$ frequency downshifts by 56 cm-1. The φ dependence of the CH2 symmetrical stretching frequency has a different pattern. From φ = 77˚ to

137˚ the $\nu_{as}CH_2$ declines monotonically by 45 cm-1 and reaches its minimum at φ = 137˚ and then increases again by 15 cm^{-1} as φ changes from 137˚ to 177˚. The magnitude of the CH_2 stretching frequency splitting ($\Delta\nu = \nu_{asym} - \nu_{sym}$) also depends on the φ angle value and varies from 70 cm^{-1} (φ = 137˚) to 21 cm^{-1} (φ = 177˚).

The CH_2 stretching frequencies depend solely on the C-H bond lengths since C-H stretches are not coupled to other vibrations. We examined the φ angle dependence of the C-H bond length of the methylene groups (Fig. 3.11B). The unperturbed CH_2 group is symmetric with both C-H bonds of equal length. However, our calculations show that at φ ≠180° the CH_2 group loses its symmetry because the C-H bonds differ. The potential energy distribution for the CH_2 group vibrations shows that the longer C11-H12 bond contributes more to the low frequency symmetric component (ν_sCH_2), while the shorter C11-H13 bond contributes more to high frequency asymmetric stretching ($\nu_{as}CH_2$). Both C-H bonds have equal length only at φ = 180°, at which the smallest frequency splitting between ν_sCH_2 and $\nu_{as}CH_2$ (~21 cm^{-1}) is calculated. The C-H bond lengths differ the most for φ = 137° where the maximum CH_2 frequency splitting occurs (~ 70 cm^{-1}).

Since φ-angle rotations result in different spatial orientations of the C-H bonds with respect to the peptide bond it is likely that conformational dependence of C-H bond lengths is a result of electronic interactions between the CH_2 group C-H bonds and the peptide bond. For example, the C-H bond length can be changed by the adjacent oxygen or nitrogen lone pairs due to the "trans" or "negative hyperconjugation" which involves the in partial delocalization of the lone pair electrons to the molecular orbitals of the C-H bonds.[8,9] The extent of this transfer is highest when the C-H bond is trans to the lone pair.

Our previous studies demonstrated a negative hyperconjugation between the nitrogen lone pair and the adjacent gly σ^*_{CH} orbitals.[1] For molecule we calculated an increased electron density population in the antibonding σ* orbital of the CH_2 group adjacent to the sp^2-hybridized nitrogen. Since the nitrogen in the peptide bond has partial sp^2 character it is likely that similar hyperconjugation occurs between C-H bonds of the CH_2 group and the adjacent peptide bond nitrogen. The magnitude of this hyperconjugation depends on the Ramachandran φ angle which determines the orientation of the peptide bond relative to the CH_2 group. The peptide bond nitrogen possesses an electron lone pair that interacts with the C=O π-orbital to give the peptide bond its unique partial double bond character. The resulting peptide bond π-orbital is symmetrically localized from both sides of the peptide bond plane. As described in the Fig. 3.12 caption, we expect the strongest hyperconjugation and maximum electron density in σ^*_{CH} orbital when the CH bond oriented close to normal to the peptide bond plane. The shape and spatial orientation of the nitrogen lone pair orbital (LPN9) are shown in Fig. 3.12.

Fig. 3.11 illustrates how φ-rotation changes the orientation of the C11H12 and C11H13 bonds with respect to peptide bond. The C11H12 bond remains close to the nitrogen lone pair LP_{N9} (see Fig. 3.12A) as φ angle changes from 77° to 177°. This C11H12 bond orientation favors hyperconjugation between the σ^*_{C11H12} and LP_{N9} which increases the population of antibonding σ^*_{C11H12} orbital and lengthens C11H12 bond.

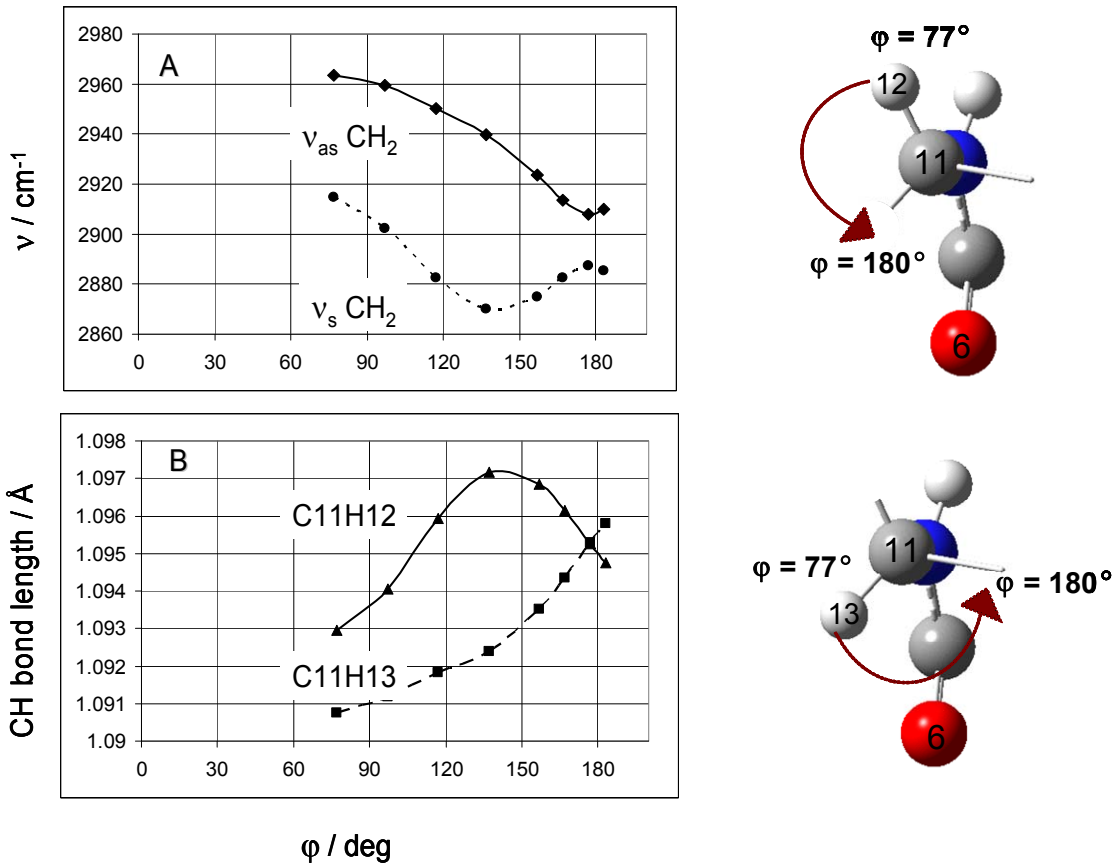

Figure 3.11: Calculated CH_2 stretching frequencies and C-H bond lengths for C11H12H13 methylene as a function of Ramachandran φ angle. Frequencies scaled to 0.98. Structures show the change in relative orientation of the C11H12 and C11H13 bonds with respect to the peptide bond plane as φ increases from 77° to 177°.

The C11H13 bond, in contrast, remains far from nitrogen lone pair cis to the carbonyl group oxygen as φ angle changes from 77° to 177° (Fig. 3.11). This creates favorable conditions for hyperconjugation between the σ_{C11H13} orbital and the diffused lone pair of the carbonyl oxygen (LP_{O6}) as shown in Fig. 3.12B. The proximity of the electronegative O6 to the H13 also shifts some electron density, increasing the positive charge on H13. As a result of both effects the C11H13 bond shortens.

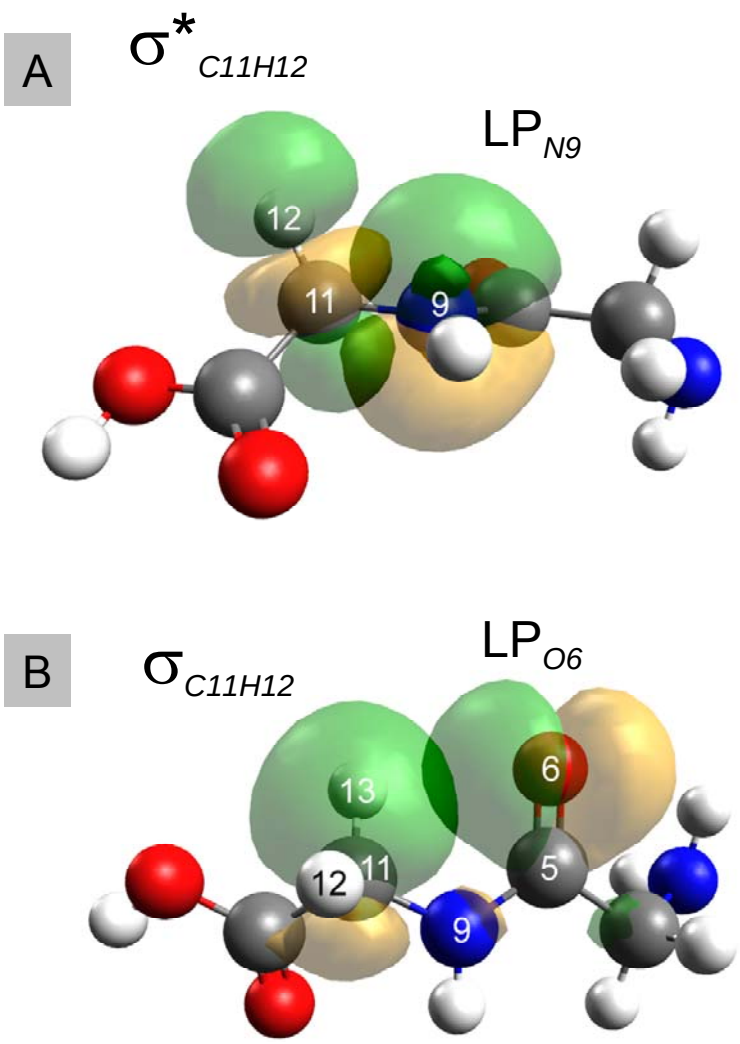

Figure 3.12: Countor plots for A antibonding σ^*_{C11H12} and lone pair LP_{N9} molecular orbitals. B σ_{C11H13} and LP_{O9} molecular orbitals for glygly conformer with φ = 137°. At this φ value the C11H12 bond is almost normal to the peptide bond plane which is favorable for hyperconjugation between the σ^*_{C11H12} orbital and the N9 lone pair. This results in the increased σ^*_{C11H12} population and elongation of the C11H12 bond. The C11H13 bond, in contrast, lies within the peptide bond plane cis to carbonyl oxygen which is favorable for hyperconjugation between bonding σ_{C11H13} orbital and lone pair of O6, which results in shortened C11H13 bond. This C-H bond nonequivalence at φ = 137° results in the largest frequency split (~ 70 cm-1) between $\nu_s CH_2$ and $\nu_{as} CH_2$.

3.2.6 Calculated ψ-dependence of the CH_2 stretching frequencies and the C-H bond lengths in diglycine

We also theoretically investigated the ψ-dependence of the CH_2 stretching frequencies for two glygly conformers where the ψ angle was changed from 0° to 180° by 20° increments. In the first φ was fixed at -77° (this corresponds to the PGII conformation) while in the second φ was fixed at 180° (fully extended). Both cases show very similar CH_2 stretching frequency ψ-dependences (Fig. 3.13) which indicates that the $C_\alpha H_2$ group stretching frequencies depend only on the dihedral angle immediately adjacent to the CH_2 group.

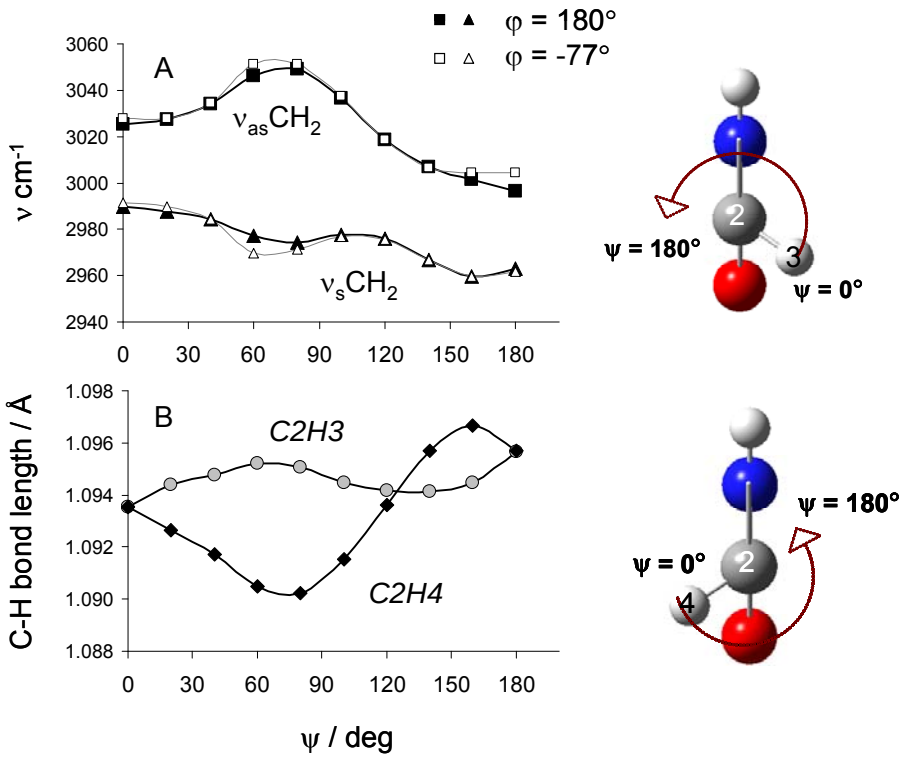

Figure 3.13: Calculated CH_2 stretching frequencies (A) ψ-dependence for two series of conformers with φ = 180° (black filled squares and triangles) and with φ = -77° (grey opened squares and triangles). B C-H bond lengths for C2H3H4 methylene as a function of Ramachandran ψ angle (φ = 180°). Frequencies scaled to 0.98. Structures show the change in orientation of the C-H bonds relative to the peptide bond plane as ψ changes from 0° to 180°.

The ψ-angle rotation around the produces CH_2 frequency shifts which are comparable in magnitude to those due to φ-angle change. The frequency of the asymmetric vibration increases ~ 25 cm^{-1} when φ changes from 0° to ~ 80°, where it reaches a maximum, and then downshifts ~ 53 cm^{-1} when ψ becomes 180° (Fig 3.13). The frequency of the symmetric stretch decreases ~ 27 cm^{-1} in a sinusoidal manner when ψ increases from 0° to 180°. The ψ-angle rotation changes the frequency splitting between the C-H asymmetric and symmetric stretches from 34 cm^{-1} to (φ = 180°) to 75 cm^{-1} (φ = 80°).

Similar to the φ-rotation, as ψ angle changes the C-H bond shortens when it approaches the carbonyl oxygen atom mostly due to the increase in bonding σ_{CH} electron density population and increase in the partial positive charges on the hydrogen atom. When C-H bond orientation is close to normal to the peptide bond plane the C-H bondlength increases mostly due to the hyperconjugation between the antibonding σ^*_{CH} and peptide bond nitrogen lone pair.

3.2.7 Conclusions

Our studies show that the $C_\alpha H$ stretching bands are potentially useful markers for polypeptide backbone conformations since the CH_2 stretching frequencies depend on their Ramachandran φ and ψ angles. Theoretical analysis shows that the frequencies of the symmetric $\nu_s CH_2$ and asymmetric $\nu_{as} CH_2$ vibrations depend primarily on the C-H bond lengths. In turn, the lengths of the C-H bonds depend on their orientation with respect to the adjacent peptide bond which is determined by Ramachandran φ and ψ angles. Molecular orbital analysis indicates that

C-H bond length is affected by redistributions of electron density between the C-H bond molecular orbitals and those of the peptide bond.

3.2.8 BIBLIOGRAPHY

(1) Bykov, S. V.; Myshakina, N. S.; Asher, S. A. *Journal of Physical Chemistry B* **2008**, *112*, 5803-5812.

(2) Kohn, W.; Sham, L. J. *Phys. Rev.* **1965**, *137*, 1697-1705.

(3) Parr, R. G.; Yang, W. *Density-functional Theory of Atoms and Molecules*, 1989.

(4) Becke, A. D. *J. Chem. Phys.* **1993**, *98*, 5648-5652.

(5) Lee, C.; Yang, W.; Parr, R. G. *Phys. Rev. B: Condens. Matter* **1988**, *37*, 785-789.

(6) Irikura, K. K.; Johnson, R. D., III; Kacker, R. N. *J. Phys. Chem. A* **2005**, *109*, 8430-8437.

(7) Halls, M. D.; Velkovski, J.; Schlegel, H. B. *Theor. Chem. Acc.* **2001**, *105*, 413-421.

(8) McKean, D. C. *Chemical Society Reviews* **1978**, *7*, 399-422.

(9) Lii, J.-H.; Chen, K.-H.; Allinger, N. L. *Journal of Physical Chemistry A* **2004**, *108*, 3006-3015.

4.0 CONFORMATIONAL PREFERENCES OF UNFOLDED POLYPEPTIDES IN SOLUTION

4.1 UV RESONANCE RAMAN ELUCIDATION OF THE TERMINAL AND INTERNAL PEPTIDE BOND CONFORMATIONS OF CRYSTALLINE AND SOLUTION OLIGOGLYCINES

The work presented in this chapter was published in *J. Phys. Chem. Lett.*, ACS ASAP. The coathors are Sergei V. Bykov and Sanford A. Asher.

Spectroscopic investigations of macromolecules generally attempt to interpret the measured spectra in terms of the summed contributions of the different molecular fragments. This is the basis of the local mode approximation in vibrational spectroscopy. In the case of resonance Raman spectroscopy independent contributions of molecular fragments require both a local mode-like behavior and the uncoupled electronic transitions. Here we show that the deep UV resonance Raman spectra of aqueous solution phase oligoglycines show independent peptide bond molecular fragment contributions indicating that peptide bonds electronic transitions and vibrational modes are uncoupled. We utilize this result to separately determine the conformational distributions of the internal and penultimate peptide bonds of oligoglycines. Our data indicate that in aqueous solution the oligoglycine terminal residues populate conformations

similar to those found in crystals (3_1-helices and β-strands), but with a broader distribution, while the internal peptide bond conformations are centered around the 3_1-helix Ramachandran angles.

4.1.1 Introduction

Spectroscopic methodologies are of a great importance in chemical analysis and for the determination of molecular structure. Interpretations of spectra generally use reductionist strategies whereby the spectrum of a macromolecule is first interpreted as the sum of the contributions of the individual molecular fragments. This first order analysis is then reanalyzed to take into account higher order phenomena such as the coupling of molecular dynamics between molecular fragments and the environment. For example, in UV resonance Raman (UVRR) spectra of polypeptides the vibrations could be localized within the individual peptide bond (PB), such that the PBs independently contribute. This would lead to spectra that are easily analyzed, where each PB vibration is not context dependent. Alternatively, spectra of polypeptides may result from coupled motion of the backbone atoms of adjacent PB.[1] This would lead to vibrational modes which depend upon their adjacent PB secondary structures.

Our previous study of a mainly ala-peptide in H_2O/D_2O mixtures indicated that the spectra of the partially deuterated chains could be roughly modeled (except for the amide I band) as a statistically weighted sum of deuterated and protonated independent segments.[2,3] This could only occur if the amide vibrations were essentially localized within the individual PB.

Here we show that the deep UV resonance Raman spectra of aqueous solution phase oligoglycines show independent peptide bond molecular fragment contributions; the peptide bonds independently resonance Raman scatter. The peptide bond electronic transitions and

vibrational modes are uncoupled. We utilize this result to separately determine the conformational distributions of the internal and penultimate peptide bonds of oligoglycines.

4.1.2 Experimental Methods

Materials. Gly_2, gly_3, gly_5 and gly_6 were purchased from Bachem (King of Prussia, PA) and used as received. Gly_2 hydrochloride (Sigma Inc.) was recrystallized from water to obtain $Gly_2{\cdot}HCl{\cdot}H_2O$ crystals. Lithium chloride (T.J Baker Inc.) was used for cocrystallization with gly_2 to grow $Gly_2{\cdot}LiCl$ crystals. Lithium perchlorate (Fisher Scientific Inc.) was used to increase the solubility of gly_5 and gly_6 in water and as an internal Raman intensity standard.

Raman measurements. For solution samples we used 204 nm Raman excitation near the maximum absorbance of the peptide bond $\pi \rightarrow \pi^*$ transition. The third harmonic of Nd:YAG laser operating at 100 Hz was anti-Stokes Raman shifted in hydrogen to 204 nm (fifth anti-Stokes) . The peptides were studied in a flow-stream to avoid any contribution from photochemical degradation processes. Scattered light was dispersed by a double spectrometer and was detected by a Princeton Instruments Spec-10:400B CCD camera (Roper Scientific). For solid samples we use pre-resonance 229 nm excitation to minimize sample photodegradation. Raman measurements were performed using an intracavity doubled Ar-ion Laser (Coherent Inc.) A custom made, rotating metal cell was used for the solid powder samples to avoid light-induced sample degradation. The crystal powder was pressed into a circular groove in the rotating metal cylinder Typical accumulation times were less then 1 min.

4.1.3 Vibrational and Electronic Coupling

Fig. 4.1 compares the 204 nm UVRR difference spectrum between gly_6 and gly_5 to that of gly_3. If there were negligible coupling between the PB vibrations the gly_3 spectrum should closely approximate the two terminal PB spectra of oligopeptides, while the gly_6-gly_5 spectrum should approximate a single internal PB vibration.

Summation of the gly_6-gly_5 difference spectra and the gly_3 spectra essentially perfectly models the UVRRS of gly_5 and gly_6 (Fig. 4.1). The differences are below shot noise levels. This result indicates the lack of coupling of peptide bond vibrations between adjacent PB. The ability to accurately model the spectral intensities indicates that couplings between these vibrations and the resonant electronic transitions are localized within each PB.

4.1.4 Internal PB Conformation Preferences

The gly_6-gly_5 spectrum differs significantly from that of gly_3 with a clear doublet spanning the CH_2 twist/Am III spectral region, while gly_3 shows a single complex bandshape. The CH_2 wagging, as well as the Am II and Am I bands of gly_6-gly_5, also differ from those of gly_3 which may imply different structural preferences of the internal and terminal residues.

In separate study reported in Chapter 4.2 of this thesis we compared the internal residue oligoglycine UVRR spectra in solution to that of solid polyglycines of known conformations. These studies indicate that the internal PBs of oligoglycines occur as a broad ensemble of conformations centered around the 3_1-extended helix conformation.

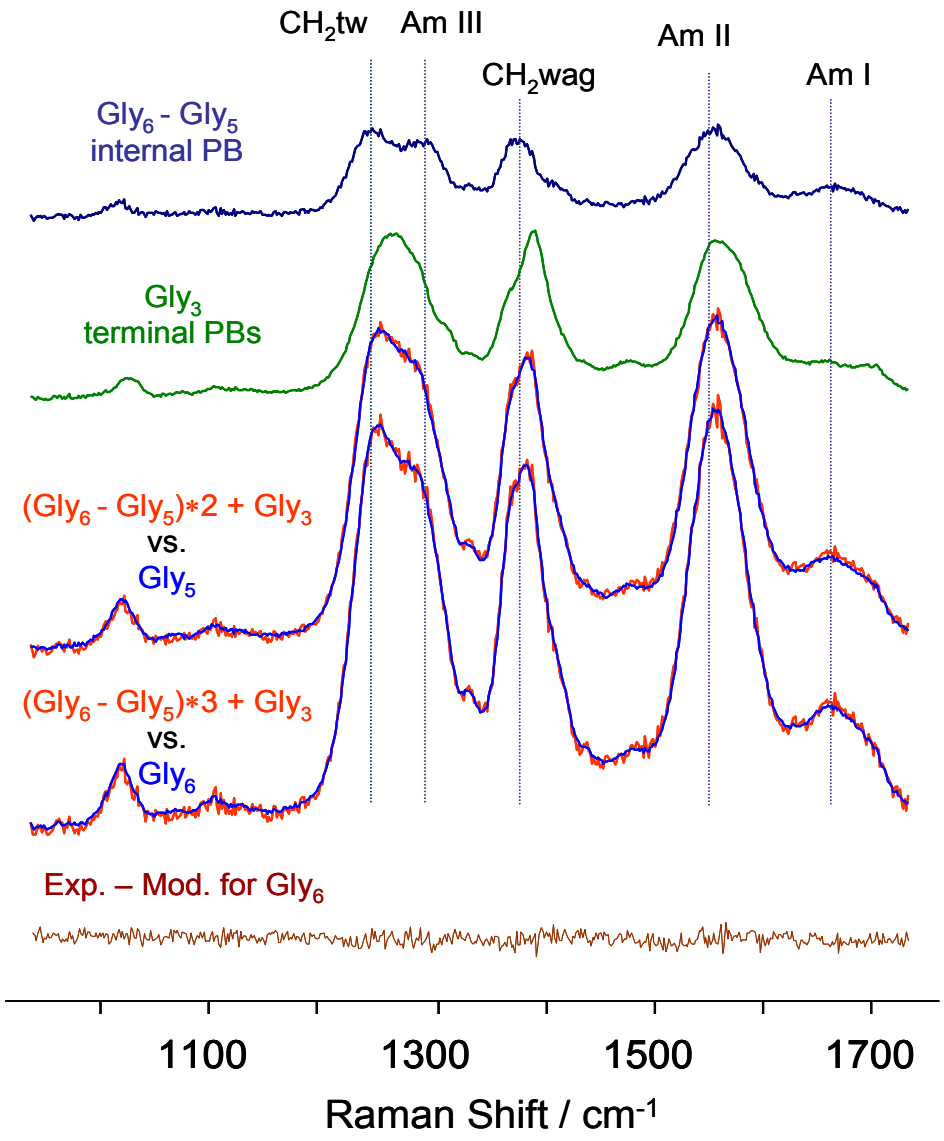

Figure 4.1: 204 nm UVRR spectra of oligoglycines in aqueous solutions containing 0.5 M $LiClO_4$, at neutral pH. The gly_6-gly_5 difference spectrum approximates the spectrum of an internal peptide bond, while that of gly_3 approximates that of the two terminal peptide bonds. This is demonstrated by the fact that the summation of these spectra accurately model gly_5 and gly_6 spectra as demonstrated by the lack of features in the bottom gly_6 difference spectrum between the experimental and modeled spectra. All the UVRRS were scaled relative to the internal standard, perchlorate 932 cm^{-1} band (not shown).

4.1.5 Penultimate PB Conformation Preferences

The UVRR spectrum of gly_3 closely approximates the spectrum of the terminal PB of longer oligoglycines. Gly_3 shows a complex amide III band shape suggesting that multiple conformational states of the peptide are populated in solution. Subtraction of the spectrum of an internal PB (gly_6-gly_5) from the spectrum of gly_3 produces a spectrum which is very similar to that of gly_2 in water (Fig. 4.2) which should approximate the spectrum of the average of the two penultimate oligoglycine PBs.

Table 4.1: Frequencies (ν) and bandwidths (w) of UVRR amide bands in the gly_3-(gly_6-gly_5) difference spectrum, gly_2 in solution and gly_2 crystals

	Gly_3-(Gly_6-Gly_5) difference spectrum	*Gly_2 in solution*	*$Gly_2 \cdot HCl \cdot H_2O$ crystals*	*$Gly_2 \cdot LiCl$ crystals*
	ν (w) /cm^{-1}	ν (w) /cm^{-1}	ν (w) /cm^{-1}	ν (w) /cm^{-1}
Am III	1261(27), 1281(33)	1245(34),1261(29), 1281(26),	1286(15)	1267(18)
CH_2 wag	1400(25)	1395(18), 1402(34)	1404(17)	1393(16)
Am II	1553(27), 1580(46)	1562(27), 1584(57)	1580(38), 1593(20)	1575(29)
Am I	1705(24)	1686(51)	1678(16)	1670(17)

We characterized the conformations of the gly_3-(gly_6-gly_5) PB and gly_2 in solution by comparing their complex amide III bands to those of the amide III bands of crystalline gly_2 derivatives of known structures.

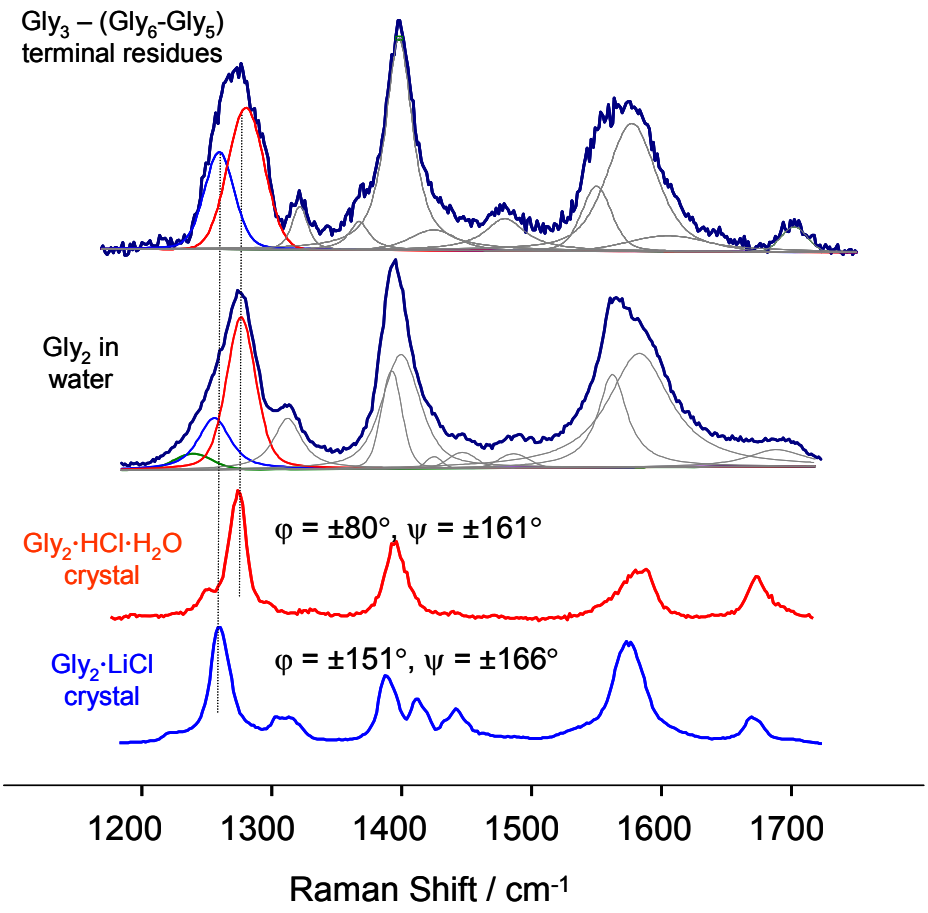

Figure 4.2: UVRR difference spectrum gly_3-(gly_6-gly_5) approximates the spectrum of the two terminal residues of oligoglycines in solution. Also shown is the spectra of gly_2 in solution and two gly_2 crystal samples of known structure: $Gly_2{\cdot}HCl{\cdot}H_2O$ ($\varphi = \pm 80°, \psi = \pm 161°$) and $Gly_2{\cdot}LiCl$ ($\varphi = \pm 154°, \psi = \pm 168°$).[5,6] The complex amide III bandshapes of the solution samples can be well modeled with the amide III bands of these crystal gly_2 derivatives.

The solution UVRR spectra of gly_3-(gly_6-gly_5) and gly_2 show amide III spectral features similar to those in the spectra of gly_2 crystals with known φ and ψ angles (Fig. 4.2). These frequencies and bandwidths are listed in Table 4.1.

Crystalline $Gly_2{\cdot}HCl{\cdot}H_2O$ have $\varphi = \pm 80°$ and $\psi = \pm 161°$ dihedral angles that are close to those of a 3_1-extended helix.[5] Crystals of $Gly_2{\cdot}LiCl$ have $\varphi = \pm 154°, \psi = \pm 168°$, which are

close to that of a β-strand.[6] The amide III band of the β-strand gly_2 is 19 cm^{-1} downshifted compare to that of the 3_1-extended helix indicating significant conformational sensitivity (Table 4.1). The amide III frequencies also depend upon the hydrogen bonding to the PB N-H since N-H bending significantly contributes to the amide III vibration. However both crystal structures have N-H hydrogen bonded to the Cl^- which implies similar HB strengths.

The amide III region of the gly_3-(gly_6-gly_5) difference spectrum, as well as that of the gly_2 spectrum have a complex shape indicating significant conformational inhomogeneity of the terminal residues.

We can estimate the conformational distribution of the solution oligoglycine terminal residues by modeling the amide III region of the gly_3-(gly_6-gly_5) difference spectrum with the well defined amide III bands of crystal gly_2 of known structures. Assuming that the integrated intensities of the amide III bands are proportional to the populations of corresponding conformations in solution, we estimate that in solution ~ 60% of terminal residues are in a 3_1-extended helix-like conformation while ~ 40% are in extended β-strand-like conformation. Modeling of the gly_2 in solution gives similar results (~ 65% in a 3_1-extended helix-like conformation and ~ 35% in an extended β-strand-like conformation).

As discussed above the internal residues of oligoglycines in solution mainly populate a 3_1-extended helix-like conformation. The higher preferences of the terminal residues for a β-strand conformation may result from the favorable interaction between terminal $-NH_3^+$ and the adjacent PB carbonyl, as well as between the terminal $-COO^-$ and the adjacent PB N-H, which are maximized for the completely extended conformation.

The amide III bands of the crystalline samples show full widths at half height of ~15 - 18 cm^{-1} which is likely to be their homogeneous bandwidth. The corresponding solution amide III

bands show almost two-fold broader bandwidths of ~ 26 - 34 cm^{-1} which indicate that the terminal residues of oligoglycines in solution populate a broad ensemble of extended conformations with some preference for the 3_1-helix.

4.1.6 Conclusion

The UV resonance Raman spectra of oligoglycines in aqueous solution can be accurately modeled as a linear sum of the spectra of their internal and terminal peptide bonds which indicates the absence of vibrational and electronic coupling between adjacent PBs in polypeptides in solution. This result significantly simplifies polypeptide UVRR spectral analysis. The UVRR spectra of the oligoglycine internal PBs significantly differ from those of the terminal PBs which implies different structural preferences. Our data indicates that in aqueous solution oligoglycine terminal residues populate a broad range of extended conformations between 3_1-helices and β-strands while the internal PBs conformation are centered around the Ramachandran angles of the 3_1-helix.

ACKNOWLEDGMENT. We thank Dr. Steven Geib for x-ray crystal structure determinations and Bhavya Sharma for help in preparing this letter. This work was supported by NIH, Grant 5R01EB002053.

4.1.7 BIBLIOGRAPHY

(1) Wang, Y.; Spiro, T. G. Vibrational and Electronic Couplings in Ultraviolet Resonance Raman Spectra of Cyclic Peptides *Biophys. Chem.* **2003**, *105*, 461-470.

(2) Mikhonin, A. V.; Asher, S. A. Uncoupled Peptide Bond Vibrations in alpha-Helical and Polyproline II Conformations of Polyalanine Peptides *J. Phys. Chem. B* **2005**, *109*, 3047-3052.

(3) Mix, G.; Schweitzer-Stenner, R.; Asher, S. A. Uncoupled Adjacent Amide Vibrations in Small Peptides *J. Am. Chem. Soc.* **2000**, *122*, 9028-9029.

(4) Bykov, S. V.; Asher, S. A. Conformation of Polyglycine in Solution *In preparation to be submitted*.

(5) Parthasarathy, R. Crystal Structure of Glycylglycine Hydrochloride *Acta Crystallogr., Sect. B* **1969**, *25*, 509-518.

(6) Mueller, G.; Maier, G.-M.; Lutz, M. Lithium Coordination to Amino Acids and Peptides. Synthesis, Spectroscopic Characterization and Structure Determination of Lithium Complexes of Neutral and Anionic Glycine and Diglycine *Inorg. Chim. Acta.* **1994**, *218*, 121-131.

4.2 SOLUTION CONFORMATIONS OF POLYGLYCINE

This work is in preparation for publication. The coathors are Sergei Bykov and Sanford Asher

Polyglycine (polygly) is an important model system for understanding the structural preferences of unfolded polypeptides in solution. We utilized UV resonance and visible Raman spectroscopy to investigate the conformational preferences of polygly peptides of different lengths in water containing LiCl and $LiClO_4$ salts. Lithium salts increase the solubility of polygly. Our study indicates that in solution the conformational ensemble of polygly, as well as central peptide bonds of gly_5 and gly_6, are dominated by the 3_1 extended helix also known as the polyglycine II conformations (PGII). This preference of the polygly backbone for the PGII conformation in solution is likely a result of favorable interactions between carbonyl dipoles in these extended helices. We found that high concentrations of Li^+ stabilize the PGII conformation in solution, most likely by polarizing the peptide bond carbonyls which makes PGII-stabilizing carbonyl-carbonyl electrostatic interactions more favorable. This ability of Li^+ to stabilize 3_1-helix conformations in solution is likely one of the key to denaturing ability of lithium salts.

4.2.1 Introduction

Polyglycine (polygly) occurs in two major structural forms in the solid state – polyglycine I (PGI) and polyglycine II (PGII). Both are extended conformations, with Ramachandran dihedral angles of φ = -140°, ψ =136° and φ = -77°, ψ = 145°. These conformations are stabilized in the solid state by inter-molecular hydrogen bonding between the amide NH and CO groups.

The PGI structure is similar to that of an anti-parallel β-sheet, where the almost fully extended backbone forms hydrogen bonds with two anti-parallel neighboring chains approximately in the same plane. PGII, in contrast, is an extended 3_1-helix structure which hydrogen bonds to the six parallel neighboring chains packed in a hexagonal array.[1] Right-handed 3_1-helix conformations are often called polyproline II conformations (PPII) since this structure was first discovered in polypro. The PPII extended helix is now believed to dominate the poorly understood denatured conformation of proteins.

While the solid state of polygly has been extensively studied, very little is known about polygly solution conformations. Oligoglycines longer than 5 residues are normally insoluble in water. Also gly has no chiral atoms, which means that polygly can not be studied by CD, the standard method used for secondary structure analysis of peptides and proteins in solution.

In the study here we utilized LiCl and $LiClO_4$ to increase the solubility of polygly chains in water. Li^+ substantially increases the solubility of gly-based peptides in water. For example, LiBr is often used to dissolve and purify silk peptides/proteins which consist mostly of gly, ala and ser residues.

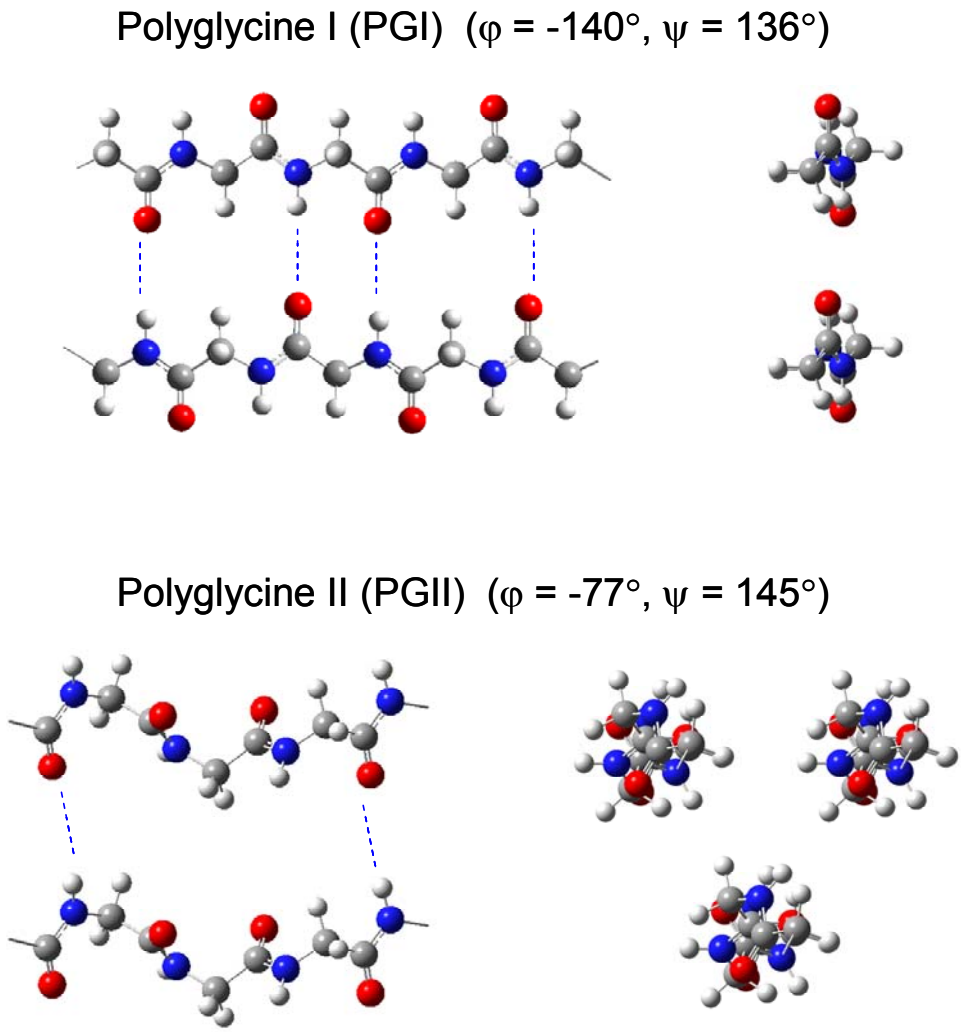

Figure 4.3: Two conformations of polygly occure in the solid state: β-sheet-like PGI and the extended 3_1-helix PGII.

Experimental data on the conformational preferences of gly-based peptides in solution are very limited. Ohnishi et al.[2] showed that the radius of gyration of a six residue gly-based peptide indicates that it is extended, but it length was estimated to be shorter than that of an ideal β-strand or PGII structure, but longer than that of an ideal α-helix. According to polarized visible Raman and FTIR measurements, gly_3 in D_2O solution forms heterogeneous ensembles of

conformations which include 3_1-helix, α-helix and β-turns.[3] Takekiyo et al. investigated Ac-Gly-NHMe in water at normal and high pressure and found that the most populated conformation is PPII.[4] Recently we investigated the conformational preferences of the terminal residues of short oligoglycines in aqueous solution and found that the terminal residues span a broad range of extended conformations with some preference for extended 3_1-helix-like conformations and a significant contribution of β-strand-like conformations.

In the work here we used UV resonance Raman and visible Raman spectroscopy to investigate the solution conformation of long polygly. We compare the spectra of polygly in solution to known solid state structures.

4.2.2 Experimental methods

Materials. Polygly, m.w. 500-5000, was purchased from Sigma-Aldrich (St. Louis, MO) and used as received. Lithium chloride (T.J Baker Inc.) and lithium perchlorate (Fisher Scientific Inc.) were used to increase the solubility of polygly. Gly_2, gly_3, gly_5 and gly_6 were purchased from Bachem (King of Prussia, PA) and used as received. Polygly in the PGI and PGII conformations were prepared by precipitation from concentrated LiCl solutions and from trifluoroacetic acid solutions as described elsewhere.[5]

Solution samples. The 204 nm Raman excitation occurs near the maximum absorbance of the peptide bond $\pi \rightarrow \pi^*$ transition. The third harmonic of a Nd:YAG laser operating at 100 Hz was anti-Stokes Raman shifted in hydrogen to 204 nm (fifth anti-Stokes) . The peptides were studied in a flow-stream to avoid contributions from photochemical degradation. Scattered light was dispersed by a double spectrometer and was detected by a Princeton Instruments Spec-10:400B CCD camera (Roper Scientific). A detailed description of the instrumentation is given

elsewhere.[6] Excitation of the Raman spectra in the CH stretching region (2700 – 3200 cm^{-1}) utilized 488 nm Ar-ion laser excitation since CH stretches are not enhanced by deep UV resonance excitation, but become overlapped by amide band overtones. A 488 nm holographic notch filter (Kaiser Optical Systems Inc.) was used for Raleigh rejection. We used 10 mg/ml concentrations for the visible Raman measurements. A temperature controlled fused silica cell (20 mm path length, Starna Cell Inc.) was used for the 488 nm studies.

Solid samples. For the amide region, we used pre-resonance 229 nm excitation to minimize sample photodegradation. Raman measurements were performed using an intracavity doubled Ar-ion laser (Coherent Inc.) Scattered light was collected using a back-scattering geometry, dispersed by a single monochromator and detected using a Princeton Instruments Spec-10:400B CCD camera (Roper Scientific). Typical accumulation times were less then 1 min. A 488 nm excitation was used for the CH stretching region. A custom made, rotating metal cell was used for the solid powder samples to avoid light-induced sample degradation. The powder was pressed into a circular groove in the rotating metal cylinder

4.2.3 Results

UV resonance Raman spectroscopy is a powerful tool for investigating polypeptide conformation. Excitation with deep ultraviolet light within the $\pi \rightarrow \pi^*$ electronic transitions of the peptide bonds results in resonance enhancement of the Raman bands associated with vibrations which distort the peptide bond ground state geometry towards that of the exited state. These amide bands result from polypeptide backbone atom stretching and bending vibrations which makes them sensitive and convenient markers for peptide and protein secondary structure.

Gly is a structurally distinct amino acid because it has no C_β atom. This dramatically alters the polygly normal modes compared to the typical amino acid. The UVRR spectrum of gly-based peptides is dominated by five bands in the amide region: the amide I, amide II, amide III, CH_2 wagging and CH_2 twisting (Fig. 4.4). The amide I band is predominantly peptide bond carbonyl stretching, which is sensitive to the carbonyl environment. The amide II and amide III bands result from complex vibrations of the peptide backbone heavy atoms which are coupled to N-H and $C_\alpha H$ bending. These bands are sensitive to polypeptide conformation and hydrogen bonding to the peptide bond N-H. The CH_2 wagging and CH_2 twisting bands result from $C_\alpha H$ deformation vibrations with some contribution from backbone C-C stretching. The CH_2 twisting band is the least sensitive to polypeptide conformation and hydrogen bonding among the amide bands.

Our previous study showed that the terminal residues in oligoglycines span a broad range of extended 3_1-helix-like and β-strand-like conformations. Terminal residues of uncapped polypeptides in solution may have distinct conformational preferences due to the electrostatic and steric interactions of the terminal carboxyl and amine groups with the adjacent peptide bonds.

To eliminate the contributions of the terminal residues to the total Raman spectra of polygly, the spectrum of gly_3 was subtracted from those of gly_5 and gly_6. Recently we showed that spectrum of gly_3 closely approximates the spectrum of the two terminal peptide bonds in longer polygly, and that the total UVRR of the oligogly in solution can be treated as a linear sum of the comprising peptide bonds. Thus, the resulting $gly_5 - gly_3$ (or $gly_6 - gly_3$) difference spectra approximate the spectra of the middle residues of the gly_5 (or gly_6).

Figure 4.4 compares the UVRR spectrum of polygly (A) to the gly_5 – gly_3 difference spectrum (B). It shows that UVRR spectrum of high molecular weight (500-5000) polygly, where the contributions from the terminal residues are negligible, is almost identical to the spectrum of the gly_5 where the contribution of the terminal residues is subtracted. This result implies that long polygly chains and central parts of the short oligogly chains populate the same conformational space in aqueous solution. The identical result was obtained for the internal residues of gly_6 (spectra not shown).

To gaint insight into the conformational preferences of the long polygly chains in solution we compared the UVRR spectra of polygly in 1.5 M $LiClO_4$** aqueous solution to that of solid polygly samples of known conformations. Polygly can adopt antiparallel β-sheet like PGI and extended 3_1-helix PGII in the solid state. These conformations can be obtained by precipitation from solution. Figure 4.4 shows the UVRRS of polygly in solution and spectra of solid polygly samples in the PG II and PGI conformations.

The CH_2 twisting mode at 1250 cm^{-1} does not show a significant frequency difference between the solid state PGI and PGII conformations, and polygly in solution. In contrast, the amide III band upshifts 75 cm^{-1} from 1216 cm^{-1} for PGI to 1291 cm^{-1} for PGII, in the solid state. The polygly amide III band in solution is at ~ 1300 cm^{-1}, similar to that of the solid PGII sample. The CH_2 wagging downshifts 29 cm^{-1} (from 1409 to 1380 cm^{-1}) between the PGI and PGII conformations, while the amide II band upshifts 44 cm^{-1}. The amide I downshifts only 8 cm^{-1}. The CH_2 wagging band frequencies and the amide II and amide I band frequencies of polygly in solution (see Table 4.2) are also very close to those of the solid state PGII conformation. The

** $LiClO_4$ is used to increase the solubility of polygly in water and as an internal Raman intensity standard.

UVRR data indicate that polygly in aqueous solutions containing Li^+ exist in a conformation close to the PGII extended helix in the solid state. The spectral frequencies of the solid state PGI and PGII conformations agree well with those calculated by Abe and Krimm.[7,8]

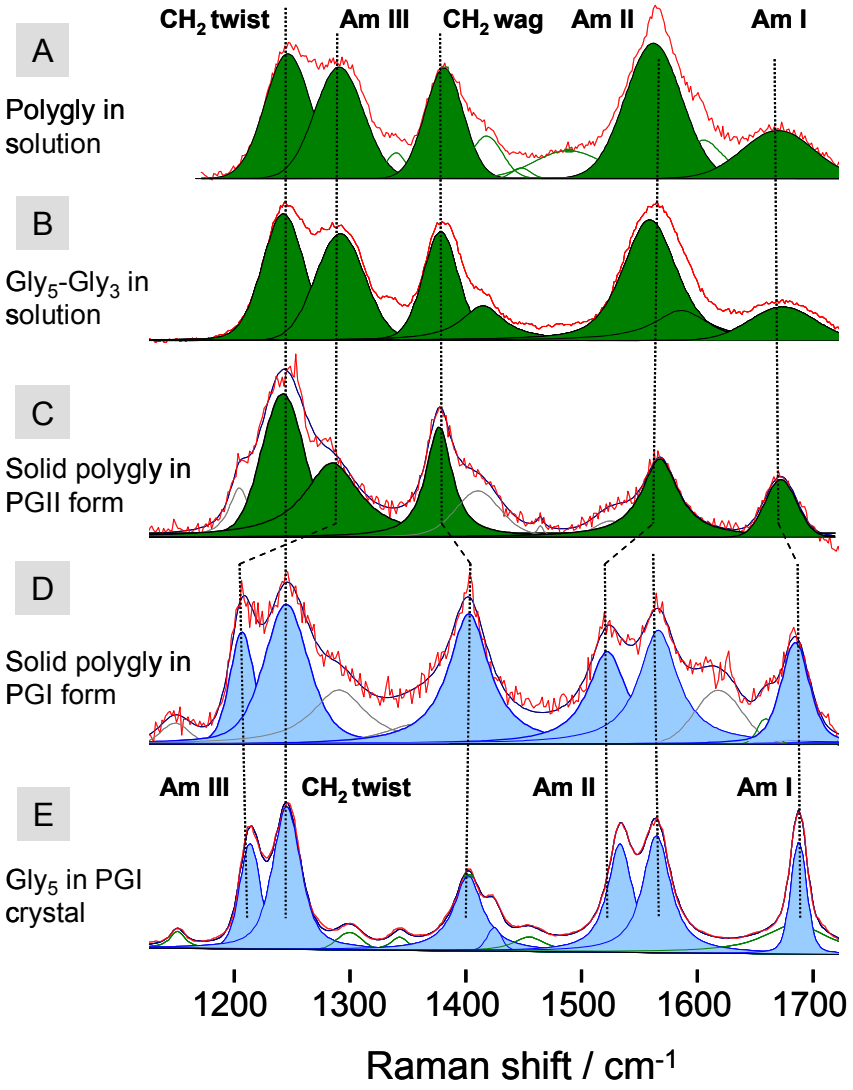

Figure 4.4: UVRR spectra of polygly. A. Polygly (~ 1 mg/ml) in 1.5 M $LiClO_4$ aqueous solution. B. Gly_5 – Gly_3 difference spectrum which approximates the spectra of the middle residues of gly_5 in solution. C. Solid polygly powder precipitated from concentrated LiCl solution (mostly PGII). D. Solid polygly precipitated from trifluoroacetic acid solution (mostly PGI conformation). E. Gly_5 PGI crystalline form. Bands from PGII conformation are marked in green, while PGI conformation bands are in blue.

Table 4.2: UVRR frequencies (ν) and bandwidths (w) of the amide bands of polygly

	polygly in 1.5 M $LiClO_4$ solution		*solid polygly, mostly PGII sample*		*solid polygly, mostly PGI sample*		*gly_5, PGI crystal*	
	ν / cm^{-1}	w / cm^{-1}	ν / cm^{-1}	w / cm^{-1}	ν / cm^{-1}	w / cm^{-1}	ν / cm^{-1}	w / cm^{-1}
$CH_{2\ twist}$	1254	42	1249	41	1253	43	1249	27
Am III	1300	58	1291	56	1216	24	1219	20
$CH_{2\ wag}$	1386	32	1380	26	1404	41	1400	28
Am II	1562	58	1563	37	1519	39	1525	25
Am I	1667	79*	1663	31	1675	28	1674	15

* The amide I band of polygly in water is unusually broad, likely due to the residual contribution from the water bending vibration.

In crystalline solids, molecular conformations are often determined by crystal packing forces which result in a single well-defined conformation. This explains the much smaller bandwidths (FWHM) of the amide II and amide III bands in the UVRRS of crystalline gly_5 of ~ 20-25 cm^{-1} (Table 4.2), as opposed to the polygly in solution FWHM of ~ 58 cm^{-1}, which is almost 3-fold broader.

4.2.4 Conformation of polygly and oligogly in solution. Evidence from the CH stretching region

Since the peptide bond includes highly polar groups such as C=O and N-H, the amide band frequencies depend not only on backbone conformation but also on its hydrogen bonding,

which will differ between solid state and solution polygly. The C-H bond is much less polar, which will minimize the dependence of the C-H stretching frequencies on the environment.

We previously showed that the gly and gly_2 $C_\alpha H_2$ group stretching vibrations show a large conformational dependence.[9] In peptides, the conformational sensitivity of the CH_2 stretching frequencies arises from hyperconjugation of the C-H bond molecular orbitals with those of the adjacent peptide bond.

Figure 4.5 compares the Raman spectra of the CH_2 stretches of polygly in solution and solid state. Table 4.3 shows the frequencies and bandwidths of the CH_2 stretching bands. The CH stretching region of solution polygly and solid state PGII are very similar. Both show the CH_2 stretch doublets with an intense symmetric stretch at 2936 cm^{-1}, and a less intense asymmetric stretch at 2976 cm^{-1}. The CH_2 stretching doublet of β-sheet-like PGI is red-shifted compared to that of PGII, with the CH_2 symmetric stretch at 2924 cm^{-1} and the asymmetric stretch at 2948 cm^{-1}, showing comparable intensities.

Gly_5 in the PGI conformation shows its symmetric stretch at 2929 cm^{-1} and its asymmetric stretch at 2950 cm^{-1}, similar to polygly, but with narrower bands. The low intensity bands in the spectrum of gly_5 (marked with the *) are due to the terminal methylene groups where the CH_2 stretching frequencies are shifted by the adjacent amine and carboxyl groups.[9]

As in the case of the amide III band, the bandwidths of the CH_2 stretches of PGII in solution and solid state are significantly broader then those in the PGI form, indicating an increased PGII conformational inhomogeneity.

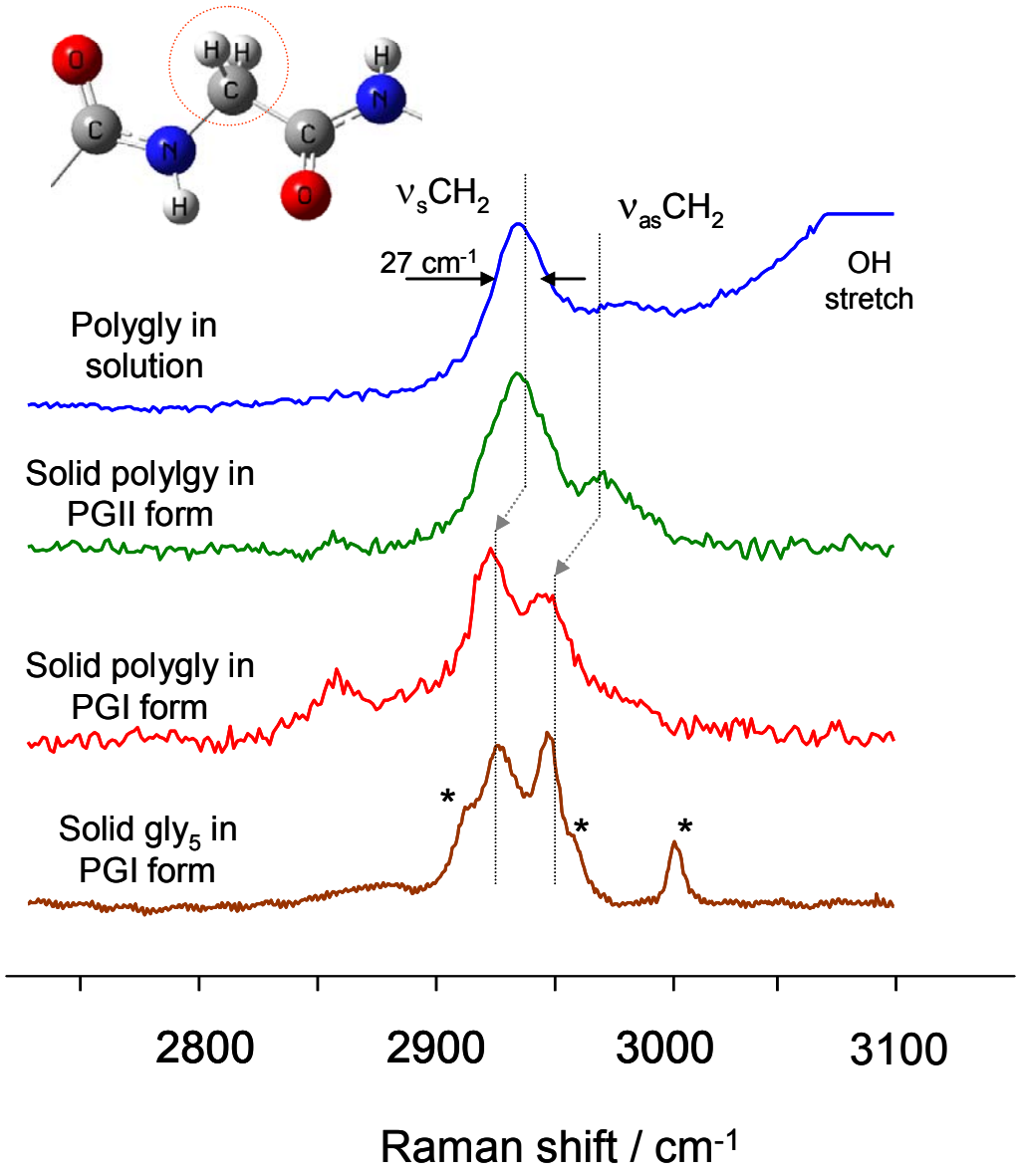

Figure 4.5: 488 excited Raman spectra of polygly in 9 M LiCl solution, solid polygly in the PGII form, solid polygly in the PGI form, gly_5 in the PGI form. The spectra of polygly in solution and solid polygly in the PGII form are essentially identical. The homogeneous FWHM of the CH_2 stretch is ~ 12 cm^{-1} as determined from spectra of gly_5 crystals. The bandwidth of the $\nu_s CH_2$ of the solution sample is more then twice that of crystalline gly, indicating solution conformational inhomogeneity. The structure on the top shows the CH_2 group in a peptide segment in the polygly chain.

Table 4.3: The gly_n frequencies and full-width-at-half-maximum (w) of the $C_\alpha H_2$ symmetric ($\nu_s CH_2$) and asymmetric ($\nu_{as} CH_2$) stretching bands in solution and solid state

	polygly in 9 M LiCl solution		*solid polygly, mostly PGII*		*solid polygly, mostly PGI*		*gly_5, PGI crystal*	
	ν / cm^{-1}	w / cm^{-1}	ν / cm^{-1}	w / cm^{-1}	ν / cm^{-1}	w / cm^{-1}	ν / cm^{-1}	w / cm^{-1}
$\nu_s CH_2$	2937	27	2936	32	2924	19	2929	21
$\nu_{as} CH_2$	2976	35	2976	30	2948	25	2950	13

4.2.5 Discussion

Polygly is the most flexible polypeptide because its lack of side chains removes steric hindrances. The polygly Ramachandran plot shows more allowed regions than for any other amino acid. Because gly is achiral, the sterically allowed regions are symmetric about ($\varphi = 0°$, $\psi = 0°$) which means that conformations with (φ, ψ) and ($-\varphi$, $-\psi$) are identical. Gly can assume virtually any ψ angle while its φ-angle has a forbidden region ($\varphi \sim 0 \pm 60°$) due to adjacent peptide bond carbonyl oxygen clashes.

This high flexibility of polygly chains makes any strictly defined conformations highly entropically unfavorable. Molecular dynamic simulations of gly derivatives, such as Ace-Gly-Nme, show a distribution of conformations with a broad population maxima which depend on the force field used for calculations.[10] In proteins gly often assumes conformations that are not sterically allowed for other amino acid residues such as a left-handed 3_{10}-helix.[11]

Our Raman data show that both internal residues of short oligoglys and long polygly homopolymers in solution populate Ramachandran angles centered on the PGII ($\varphi \sim -77°$, $\psi \sim 145°$) or 3_1 extended helix, which are not significantly populated for gly in folded proteins.[12,13]

4.2.6 Effect of Li+ on polygly in solution

Polygly chains longer than 5 residues are insoluble in pure water. Lithium salts can significantly increase the solubility of polygly. The small Li^+ ions produce strong electrostatic fields and strongly interact with water oxygen atoms to form stable $Li^+(H_2O)n$ complexes, where n depends on the Li^+ concentration. Some spectroscopic studies indicate that the Li^+ ion can directly bind to the amide groups at the carbonyl oxygens due to the carbonyl group large dipole moment.[14-16] Li^+ may also compete with the peptide bond N-H for hydrogen bonding to water oxygens.

In order to gain insight into the specific influence of the lithium salts on the peptide bond we investigated the Li^+ induced perturbations in the UVRR spectra of gly_3. Figure 4.6 shows the spectra of the gly_3 at low (0.3 M) and high (9 M) Li^+ concentrations at 10°C and 60°C. The polypeptide amide band frequencies in aqueous solution are temperature dependent because increaced temperature decreases the PB hydrogen bonding to water.[17,18]

At low (0.3 M) Li^+ concentrations the gly_3 spectra show the temperature induced frequency shifts which are typical for a water exposed peptide bond. In H_2O the amide II and amide III bands are the most temperature dependent and downshift -4.3 and -3.7 cm^{-1} as the temperature increases from 10°C to 60°C. The amide I band slightly upshifts 1.6 cm^{-1} (Fig. 4.7, Table 4.4).

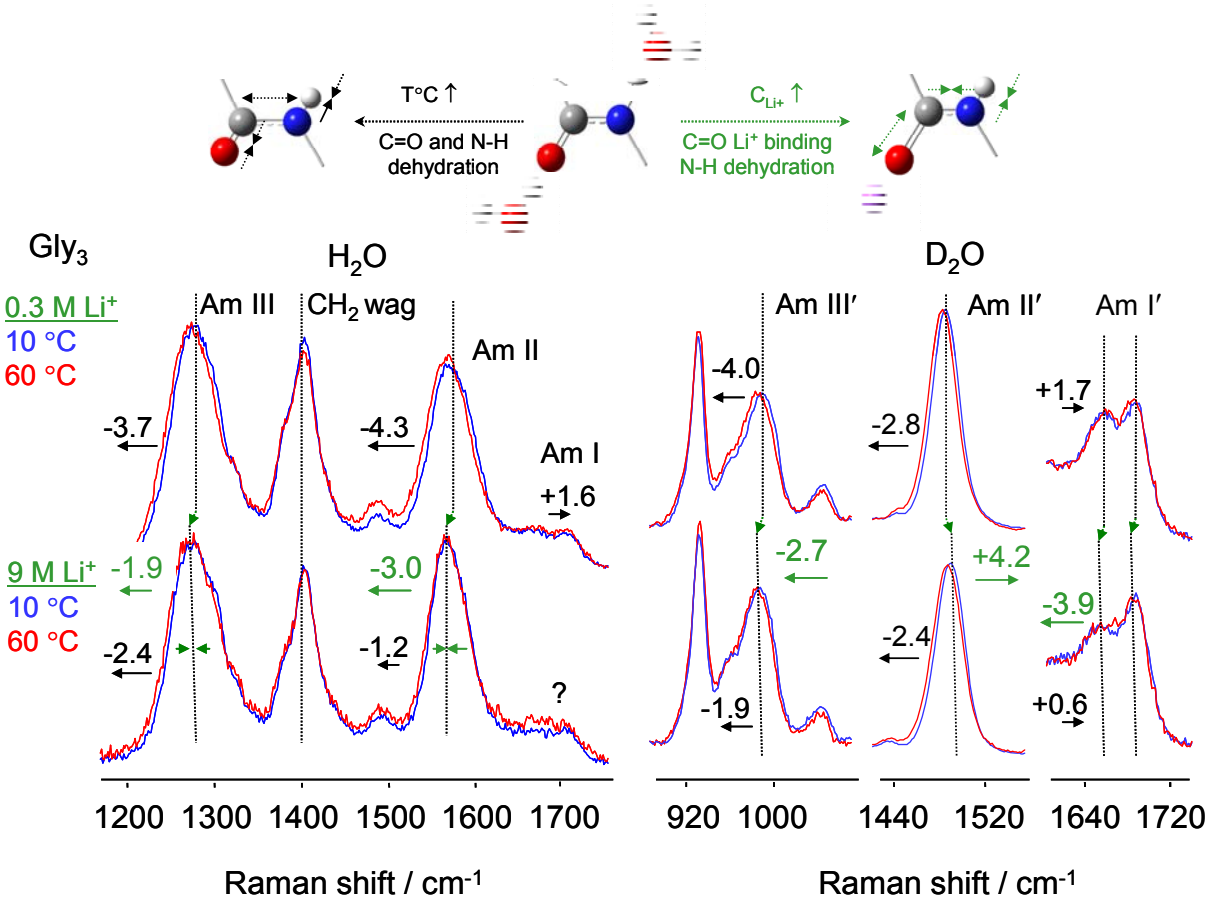

Figure 4.6: UVRR spectra of gly_3 in H_2O (left) and D_2O (right) at 0.3 M (top) and 9 M (bottom) of Li^+. Blue 10°C, red 60°C. H_2O and D_2O contributions are numerically subtracted. The temperature induced frequency shifts between 10 °C and 60 °C are shown by black arrows. Green arrows indicate Li^+ induced band shifts and band narrowing at 10 °C. The spectra are arbitrarily scaled. The molecular structures above schematically show the effects of dehydration and Li^+ binding to the carbonyl oxygens on the PB lengths.

The amide II and amide III band frequencies are sensitive to hydrogen bonding change since these vibrations have a significant contribution from N-H bending. Temperature increases weaken hydrogen bonding between N-H and water, making N-H bonds shorter which downshifts the amide II and amide III frequencies. In contrast, weakening of the hydrogen bonding between the PB carbonyl and water results in C=O bond shortening and upshifting of the amide I band

(C=O stretch). The temperature induced change in the C=O, C-N and N-H bond length is schematically shown in Fig. 4.7.

At high concentrations of Li^+ the temperature induced downshifts of the amide II and amide III bands decrease. The amide II band downshifts only by -1.2 cm^{-1} while the amide III band downshifts -2.4 cm^{-1} as the temperature increases from 10 °C to 60 °C in 9M LiCl (Fig. 4.7 and Table 4.4). This decreased temperature dependence of the amide II and amide III bands in concentrated Li^+ solutions indicates a change in the hydrogen bonding to the peptide N-H group.

The amide II band is the most affected by Li^+. At 10 °C the amide II band downshifts -3 cm^{-1} upon increasing the LiCl concentration from 0.3 M to 9 M. This downshift is likely due to weakening of the hydrogen bonding between the peptide bond N-H and water, probably due to N-H dehydration. The small Li^+ has a high charge density and complexes with 4-6 water molecules in its first solvation shell. In 9 M LiCl most of the water molecules are oxygen bound to Li^+, decreasing the hydrogen bonding of water to the peptide bond N-H.

High Li^+ concentrations significantly narrow the amide II bandwidth ~ 20% (10.6 cm^{-1}), which indicates a decrease of gly_3 conformational distribution. The amide III band also narrows ~ 5%. This smaller bandwidth change may be due to smaller amide III sensitivity to the particular conformational alterations. For instance, if a decrease in the conformational distribution results from a stabilization of 31-helix over β-strand, this would mainly alter the Ramachandran φ angle. The amide III band, in turn, shows only moderate φ dependence.[18]

For additional insight into the Li^+ effect on the peptide bond, we investigated the influence of temperature and lithium salts on the UVRR spectra of the gly_3 in D_2O. In D_2O the O-D bending band is significantly downshifted from the amide I region making it easy to

determine the amide I′ frequencies. N-H deuteration also dramatically changes the normal mode compositions of the amide II′ band, which becomes almost a pure C-N stretch.

The amide II′ band response to Li^+ is opposite to that of the protonated amide II band. The amide II′ band upshifts 4.2 cm^{-1} as the concentration of Li^+ increases from 0.3 M to 9 M in contrast to the -3 cm^{-1} downshift of the protonated amide II. This opposite frequency response results from the difference in normal mode composition of the amide II and amide II′ bands. Upon PB deuteration the amide II′ completely loses its N-H(D) bending component, and becomes almost a pure C-N stretch. Thus, the hydrogen bonding to the N-D will not directly affect the amide II' frequency. However hydrogen bonding to the PB N-D and C=O still indirectly affects the C-N bond length and the amide II′ frequencies. For example, strong interaction of Li^+ with the C=O elongates it, which shortens the adjacent C-N bond to increase the amide II′ frequency. The C=O elongation results in a -3.9 cm^{-1} amide I′ band frequency downshift upon the Li^+ concentration increase (Fig. 4.7, Table 4.5). Note that the amide I band of gly_3 appears as a doublet because the N-terminus and C-terminus amide I frequencies differ.

The amide II′ and amide III′ bands frequencies lose their conformational sensitivity upon peptide bond N-H deuteration since the N-D and $C_\alpha H$ bending motions do not couple. As a result, the amide II′ amide III′ bands do not show any significant bandwidth change in D_2O upon the Li^+ concentration increase.

Table 4.4: Band frequencies (ν), FWHM bandwidths (w), temperature dependences of band frequencies (Δν/ΔT) and temperature dependences of bandwidths (Δw/ΔT) for the amide bands in the Raman spectra of gly_3 in H_2O solution

	Gly_3 in H_2O, 0.3 M Li^+						Gly_3 in H_2O, 9 M Li^+						effect of Li^+ at 10°C	
	10° C		60° C		Δν/ΔT	Δw/ΔT	10° C		60° C		Δ ν/ΔT	Δ w/ΔT	Δ ν	Δ w
	ν / cm^{-1}	w / cm^{-1}	ν / cm^{-1}	w / cm^{-1}	cm^{-1}/°C	cm^{-1} / °C	ν / cm^{-1}	w / cm^{-1}	ν / cm^{-1}	w / cm^{-1}	cm^{-1} / °C	cm^{-1} / °C	cm^{-1}	cm^{-1}
Am III	1276.3	63.8	1272.6	65.3	- 0.08	0.03	1274.4	60.4	1272.0	61.5	- 0.05	0.02	-1.9	-3.4
Am II	1571.7	62.9	1567.4	63.0	- 0.09	0.002	1568.7	52.3	1567.5	55.2	- 0.03	0.06	-3.0	-10.6
Am I	1663.5 1708.9	100.1 23.4	1665.1 1708.5	100.6 24.4	-	-	-	-	-	-	-	-	-	-

Table 4.5: Band frequencies (ν), FWHM bandwidths (w), temperature dependences of band frequencies (Δν/ΔT) and temperature dependences of bandwidths (Δw/ΔT) for the amide bands in the Raman spectra of gly_3 in D_2O solution

	Gly_3 in D_2O, 0.3 M Li^+						Gly_3 in D_2O, 9 M Li^+						effect of Li^+ at 10°C	
	10° C		60° C		Δν/ΔT	Δw/ΔT	10° C		60° C		Δ ν/ΔT	Δ w/ΔT	Δ ν	Δ w
	ν / cm^{-1}	w / cm^{-1}	ν / cm^{-1}	w / cm^{-1}	cm^{-1} / °C	cm^{-1} / °C	ν / cm^{-1}	w / cm^{-1}	ν / cm^{-1}	w / cm^{-1}	cm^{-1} / °C	cm^{-1} / °C	cm^{-1}	cm^{-1}
Am III′	989.2	33.9	985.2	37.3	-0.08	0.07	986.5	34.1	984.6	34.7	-0.04	0.01	-2.7	0.2
Am II′	1485.4	28.8	1482.6	29.5	-0.06	0.02	1489.6	29.2	1487.2	29.7	-0.05	0.01	4.2	0.4
Am I′	1661.0 1690.5	49.7 20.3	1662.7 1689.8	52.5 21.4	0.03 -0.01	0.06 0.02	1657.1 1689.9	56.8 24.1	1657.7 1688.7	59.1 23.2	0.01 0.03	0.05 -0.02	-3.9 -0.6	7.1 3.8

4.2.7 Peptide bond carbonyl dipole-dipole interaction

Initially, Ramachandran explained the allowed regions of the peptide bond φ and ψ angles in terms of hard sphere repulsions between atoms. But this simple explanation results in significant discrepancies between the expected allowed regions in the classical Ramachandran plot and the observed φ, ψ distributions found in high-resolution protein structures. For example, the steric interactions do not account for the diagonal shape of the α_R and α_L region and for the partitioning of the β-region into two diagonal population maxima, the β-strand and PPII regions. It has been shown that these phenomena can be explained by electrostatic interactions within the polypeptide backbone, particularly dipole-dipole interactions.[19]

Maccallum et al. pointed out the importance of the C=O dipole-dipole interactions in stabilizing β-sheet and PPII conformations.[20] Interactions between N-H dipoles appear to be less important because of the significantly lower N and H atom partial charges. Carbonyl-carbonyl dipole interaction energies were also shown to stabilize partially allowed conformations of asp and polyasp.[21] Calculations show that for an antiparallel bis-propanone dimer carbonyl-carbonyl interactions can be as high as ~ -22 kJ/mol, which is comparable to a medium strength hydrogen bond.[22]

Ho and Brasseur[23] analyzed the Ramachandran plot of polygly in detail and also calculated electrostatic interactions. They showed that the energy minima in the carbonyl dipole-dipole interaction map correspond to regions populated by 3_1-helix conformations (left and right-handed) in the Ramachandran map (Fig. 4.7).

Thus, the narrowing of the gly_3 conformational distribution observed at high Li^+ concentrations as indicated by the narrowing of the UVRR amide bands most likely results from stabilization of 3_1-helix-like conformations in solution. The strong electrostatic fields created by Li^+ cations polarize the peptide bond carbonyls, strengthening peptide bond carbonyl dipole-dipole interactions and making the solution PGII conformation more favorable.

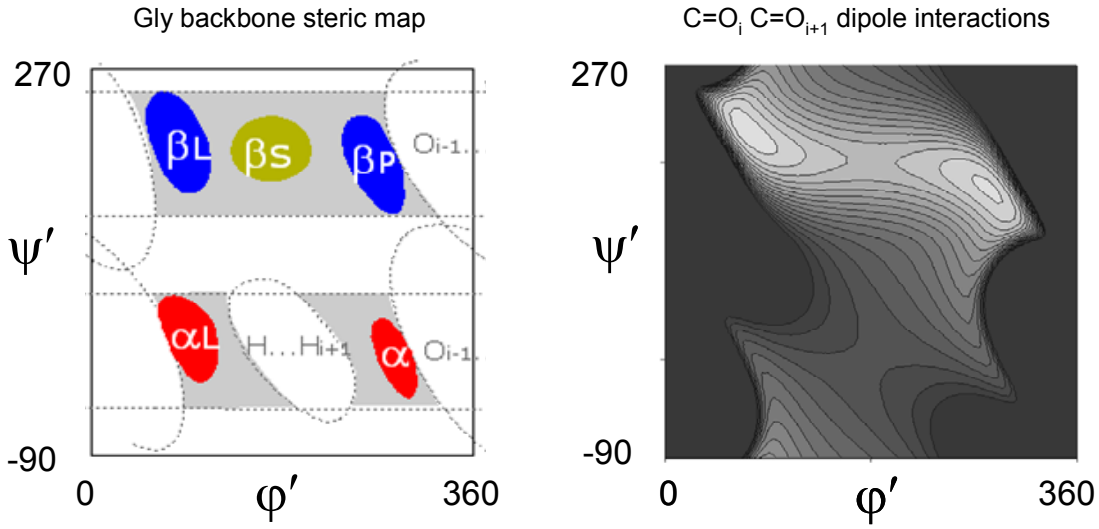

Figure 4.7: Comparison of the Ramachandran plot and calculated energies map [kcal/mol] of the carbonyl-carbonyl dipole interactions for polygly (light areas correspond to the energy minima). βL and βP regions on the Ramachandran plot correspond to 3_1-helices (left and right-handed). 3_1 regions coincide with the energy map minima. Plots are shown in shifted ψ′, φ′coordinates to avoid disruption of the β-regions on Ramachandran plot. This figure was kindly provided by Dr. Bosco Ho.

4.2.8 Conclusions

We utilized UV resonance Raman and visible Raman spectroscopy to investigate the conformation of the most flexible polypeptide, polygly in aqueous solution. Our data indicate that long polygly chains (500-5000), as well as the central residues of the gly_5 and gly_6 in solution assume an extended helix PGII-like (or 3_1-helix) conformation. Although polygly chains in solution show a preference for PGII conformations, they still maintain significant conformational freedom which is apparent from the increased solution bandwidths of the conformationally sensitive amide and CH_2 stretching bands.

High Li^+ concentrations significantly narrow the amide bandwidths, especially that of the amide II band, which suggests a polygly conformational ensemble narrowing which probably results from the stabilization of the PGII conformation by the Li^+ polarization of the peptide bond carbonyls and strengthening polypeptide backbone carbonyl dipole-dipole interactions. This Li^+ stabilization of the 3_1-helix-like conformations in solution is likely one of the origins of the protein denaturing ability of lithium salts.

ACKNOWLEDGMENT. This work was supported by NIH, Grant 5R01EB002053.

4.2.9 Bibliogrpahy

(1) Crick, F. H. C.; Rich, A. *Nature (London, United Kingdom)* **1955**, *176*, 780-781.

(2) Ohnishi, S.; Kamikubo, H.; Onitsuka, M.; Kataoka, M.; Shortle, D. *J. Am. Chem. Soc.* **2006**, *128*, 16338-16344.

(3) Schweitzer-Stenner, R.; Eker, F.; Huang, Q.; Griebenow, K. *J Am Chem Soc 2001*, *123*, 9628-9633.

(4) Takekiyo, T.; Imai, T.; Kato, M.; Taniguchi, Y. *Biochim. Biophys. Acta, Proteins Proteomics* **2006**, *1764*, 355-363.

(5) Wildman, K. A. H.; Wilson, E. E.; Lee, D.-K.; Ramamoorthy, A. *Solid State Nuclear Magnetic Resonance* **2003**, *24*, 94-109.

(6) Bykov, S.; Lednev, I.; Ianoul, A.; Mikhonin, A.; Munro, C.; Asher, S. A. *Applied Spectroscopy* **2005**, *59*, 1541-1552.

(7) Abe, Y.; Krimm, S. *Biopolymers* **1972**, *11*, 1817-1839.

(8) Abe, Y.; Krimm, S. *Biopolymers* **1972**, *11*, 1841-1853.

(9) Bykov, S. V.; Myshakina, N. S.; Asher, S. A. *Journal of Physical Chemistry B* **2008**, *112*, 5803-5812.

(10) Hu, H.; Elstner, M.; Hermans, J. *Proteins: Struct., Funct., Genet.* **2003**, *50*, 451-463.

(11) Lovell, S. C.; Davis, I. W.; Arendall, W. B., III; de Bakker, P. I. W.; Word, J. M.; Prisant, M. G.; Richardson, J. S.; Richardson, D. C. *Proteins: Struct., Funct., Genet.* **2003**, *50*, 437-450.

(12) Cubellis, M. V.; Caillez, F.; Blundell, T. L.; Lovell, S. C. *Proteins: Structure, Function, and Bioinformatics* **2005**, *58*, 880-892.

(13) Stapley, B. J.; Creamer, T. P. *Protein Science* **1999**, *8*, 587-595.

(14) Balasubramanian, D.; Shaikh, R. *Biopolymers* **1973**, *12*, 1639-1650.

(15) Rodgers, M. T.; Armentrout, P. B. *Acc. Chem. Res.* **2004**, *37*, 989-998.

(16) Imai, T.; Kinoshita, M.; Hirata, F. *Bull. Chem. Soc. Jpn.* **2000**, *73*, 1113-1122.

(17) Mikhonin, A. V.; Ahmed, Z.; Ianoul, A.; Asher, S. A. *Journal of Physical Chemistry B* **2004**, *108*, 19020-19028.

(18) Mikhonin, A. V.; Bykov, S. V.; Myshakina, N. S.; Asher, S. A. *Journal of Physical Chemistry B* **2006**, *110*, 1928-1943.

(19) Ho, B. K.; Thomas, A.; Brasseur, R. *Protein Sci.* **2003**, *12*, 2508-2522.

(20) Maccallum, P. H.; Poet, R.; Milner-White, E. J. *J. Mol. Biol.* **1995**, *248*, 361-373.

(21) Deane, C. M.; Allen, F. H.; Taylor, R.; Blundell, T. L. *Protein Eng.* **1999**, *12*, 1025-1028.

(22) Allen, F. H.; Baalham, C. A.; Lommerse, J. P. M.; Raithby, P. R. *Acta Crystallogr., Sect. B: Struct. Sci.* **1998**, *B54*, 320-329.

(23) Ho, B. K.; Brasseur, R. *BMC Structural Biology* **2005**, *5*, No pp. given.

4.3 UV RESONANCE RAMAN DETERMINATION OF SOLUTION CONFORMATIONS OF UNFOLDED POLY-L-LYSINE AND POLY-L-GLUTAMIC ACID

This work was published in *J. Am. Chem. Soc.*, 2005, 127(21), 7712-7720. Coauthors are Aleksandr V. Mikhonin, Nataliya S. Myshakina, Sergei V. Bykov and Sanford A. Asher. Only a fraction of the published work has been presented in this chapter. The author of the thesis was directly involved into experimental work on determination of the conformational preferences and discussion of the experimental results presented here. Specifically he investigated the UVRR and CD spectral signatures of the β-sheet PLL + PGA mixture.

UV Resonance Raman (UVR) spectroscopy was used to examine the solution conformation of poly-L-Lysine (PLL) and poly-L-Glutamic acid (PGA) in their non-α-helical states. UVR measurements indicate that at pH = 2 PLL and pH = 9 PGA exist mainly in a mixture of PPII and a novel left-handed 2.5_1-helical conformation, which is an extended β-strand-like conformation with $\Psi \sim +170°$ and $\Phi \sim -130°$. Both of these conformations are highly exposed to water. We see no evidence of any disordered "random coil" states. In addition, we find that a PLL and PGA mixture at neutral pH is ~60% β-sheet, and contains PPII and extended 2.5_1-helix conformations. The β-sheet conformation shows little evidence of amide backbone hydrogen bonding to water.

4.3.1 Introduction

The primary sequence of a protein encodes both the native structure as well its folding mechanism[1-8] (in the absence of chaperones or posttranslational modifications). The arguably most important problem in enzymology is to translate the primary sequence into the encoded protein folding mechanism(s), and to use this information to predict the ultimate native structure from the primary sequence information. In general, the native conformation(s) are thought to be located at distinct minima in the potential energy landscape.[9-15] The native conformation occurs when the protein environment favors folding.[16-20]

Until recently, protein unfolded states were assumed to consist of random coil conformations, where the polypeptide chains would adopt energetically allowed, but randomly distributed Φ and Ψ dihedral angles. Ideally, these structures were considered to be completely disordered with no correlations between adjacent peptide bonds Φ and Ψ Ramachandran dihedral angles.[21] However, this assumption has recently been seriously challenged.[22-28]

This work has been aided by new experimental studies which characterize peptide conformations[34-49]. What is most needed to make rapid continuing progress is additional experimental insight into protein folding motifs and the energy landscapes that surround these structures.

We[50-52], as well as others[53-58], have been developing UV Raman spectroscopy (UVRS) to probe protein structure and dynamics. We recently examined the first stages in unfolding of α-helices and discovered that a mainly ala 21-residue peptide melts from an α-helix conformation into a polyproline II conformation (PPII).[34]

In the work here we now examine peptide conformations of poly-L-glutamic acid (PGA) and poly-L-Lysine (PLL) under conditions where their sidechains are charged. We find that they occur in a mixture of PPII and a novel conformation, which is a subset of extended β-strand conformations, but which is best described as a 2.5_1 helix. If the sidechain charges are neutralized these peptides form α-helices, while if peptides with oppositely charged sidechains are mixed, they form β-sheet conformations.[59]

We have developed insights into peptide secondary structures through examinations of their ~200 nm UV resonance Raman spectra. We obtain the most information from the amide III_3 ($AmIII_3$) vibration whose frequency we earlier found was correlated to the peptide conformational Ramachandran Ψ angle.[34,60,61] We have recently developed quantitative relationships between peptide bond $AmIII_3$ frequencies the peptide bond Ψ angle and its hydrogen bonding pattern.[61] In the work here these relationships are used to estimate the conformational energy differences between the PPII and 2.5_1 helix conformations.

The work here shows clearly that the UVRS spectra of β-sheet conformations significantly differ from those of PPII and 2.5_1-helix ("single" β-strand) conformations. This ability to discriminate between conformations may prove useful for early detection of amyloidal fibril formation in solutions of proteins.[62]

4.3.2 Experimental Section

Sample preparation. Poly-L-Lysine HCl (PLL, MW_{vis} = 28,500, MW_{LALLS} = 20,200) and the sodium salt of poly-L-Glutamic acid (PGA, MW_{vis} – 17,000, MW_{mALLS} = 8853) were purchased from Sigma Chemical, and used as received. Solution spectra of PLL and PGA were

measured at pH=2 and pH=9, respectively, to ensure the absence of α-helix contributions. The mixed PLL and PGA neutral pH sample solutions contained identical concentrations of lysine and glutamic acid residues. These samples were freshly prepared before the Raman measurements. The total peptide concentrations were kept below 0.3 mg/ml to avoid gel formation.

The 21-residue alanine-based peptide AAAAA(AAARA)$_3$A (AP) was prepared (HPLC pure) at the Pittsburgh Peptide Facility by using the solid-state peptide synthesis method. The AP solutions in water contained 1 mg/ml concentrations of AP, and 0.2 M concentrations of sodium perchlorate, which was used as an internal intensity and frequency standard. All Raman spectra were normalized to the intensity of the ClO_4^- Raman band (932 cm^{-1}).

A_5 and A_3 peptides were purchased from Bachem Bioscience Inc. (King of Prussia, PA), and used as received. The $A_5 - A_3$ Raman difference spectral measurements utilized identical molar concentrations of A_5 and A_3 (0.34 mg/ml and 0.2 mg/ml, respectively) in solutions containing identical sodium perchlorate concentrations (0.2 M). We normalized the Raman spectra to the intensity of the 932 cm^{-1} perchlorate internal standard band. The $A_5 - A_3$ difference spectra were calculated by subtracting the normalized A_3 spectrum from the normalized A_5 spectrum at each temperature.

The undecapeptide XAO (MW=985) was prepared (HPLC pure) at the Pittsburgh Peptide Facility by using the solid-state peptide synthesis method. The sequence of this peptide is Ac-XXAAAAAAAOO-amide, where all amino acids are in their L form, A is ala, X is diaminobutyric acid (side chain $CH_2CH_2NH_3^+$), and O is ornithine (side chain $(CH_2)_3NH_3^+$). We used 1 mg/ml solutions of XAO-peptide containing 0.15 M of sodium perchlorate. The UVRR spectra of XAO were also normalized to the ClO_4^- Raman band intensity.

UV resonance Raman instrumentation. The Raman instrumentation has been described in detail elsewhere.[51,63] A Coherent Infinity Nd:YAG laser produced 355 nm (3rd harmonic) 3 nsec pulses at 100 Hz. This beam was Raman shifted to 204 nm (5th anti-Stokes) by using a 1 m tube filled with hydrogen (60 psi). A Pellin Broca prism was used to select the 204 nm excitation beam. The Raman scattered light was imaged into a subtractive double spectrometer[64] and the UV light was detected by a Princeton Instruments solar blind ICCD camera. All samples were measured in a thermostatted free surface flow stream.

4.3.3 Results and Discussion

4.3.3.1 Unfolded States of PLL and PGA

Fig. 4.8 shows the 204 nm UV Raman (UVR) spectra of the unfolded conformations of PLL (pH=2) and PGA (pH=9) at high (+70 °C) and low (0 °C) temperatures. At these pH values PLL and PGA have charged sidechains, whose repulsions prevent formation of α-helical conformations. The UVRR spectra of the PLL and PGA samples are essentially identical. Further, the insignificant spectral shifts occurring between the low and high temperature spectra indicate a lack of conformational transitions over this temperature range.

The 0 °C spectra show the AmI bands at ~1670 cm^{-1} (mainly CO s), the AmII bands at ~1564 cm^{-1} (mainly out of phase combination of CN s and NH b), the (C)C_α-H bending bands at ~1396 cm^{-1} and a complex series of bands in the AmIII region between 1210 and 1350 cm^{-1}. The AmIII region contains at least 4 resolved bands, which as discussed below derive from two conformations in equilibrium. We assign these two conformations to a polyproline II conformation (PPII, P superscript) and an extended β-strand-like conformation (S superscript).

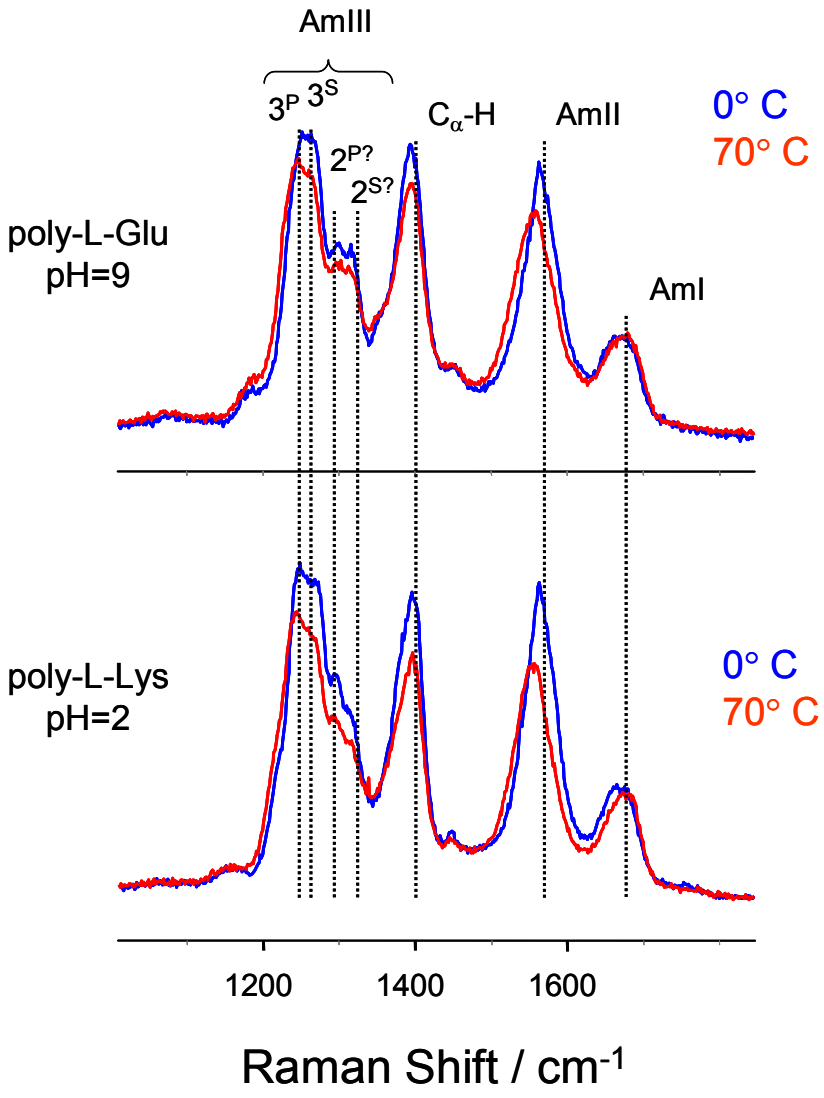

Figure 4.8: 204 nm UVRR spectra of unfolded states of PGA (pH = 9) and PLL (pH = 2) in water at 0 °C and at 70 °C.

As discussed below, the latter conformation can be described as an extended 2.5_1-helix. As evident from previous UVR studies[36,37,52,60] the AmIII bands are significantly more sensitive to conformation than are the AmI and AmII, bands that are more typically used by IR absorption and normal non resonance Raman secondary structure studies. Moreover, the UVR $AmIII_3$ band is independently contributed by the individual peptide bonds in the polypeptides with no

evidence of inter-amide coupling,[37,65] in contrast to commonly utilized AmI band.[37,40] This important observations dramatically simplify the spectral analysis in AmIII region.

Thus, we enumerate these bands as $AmIII_3^S$ (~1271 cm^{-1} (PLL) and ~1272 cm^{-1} (PGA)), and $AmIII_3^P$ (~1245 cm^{-1} (PLL) and ~1249 cm^{-1} (PGA), and $AmIII_2^{S?}$ (~1316 cm^{-1} (PLL) and ~1319 cm^{-1} (PGA)), $AmIII_2^{P?}$ (~1296 cm^{-1} (PLL) and ~1298 cm^{-1} (PGA)), where the subscripts label different amide III spectral region bands as we recently discussed in detail,[36] and the superscript question mark labels assignments which remain uncertain.

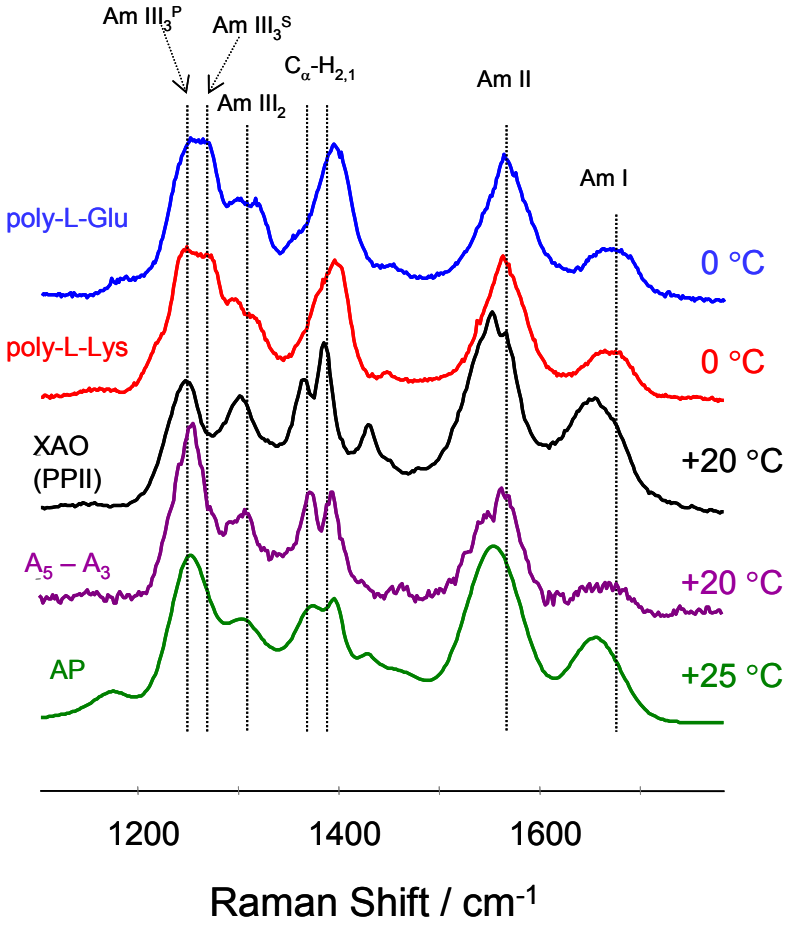

Figure 4.9: Comparison of 204 nm UVR spectra of unfolded states of PGA (pH=9) and PLL (pH=2) in water at 0 °C to the spectra of the PPII states of alanine-rich peptides XAO, AP, A_5-A_3 at 0 °C.

The temperature dependence of the spectra involves small downshifts for the AmIII and AmII bands and small upshifts for the AmI band (Table 4.6). This temperature dependence is characteristic of peptide backbone conformations where the amide carbonyl and N-H groups are hydrogen bonded to water.[34,36,66] The shifts occur because the water-amide hydrogen bond strengths decrease as the temperature increases.[34] This favors a peptide bond resonance form with stronger bonding for the carbonyl and weaker bonding for the C(O)-N linkage, which result in the observed amide band shifts.

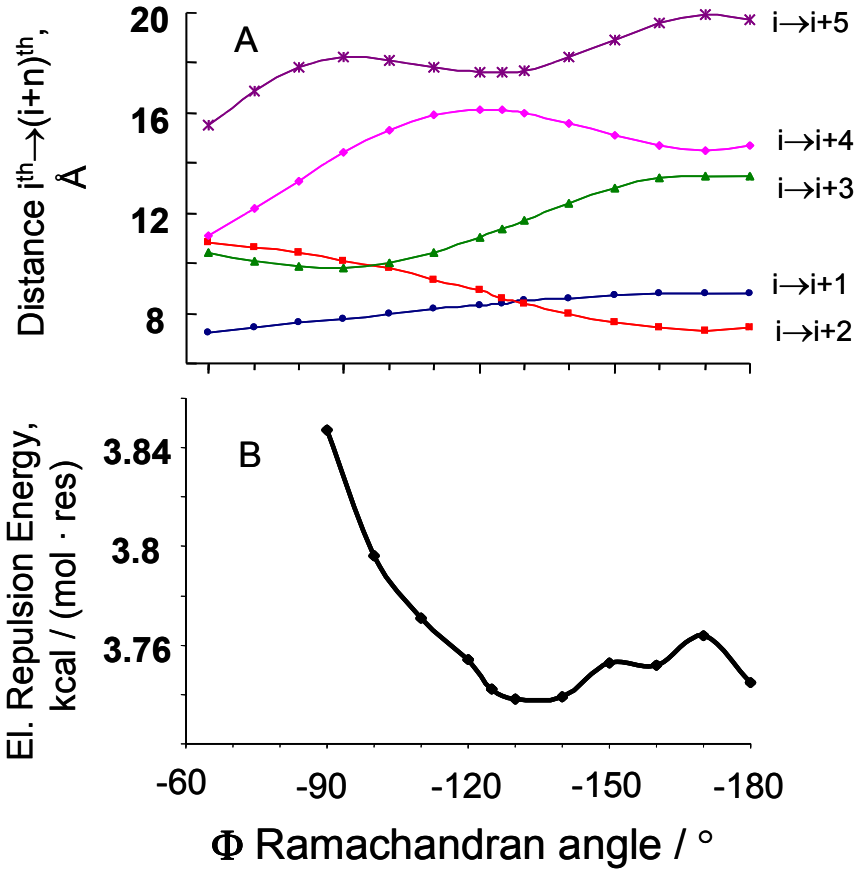

Figure 4.10: A Distances between the i-th and (i+k)-th sidechain charges of PGA as a function of Φ Ramachandran angle as calculated using Hyperchem. B) Electrostatic repulsion energy between the sidechains as a function of Φ Ramachandran angle. NOTE: The Ψ angle is fixed at the value of 170° estimated from the UV Raman data.

Table 4.6: Temperature dependence of amide UV Raman bands of non-α-helical poly-peptides: pH = 2 PLL, pH = 9 PGA, and PPII peptides: XAO, Ala_5-Ala_3, AP

	XAO-peptide >80% PPII, neutral pH		*Ala5 – Ala3 essentially PPII, neutral pH*		*AP essentially PPII, neutral pH*		*PLL unfolded (PPII + extended), pH=2*		*PGA unfolded (PPII + extended), pH=9*	
	dν/dT	$\nu_{60℃}$, cm^{-1}	*dν/dT*	$\nu_{50℃}$, cm^{-1}	*dν/dT*	$\nu_{60℃}$, cm^{-1}	*dν/dT*	$\nu_{70℃}$, cm^{-1}	*dν/dT*	$\nu_{70℃}$, cm^{-1}
AI	0.02 ± ±0.01	1659	0.052± ±0.02	1667	0.052± ±0.02	1659	0.06	1673	0.03	1673
AII	-0.14± ± 0.01	1545	-0.14 ± ± 0.01	1558	-0.14 ± ± 0.01	1548	-0.15	1553	-0.13	1555
$C_\alpha H_{(1)}$	0.008± ±0.016	1388	-0.015± ± 0.02	1397	-0.015± ± 0.02	1399	-0.01	1399	0.02	1396
$C_\alpha H_{(2)}$	0.018± ±0.017	1365	-0.01 ± ± 0.02	1373	-0.01 ± ± 0.03	1377 broad	-0.04	1377	0.036	1359
$AIII_2$	-0.03 ± ± 0.02	1300	-0.03 ± ± 0.01	1305	-0.03 ± ± 0.01	1311	-0.033 -0.036	1313 1293	-0.003 -0.006	1319 1298
$AIII_3^S$ (2.5_1-helix)	N/A	N/A	N/A	N/A	N/A	N/A		1270		1269
$AIII_3^P$ (PPII)	-0.10 ± ± 0.02	1241	-0.094± ± 0.018	1250	-0.094± ± 0.018	1247	-0.1	1242	-0.12	1240

Table 4.7: Temperature dependencies of amide UV Raman bands of PLL-PGA mixture

	PLL-PGA mixture, ~60% β-sheet, ~40% unfolded, a neutral pH		*PLL-PGA mixture, pure PPII, 2.5$_1$ conformationsb neutral pH*		*PLL-PGA mixture, pure β-sheet spectrumc neutral pH*	
	dν/dT	*$\nu_{70°C}$, cm^{-1}*	*dν/dT*	*$\nu_{70°C}$, cm^{-1}*	*dν/dT*	*$\nu_{70°C}$, cm^{-1}*
AI	0.022	1668	0.045		0.018	1672
AII	-0.071	1548	-0.14		-0.005	1550
$C_\alpha H_{(1)}$	-0.007	1402	0.005		-0.031	1403
$C_\alpha H_{(2)}$	0	1381	-0.005		0	1379 weak
$AIII_2$	0	1290 1310	-0.03			
$AIII_3$	-0.062	1239	-0.11		-0.003	1228

$AmIII_3^P$ band (~1245 cm^{-1}) signals PPII conformations. Fig. 4.9 compares the 204 nm UVR spectra of the unfolded PGA and PLL samples to spectra of the three ala-based peptides: XAO, AP, and A_5-A_3 under conditions where they are predominantly in PPII conformations. The observed $AmIII_3^P$ band frequency closely coincides with the $AmIII_3$ frequency of the PPII conformations of XAO, AP, A_5-A_3. Since we know that the $AmIII_3$ frequency strongly depends on the Ψ angle,[34,60] (and to much lesser degree on allowed Φ angles[34,60,67-69]) we conclude that both PLL and PGA have solution conformations with Ψ angles similar to that of the PPII conformation.

Table 4.8: Distances between ionized sidechain charges in PLL and PGA for Ψ and Φ angles of PPII and 2.5_1 helix conformations

	Distance between sidechain charges	*PPII* $\Psi = +145°, \quad \Phi = -75°$	*Extended 2.5_1-helix* $\Psi = +170°, \quad \Phi = -130°$
PLL	i→i+1	11.245	11.67
	i→i+2	12.389	10.146
	i→i+3	9.232	12.266
	i→i+4	16.427	18.130
PGA	i→i+1	8.328	8.421
	i→i+2	9.852	8.639
	i→i+3	9.232	11.381
	i→i+4	14.563	16.101

The coincidence in frequency and the similar temperature dependencies (Table 4.6) of the $AmIII_3^P$ bands to those of PPII conformations militates for the assignment of this band to PPII conformations of PGA and PLL. This conclusion is consistent with previous studies which also concluded that the unfolded state(s) of PLL and PGA have significant PPII content.[22,70-81]

The PPII structure is a commonly observed non-α-helix low energy conformation because of its stabilization by peptide-water interactions.[72,82,83] This open conformation permits the simultaneous hydrogen bonding of water to amide bonds, as well as important bridging hydrogen bonds between water molecules. In addition, Hinderacker and Raines[84] recently proposed an additional PPII stabilization mechanism. They proposed that the PPII conformation is stabilized because of especially favorable n-π* interactions between the carbonyl oxygen of peptide bonds and the carbonyl carbons of adjacent peptide bonds. Whatever the case, investigators now find that the unfolded states of many proteins[71,82,85-89] as well as the unfolded

states of moderate and long peptides[35,70-73], and even small peptides[90-92] contain significant fractions of PPII.

$AmIII_3^S$ band (~1271 cm^{-1}) signals the presence of a 2.5_1-helix conformation. The electrostatic repulsions between the PLL and PGA charged sidechains prevent formation of α-helical conformations, and should force more extended conformations, such as PPII and/or extended β-strand(s). The PPII conformation clearly does not require sidechain repulsion since it occurs for polyalanine derivatives such as AP and XAO.[34,35,93] Further, the K7 peptide shows significant PPII content at pH = 12 in the absence of salt as well as in 4 M NaCl.[70]

The pH = 2 PLL and pH = 9 PGA spectra also show a second $AmIII_3$ region band at ~1271 cm^{-1} denoted as $AmIII_3^S$ (Fig. 4.8 and 4.9). This band is absent in mainly PPII ala-based peptides with neutral side chains. Thus, it must result from the additional PLL and PGA electrostatic repulsions between ionized side chains. We expect that these repulsions will induce a more extended conformation with a Ramachandran angle greater than the Ψ = 145° of the PPII conformation. Given the dependence of the $AmIII_3$ frequency on the Ψ angle that we previously demonstrated,[34,36,60] we expect a new $AmIII_3$ band to occur at a higher frequency, as observed.

Because of the severe overlap with the $AmIII_3^P$ bands it is not possible to accurately determine the $AmIII^S$ temperature dependence. However, the temperature dependence is qualitatively similar to that of fully exposed conformations like PPII. Thus, we assign the conformation to an extended β-strand like conformation (2.5_1-helix, see below), and conclude that these PGA and PLA samples contain a mixture of PPII and extended β-strand-like conformations.

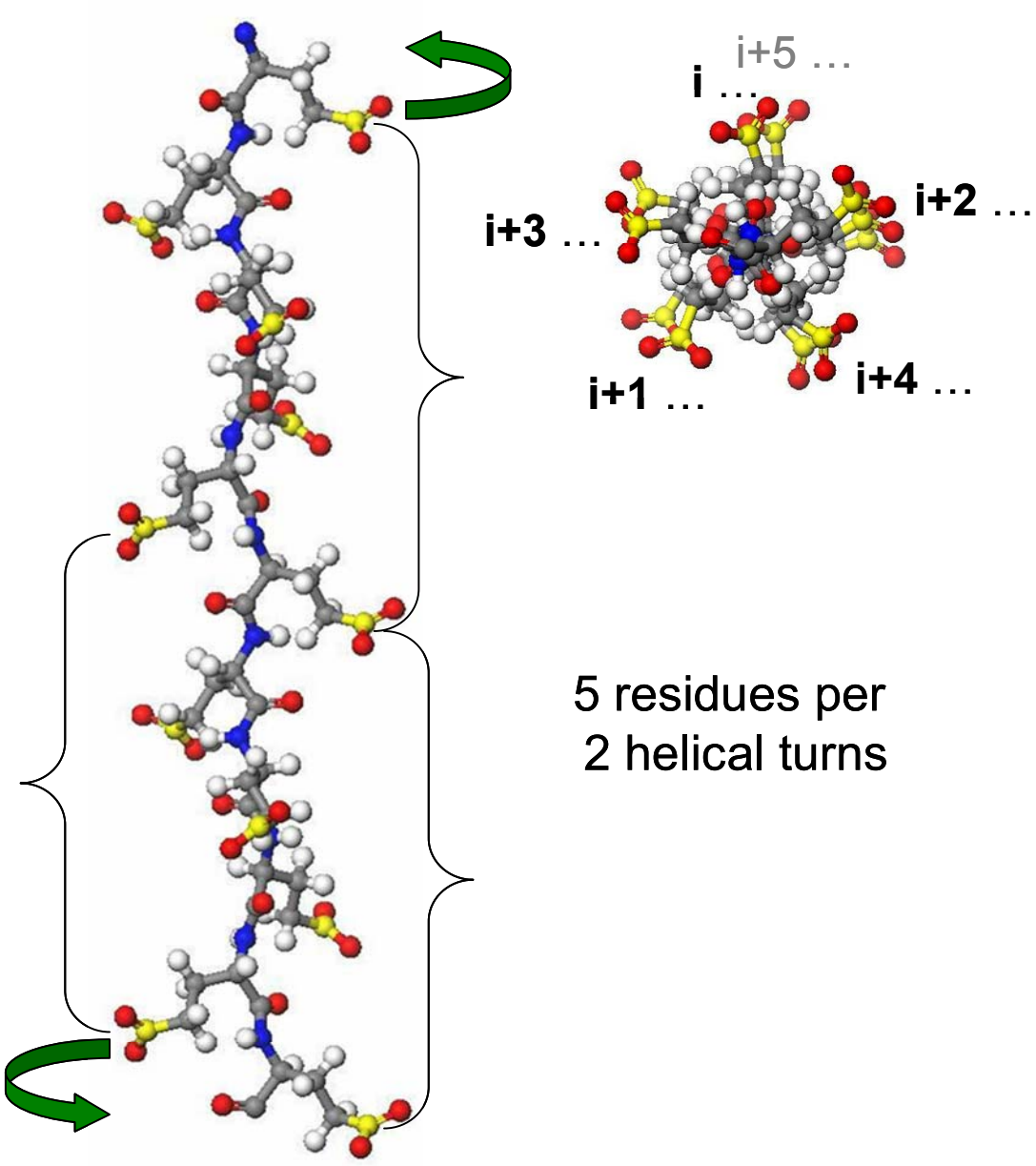

Figure 4.11: Visualization of 2.5$_1$-helix in PGA (Ψ = +170°, Φ = −130°). This structure occurs in both ionized PLL and PGA due to electrostatic repulsion between bulky and charged sidechains. Carboxyl carbons of glu side-chains are shown in yellow.

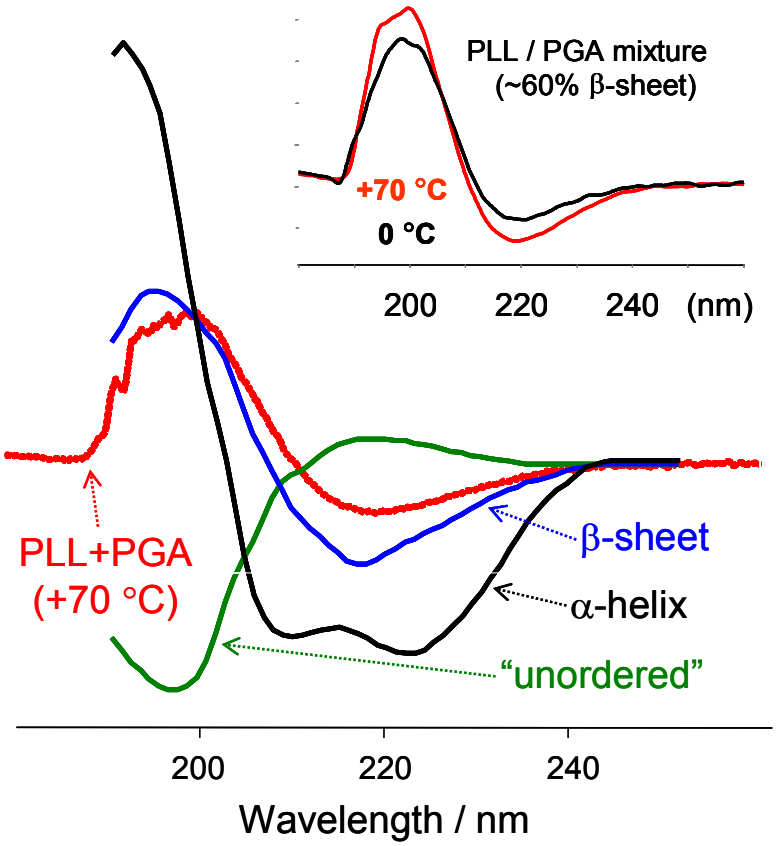

Figure 4.12: CD spectra of different peptide and protein conformations to that of a neutral pH mixture of PLL + PGA at +70 °C. This sample obviously contains a significant fraction of β-sheet, due to the similarity of the PLL and PG mixture CD spectrum to that of the β-sheet. The pure secondary structure CD spectra were obtained from the Lawrence Livermore National Laboratory website:
http://www-structure.llnl.gov/cd/cdtutorial.htm

Assuming similar Raman cross sections for these conformations, we roughly estimate that "unfolded" PLL and PGA both consist of ~60% PPII and ~40% β-strand. In contrast, we only detect very small contributions from β-strand-like conformations in AP at high temperature.[36] The lack of a temperature dependence of the relative intensity ratios suggests that these conformations have similar energies.

It should be noted that Raman Optical Activity studies of "unfolded" peptides and proteins show positive features between ~1314 to ~1325 cm^{-1}, which are thought to signal the PPII conformation.[93-96] The large frequency spread for these positive bands may indicate the existence of a variety of PPII-like left-handed helical conformations with significantly differing Ψ and Φ angles.

Whatever the case, we detect only PPII and extended β-strand-like conformations which significantly differ spectrally from those of β-sheet conformations (Compare Figs. 4.9, 4.14 and 4.15).

The ~1271 cm^{-1} $AmIII_3^S$ band frequency corresponds to β-strand-like Ψ angle of ~170°, if we neglect any Φ angle frequency dependence. This neglect of the Φ angle dependence is justified in view of the known small Φ angle amide III frequency dependence[60,67] and the fact that only modest changes in the Φ angle are likely to occur between the relevant conformations with different Ψ angles. Further, we and others recently estimated that the Ψ angle dependence can result in up to ~110 cm^{-1} shift,[61] while Φ angle only in no more than 20 cm^{-1} $AmIII_3$ frequency shift.[67,68]

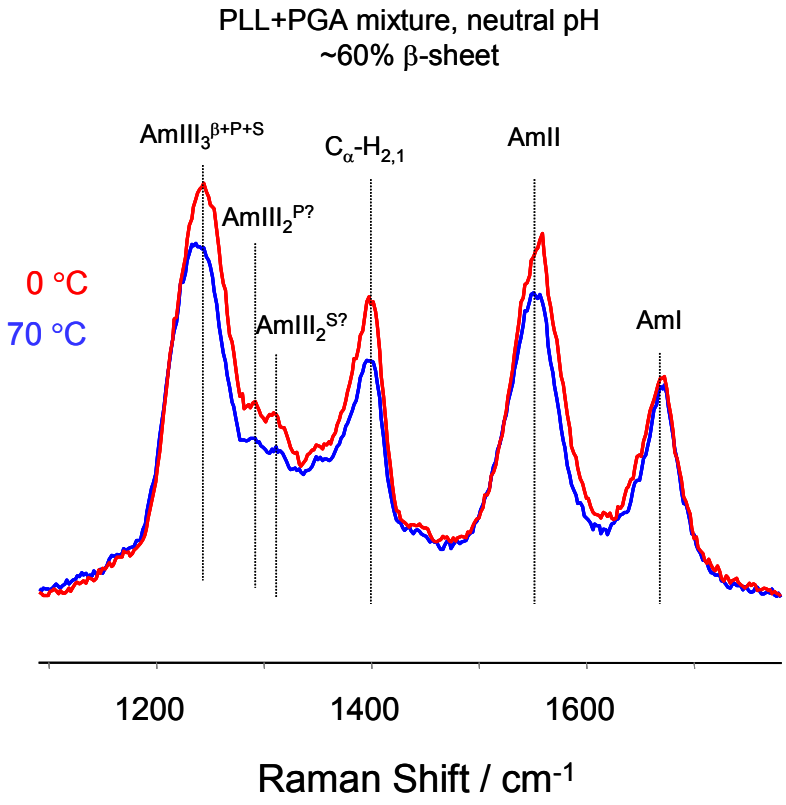

Figure 4.13: 204 nm UVR spectra of neutral pH PLL-PGA mixture at 0 and +70 °C.

The β-strand-like conformation is a 2.5_1-helix. We developed insight into this new conformation by examining the dependence of the electrostatic repulsion energies on the Φ angle, for a fixed Ψ = +170° (Fig. 4.10). We utilized the HyperChem© amino acid data base to construct approximate structures to estimate the distances between charges located on PLL and PGA side chains. Fig. 4.10 shows that the total electrostatic repulsion energy has a minimum near Φ ~ −130° for PGA. The situation for PLL has the same trend (Table 4.8).

Fig. 4.11 indicates a rough structure for our PGA minimum repulsion energy conformation which utilizes the determined Ψ and Φ angles of +170° and −130°, respectively. The resulting extended β-strand occurs as a 2.5_1-helix conformation.

Krimm and Mark's[97] previous theoretical study of conformations of polypeptides with ionized sidechains, also proposed that the charged sidechains of PLL and PGA stabilize a helical conformation with approximately 2.5 residues per helical turn. They also showed that the number of residues per turn was essentially independent of sidechain length for side chains equal to or longer than that of glutamic acid. However, for a 64-residue PGA they proposed a minimum energy conformation with $\Psi = -170°$ and $\Phi = -155°$ (in their original paper they used an older definition for the Ψ and Φ angles).[98] Future work will be required to discriminate between these very similar structures in order to determine the actual Φ angles for these structures.

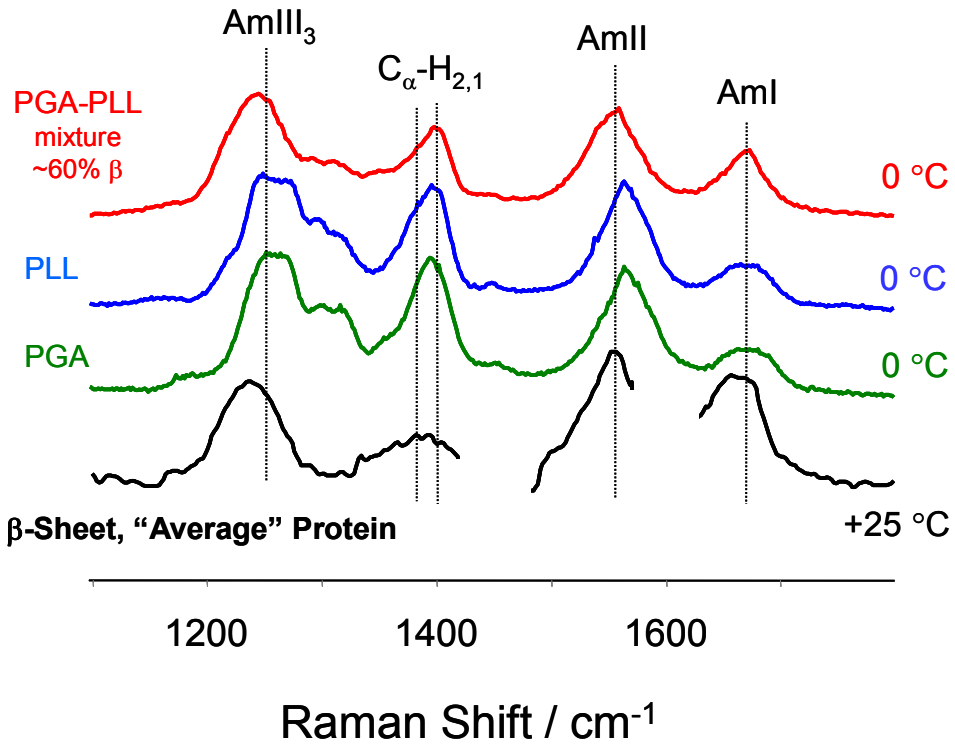

Figure 4.14: 204 nm UVR spectra of PLL-PGA mixture at 0 °C, and those of the PPII and β-strand (2.5_1-helix) conformations of PLL and PGA. Also shown is the β-sheet basis spectrum determined by Chi et al.[52] from a library of proteins.

Our study here is the first, to our knowledge, to experimentally detect a stable 2.5_1-helix conformation in peptides and proteins. We also compared the distances between charges in our putative 2.5_1-helix to those in a PPII helix. Table 4.8 shows that the larger separation distances occur in the 2.5_1-helix compared to the PPII helix. This lowers the 2.5_1-helix total energy such that it is very close to that of the PPII conformation.

Our spectral data and the lack of a significant temperature dependence of the relative Raman intensities clearly demonstrate that these conformations are close in energy. Given our present inability to accurately curve resolve the PPII peak from the 2.5_1 $AmIII_3$ peaks, our incomplete understanding of the degeneracies of these two conformation, the unknown dependence of the Raman cross sections on conformation, and the measured modest temperature dependence, on the basis of the relative intensity ratios, we can only visually roughly estimate from the relative Raman intensities that the 2.5_1 conformations of PLL and PGA are < 300 cal/mol higher in energy than the PPII conformation at room temperature (however, see below). We are in the process of modeling this 2.5_1 helix conformation to better determine its detailed geometry.

Our observations of the 2.5_1 helix was, in fact, partially presupposed by Tiffany and Krimm[22] who originally proposed that aqueous solution denatured states of PLL and PGA would contain some local order and would not be in a completely "disordered" form. The structure was suggested to involve an extended 3_1-helix or a PPII helix, which is also left-handed helix, with three amino acid residues per turn, with Φ and Ψ Ramachandran angles of -75° and 145°, respectively. In addition, more recent studies report evidence for PPII content in "unfolded" PLL and PGA.[70-78,94-96]

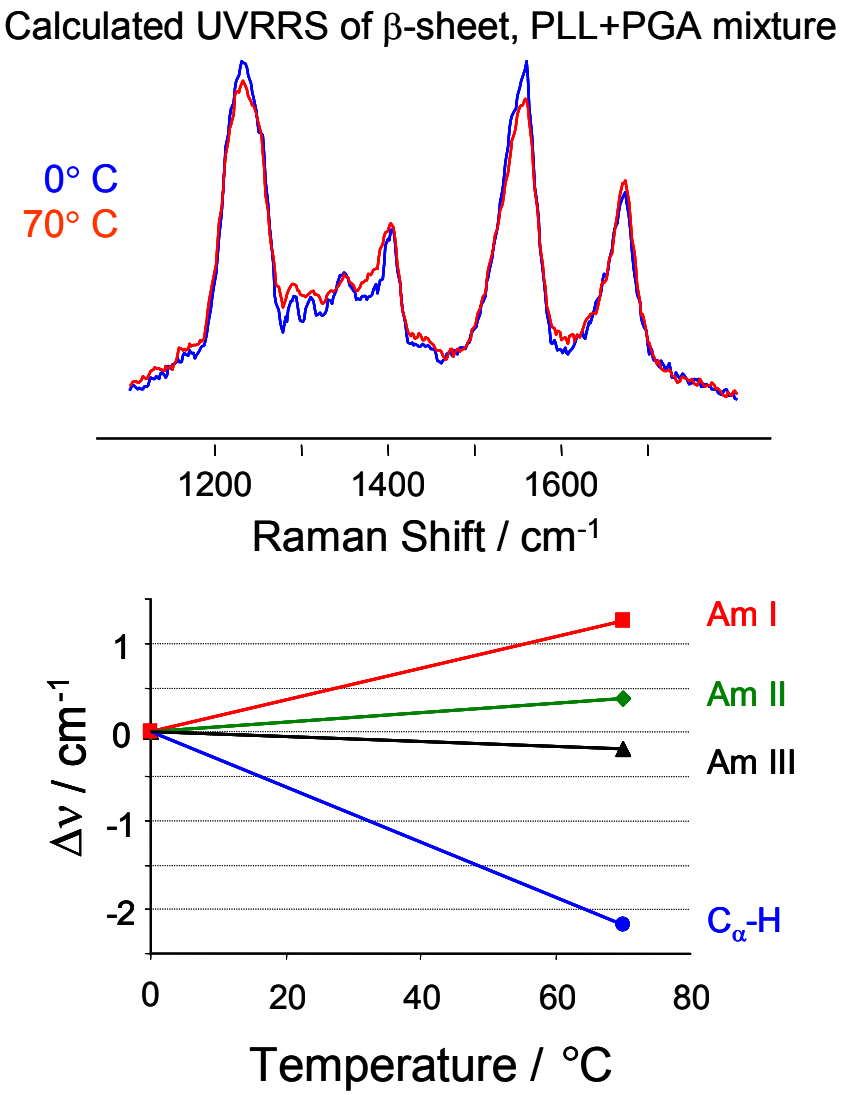

Figure 4.15: Calculated 204 nm UVRS of PLL-PGA mixture β-sheet spectrum at 0 and +70 °C. The contributions from the PLL and PGA PPII and β-strand (2.5_1-helix) conformations were numerically removed (See text for details). UVR bands of β-sheet show a very small temperature dependence compoared to PPII (Table 4.7).

4.3.4 PLL + PGA β-Sheet Conformation

Equimolar mixtures of PLL and PGA at neutral pH are known to form antiparallel β-sheets.[59] This is clearly demonstrated in the Fig. 4.12 comparison of the CD spectrum of a

PLL-PGA mixture to the CD spectra of α-helical, β-sheet and "unordered" peptides. The PLL-PGA mixture spectrum, especially the ~217 nm negative feature, clearly demonstrates a significant fraction of β-sheet. In addition, the CD spectra of the PLL-PGA mixture shows an increasing 217 nm trough as the temperature increases, which indicates that the β-sheet content slightly increases with temperature (see inset to Fig. 4.12).

Fig. 4.13 shows that the UVR spectra of the PLL-PGA mixture at 0 and +70 °C. The entire $AmIII_3$ band profile of the PLL-PGA mixture is red-shifted compared to unfolded PLL and PGA (Figs. 4.8, 4.9 and 4.14, Tables 4.6 and 4.7) due to formation of the antiparallel β-sheet structure. Fig. 4.13 shows that overall spectra of the PLL-PGA mixture are almost independent of temperature, indicating that the β-sheet conformation does not melt significantly over this temperature range. Further, the temperature dependence of the AmI, II and III band frequencies in the PLL-PGA mixture (~60% β-sheet) is significantly decreased (~2-fold) compared to those in the PPII and β-strand (2.5_1-helix) conformations due to the decreased peptide-water hydrogen bonding of the β-sheet structure.

Calculation of pure β-sheet spectrum from PLL-PGA mixture UV Raman spectra. The Figs. 4.13 and 4.14 PLL-PGA mixture UVR spectra are broad and show high frequency shoulders. This contrasts with the AmIII symmetric bandshape found by Chi et al.[52] for the β-sheet conformation of a library of proteins (Fig. 4.14). Thus, the PLL-PGA mixture sample appears to contain additional peptide conformations. Since the PLL and PGA sidechains are highly ionized at this neutral pH, it is likely that these other conformations are the extended 2.5_1-helix and the PPII conformations discussed above.

We can calculate the pure β-sheet PGA-PLL Raman spectrum by subtracting off the spectra of these other conformations. We assume that the spectra of these other conformations

are the sum of the individual PLL and PGA PPII and β-strand (2.5_1-helix) spectra. The criteria for the amounts subtracted are that the resultant spectra (Fig. 4.14) best fit the β-sheet spectrum of Chi et al.[52] (except that we do not include the amide I region in the fit due to the potential residual contribution of the water bending band). We find non β-sheet conformation fractions of 42% at 0 °C, and 35% at 70 °C. Thus, the β-sheet content slightly increases with temperature.

Fig. 4.15 shows these calculated pure β-sheet spectra at 0 and 70 ºC. The β-sheet AmIII peak is symmetric without any shoulders and is similar to that found by Chi et al[52] (Compare Figs. 4.14 and 4.15). As also shown in Fig. 4.15 the pure PLL-PGA mixture β-sheet spectrum shows a ~10-fold decreased temperature frequency dependence for the AmII and III bands and a ~3 fold decreased AmI band frequency dependence than occurs for the PPII and 2.5_1-helix conformations. This is expected due to the decreased water-amide bond hydrogen bonding of the β-sheet; since the β-sheet satisfies its hydrogen bonding mainly through inter-peptide hydrogen bonds.

The large UVRS spectral differences between the PLL-PGA mixture pure β-sheet conformation and that of PLL and PGA in their unfolded states (compare Figs. 4.15 and 4.14) offers opportunities for characterizing subtle issues of β-sheet conformation. This could be valuable in kinetic and steady state investigations of systems such as amyloid fibrils.[62]

4.3.5 Conclusions

Our study of unfolded states of PLL and PGA indicates that they exist as a mixture of PPII and the extended 2.5_1-helix (β-strand-like) conformations. The charged side chains of pH=2 PLL and pH=9 PGA force the PLL and PGA chains in water to adopt a more extended

conformations that minimize interchain repulsions. The β-sheet structure of the PLL-PGA mixture showed little evidence for hydrogen bonding between the polypeptide backbone and water.

AKNOWLEGMENTS. We thank NIH grant 8 RO1 EB002053021 for financial support.

4.3.6 BIBLIOGRAPHY

(1) Creighton, T. E. Protein Folding; W. H. Freeman: Ney York, **1992**.

(2) Baldwin, R. L. Nature **1990**, 346, 409-410.

(3) Kim, P. S.; Baldwin, R. L. Annu. Rev. Biochem. **1990**, 59, 631-660.

(4) Matthews, C. R. Annu. Rev. Biochem. **1993**, 62, 653-683.

(5) Fernandez-Carneado, J.; Grell, D.; Durieux, P.; Hauert, J.; Kovacsovics, T.; Tuchscherer, G. Bioploymers (Peptide Sci.) **2000**, 55, 451-458.

(6) Bryngelson, J. D.; Onuchic, J. N.; Socci, N. D.; Wolynes, P. G. Proteins: Struct., Funct., Genet. **1995**, 21, 167-195.

(7) Thirumalai, D.; Woodson, S. A. Acc. Chem. Res. **1996**, 29, 433-439.

(8) Pennisi, E. Science **1996**, 273, 426-428.

(9) Chan, H. S.; Dill, K. A. Proteins **1998**, 30, 2-33.

(10) Dill, K. A. Biochemistry **1990**, 29, 7133-7155.

(11) Pokarowski, P.; Kolinski, A.; Skolnick, J. Biophys. J. **2003**, 84, 1518-1526.

(12) Jewett, A. I.; Pande, V. S.; Plaxco, K. W. J. Mol. Biol. **2003**, 326, 247-253.

(13) Hardin, C.; Eastwood, M. P.; Prentiss, M.; Luthey-Schulten, Z.; Wolynes, P. G. J. Comp. Chem. **2002**, 23, 138-146.

(14) Alm, E.; Baker, D. Proc. Natl. Acad. Sci. U.S.A. **1999**, 96, 11305-11310.

(15) Socci, N. D.; Onucic, J. N.; Wolynes, P. G. Proteins **1998**, 32, 136-158.

(16) Anfinsen, C. B. Science **1973**, 181, 223-230.

(17) Mayor, U.; Guydosh, N. R.; Johnson, C. M.; Grossmann, J. G.; Sato, S.; Jas, G. S.; Freund, S. M. V.; Alonso, D. O. V.; Daggett, V.; Fersht, A. R. Nature **2003**, 421, 863-867.

(18) Myers, J. K.; Oas, T. G. Annu. Rev. Biochem. **2002**, 71, 783-815.

(19) Mirny, L.; Shakhnovich, E. Annu. Rev. Biophys. Biomol. Struct. **2001**, 30, 361-396.

(20) Englander, S. W. Annu. Rev. Biophys. Biomol. Struct. **2000**, 29, 213-238, 213 Plates.

(21) Flory, P. J. Statistical Mechanics of Chain Molecules, 1969.

(22) Tiffany, M. L.; Krimm, S. Biopolymers **1968**, 6, 1379-1382.

(23) Pappu, R. V.; Srinivasan, R.; Rose, G. D. Proc. Natl. Acad. Sci. U.S.A. **2000**, 97, 12565-12570.

(24) Srinivasan, R.; Rose, G. D. Proc. Natl. Acad. Sci. U.S.A. **1999**, 96, 14258-14263.

(25) Marqusee, S.; Robbins, V. H.; Baldwin, R. L. Proc. Natl. Acad. Sci. U.S.A. **1989**, 86, 5286-5290.

(26) Pal, D.; Suhnel, J.; Weiss, M. S. Angew. Chem., Intl. Edition **2002**, 41, 4663-4665.

(27) Watson, J. D.; Milner-White, E. J. J. Mol. Biol. **2002**, 315, 183-191.

(28) Watson, J. D.; Milner-White, E. J. J. Mol. Biol. **2002**, 315, 171-182.

(29) Sreerama, N.; Woody, R. W. Proteins **1999**, 36, 400-406.

(30) Park, C.; Carlson, M. J.; Goddard, W. A. I. J. Phys. Chem. A **2000**, 104, 2498-2503.

(31) Wu, X.; Wang, S. J. Phys. Chem. B **2001**, 105, 2227-2235.

(32) Wieczorek, R.; Dannenberg, J. J. J. Am. Chem. Soc. **2003**, 125, 8124-8129.

(33) Avbelj, F.; Fele, L. J. Mol. Biol. **1998**, 279, 665-684.

(34) Asher, S. A.; Mikhonin, A. V.; Bykov, S. B. J. Am. Chem. Soc. **2004**, 126, 8433-8440.

(35) Shi, Z.; Olson, C. A.; Rose, G. D.; Baldwin, R. L.; Kallenbach, N. R. Proc. Natl. Acad. Sci. U.S.A. **2002**, 99, 9190-9195.

(36) Mikhonin, A. V.; Ahmed, Z.; Ianoul, A.; Asher., S. A. J. Phys. Chem. B **2004**, 108, 19020-19028.

(37) Mikhonin, A. V.; Asher, S. A. J. Phys. Chem. B **2005**, 109, 3047-3052.

(38) Woutersen, S.; Hamm, P. J. Chem. Phys. **2001**, 114, 2727-2737.

(39) Eker, F.; Cao, X.; Nafie, L.; Schweitzer-Stenner, R. J. Am. Chem. Soc. **2002**, 124, 14330-14341.

(40) Fang, C.; Wang, J.; Charnley, A. K.; Barber-Armstrong, W.; Smith, A. B.; Decatur, S. M.; Hochstrasser, R. M. Chem. Phys. Letters **2003**, 382, 586-592.

(41) Fang, C.; Wang, J.; Kim, Y. S.; Charnley, A. K.; Barber-Armstrong, W.; Smith, A. B., III; Decatur, S. M.; Hochstrasser, R. M. J. Phys. Chem. B **2004**, 108, 10415-10427.

(42) Eker, F.; Griebenow, K.; Cao, X.; Nafie, L. A.; Schweitzer-Stenner, R. Biochemistry **2004**, 43, 613-621.

(43) Demirdoeven, N.; Cheatum, C. M.; Chung, H. S.; Khalil, M.; Knoester, J.; Tokmakoff, A. J. Am. Chem. Soc. **2004**, 126, 7981-7990.

(44) Hamm, P.; Lim, M.; DeGrado, W. F.; Hochstrasser, R. M. Proc. Natl. Acad. Sci. U.S.A. **1999**, 96, 2036-2041.

(45) Kocak, A.; Luque, R.; Diem, M. Biopolymers **1998**, 46, 455-463.

(46) Woutersen, S.; Hamm, P. J. Physics.: Condensed Matter **2002**, 14, R1035-R1062.

(47) Woutersen, S.; Hamm, P. J. Chem. Phys. **2001**, 115, 7737-7743.

(48) Eker, F.; Griebenow, K.; Cao, X.; Nafie, L. A.; Schweitzer-Stenner, R. Proc. Natl. Acad. Sci. U.S.A. **2004**, 101, 10054-10059.

(49) Pimenov, K. V.; Bykov, S. V.; Mikhonin, A. V.; Asher, S. A. J. Am. Chem. Soc. **2005**, 127, 2840-2841.

(50) Asher, S. A. Handbook of Vibrational Spectroscopy, John Whiley & Sons, Ltd. **2001**, 1, 557-571.

(51) Lednev, I. K.; Karnoup, A. S.; Sparrow, M. C.; Asher, S. A. J. Am. Chem. Soc. **1999**, 121, 8074-8086.

(52) Chi, Z.; Chen, X. G.; Holtz, J. S. W.; Asher, S. A. Biochemistry **1998**, 37, 2854-2864.

(53) Wen, Z. Q.; Thomas, G. J., Jr. Biochemistry **2000**, 39, 146-152.

(54) Wang, D.; Zhao, X.; Shen, T.-J.; Ho, C.; Spiro, T. G. J. Am. Chem. Soc. **1999**, 121, 11197-11203.

(55) Kim, J. E.; Pan, D.; Mathies, R. A. Biochemistry **2003**, 42, 5169-5175.

(56) Serban, D.; Arcineigas, S. F.; Vorgias, C. E.; Thomas, G. J., Jr. Protein Sci. **2003**, 12, 861-870.

(57) Haruta, N.; Kitagawa, T. Biochemistry **2002**, 41, 6595-6604.

(58) Thomas, G. J., Jr. Annu. Rev. Biophys. Biomol. Struct. **1999**, 28, 1-27.

(59) Ismail, A. A.; Mantsch, H. H. Biopolymers **1992**, 32, 1181-1186.

(60) Asher, S. A.; Ianoul, A.; Mix, G.; Boyden, M. N.; Karnoup, A.; Diem, M.; Schweitzer-Stenner, R. J. Am. Chem. Soc. **2001**, 123, 11775-11781.

(61) Mikhonin, A. V.; Asher, S. A. Submitted to J. Am. Chem. Soc. **2005**, Manuscript # ja052009c.

(62) Lednev, I. K.; Carlsen, A.; Ermolenkov, V. V.; He, W.; Higashiya, S.; Topilina, N.; Wells, C. C.; Welch, J. T.; Xu, M. Book of Abstracts. 31st Annual Meeting of FACSS, Portland, OR, October 3-7; **2004**, p. 142.

(63) Lednev, I. K.; Karnoup, A. S.; Sparrow, M. C.; Asher, S. A. J. Am. Chem. Soc. **2001**, 123, 2388-2392.

(64) Bykov, S. B.; Lednev, I. K.; Ianoul, A.; Asher, S. A. In Preparation **2005**.

(65) Mix, G.; Schweitzer-Stenner, R.; Asher, S. A. J. Am. Chem. Soc. **2000**, 122, 9028-9029.

(66) Torii, H.; Tatsumi, T.; Tasumi, M. J. Raman Spectrosc. **1998**, 29, 537-546.

(67) Ianoul, A.; Boyden, M. N.; Asher, S. A. J. Am. Chem. Soc. **2001**, 123, 7433-7434.

(68) Mirkin, N. G.; Krimm, S. J. Phys. Chem. A **2002**, 106, 3391-3394.

(69) Abbruzzetti, S.; Viappiani, C.; Small, J. R.; Libertini, L. J.; Small, E. W. J. Am. Chem. Soc. **2001**, 123, 6649-6653.

(70) Rucker, A. L.; Creamer, T. P. Protein Sci. **2002**, 11, 980-985.

(71) Smyth, E.; Syme, C. D.; Blanch, E. W.; Hecht, L.; Vasak, M.; Barron, L. D. Biopolymers **2001**, 58, 138-151.

(72) Woody, R. W. Adv. Biophys. Chem. **1992**, 2, 37-79.

(73) Keiderling, T. A.; Silva, R. A.; Yoder, G.; Dukor, R. K. Bioorg. & Med. Chem. **1999**, 7, 133-141.

(74) Drake, A. F.; Siligardi, G.; Gibbons, W. A. Biophysical Chemistry **1988**, 31, 143-146.

(75) Wilson, G.; Hecht, L.; Barron, L. D. J. Chem. Soc., Faraday Trans., **1996**, 92, 1503-1509.

(76) Yasui, S. C.; Keiderling, T. A. J. Am. Chem. Soc. **1986**, 108, 5576-5581.

(77) Birke, S. S.; Agbaje, I.; Diem, M. Biochemistry **1992**, 31, 450-455.

(78) Paterlini, M. G.; Freedman, T. B.; Nafie, L. A. Biopolymers **1986**, 25, 1751-1765.

(79) Dukor, R. K.; Keiderling, T. A. Biopolymers **1991**, 31, 1747-1761.

(80) Dukor, R. K.; Keiderling, T. A. Pept., Proc. Eur. Pept. Symp., 20th **1989**, 519-521.

(81) Dukor, R. K.; Keiderling, T. A.; Gut, V. Intl. J. Peptide & Protein Research **1991**, 38, 198-203.

(82) Bochicchio, B.; Tamburro, A. M. Chirality **2002**, 14, 782-792.

(83) Mezei, M.; Fleming, P. J.; Srinivasan, R.; Rose, G. D. Proteins: Structure, Function, and Bioinformatics **2004**, 55, 502-507.

(84) Hinderaker, M. P.; Raines, R. T. Protein Sci. **2003**, 12, 1188-1194.

(85) Shi, Z.; Woody, R. W.; Kallenbach, N. R. Adv. Prot. Chem. **2002**, 62, 163-240.

(86) Adzhubei, A. A.; Sternberg, M. J. E. J. Mol. Biol. **1993**, 229, 472-493.

(87) Syme, C. D.; Blanch, E. W.; Holt, C.; Jakes, R.; Goedert, M.; Hecht, L.; Barron, L. D. Eur. J. Biochem. **2002**, 269, 148-156.

(88) Sreerama, N.; Woody, R. W. Biochemistry **1994**, 33, 10022-10025.

(89) Cao, W.; Bracken, C.; Kallenbach, N. R.; Lu, M. Protein Sci. **2004**, 13, 177-189.

(90) Gnanakaran, S.; Hochstrasser, R. M. J. Am. Chem. Soc. **2001**, 123, 12886-12898.

(91) Woutersen, S.; Hamm, P. J. Phys. Chem. B **2000**, 104, 11316-11320.

(92) Schweitzer-Stenner, R.; Eker, F.; Huang, Q.; Griebenow, K.; Mroz, P. A.; Kozlowski, P. M. J. Phys. Chem. B **2002**, 106, 4294-4304.

(93) McColl, I. H.; Blanch, E. W.; Hecht, L.; Kallenbach, N. R.; Barron, L. D. J. Am. Chem. Soc. **2004**, 126, 5076-5077.

(94) Barron, L. D.; Blanch, E. W.; Hecht, L. Adv. Prot. Chem. **2002**, 62, 51-90, 51 plate.

(95) Blanch, E. W.; McColl, I. H.; Hecht, L.; Nielsen, K.; Barron, L. D. Vibrational Spectrosc. **2004**, 35, 87-92.

(96) McColl, I. H.; Blanch, E. W.; Gill, A. C.; Rhie, A. G. O.; Ritchie, M. A.; Hecht, L.; Nielsen, K.; Barron, L. D. J. Am. Chem. Soc. **2003**, 125, 10019-10026.

(97) Krimm, S.; Mark, J. E. Proc. Natl. Acad. Sci. U.S.A. **1968**, 60, 1122-1129.

(98) Note, that Krimm and Mark in their paper (Ref 97) used old Psi- and Fi- angle convention, since the modern one was not yet in effect. Thus, their Psi = +10 deg and Fi= +25 deg correspond to -170 deg and -155 deg of the modern convention, respectively.

5.0 UV RESONANCE RAMAN STUDIES OF POLYPEPTIDE FAST CONFORMATIONAL DYNAMICS

This work was published in *Journal of Physical Chemistry B* 2007, 111, 3280-3292. Coauthors are *Mikhonin, A. V.; Asher, S. A.; Bykov, S. V.; Murza, A.* Only a fraction of the published work has been presented in this chapter. The author of the thesis performed most of the experiment planning, sophisticated experimental work and labor-intensive initial data treatment. He was also involved into further data analysis and results discussion.

5.1 UV RAMAN SPATIALLY RESOLVED MELTING DYNAMICS OF ISOTOPICALLY LABELED POLYALANYL PEPTIDE: SLOW α-HELIX MELTING FOLLOWS 3_{10}-HELICES AND π-BULGES PREMELTING

We used UV resonance Raman to examine the spatial dependence of the T-jump secondary structure relaxation of an isotopically labeled 21-residue mainly ala peptide, AdP. The AdP penultimate ala residues were perdeuterated, leaving the central residues hydrogenated, to allow separate monitoring of melting of the middle versus the end peptide bonds. For 5 to 30 °C T-jumps, the central peptide bonds show a ~2-fold slower relaxation time (189±31 ns) than do the exterior peptide bonds (97±15 ns). In contrast, for a 20 to 40 ºC T-jump, the central peptide bond relaxation appears to be faster (56±6 ns) than that of the penultimate peptide bonds

(131±46 ns). We show that if the data are modeled as a 2-state transition, we find that only exterior peptide bonds show anti-Arrhenius folding behavior; while the middle peptide bonds show both normal Arrhenius-like folding and unfolding. This anti-Arrhenius behavior results from the involvement of π-bulges/helices and 3_{10}-helix states in the melting. The unusual temperature dependence of the (un)folding rates of the interior and exterior peptide bonds is due to the different relative (un)folding rates of 3_{10}-helices, α-helices and π-bulges/helices. Pure α-helix unfolding rates are ~12-fold slower (~1 μsec) than that of π-bulges and 3_{10}-helices. In addition, we also find that the α-helix is most stable at the AdP N-terminus where eight consecuitive ala occur; whereas the three hydrophilic arg located in the middle and at the C-terminus destabilize the α-helix in these regions and induce defects such as π-bulges and 3_{10}-helices.

5.1.1 INTRODUCTION

The classical picture of α-helix melting envisions an elementary process whereby individual peptide bonds at the ends of the α-helix rotate from conformations with α-helical Ramachandran Ψ and Φ dihedral angles to random coil conformations with uncorrelated, but allowed Ramachandran Ψ and Φ dihedral angles.[1-3] This melting also involves breaking the intra-α-helical hydrogen bonds. This highly simplistic view is the basis for the standard theories which are used to model the cooperativity in melting from the α-helix to its melted conformational state(s). This helix↔coil transition for short helix-forming peptides has recently been the subject of numerous experimental[4-52] and theoretical[53-116] investigations.

This simple view of α-helix melting is now being challenged, because it appears that simple α-helical peptides in aqueous solutions often melt to PPII-like conformations,[117-124] which are stabilized mainly by peptide bond-water interactions.[117,125-128] Whether unfolded proteins and peptides exist in "PPII-like" or "random coil" conformations is in active debate in the protein and peptide folding community. However, most recent publications support the existence of PPII-like conformations in proteins[121,129-132] and peptides[117-124,133-139]. Fewer studies support the existence of random coil conformations.[62,140] As pointed out in recent reviews,[125,126,141,142] unfolded peptides and proteins show strong CD signals, which are hard to understand if these unfolded peptides and proteins were truly disordered. These CD spectra are similar to those found for polypro. In addition, even single peptide bonds of dipeptides in aqueous solution, which were previously expected to be disordered, have recently been found to show PPII-like spectra.[136,137] Thus, we conclude that there is no convincing evidence in favor of melting to, or even for the existence of random coil peptides in solution.

Thus, the standard theories for α-helix formation and melting must be modified to include the fact that the transition is not between an ordered α-helix and a disordered random coil conformation, but rather the transition is between two ordered conformations. Further, this transition must be more complex, since at least one additional interfacial state must occur to connect the α-helix segment to the PPII segment, due to the steric features that prevent any simple connection.[68]

Given these complications, it is somewhat surprising that existing theory predicts the α-helix melting behavior pretty well. In most cases, the melting relaxation kinetics appears to follow a single exponential decay.[4-6,10,13-15,17,18,21,26] It should, however, be noted that clear departures from simple theory to date have been observed such as an α-helix peptide position

dependence for the melting kinetics by Werner et al.'s[10], Huang et al.'s[32] and Ramajo et al.'s[25] time-resolved IR isotopically (C=O) labeled spectral study of the unfolding kinetics of ~20-residue α-helical peptides. In addition, Huang et al.[32-34] and Bredenbeck et al.[22] found evidence for nonexponential relaxation. Theoretical models have been proposed to explain the observed nonexponential kinetics.[33,63]

We recently used UV resonance Raman (UVRR) spectroscopy[7] to examine the spatial dependence of melting of an isotopically labeled mainly ala α-helical peptide, AdP. UVRR spectroscopy is a powerful method to quantitatively determine peptide secondary structures.[4,7,135,143-153] UV excitation within the peptide bond $\pi' \rightarrow \pi^*$ transition selectively enhances a number of amide vibrations, whose frequencies and intensities report on the polypeptide backbone conformation.[4,135,143-145,154-157] The UVRR spectra are highly resolved. Laser induced temperature-jump (T-jump) kinetic UVRR measurements allow detailed studies of peptide unfolding.[4-6] In these studies the temperature of the peptide aqueous solution is increased within nsec by an IR laser pulse whose wavelength is completely absorbed by a water combination band. The temperature increase initiates peptide unfolding. A subsequent 204 nm UV excitation pulse at the appropriate delay time after the T-jump excites the UVRR spectra.

These UVRR spectra can be used to monitor the relaxation of the peptide conformation. For natural abundance AP we previously observed[4-6] a simple moderately cooperative melting curve with apparently simple single exponential relaxation kinetics (~200 nsec). The only indication of complexity in the kinetics came from a 2-state analysis of the temperature dependence which demonstrated an anti-Arrhenius temperature dependence for α-helix folding rate constant. The relaxation kinetics observed were similar to the melting behaviors observed for similar α-helical polypeptides.[4-6,10,13-15,17,18,21]

In a previous study we isotopically labeled AP in order to separately monitor the end peptide bonds melting versus that of the interior peptide bonds.[7] We found that the central peptide bonds have a higher equilibrium melting temperature than do the end peptide bonds. In the work here we directly examine the spatial dependence of unfolding kinetics for this partially deuterated peptide, AdP. As discussed below we find faster relaxation kinetics for the end peptide bonds compared to the middle for a 5 to 30 °C T-jump. In contrast, we find slower relaxation kinetics for the end peptide bonds compared to the middle for the 20 to 40 °C T-jump. We find that this behavior results from different relative contributions in the different regions of slower melting pure α-helices and faster melting π-bulges and 3_{10}-helices to the observed melting kinetics.

The AdP kinetic data can be adequately fit by single exponentials, within the S/N of our data. However, if we apply a two-state model similar to that of Lednev et al.[4] we calculate strong anti-Arrhenius behavior for folding of the end peptide bonds, whereas, the middle peptide bond (un)folding shows a normal Arrhenius behavior. This apparent anti-Arrhenius behavior results from involvement of additional states. These results are consistent with recent evidence that the ends of AdP-like peptides are frayed.[7,12,23,25,28,29,31,37,43,75,80] We successfully model the observed anti-Arrhenius behavior by taking into account π-bulge and 3_{10}-helical conformation melting, in addition to that of pure α-helix. This model is supported by recent studies by us and others, which report evidence for 3_{10}-helix[56,72,74,86,158-171] and π-helix/bulge[57,98,166,171-174] conformations in ala-rich peptides. Further, our model also explains the complicated nonexponential behavior observed earlier by Huang et al.[34] and Bredenbeck et al.[22] for similar peptides.

5.1.2 EXPERIMENTAL SECTION

Materials. The partially deuterated 21-residue alanine-based peptide (AdP) as well as its natural abundance analog AP (also called Fs), were synthesized by AnaSpec. Inc. The eight terminal ala at the amino end and the six terminal ala at the carboxyl end of the AdP peptide were perdeuterated while maintaining a non-deuterated center (AdAdAdAdAdAdAd-RAAAA-RAdAdAdAd-RAdAd, where the bold letters label the 2,3,3,3-deuterated residues).

The AdP purity as well as the position of deuterated amino-acid residues was independently verified by MALDI MS analysis kindly performed by Anton Karnoup (The Dow Chemical Company, Midland, MI). Analysis was carried out using a Voyager DE-STR MALDI-TOF mass spectrometer (Applied Biosystems) operated in reflectron and post-source decay (PSD) modes.

T-jump Raman Spectral Measurements. The UV Raman spectrometer is described in detail elsewhere.[4,175] Briefly, the third harmonic of a Coherent Infinity Nd:YAG laser operating at 90 Hz with a 3 nsec pulse width was Raman shifted five anti-Stokes harmonics in 40 psi hydrogen gas to 204 nm to excite the amide band UVRR spectra. The Raman scattered light was collected at an angle close to backscattering and dispersed with a partially subtractive double monochromator. The Raman scattered light was detected by using a Princeton Instruments Spec-10:400B CCD camera (Roper Scientific). We used spectral accumulation times of ~5 min with spectral resolutions of ~10 cm^{-1}.

To selectively heat the water solvent, we Raman-shifted the 1.06-μm Nd YAG fundamental to 1.9 μm (1st H_2 Stokes shift) by using a 1-m Raman shifter (Light Age Inc.; 1000 psi H_2) to obtain 1.5 mJ pulse energies at our 90 Hz repetition rate. This 1.9 μm excitation is

absorbed by a water combination band and the energy is thermalized in psec by vibrational relaxation.

We studied T-jumps from 5 to 30 °C and from 20 to 40 °C. These T-jumps were obtained by focusing the 1.5 mJ 1.9 μm laser pulses to a ~300 μm diameter spot in the flowing sample stream. To ensure that the Raman signal was obtained from the sample volume maximally heated by the IR pulse[4] we adjusted the sample absorbance at 204 nm to 40 cm^{-1} by utilizing a 15 mg/ml concentration of AdP.

We independently verified the magnitude of the T-jump by measuring the pump beam energy dependence of the 204 nm excited ~3000 cm^{-1} water Raman band. This band shows a large, well-known frequency and band shape temperature dependence.[4,176,177] We constructed a T-jump calibration curve as described by Lednev et al.[4], by using the UVRR water difference spectrum in the presence versus absence of the IR pump beam to determine the actual T-jump in the probed volume.

There exist low temporal frequency variations of the measured Raman spectral intensities that can interfere with the T-jump spectral measurements. These variations may derive from variations in the UV laser pulse energy at the sample. Alternatively this variation may derive from low frequency motion of the sample stream, which may correlate with changes in the sample stream surface. We found that we could remove this fluctuation in the spectra by measuring for each time delay two duplicate T-jump spectra which were bracketed by identically measured cold spectra where the T-jump pump pulses were blocked. We only accepted as valid, T-jump spectra which were bracketed by essentially identical cold UVRR spectra. This allowed us to ignore the set of fluctuations which did not span the time scale of repeated T-jump measurements.

Determination of AdP secondary structure composition. We determined the secondary structure composition from the steady state and transient spectra for the AdP C_α-H peptide bonds in the center, and for the C_α-D penultimate amide bonds by fitting the experimentally measured spectra to a linear combination of the four basis spectra of the α-helix and PPII conformations of the C_α-H and C_α-D peptide bonds, as deteremined earlier.[145] The fits were obtained by using least-squares criteria. In this modeling, we assume that each of the amide groups scatter independently,[178] and the spectra derived from the previously determined basis spectra of the α-helix and PPII conformations,[4,120,145] taking into account that the PPII basis spectra were previously[4] incorrectly denoted as deriving from the "random coil" conformation.

We deconvoluted the 82 ºC PPII spectrum of AdP into a minimum number of bands as in Lednev et al.[4] We then determined the temperature dependence of the band intensities, bandwidths and frequencies in spectra measured of AdP at 52, 62, 70 and 82 ºC, temperatures at which AP and, thus, AdP is predominantly PPII.[4,6,120] We assumed that this observed linear temperature dependence extrapolates down to 0 ºC, and calculated the pure temperature dependent PPII spectra of AdP. Since the individual PPII peptide bonds independently contribute to the UVRR spectra,[178] the AdP PPII spectra have a 35 % contribution from the C_α-H PPII peptide bonds (7 out of 20 bonds) and a 65% contribution from the C_α-D PPII peptide bonds (13 out of 20 bonds). We subtracted the necessary amount of the temperature dependent C_α-H AP PPII spectra from the AdP PPII spectra to uniquely calculate the temperature dependent C_α-D AdP PPII spectra.

We know that AdP is ~53% α-helix-like at 5 °C.[4,6,7,171] Since AdP contains 35% C_α-H peptide bonds and 65% C_α-D peptide bonds, and the C_α-H b Raman band derives only from the C_α-H peptide bond PPII Raman spectrum,[4,144,145,154] we can determine the C_α-H PPII fraction at 5

°C directly from the C_α-H b band intensity. This C_α-H PPII fraction knowledge allows us to directly estimate the C_α-D PPII and C_α-H α-helix-like fractional compositions. We can also calculate the pure C_α-D peptide bond α-helix-like basis spectrum by subtracting the calculated 5 °C C_α-D peptide bond PPII spectrum, as well as the calculated 5 °C C_α-H peptide bond PPII and α-helix spectra from the measured 5 °C AdP spectrum. We assume that this α-helix-like basis spectrum is independent of temperature.[4,179]

5.1.3 RESULTS

5.1.3.1 AdP UV Resonance Raman Spectra

Fig. 5.1 shows the 5 °C 204 nm excited UVRR spectra of aqueous solutions of the 21 amino acid residue peptides AdP and AP, where AP is the non-deuterated analog of AdP. At 5 °C, AdP and AP are ~53 % α-helix-like and ~47 % PPII.[4,6,7,120,171] We previously calculated the UVRR spectra of the individual α-helix-like and PPII conformations.[7,145] Most recently we showed that the 5 °C α-helix-like conformations actually consist of ~24% pure α-helix, ~20% π-bulges/helices, and ~9% 3_{10}-helices whose spectra overlap (see below).[171]

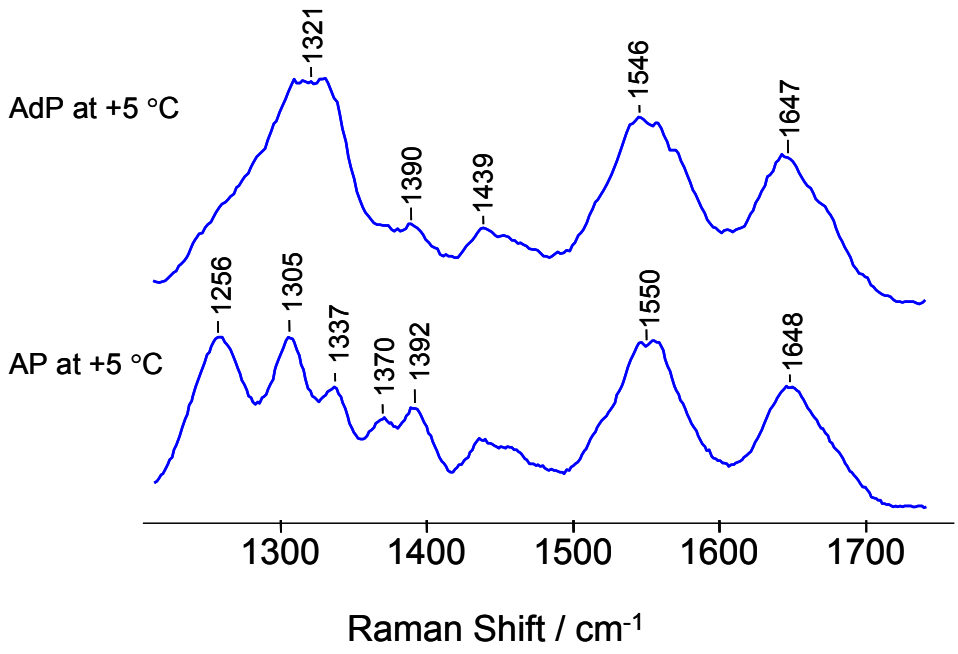

Figure 5.1: 204 nm UV Resonance Raman spectra of AdP (15 mg/mL) and its non-deuterated analog AP (3 mg/mL) at 5 ºC. The AP solution contained 0.2 M $NaClO_4$.

As discussed in detail elsewhere,[145,171] α-helix-like AP conformations display a triplet of bands in the amide III region. The 1261 cm^{-1} $AmIII_{3H}$ band was originally[145] assigned to the "classical α-helix AmIII band" and involves mainly N-H bending (b), C-N stretching (s) and possibly C_α-C s. However, we recently showed that this $AmIII_{3H}$ band has contributions not only from pure α-helix conformations but also from overlapping bands due π-bulges and 3_{10}-helices at T<30 °C, that broaden the $AmIII_{3H}$ band.[171] The 1306 cm^{-1} band was assigned to the $AmIII_2$ vibration, which mainly involves C_α-C s, N-C s, with possibly a small amount of C-N s and N-H b,[145] while the 1337 cm^{-1} band was assigned to the $AmIII_1$ band which derives from a vibration mainly involving C_α-C s and N-C s with possibly a small amount of C-N s.[145] The α-helix-like AmII band, which occurs at 1542 cm^{-1} is mainly associated with C-N s and N-H ib, while the 1647 cm^{-1} α-helix-like Am I band involves mainly C=O s.[145,186]

We demonstrated earlier[145] that the AmIII band triplet of the AP PPII conformation occurs at 1245 ($AmIII_3$), 1303 ($AmIII_2$) and 1337 cm^{-1} ($AmIII_1$), with the 1245-cm^{-1} band labeled as the "classical AmIII band". The PPII conformation of AP also shows a doublet at 1370 and 1394 cm^{-1} which mainly derives from C_α-H b with maybe some contribution from CH_3 umbrella modes. These C_α-H bands are absent in the α-helix conformation.[4,144,145,154,187]

The AP PPII conformation AmII and AmI bands are upshifted and broadened compared to those of the α-helix-like conformations.[4,145] AmII appears at 1558 cm^{-1}, while AmI appears at 1655 cm^{-1} in the PPII conformation. There are also relatively broad arg side chain bands, one of which occurs at ~1646 cm^{-1} in water and overlaps the AP AmI band.[178] In contrast, this arg band in D_2O is much sharper, and occurs at ~1614 cm^{-1}, well separated from the AmI' band.[178]

The AdP UVRR spectra are much more complex because of contributions from both C_α-H and C_α-D peptide bonds which occur in both α-helix-like and PPII conformations. Mikhonin and Asher[178] recently demonstrated that the peptide amide III – C_α-H bands region UVRR spectra result from the independent UVRR contributions of the different peptide bonds. Thus, the spectra of AdP can be considered to result from independent scattering from C_α-H and C_α-D peptide bonds in α-helix-like and PPII conformations.

The C_α-D peptide bonds show UVRR spectra[144,145] that differ from those of natural abundance AP mainly in an upshift of the C_α-D peptide bond amide III band envelope to ~1321 cm^{-1}. In AdP, the 1321 cm^{-1} band dominates the amide III spectral region (Fig. 5.1). Deuteration of the ala residue C_α-H decouples the NH bend from the C_α-H bending motion.[144] The resulting C_α-D amide III band no longer shows a triplet, but displays a complex bandshape with an increased Raman cross section.[7,144,145] The loss of C_α-H bending coupling leaves this band's frequency insensitive to the peptide bond conformational difference between the α-helix and

PPII conformations.[7,144,145] However, the Raman cross section of this band is much larger for the PPII conformation,[145] due to the hypochromism present in the α-helix conformation.[188-197]

Although the C_α-H ala CH_3 sidechain umbrella bending vibration contributes to the 1370-1400 cm^{-1} spectral region,[186] the intensity in this region is dominated by the resonantly enhanced C_α-H b doublet of the C_α-H ala PPII conformation.[120,145] Thus, changes in PPII concentration dominate the intensity changes within this spectral region. Furthermore, the CH_3 umbrella UVRR bands are expected to be insensitive to conformational changes in the peptide backbone, as shown recently.[145]

5.1.3.2 Transient AdP UVRR Difference Spectra

Fig. 5.2 shows a series of calculated UVRR difference spectra measured at different delay times subsequent to a T-jump. The raw spectra were obtained by measuring UVRR spectra at specified delay times after the T-jump. The time delay difference spectra shown in Fig. 5.2 were calculated by subtracting a spectrum measured 10 nsec after the T-jump from the individual time delayed spectra. We utilized T-jumps which increased the sample temperature from 5 to 30 °C, and from 20 to 40 °C.

We subtracted the 10 nsec delay spectra from the original T-jump difference spectra to selectively remove spectral changes which derive from sample non-conformational temperature changes.[4-6,120] We earlier showed that these non-conformational changes derive from a decreased hydrogen bond strength to water at elevated temperatures.[4,6,120,135,145] This allows us to concentrate on spectral alterations induced by conformational changes, which occur at later times. Our previous AP studies[4-6,120] clearly showed that no conformational changes occur until longer (>50 nsec) delay times.

The main Fig. 5.2 UVRR difference features occur as bands at 1320 and 1381 cm^{-1} whose intensities increase with the time delay after the T-jump. The 1320 cm^{-1} feature derives from an AmIII band intensity increase from the C_α-D peptide bonds of AdP due to the increasing PPII concentration. Melting to the PPII conformation results in hyperchromism[188-197] of the resonant absorption band and a consequent hyperchromism of the Raman cross sections.[145] The 1381 cm^{-1} intensity increase results from the appearance of the C_α-H b band of the AdP melted C_α-H PPII conformation.[120]

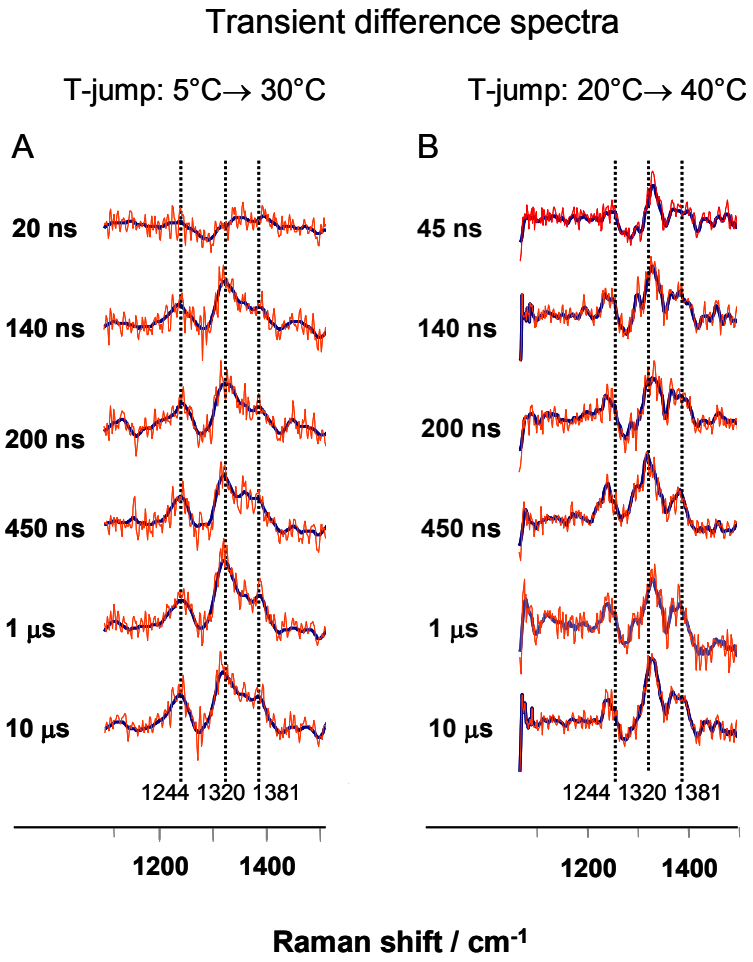

Figure 5.2: T-jump difference UVRR spectra of AdP at different delay times between the pump and probe laser pulses. These difference spectra were obtained by subtracting the 10 nsec delay time spectra from each of the longer delay time spectra. A. Difference spectra for a T-jump from 5 to 30 °C. B. Difference spectra for a T-jump from 20 to 40 °C.

Modeling the Transient Temperature Dependence of AdP Secondary Structure. We used the calculated AP and AdP pure secondary structure-Raman spectra (PSSRS) to determine the time delay dependent secondary structure composition for each observed transient AdP UVRR spectrum at each T-jump. Fig. 5.3A shows the calculated temperature-dependent PPII C_α-H peptide bond and C_α-D peptide bond basis spectra, and the temperature-independent α-helix C_α-H peptide bond and C_α-D peptide bond basis spectra.[4,145]

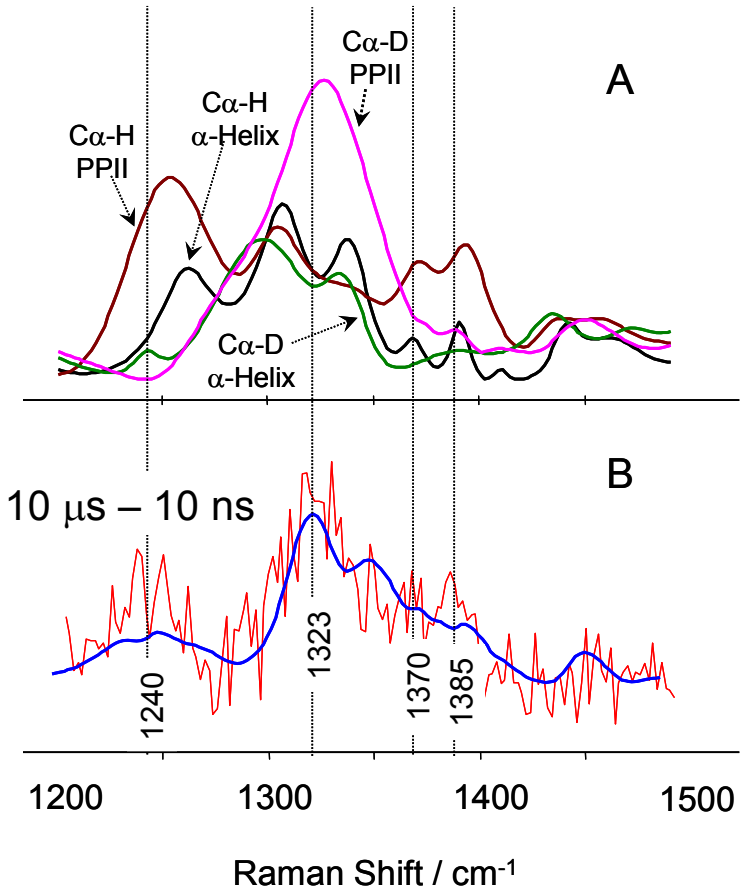

Figure 5.3: Calculated 30 °C pure secondary structure spectra of AdP: Cα-H peptide α-helix-like conformation (black); Cα-H peptide bond PPII conformation (brown); Cα-D peptide α-helix-like conformation (green); and Cα-D peptide PPII conformation (magenta). B. measured transient difference spectrum obtained after a time delay of 10 μs during a T-jump from 5 to 30 °C (red); Best fit of AmIII – Cα-H region (1200-1480 cm^{-1}) to a linear combination of the AdP basis spectra shown in Fig. 5.5A (blue).

We did not attempt to resolve the underlying pure α-helix, π-helix/bulge and 3_{10}-helix conformations recently discovered by Mikonin and Asher[171] in these transient spectra given our limited S/N. The affect of their contribution is to broaden the C_α-H peptide bond "α-helix-like" $AmIII_3$ band.[171]

We can precisely determine AdP PPII fractions for the C_α-H peptide bonds using the basis spectra, since the C_α-H b band(s) between 1380-1400 cm^{-1} (Fig. 5.4A) serves as an isolated, extremely sensitive non-α-helical marker.[4,144,145,154] For the C_α-D peptide bonds, C_α-D deuteration breaks the coupling between the C_α-D b and N-H b motions, which makes the C_α-D AmIII band frequency insensitive to the Ψ Ramachandran angle.[144,145] However, it is still possible to reliably find the C_α-D PPII fraction by using the normalized basis spectra, because the intensity of the C_α-D PPII AmIII band is more than 2-fold greater than that of C_α-D "α-helix-like" AmIII band (Fig. 5.3A)[145] due to hypochromic excitonic interactions in the α-helix.[188-197] Using this approach we can reliably estimate the PPII fractional compositions in AdP C_α-H center peptide bonds as well as in the C_α-D end peptide bonds from the different transient spectra shown in Fig. 5.2 at different delay times, t, subsequent to T-jumps from 5 to 30 °C, and 20 to 40 °C.

5.1.3.3 AdP Mono-Exponential Relaxation Rates

Figs. 5.4A and B show the time dependence of the calculated total PPII concentration of AdP, as well as the individual end C_α-D PPII and the center C_α-H PPII concentrations for the T-jumps from 5 to 30 ºC and 20 to 40 ºC, respectively. Using mono-exponential fitting for total PPII concentration (C_α-D plus C_α-H peptide bonds), we find the relaxation time ($\tau_R=k_R^{-1}$) of 116±17 ns (Fig. 5.4A, Table 5.1) for the T-jump from 5 to 30 ºC, whereas for the T-jump from

20 to 40 ºC we find a 109±27 ns relaxation time (Fig. 5.4B, Table 5.1). These relaxation times are identical (within the experimental error) to that found earlier by Lednev and coworkers[4] for AP peptide, the natural abundance analog of AdP. Specifically Lednev et al.[4] found 180±60 ns, 120±50 ns and 70±30 ns relaxation times for T-jumps from 4 to 37 ºC, from 4 to 48 ºC and from 4 to 64 ºC, respectively.

As pointed out by Lednev et al.[4] if the α-helix melting in AdP were truly a two-state transition, the α-helix folding, k_F and unfolding rate constants, k_U could be simply calculated from the "two-state" relaxation rate constant relationship $k_R = k_U + k_F$, and from the two-state equilibrium constant $K_{EQ}= kU/k_F$ independently obtained from the measured equilibrium UVRR spectra.[4,7] If we use the two-state model, then the C_α-H center (un)folding rate constant shows a "normal" Arrhenius behavior. In contrast, the C_α-D ends folding rate constant decreases with increasing temperature. This is an apparent anti-Arrhenius behavior (with negative folding activation barrier). As expected, the end peptide bonds melt at lower temperatures than do the middle peptide bonds.[7] However, our kinetic results are quite unusual. For the 5 to 30 ºC we calculate a 2-fold faster relaxation time for the end peptide bonds (97±15 ns, Fig. 5.4C) than that of the middle (189±31 ns, Fig. 5.4E). In contrast, for the 20 to 40 ºC T-jump we calculate a somewhat slower relaxation time for the end peptide bonds (131±46 ns, Fig. 5.4D) than the middle (56±6 ns, Fig. 5.4F).

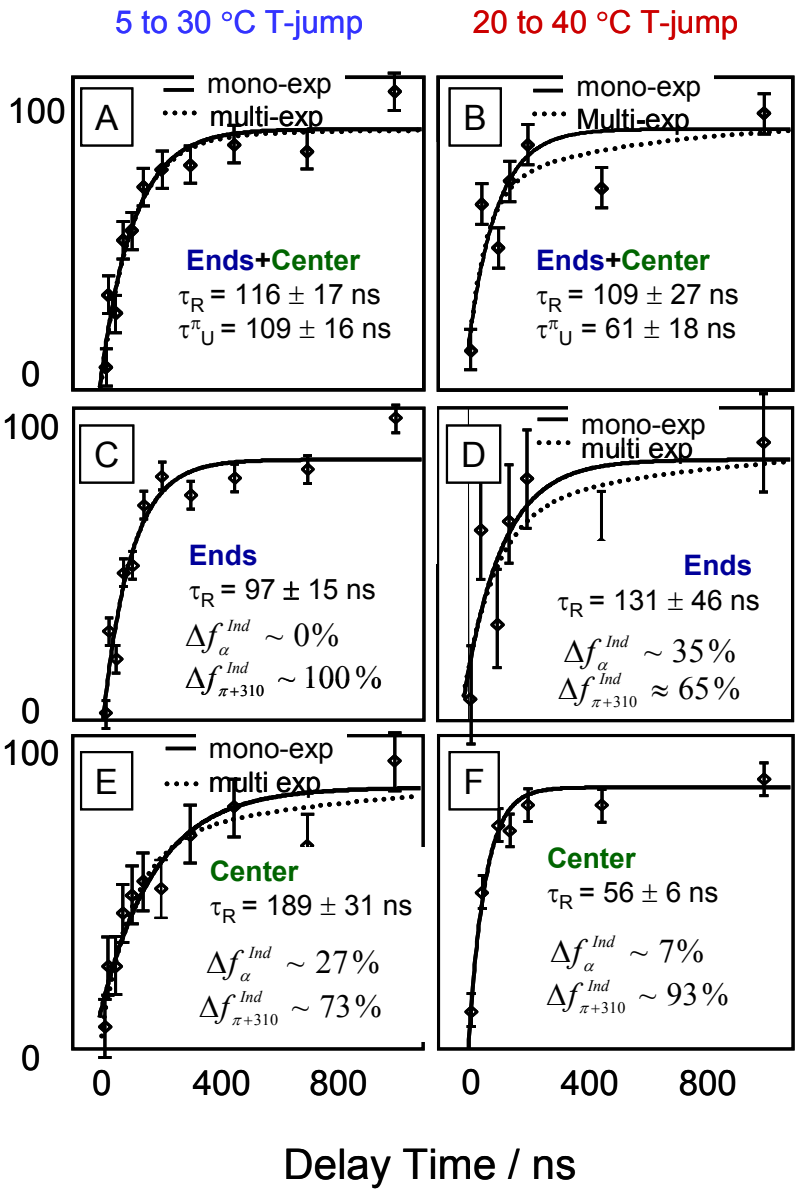

Figure 5.4: T-jump relaxation of the total PPII concentration (A and B) as well as the PPII concentrations of the end Cα-D (C and D) and center peptide bonds (E and F) due to T-jumps from 5 to 30 °C and 20 to 40 °C. Unfolding is monitored by changes in the relative compositions of the basis spectra shown in Fig. 5.3. The mono-exponential relaxation times are τ_{total} = 114 ± 46 ns, τ_{end} = 89 ±17 ns and τ_{cen} = 188 ± 46 ns for the T-jump from 5 to 30 ºC; and τ_{total} = 96 ± 39 ns, τ_{end} = 122±51 ns and τ_{cen} = 54 ± 11 ns for the T-jump from 20 to 40 °C. The dotted lines in Figs. 5.4A and 5.4B are fits to multi-exponential kinetics for the total PPII concentrations. These fits find the unfolding times, τ^{π}_{U}, for π-bulges (or 3_{10}-helices) of 109±24 ns for the 5 to 30 ºC T-jump and 61±23 ns for the 20 to 40 ºC T-jump.

If this data are modeled as if they result from a two-state transition, we find that the folding rate constants for the AdP end peptide bonds show the strong anti-Arrhenius behavior with negative activation energy barrier (Table 5.1). In contrast, we find that all the (un)folding rate constants for the AdP center peptide bonds show the normal Arrhenius-like behavior with positive activation energy barriers (Table 5.1).

The anti-Arrhenius behavior of AdP ends folding rate constants indicates that the AdP ends melting is clearly not a two-state state process, and that the additional states must be involved in the α-helix melting. This is consistent with the recent reports that indicate that the ends of AP and AdP-like peptides are frayed.[7,12,23,25,28,29,31,37,43,75,80]

In contrast, the normal Arrhenius-like behavior of AdP center (un)folding rate constants, at the first glance, could indicate that the AdP center melting occurs in "two-state-like" mechanism. However, the Table 5.1 calculated "two-state" activation energy barriers of ~10-35 kcal/mol·peptide bond (kcal/mol·PB) are much higher than those of ~2–4 kcal/mol·PB estimated earlier for ala-rich peptides both theoretically[56,89,93] and experimentally.[171]

Below we explain this unusual kinetic behaviors of both AdP ends and AdP center in terms of competition between the slower melting pure α-helices, and faster melting π-bulges and 3_{10}-helices.

Table 5.1: Two-State Kinetic Parameters and Equilibrium Constant for α-Helix↔PPII Conformational Transition Calculated for AdP, AdP, and the C_α-H Center and AdP C_α-D End Peptide Bonds

	Final T-jump Temperature, °C		*Activation Energy, ΔG, kcal/mol·PB*
	+30 °C	*+40 °C*	
Relaxation time, $\tau_R=(k_R)^{-1}$ / ns			
C_α-H + C_α-D	116 ± 17 ns	109 ± 27 ns	1.0 ± 5.5
C_α-H Center	189 ± 31 ns	56 ± 6 ns	22.8 ± 3.6
C_α-D Ends	97 ± 15 ns	131 ± 46 ns	–5.6 ± 7.3
Equilibrium constant,a $K_{EQ}=f_{PPII}/f_\alpha$			
C_α-H + C_α-D	3.35	5.25	
C_α-H Center	0.75	2.03	
C_α-D Ends	9.0	19.0	
Unfolding time constant, $\tau_U=(k_U)^{-1}$, ns			
C_α-H + C_α-D	150 ± 28 ns	130 ± 39 ns	2.7 ± 6.5
C_α-H Center	440 ± 100 ns	84 ± 11 ns	31.2 ± 4.9
C_α-D Ends	108 ± 19 ns	138 ± 51 ns	–4.6 ± 7.7
Folding time constant, $\tau_F=(k_F)^{-1}$, ns			
C_α-H + C_α-D	502 ± 91 ns	684 ± 202 ns	–5.8 ± 6.5
C_α-H Center	332 ± 75 ns	164 ± 21 ns	13.3 ± 4.9
C_α-D Ends	971 ± 167 ns	2620 ± 970 ns	–18.7 ± 7.7

5.1.4 DISCUSSION

We show below that this apparent anti-Arrhenius behavior (Table 5.1) is the result of the failure of the two-state model to describe both the conformational equilibrium and the dynamics of AP or AdP melting. As shown below, we can model the observed melting behavior by including the melting of 3_{10}-helical and π-bulge conformational states[171], in addition to that of pure α-helix (Fig. 5.5 and Table 5.2). This modeling explains the observed apparent anti-Arrhenius behavior (Table 5.1). The individual (un)folding rate constants for pure α-helices, π-bulges and 3_{10}-helices show normal Arrhenius behavior (Table 5.3).

5.1.4.1 Resolved AdP Equilibrium Melting Curves show melting of α-Helix, π-Helix/Bulge and 3_{10}-Helix Conformations

Recently we showed that the "α-helix-like" UVRR spectra of AP, which is the natural abundance analog of AdP contains contributions from π-bulges/helices and 3_{10}-helices.[171] Fig. 5.5 shows the melting curves for AP (and, thus, AdP) and demonstrates that the pure α-helix, π-helix/bulge and 3_{10}-helix conformations have different melting curves. The π-bulges/helices and 3_{10}-helices melt at lower temperatures than the pure α-helices, and are fully melted by 30 °C. The decreased T_m values for the π-bulge and 3_{10}-helix conformations results from their less optimized intra-peptide hydrogen bonding compared to that of the α-helix. The more solvent exposed π-bulges[198] and 3_{10}-helices (type III turns)[199] populate due to the increased peptide bond-water hydrogen bond strengths at lower temperatures.[4,120,135,145]

The arrows in Fig. 5.5 show the temperature intervals for the 5→30 °C and 20→40 °C T-jumps, while Table 5.2 summarizes the α-helical, 3_{10}-helical and π-bulge/helical fractions of

AdP at initial and final T-jump temperatures. Clearly, different conformations are melting to the PPII conformation at the different intial and final T-jump temperatures. These different conformations have different (un)folding rates and different relative contributions to the net AP melting kinetics at the different temperatures (Fig. 5.5).

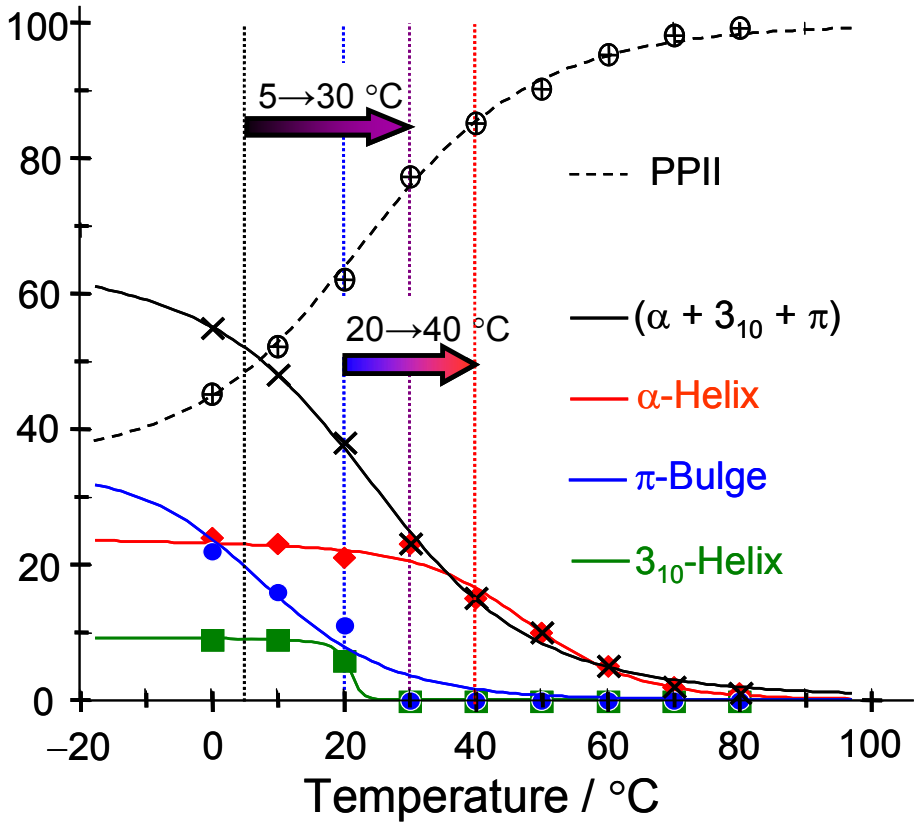

Figure 5.5: Melting/formation curves for AdP "α-helix-like" conformations. (×) – Original "α-helix" melting curve as reported for the natural abundance analog of AdP, AP, by Lednev et al. [Ref 4,6] which is actually the sum of the individual α- π- and 3_{10}-helical melting curves; (♦) – Pure α-helix melting; (■) – 310-helix (type III turn) melting; (●)– π-bulge (π-helix) melting. (⊕) – PPII formation. Arrows show the conformational differences spanned by the 5 to 30 °C and 20 to 40 °C T-jumps. Adapted from [Ref 171]

Below we show that the AdP π-bulge and 3_{10}-helix conformations have ~12-fold faster unfolding rates than that of pure α-helix conformation (Table 5.3). Thus, the lower temperature T-jumps predominantly samples the faster melting π-bulge and 3_{10}-helix conformations (Fig. 5.5). In contrast, the higher temperature T-jump (Fig. 5.5) samples a larger fraction of pure α-helix melting with slower (un)folding rates.

Table 5.2: Total equilibrium concentrations of AdP α-helix like conformations (including both C_α-H and C_α-D peptide bonds) at initial and final T-jump temperatures

Temperature, °C	*α-helix fractiona, %*	*π-helix/bulge fractiona, %*	*3_{10}-helix fractiona, %*	*Total α-helix-like fractionb, %*
+5 °C	24%	20%	9%	53%
+30 °C	23%	0%	0%	23%
	$\Delta f_\alpha = 1\%$	$\Delta f_\pi = 20\%$	$\Delta f_{310} = 9\%$	$\Delta f_{\alpha+\pi+310} = 30\%$
+20 °C	22%	11%	6%	39%
+40 °C	15%	0%	0%	15%
	$\Delta f_\alpha = 7\%$	$\Delta f_\pi = 11\%$	$\Delta f_{310} = 6\%$	$\Delta f_{\alpha+\pi+310} = 24\%$

Our results here explain the complicated non-exponential and/or multi-exponential behavior of melting kinetics of alanine-rich peptides previously observed.[22,34] Specifically, the heterogeneity of the low temperature α-helical ensembles (Fig. 5.5) explains the observed complicated kinetic behavior for low initial T-jump temperatures.[22,34] In contrast, the homogeneity of the above room temperature α-helical ensembles (Fig. 5.5) explains the essentially mono-exponential melting behavior of these peptides for higher initial temperature T-jumps.[22,34]

Table 5.3: Kinetic parameters for AdP pure α-Helix, π-Bulge and 3_{10}-Helix (un)folding, calculated from the overall (C_α-H and C_α-D peptide bond) kinetic and equilibrium data, as well as from the individual C_α-H center peptide bonds and and C_α-D end peptide bond kinetic and equilibrium data[††]

	Final T-jump Temperature, °C		*Activation Energy, ΔG / kcal/mol·PB*
	+30 °C	*+40 °C*	
Equilibrium constant, $K_{EQ}=f_{PPII}/f_\alpha$			
C_α-H + C_α-D	3.35	5.25	
C_α-H Center	0.75	2.03	
C_α-D Ends	9.0	19.0	
Mono-exp relaxation time, $\tau_R=(k_R)^{-1}$ / ns			
C_α-H + C_α-D	116 ± 17 ns	109 ± 27 ns	1.0 ± 5.5
C_α-H Center	189 ± 31 ns	56 ± 6 ns	22.8 ± 3.6
C_α-D Ends	97 ± 15 ns	131 ± 46 ns	–5.6 ± 7.3
Pure conformation folding time, $\tau_F = (k_F)^{-1}$ / ns			
Pure α-Helix	4421 ± 802 ns	3553 ± 1207 ns	4.1 ± 7.2
π-Bulge and/or 3_{10}-Helix	τ_F >> 109 ns	τ_F >> 61 ns	4.1 ± 7.2
Pure conformation unfolding time, $\tau_U = (k_U)^{-1}$ / ns			
Pure α-Helix	1321 ± 239 ns	677 ± 230 ns	12.6 ± 7.2
π-Bulge and/or 3_{10}-Helix b	109 ± 16 ns	61 ± 18 ns	11.0 ± 6.2
Pure conformation relaxation time, $(1/\tau_U + 1/\tau_F)^{-1}$ / ns			
Pure α-Helix	1017 ± 148 ns	568 ± 165 ns	11.0 ± 6.2
π-Bulge and/or 3_{10}-Helix	109 ± 16 ns	61 ± 18 ns	11.0 ± 6.2
Relative contributions of slower pure α-helix relaxation to the observed relaxation kinetics, Δf_α / %			
C_α-H + C_α-D	5 ± 8 %	29 ± 14 %	
C_α-H Center	27 ± 9 %	7 ± 12 %	
C_α-D Ends	–3 ± 9 %	35 ± 22 %	
Relative contributions of faster π-bulges and 3_{10}-helix relaxations to the observed relaxation kinetics, $\Delta f_{\pi+310}$ / %			
C_α-H + C_α-D	95 ± 8 %	69 ± 14 %	
C_α-H Center	73 ± 9 %	93 ± 12 %	
C_α-D Ends	103 ± 9 %	65 ± 22 %	

[††] For the detailed description of Modeling for Individual C_α-H Center and C_α-D End Peptide Bonds Melting Kinetics see Mikhonin, A. V.; Asher, S. A.; Bykov, S. V.; Murza, A. Journal of Physical Chemistry B 2007, 111, 3280-3292.

5.1.4.2 Dynamics of Center Cα-H Peptide Bond Unfolding.

Figs. 5.4E and 5.4F show the time-dependent changes in the PPII concentration of the central AdP C_α-H peptide bonds due to the T-jumps from 5 to 30 ºC and from 20 to 40 ºC. The unfolding kinetics of C_α-H peptide bonds shown in Figs. 5.4E and 5.4F, depend upon the T-jump initial and final temperatures. We find that for the 5 to 30 °C T-jump the C_α-H peptide bonds show a 189±31 ns mono-exponential unfolding relaxation time (Fig. 5.4E), while for the 20 to 40 °C T-jump we obtained 56±6 ns relaxation time (Fig. 5.4F).

The 189±31 ns mono-exponential relaxation time calculated for the 5 to 30 °C T-jump (Fig. 5.4C and Table 5.3) indicates that the slow α-helix melting (1017±148 ns at 30 °C) contributes to the observed kinetics. However, the observed kinetics is dominated by the fast π-bulge and 3_{10}-helix melting (109±16 ns at 30 °C). We roughly estimate a ~73% contribution from the π-bulges and 3_{10}-helices to the C_α-H center peptide bonds kinetics; and a ~27% contribution from pure α-helix melting (Fig. 5.4D and Table 5.3).

In contrast, the 56±6 ns mono-exponential relaxation time found for the 20 to 40 °C T-jump (Fig. 5.4D, Table 5.3), surprisingly indicates that the C_α-H center peptide bond kinetics are dominated by π-bulge and 3_{10}-helix melting (61±18 ns at 40 °C), with little contribution of slow α-helix melting (568±165 ns at 40 °C). This is a surprising result, since at 20 °C "α-helix-like" segments[6] are assumed to preferrentially occur in the middle of the peptide, and thus α-helix melting should dominate the observed C_α-H center peptide bond kinetics. This suggests that the α-helix stability/propensity in AdP is position-dependent (see below). Specifically, we suggest below that the AdP N-terminus has the higher α-helical propensity than does the AdP middle and C-terminal regions.

5.1.4.3 Dynamics of Center Cα-H versus End Cα-D Peptide Bond Unfolding

The Figs. 5.4C and 5.4E show that for the 5 to 30 °C T-jump, the AdP center unfolds slower (189±31 ns) than do the ends (97±15 ns). We also estimated that at 30 °C the relaxation time of pure α-helices is 1017±148 ns, whereas that of π-bulges and 3_{10}-helices is 109±16 ns (Table 5.3). If the relaxation rates of these "α-helix-like" species are independent of location in the AdP chain, we can conclude that the melting of π-bulges and 3_{10}-helices dominate both the AdP C_α-D ends (~100%) and C_α-H center (~73%) melting kinetics (Table 5.3). However, pure α-helix melting also have a small contribution (~27%) to the C_α-H center melting kinetics for the 5 to 30 °C T-jump (Table 5.3). These kinetic results are consistent with the Fig. 5.5 equilibrium melting curves obtained for pure α-helix, π-bulge and 3_{10}-helix conformations,[171] as well as with the earlier studies of us[7] and others[12,23,25,28,29,31,37,43,75,80], which indicate that the ends of AdP-like peptides are frayed.

In contrast, for the 20 to 40 °C T-jump, the center of AdP unfolds faster (56±6 ns, Fig. 5.4F) than do the ends (131±46 ns, Fig. 5.4D). The faster center melting for the 20 to 40 °C T-jump, especially given the higher T_m of the center peptide bonds[7] appears initially surprising. We suggest that the faster melting of π-bulges and 3_{10}-helices still dominate both the C_α-H center (~93%) and C_α-D ends (~65%) melting kinetics. However, we surprisingly find that the pure α-helix melting contributes ~35% to the C_α-D ends melting kinetics, and contributes very little to the C_α-H center kinetics (Table 5.3). These results can only be understood if one of the AdP termini has a significantly higher pure α-helix propensity than the AdP center and the other terminus.

We propose that the AdP N-terminus has a higher α-helix propensity, than the middle and C-terminus. Such a preference would derive from the AdP primary sequence. Specifically,

the N-terminus of AdP contains a sequence of eight ala, which stabilize the α-helix conformation.[52] In contrast, three hydrophilic arg are distributed within the AdP center and C-terminus. These three arg partially destabilize the α-helices and favor formation of the water-mediated α-helical defects such as π-bulges[198] and 3_{10}-helices.[199]

On the first sight, our results contradict Vila et al.'s theoretical study,[200] which suggests that polar long side chains (such as arg) stabilize the α-helix by protecting of the helical amides from water hydrogen bonding. However, Vila et al.'s studies ignored sidechain charge-charge interactions, which are absent in their peptide, but are present in AdP. A more realistic approximation of the AdP case is provided by the NMR and CD studies of Kallenbach's group,[52] where the guest charged residue (lys or ornithine) are inserted inside the ala sequence flanked by other charged residues. In accordance with our findings, Kallenbach's studies also clearly show that charged residues destabilize the α-helix conformation.

The higher α-helix stability at the AdP N-terminus also agrees well with the MD simulation studies of Sorin and Pande,[72] which suggested that the N-terminus of 21-residue α-helical Fs-peptide (which is a natural abundance analog of AdP) has a higher α-helical content than occurs in the middle and at the C-terminus. These MD studies also suggest that the arginines destabilize α-helices in Fs (and, thus, in AdP). We suggest that these hydrophilic arg are likely not only to partially destabilize α-helices but also induce the formation of water-mediated α-helical defects such as π-bulges[198] and 3_{10}-helices (type III turns)[199] at low temperatures, at which the peptide bond-water hydrogen bonding strength increases.[120,135,145]

Whatever the case, our calculated ~4.4 and ~1.3 μsec (+30 °C) and ~3.6 and ~0.7 μsec (+40 °C) pure α-helix folding and unfolding times (Table 5.3), respectively, are much slower than the (un)folding times previously reported for similar peptides. It is now obvious that the

~100–200 ns relaxation times typically reported for ala-rich peptides,[4-6,10,13,17,18,22,25,32-35,120] signal the dominating contribution of π-bulge and/or 3_{10}-helix melting to the observed overall relaxation kinetics. In addition, it is also clear that at least some of the observed deviations from the mono-exponential behavior[22,33,34] for ala-rich peptide melting results from the temperature dependence of the relative contributions of pure α-helices, π-bulges and 3_{10}-helices melting to the overall relaxation kinetics. We believe our results here are the first experimental ones to resolve the kinetic behavior of the different α-helix like conformations.

The ~10-fold slower pure α-helix melting and formation rates found for AdP deserve the attention of theoreticians and experimentalists. Specifically, this decreased pure α-helix melting rate will significantly impact the competition between the parallel folding of different structural motifs.

5.1.5 CONCLUSIONS

We examined the relaxation kinetics of a 21 amino acid residues mainly ala peptide AdP, which contains three arg to give solubility. This peptide is ≥55% α-helix-like at 0 ºC and melts to a PPII conformation at higher temperature. Previous isotopic substitution studies demonstrated a significantly higher T_M=32 ºC for the 6 center residues compared to a T_M=5 ºC for the end residues.[7] We used T-jump measurements to examine the melting kinetics. We find that the middle AdP peptide bonds show a relaxation time ~2-fold slower than the end residues for 5 to 30 °C T-jump. In contrast, for a 20 to 40 °C T-jump the middle AdP peptide bonds appear to show faster kinetics than the end AdP peptide bonds.

We explain the observed kinetics in terms of different relative contributions of different α-helix-like motifs such as pure α-helices, π-bulges and 3_{10}-helices to the observed melting kinetics. We estimated that the melting rate constant of pure α-helices is ~12-fold slower than those of π-bulges and 3_{10}-helices (Table 5.3). This strikingly suggests that the pure α-helix (un)folding occurs at ~μsec time scale at room temperature.

For 5 to 30 °C T-jump, the faster melting of π-bulges and 3_{10}-helices dominate both the AdP ends and center kinetics, with also a minor contribution of slower pure α-helix melting to the AdP center kinetics. In contrast, for 20 to 40 °C T-jump the faster melting of π-bulges and 3_{10}-helices dominates both the AdP ends and center kinetics, whereas there is also a minor contribution of slower pure α-helix melting to the AdP ends kinetics. These surprising results can be explained in terms of a higher pure α-helical propensity at the AdP N-terminus compared to the middle and C-terminus.

The higher stability of pure α-helix at the AdP N-terminus can be understood in terms of AdP primary sequence. Specifically, three hydrophilic arg located in the AdP middle and at the AdP C-terminus destabilize the pure α-helices and induce formation of water-mediated α-helical defects (such as π-bulges and 3_{10}-helices), which melt faster.

Summarizing, we believe that our results here are the first experimental ones to quantitatively show that the folding mechanism of end residues of ala-rich peptides significantly differs from that of middle residues in terms of different relative contributions of different "α-helix-like" species to the melting kinetics. In addition, we for the first time measured the kinetic (un)folding rate constants for pure α-helices, 3_{10}-helices and π-bulges in ala-rich peptides of ~20 residues long. Thus, our results not only directly demonstrate that α-helix melting and formation

in peptides are not a simple two-state processes but also provide an important quantitative basis for testing theoretical studies in the field of peptide and protein folding.

AKNOWLEGMENTS. We gratefully acknowledge Ahmed Zeeshan, Bhavya Sharma, Konstantin Pimenov, Dr. Jon Scaffidi and Dr. Natalyia Myshakina for useful discussions. We thank Dr. Leon J. Gleser, Dr. Sunil Saxena and Dr. Carlos Gomes for their assistance in the statistical evaluation. We also thank Mr. Anton Karnoup who performed the MALDI MS analysis to verify the AdP sequence. This work was supported by NIH grant GM8RO1EB002053-24.

5.1.6 BIBLIOGRAPHY

(1) Creighton, T. E. Protein Structure, Second Edition, 1997.

(2) Zimm, B. H.; Bragg, J. K. J. Chem. Phys. **1959**, 31, 526.

(3) Poland, D.; Scheraga, H. A. J. Phys. Chem. **1966**, 45, 2071.

(4) Lednev, I. K.; Karnoup, A. S.; Sparrow, M. C.; Asher, S. A. J. Am. Chem. Soc. **1999**, 121, 8074.

(5) Lednev, I. K.; Karnoup, A. S.; Sparrow, M. C.; Asher, S. A. J. Am. Chem. Soc. **1999**, 121, 4076.

(6) Lednev, I. K.; Karnoup, A. S.; Sparrow, M. C.; Asher, S. A. J. Am. Chem. Soc. **2001**, 123, 2388.

(7) Ianoul, A.; Mikhonin, A.; Lednev, I. K.; Asher, S. A. J. Phys. Chem. A **2002**, 106, 3621.

(8) Lockhart, D. J.; Kim, P. S. Science **1992**, 257, 947.

(9) Lockhart, D. J.; Kim, P. S. Science **1993**, 260, 198.

(10) Werner, J. H.; Dyer, R. B.; Fesinmeyer, R. M.; Andersen, N. H. J. Phys. Chem. B **2002**, 106, 487.

(11) Gruebele, M. Annu. Rev. Phys. Chem. **1999**, 50, 485.

(12) Fesinmeyer, R. M.; Peterson, E. S.; Dyer, R. B.; Andersen, N. H. Protein Sci. **2005**, 14, 2324.

(13) Williams, S.; Causgrove, T. P.; Gilmanshin, R.; Fang, K. S.; Callender, R. H.; Woodruff, W. H.; Dyer, R. B. Biochemistry **1996**, 35, 691.

(14) Dyer, R. B.; Gai, F.; Woodruff, W. H.; Gilmanshin, R.; Callender, R. H. Acc. Chem. Res. **1998**, 31, 709.

(15) Callender, R.; Dyer, R. B.; Gilmanshin, R.; Woodruff, W. H. Annu. Rev. Phys. Chem. **1998**, 49, 173.

(16) Causgrove, T. P.; Dyer, R. B. Chemical Physics **2006**, 323, 2.

(17) Thompson, P. A.; Eaton, W. A.; Hofrichter, J. Biochemistry **1997**, 36, 9200.

(18) Thompson, P. A.; Munoz, V.; Jas, G. S.; Henry, E. R.; Eaton, W. A.; Hofrichter, J. J. Phys. Chem. B **2000**, 104, 378.

(19) Kubelka, J.; Hofrichter, J.; Eaton, W. A. Curr. Opin. Struc. Biol. **2004**, 14, 76.

(20) Lapidus, L. J.; Eaton, W. A.; Hofrichter, J. Proc. Natl. Acad. Sci. U.S.A. **2000**, 97, 7220.

(21) Lapidus, L. J.; Eaton, W. A.; Hofrichter, J. J. Mol. Biol. **2002**, 319, 19.

(22) Bredenbeck, J.; Helbing, J.; Kumita, J. R.; Woolley, G. A.; Hamm, P. Proc. Natl. Acad. Sci. U.S.A. **2005**, 102, 2379.

(23) Decatur, S. M.; Antonic, J. J. Am. Chem. Soc. **1999**, 121, 11914.

(24) Decatur, S. M. Biopolymers **2000**, 54, 180.

(25) Ramajo, A. P.; Petty, S. A.; Starzyk, A.; Decatur, S. M.; Volk, M. J. Am. Chem. Soc. **2005**, 127, 13784.

(26) Pozo Ramajo, A.; Petty, S. A.; Volk, M. Chem. Phys. **2006**, 323, 11.

(27) Gooding, E. A.; Ramajo, A. P.; Wang, J.; Palmer, C.; Fouts, E.; Volk, M. Chem. Commun. **2005**, 5985.

(28) Silva, R. A.; Kubelka, J.; Bour, P.; Decatur, S. M.; Keiderling, T. A. Proc. Natl. Acad. Sci. U.S.A. **2000**, 97, 8318.

(29) Yoder, G.; Pancoska, P.; Keiderling, T. A. Biochemistry **1997**, 36, 15123.

(30) Keiderling, T. A.; Silva, R. A.; Yoder, G.; Dukor, R. K. Bioorgan. Med. Chem. **1999**, 7, 133.

(31) Decatur, S. M. Accounts Chem. Res. **2006**, 39, 169.

(32) Huang, C.-Y.; Getahun, Z.; Wang, T.; DeGrado, W. F.; Gai, F. J. Am. Chem. Soc. **2001**, 123, 12111.

(33) Huang, C.-Y.; Getahun, Z.; Zhu, Y.; Klemke, J. W.; DeGrado, W. F.; Gai, F. Proc. Natl. Acad. Sci. U.S.A. **2002**, 99, 2788.

(34) Huang, C.-Y.; Klemke, J. W.; Getahun, Z.; DeGrado, W. F.; Gai, F. J. Am. Chem. Soc. **2001**, 123, 9235.

(35) Wang, T.; Zhu, Y.; Getahun, Z.; Du, D.; Huang, C.-Y.; DeGrado, W. F.; Gai, F. J. Phys. Chem. B **2004**, 108, 15301.

(36) Wang, T.; Du, D.; Gai, F. Chem. Phys. Lett. **2003**, 370, 842.

(37) Rohl, C. A.; Baldwin, R. L. Biochemistry **1994**, 33, 7760.

(38) Chakrabartty, A.; Kortemme, T.; Baldwin, R. L. Protein Sci. **1994**, 3, 843.

(39) Scholtz, J. M.; Marqusee, S.; Baldwin, R. L.; York, E. J.; Stewart, J. M.; Santoro, M.; Bolen, D. W. Proc. Natl. Acad. Sci. U.S.A. **1991**, 88, 2854.

(40) Marqusee, S.; Baldwin, R. L. Proc. Natl. Acad. Sci. U.S.A. **1987**, 84, 8898.

(41) Marqusee, S.; Robbins, V. H.; Baldwin, R. L. Proc. Natl. Acad. Sci. U.S.A. **1989**, 86, 5286.

(42) Padmanabhan, S.; Marqusee, S.; Ridgeway, T.; Laue, T. M.; Baldwin, R. L. Nature **1990**, 344, 268.

(43) Venyaminov, S. Y.; Hedstrom, J. F.; Prendergast, F. G. Proteins **2001**, 45, 81.

(44) Cochran, D. A. E.; Doig, A. J. Protein Sci. **2001**, 10, 1305.

(45) Cochran, D. A. E.; Penel, S.; Doig, A. J. Protein Sci. **2001**, 10, 463.

(46) Miller, J. S.; Kennedy, R. J.; Kemp, D. S. Biochemistry **2001**, 40, 305.

(47) Kennedy, R. J.; Walker, S. M.; Kemp, D. S. J. Am. Chem. Soc. **2005**, 127, 16961.

(48) Heitmann, B.; Job, G. E.; Kennedy, R. J.; Walker, S. M.; Kemp, D. S. J. Am. Chem. Soc. **2005**, 127, 1690.

(49) Goch, G.; Maciejczyk, M.; Oleszczuk, M.; Stachowiak, D.; Malicka, J.; Bierzynski, A. Biochemistry **2003**, 42, 6840.

(50) Gans, P. J.; Lyu, P. C.; Manning, M. C.; Woody, R. W.; Kallenbach, N. R. Biopolymers **1991**, 31, 1605.

(51) Kallenbach, N. R.; Lyu, P.; Zhou, H. Circular Dichroism and the Conformational Analysis of Biomolecules **1996**, 201.

(52) Spek, E. J.; Olson, C. A.; Shi, Z.; Kallenbach, N. R. J. Am. Chem. Soc. **1999**, 121, 5571.

(53) Doruker, P.; Bahar, I. Biophys. J. **1997**, 72, 2445.

(54) Scholtz, J. M.; Qian, H.; York, E. J.; Stewart, J. M.; Baldwin, R. L. Biopolymers **1991**, 31, 1463.

(55) Scholtz, J. M.; Baldwin, R. L. Annu. Rev. Biophys. Biomol. Struct. **1992**, 21, 95.

(56) Young, W. S.; Brooks, C. L., III. J. Mol. Biol. **1996**, 259, 560.

(57) Shirley, W. A.; Brooks, C. L., III. Proteins **1997**, 28, 59.

(58) Tobias, D. J.; Brooks, C. L., III. Biochemistry **1991**, 30, 6059.

(59) Brooks, C. L., III. J. Phys. Chem. **1996**, 100, 2546.

(60) Ohkubo, Y. Z.; Brooks, C. L., III. Proc. Natl. Acad. Sci. U.S.A. **2003**, 100, 13916.

(61) Garcia, A. E.; Sanbonmatsu, K. Y. Proc. Natl. Acad. Sci. U.S.A. **2002**, 99, 2782.

(62) Gnanakaran, S.; Garcia, A. E. Proteins **2005**, 59, 773.

(63) Hummer, G.; Garcia, A. E.; Garde, S. Phys. Rev. Lett. **2000**, 85, 2637.

(64) Hummer, G.; Garcia, A. E.; Garde, S. Proteins **2001**, 42, 77.

(65) Nymeyer, H.; Garcia, A. E. Proc. Natl. Acad. Sci. U.S.A. **2003**, 100, 13934.

(66) Paschek, D.; Gnanakaran, S.; Garcia, A. E. Proc. Natl. Acad. Sci. U.S.A. **2005**, 102, 6765.

(67) Daggett, V.; Levitt, M. J. Mol. Biol. **1992**, 223, 1121.

(68) Fitzkee, N. C.; Rose, G. D. Protein Sci. **2004**, 13, 633.

(69) Doshi, U.; Munoz, V. Chem. Phys. **2004**, 307, 129.

(70) Doshi, U. R.; Munoz, V. J. Phys. Chem. B **2004**, 108, 8497.

(71) Munoz, V.; Serrano, L. J. Mol. Biol. **1995**, 245, 297.

(72) Sorin, E. J.; Pande, V. S. Biophys. J. **2005**, 88, 2472.

(73) Sorin, E. J.; Pande, V. S. J. Comp. Chem. **2005**, 26, 682.

(74) Sorin, E. J.; Rhee, Y. M.; Shirts, M. R.; Pande, V. S. J. Mol. Biol. **2006**, 356, 248.

(75) Zagrovic, B.; Jayachandran, G.; Millett, I. S.; Doniach, S.; Pande, V. S. J. Mol. Biol. **2005**, 353, 232.

(76) Bertsch, R. A. The early events of protein folding: simulations of polyalanine folding into an alpha-helix, 1998.

(77) Bertsch, R. A.; Vaidehi, N.; Chan, S. I.; Goddard, W. A., III. Proteins **1998**, 33, 343.

(78) Ferrara, P.; Apostolakis, J.; Caflisch, A. J. Phys. Chem. B **2000**, 104, 5000.

(79) Irbaeck, A.; Mohanty, S. Biophys. J. **2005**, 88, 1560.

(80) Doig, A. J. Biophys. Chem. **2002**, 101-102, 281.

(81) Doig, A. J.; Errington, N.; Iqbalsyah, T. M. Protein Folding Handbook **2005**, 1, 247.

(82) Kim, J. G.; Fukunishi, Y.; Nakamura, H. Chem. Phys. Lett. **2004**, 392, 34.

(83) Levy, Y.; Jortner, J.; Becker, O. M. Proc. Natl. Acad. Sci. U.S.A. **2001**, 98, 2188.

(84) Nguyen, H. D.; Marchut, A. J.; Hall, C. K. Protein Sci. **2004**, 13, 2909.

(85) Peng, Y.; Hansmann, U. H. E.; Alves, N. A. J. Chem. Phys. **2003**, 118, 2374.

(86) Takano, M.; Yamato, T.; Higo, J.; Suyama, A.; Nagayama, K. J. Am. Chem. Soc. **1999**, 121, 605.

(87) Takano, M.; Nagayama, K.; Suyama, A. J. Chem. Phys. **2002**, 116, 2219.

(88) Takano, M.; Nakamura, H. K.; Nagayama, K.; Suyama, A. J. Chem. Phys. **2003**, 118, 10312.

(89) Mortenson, P. N.; Evans, D. A.; Wales, D. J. J. Chem. Phys. **2002**, 117, 1363.

(90) Ulmschneider, J. P.; Jorgensen, W. L. J. Chem. Phys. **2003**, 118, 4261.

(91) Ulmschneider, J. P.; Jorgensen, W. L. J. Am. Chem. Soc. **2004**, 126, 1849.

(92) Tirado-Rives, J.; Jorgensen, W. L. Biochemistry **1991**, 30, 3864.

(93) Tirado-Rives, J.; Maxwell, D. S.; Jorgensen, W. L. J. Am. Chem. Soc. **1993**, 115, 11590.

(94) Mitsutake, A.; Okamoto, Y. J. Chem. Phys. **2000**, 112, 10638.

(95) Samuelson, S.; Martyna, G. J. J. Phys. Chem. B **1999**, 103, 1752.

(96) Hansmann, U. H. E.; Okamoto, Y. J. Chem. Phys. **1999**, 110, 1267.

(97) Wu, X.; Wang, S. J. Phys. Chem. B **2001**, 105, 2227.

(98) Wang, Y.; Kuczera, K. J. Phys. Chem. B **1997**, 101, 5205.

(99) Van Giessen, A. E.; Straub, J. E. J. Chem. Theory Comput. **2006**, 2, 674.

(100) Chakrabartty, A.; Baldwin, R. L. Adv. Prot. Chem. **1995**, 46, 141.

(101) Chakrabartty, A.; Schellman, J. A.; Baldwin, R. L. Nature **1991**, 351, 586.

(102) Arashiro, E.; Drugowich de Felicio, J. R.; Hansmann, U. H. E. Phys. Rev. E **2006**, 73, 040902/1.

(103) Soto, P.; Mark, A. E. J. Phys. Chem. B **2002**, 106, 12830.

(104) Peng, Y.; Hansmann, U. H. E. Biophys. J. **2002**, 82, 3269.

(105) Smith, A. V.; Hall, C. K. Proteins **2001**, 44, 344.

(106) Alves, N. A.; Hansmann, U. H. E. Physica A **2001**, 292, 509.

(107) Pellegrini, M.; Gronbech-Jensen, N.; Doniach, S. Physica A **1997**, 239, 244.

(108) Klein, C. T.; Mayer, B.; Koehler, G.; Wolschann, P. Theochem **1996**, 370, 33.

(109) Hoffmann, D.; Knapp, E.-W. Eur. Biophys. J. **1996**, 24, 387.

(110) Scheraga, H. A.; Vila, J. A.; Ripoll, D. R. Biophys. Chem. **2002**, 101-102, 255.

(111) Zhang, W.; Lei, H.; Chowdhury, S.; Duan, Y. J. Phys. Chem. B **2004**, 108, 7479.

(112) Rathore, N.; Yan, Q.; de Pablo, J. J. J. Chem. Phys. **2004**, 120, 5781.

(113) Agostini, F. P.; Soares-Pinto, D. D. O.; Moret, M. A.; Osthoff, C.; Pascutti, P. G. J. Comput. Chem. **2006**, 27, 1142.

(114) Baumketner, A.; Shea, J. E. Phys. Rev. E **2003**, 68, 051901/1.

(115) Baumketner, A.; Shea, J. E. Condens. Matter Phys. **2004**, 38, 421.

(116) Ho, B. K.; Dill, K. A. PLoS Comput. Biol. **2006**, 2, 228.

(117) Mezei, M.; Fleming, P. J.; Srinivasan, R.; Rose, G. D. Proteins **2004**, 55, 502.

(118) Kentsis, A.; Mezei, M.; Gindin, T.; Osman, R. Proteins **2004**, 55, 493.

(119) Blanch, E. W.; Morozova-Roche, L. A.; Cochran, D. A. E.; Doig, A. J.; Hecht, L.; Barron, L. D. J. Mol. Biol. **2000**, 301, 553.

(120) Asher, S. A.; Mikhonin, A. V.; Bykov, S. B. J. Am. Chem. Soc. **2004**, 126, 8433.

(121) Adzhubei, A. A.; Sternberg, M. J. E. J. Mol. Biol. **1993**, 229, 472.

(122) Chen, K.; Liu, Z.; Kallenbach, N. R. Proc. Natl. Acad. Sci. U.S.A. **2004**, 101, 15352.

(123) Garcia, A. E. Polymer **2004**, 45, 669.

(124) Pappu, R. V.; Rose, G. D. Protein Sci. **2002**, 11, 2437.

(125) Bochicchio, B.; Tamburro, A. M. Chirality **2002**, 14, 782.

(126) Woody, R. W. Adv. Biophys. Chem. **1992**, 2, 37.

(127) Fleming, P. J.; Fitzkee, N. C.; Mezei, M.; Srinivasan, R.; Rose, G. D. Prot. Sci. **2005**, 14, 111.

(128) Eisenhaber, F.; Adzhubei, A. A.; Eisenmenger, F.; Esipova, N. G. Biofizika **1992**, 37, 62.

(129) Bochicchio, B.; Pepe, A.; Tamburro, A. M. Chirality **2005**, 17, 364.

(130) Blanch, E. W.; Gill, A. C.; Rhie, A. G. O.; Hope, J.; Hecht, L.; Nielsen, K.; Barron, L. D. J. Mol. Biol. **2004**, 343, 467.

(131) Blanch, E. W.; Kasarda, D. D.; Hecht, L.; Nielsen, K.; Barron, L. D. Biochemistry **2003**, 42, 5665.

(132) Blanch, E. W.; Robinson, D. J.; Hecht, L.; Barron, L. D. Journal of General Virology **2001**, 82, 1499.

(133) Shi, Z.; Olson, C. A.; Rose, G. D.; Baldwin, R. L.; Kallenbach, N. R. Proc. Natl. Acad. Sci. U.S.A. **2002**, 99, 9190.

(134) McColl, I. H.; Blanch, E. W.; Hecht, L.; Kallenbach, N. R.; Barron, L. D. J. Am. Chem. Soc. **2004**, 126, 5076.

(135) Mikhonin, A. V.; Myshakina, N. S.; Bykov, S. V.; Asher, S. A. J. Am. Chem. Soc. **2005**, 127, 7712.

(136) Gokce, I.; Woody, R. W.; Anderluh, G.; Lakey, J. H. J. Am. Chem. Soc. **2005**, 127, 9700.

(137) Kim, Y. S.; Wang, J.; Hochstrasser, R. M. J. Phys. Chem. B **2005**, 109, 7511.

(138) Woutersen, S.; Hamm, P. J. Phys. Chem. B **2000**, 104, 11316.

(139) Rucker, A. L.; Creamer, T. P. Protein Sci. **2002**, 11, 980.

(140) Makowska, J.; Rodziewicz-Motowidlo, S.; Baginska, K.; Vila, J. A.; Liwo, A.; Chmurzynski, L.; Scheraga, H. A. Proc. Natl. Acad. Sci. U.S.A. **2006**, 103, 1744.

(141) Shi, Z.; Chen, K.; Liu, Z.; Kallenbach, N. R. Chem. Rev. **2006**, 106, 1877.

(142) Shi, Z.; Woody, R. W.; Kallenbach, N. R. Adv. Prot. Chem. **2002**, 62, 163.

(143) Chi, Z.; Chen, X. G.; Holtz, J. S. W.; Asher, S. A. Biochemistry **1998**, 37, 2854.

(144) Asher, S. A.; Ianoul, A.; Mix, G.; Boyden, M. N.; Karnoup, A.; Diem, M.; Schweitzer-Stenner, R. J. Am. Chem. Soc. **2001**, 123, 11775.

(145) Mikhonin, A. V.; Ahmed, Z.; Ianoul, A.; Asher., S. A. J. Phys. Chem. B **2004**, 108, 19020.

(146) Chi, Z.; Asher, S. A. Biochemistry **1998**, 37, 2865.

(147) Chi, Z.; Asher, S. A. Biochemistry **1999**, 38, 8196.

(148) Shashilov, V. A.; Xu, M.; Ermolenkov, V. V.; Lednev, I. K. J. Quant. Spectrosc. Radiat. Transfer **2006**, 102, 46.

(149) Xu, M.; Ermolenkov, V. V.; He, W.; Uversky, V. N.; Fredriksen, L.; Lednev, I. K. Biopolymers **2005**, 79, 58.

(150) Copeland, R. A.; Spiro, T. G. Biochemistry **1987**, 26, 2134.

(151) JiJi, R. D.; Balakrishnan, G.; Hu, Y.; Spiro, T. G. Biochemistry **2006**, 45, 34.

(152) Spiro, T. G.; Smulevich, G.; Su, C. Biochemistry **1990**, 29, 4497.

(153) Lednev, I. K.; Ermolenkov, V. V.; He, W.; Xu, M. Anal. Bioanal. Chem. **2005**, 381, 431.

(154) Wang, Y.; Purrello, R.; Jordan, T.; Spiro, T. G. J. Am. Chem. Soc. **1991**, 113, 6359.

(155) Topilina, N. I.; Higashiya, S.; Rana, N.; Ermolenkov, V. V.; Kossow, C.; Carlsen, A.; Ngo, S. C.; Wells, C. C.; Eisenbraun, E. T.; Dunn, K. A.; Lednev, I. K.; Geer, R. E.; Kaloyeros, A. E.; Welch, J. T. Biomacromolecules **2006**, 7, 1104.

(156) Ahmed, Z.; Asher, S. A. Biochemistry **2006**, 45, 9068.

(157) Ahmed, Z.; Beta, I. A.; Mikhonin, A. V.; Asher, S. A. J. Am. Chem. Soc. **2005**, 127, 10943.

(158) Miick, S. M.; Martinez, G. V.; Fiori, W. R.; Todd, A. P.; Millhauser, G. L. Nature **1992**, 359, 653.

(159) Fiori, W. R.; Miick, S. M.; Millhauser, G. L. Biochemistry **1993**, 32, 11957.

(160) Millhauser, G. L. Biochemistry **1995**, 34, 3873.

(161) Martinez, G.; Millhauser, G. J. Struct. Biol. **1995**, 114, 23.

(162) Millhauser, G. L.; Stenland, C. J.; Bolin, K. A.; van de Ven, F. J. M. J. Biomol. NMR **1996**, 7, 331.

(163) Hanson, P.; Martinez, G.; Millhauser, G.; Formaggio, F.; Crisma, M.; Toniolo, C.; Vita, C. J. Am. Chem. Soc. **1996**, 118, 271.

(164) Millhauser, G. L.; Stenland, C. J.; Hanson, P.; Bolin, K. A.; van de Ven, F. J. M. J. Mol. Biol. **1997**, 267, 963.

(165) Hanson, P.; Anderson, D. J.; Martinez, G.; Millhauser, G.; Formaggio, F.; Crisma, M.; Toniolo, C.; Vita, C. Mol. Phys. **1998**, 95, 957.

(166) Armen, R.; Alonso, D. O. V.; Daggett, V. Protein Sci. **2003**, 12, 1145.

(167) Long, H. W.; Tycko, R. J. Am. Chem. Soc. **1998**, 120, 7039.

(168) Topol, I. A.; Burt, S. K.; Deretey, E.; Tang, T.-H.; Perczel, A.; Rashin, A.; Csizmadia, I. G. J. Am. Chem. Soc. **2001**, 123, 6054.

(169) Podtelezhnikov, A. A.; Wild, D. L. Proteins **2005**, 61, 94.

(170) Han, W.-G.; Elstner, M.; Jalkanen, K. J.; Frauenheim, T.; Suhai, S. Int. J. Quantum Chem. **2000**, 78, 459.

(171) Mikhonin, A. V.; Asher, S. A. J. Am. Chem. Soc. **2006**, 128, 13789.

(172) Lee, K.-H.; Benson, D. R.; Kuczera, K. Biochemistry **2000**, 39, 13737.

(173) Mahadevan, J.; Lee, K.-H.; Kuczera, K. J. Phys. Chem. B **2001**, 105, 1863.

(174) Feig, M.; MacKerell, A. D., Jr.; Brooks, C. L., III. J. Phys. Chem. B **2003**, 107, 2831.

(175) Bykov, S. V.; Lednev, I. K.; Ianoul, A.; Mikhonin, A. V.; Munro, C. H.; Asher, S. A. Appl. Spectrosc. **2005**, 59, 1541.

(176) Walrafen, G. E.; Fisher, M. R.; Hokmabadi, M. S.; Yang, W. H. J. Chem. Phys. **1986**, 85, 6970.

(177) Risovic, D.; Furic, K. J. Raman Spectrosc. **2005**, 36, 771.

(178) Mikhonin, A. V.; Asher, S. A. J. Phys. Chem. B **2005**, 109, 3047.

(179) Mikhonin, A. V.; Bykov, S. V.; Myshakina, N. S.; Asher, S. A. J. Phys. Chem. B **2006**, 110, 1928.

(180) Nelles, O. Nonlinear System Identefication, **2001**, Springer.

(181) Dennis, J. E.; Schnabel, R. B. Numerical Methods for Unconstrained Optimization and Nonlinear Equation, **1983**, Prentice.

(182) Budil, D. E.; Lee, S.; Saxena, S.; Freed, J. H. J. Magn. Reson., Ser. A **1996**, 120, 155.

(183) Gleser, L. J. Statistical Science **1998**, 13, 277.

(184) Grams/32AI User's Guide, **2001**, Galactic Industries Corporation.

(185) Wadsworth, H. M. Handbook of Statistical Methods for Engineers and Scientists, **1990**, McGraw.

(186) Lee, S.-H.; Krimm, S. Biopolymers **1998**, 46, 283.

(187) Pimenov, K. V.; Bykov, S. V.; Mikhonin, A. V.; Asher, S. A. J. Am. Chem. Soc. **2005**, 127, 2840.

(188) Copeland, R. A.; Spiro, T. G. J. Am. Chem. Soc. **1986**, 108, 1281.

(189) Tanaka, M.; Tanaka, J. Molecular Physics **1970**, 19, 889.

(190) Rosenheck, K.; Doty, P. Proc. Natl. Acad. Sci. USA **1961**, 47, 1775.

(191) Moffit, W. Proc. Natl. Acad. Sci. U.S.A. **1956**, 42, 736.

(192) Schellman, J. A.; Becktel, W. J. Biopolymers **1983**, 22, 171.

(193) Momii, R. K.; Urry, D. W. Macromolecules **1968**, 1, 372.

(194) Painter, P. C.; Koenig, J. L. Biopolymers **1976**, 15, 241.

(195) Weissbluth, M. Q. Rev. Biophys. **1971**, 4, 1.

(196) Rhodes, W.; Barnes, D. G. J. Chim. Phys. PCB **1968**, 65, 78.

(197) McLachlan, A. D.; Ball, M. A. Molecular Physics **1964**, 8, 581.

(198) Cartailler, J.-P.; Luecke, H. Structure **2004**, 12, 133.

(199) Sundaralingam, M.; Sekharudu, Y. C. Science **1989**, 244, 1333.

(200) Vila, J. A.; Ripoll, D. R.; Scheraga, H. A. Proc. Natl. Acad. Sci. U.S.A. **2000**, 97, 13075.

6.0 THESIS SUMMARY

We developed a sensitive and incisive technique for the investigation of peptides and proteins. We demonstrated the utility of UV resonance Raman spectroscopy by investigating the solution conformational preferences of polyglycine, poly-L-lysine and poly-L-glutamic acid in steady-state equilibrium conditions as well as by observing fast conformational dynamics in 21 residue alanine-based peptide AdP with a few nanosecond time resolution.

We built a state-of-the-art tunable UV Raman spectrometer for the 193 – 270 nm spectral region. This instrument allows for steady state and transient UV Raman measurements. For steady-state measurements we utilize 5 KHz Ti-sapphire continuously tunable lasers which are frequency doubled/quadrupled/mixed down to the deep UV. For transient Raman measurements we utilize a Coherent Infinity YAG laser to generate nsec IR pump laser pulses to generate a T-jump and a second Coherent Infinity YAG laser, which is frequency tripled and Raman shifted into the deep UV (204 nm), for transient UV Raman excitation. Numerous other UV excitation frequencies can be utilized for selective excitation of chromophoric groups for transient Raman measurements. We constructed a subtractive dispersion double monochromator to minimize stray light. We utilize a new CCD camera which responds efficiently to UV light, as opposed to the previous CCD and photodiode detectors which required noisy intensifiers for detecting UV-light. For the T-jump measurements we use a second camera to simultaneously acquire the

Raman spectra of the water stretching bands (2500 – 4000 cm^{-1}) whose band-shapes and frequencies report the sample temperature.

A crucial part in the development of any spectroscopic methodology is the search and development of a detailed understanding of new spectroscopic conformational markers. We continued the search for new polypeptide backbone conformational markers using both experimental data and theoretical modeling. We experimentally and theoretically examined the conformation, pH and temperature dependence of the CH_2 stretching frequencies of glycine in solution and in the crystalline state. The symmetric ($\nu_s CH_2$) and asymmetric ($\nu_{as} CH_2$) stretching frequencies show a significant dependence on amino acid conformation. We quantified the relation between the frequency splitting ($\Delta = \nu_{as} CH_2 - \nu_s CH_2$) and the ξ angle which determines the gly conformational geometry. This relation allows us to determine the conformation of gly directly from the Raman spectral frequencies. As a next step, we investigated the conformational dependence of the $C_\alpha H_2$ stretching frequencies in gly-based polypeptides. We experimentally demonstrated a strong dependence of the $C_\alpha H_2$ stretching frequencies on the peptide conformation using crystalline glygly derivatives of known x-ray structure. Then we theoretically modeled the φ and ψ dependences of the CH_2 stretching frequencies. Our research indicates that $C_\alpha H_2$ stretching vibrations are sensitive markers of the polyglycine backbone conformation. We then utilized this knowledge to identify the conformational preferences of polyglycine in aqueous solution.

Spectroscopic investigations of macromolecules generally attempt to interpret the measured spectra in terms of the summed contributions of the different molecular fragments which significantly simplify the analysis. We demonstrate that the deep UV resonance Raman spectra of aqueous solution phase oligoglycines show independent peptide bond molecular

fragment contributions; the peptide bonds independently resonance Raman scatter. The different peptide bond electronic transitions and vibrational modes are independent. We utilize this result to separately determine the conformational distributions of the internal and penultimate peptide bonds of oligoglycines. Glycine based polypeptides possess greater conformational freedom due to the lack of side chains which makes polygly an important model system for investigating the conformational preferences of the polypeptide backbone in solution, in general and for understanding the nature of the unfolded states, in particular.

We utilized UV resonance and visible Raman spectroscopy to investigate conformational preferences of glycine based peptides of different lengths in water containing LiCl and $LiClO_4$ salts. Lithium salts are used to increase the solubility of polygly chains longer than 5 residues. Our study indicates that in solution polygly as well as central residues of gly_5 and gly_6 assume conformations with φ and ψ angles centered around the 3_1-helix while terminal residues populate conformations similar to those found in crystals (3_1-helices and β-strands), but with broader distributions. This preference of polygly to 3_1-helix conformation in solution is likely a result of favorable interaction of the carbonyl dipoles in these extended helices. We found that high concentrations of Li^+ additionally stabilizes the PGII conformation in solution, most likely due to its polarizing effect on the peptide bond carbonyls which makes carbonyl-carbonyl electrostatic interactions more favorable.

We also used UV resonance Raman spectroscopy to examine the solution conformation of poly-L-Lysine and poly-L-Glutamic acid in their unfolded, non-α-helical states. UVR measurements indicate that at pH=2 PLL and pH=9 PGA exist mainly in a mixture of PPII and a left-handed 2.5_1-helical conformation, which is an extended β-strand-like conformation with $\Psi \sim +170°$ and $\Phi \sim -130°$. Both of these conformations are highly exposed to water. The energies

of these conformations are very similar. We see no evidence of any disordered "random coil" states. In addition, we find that a PLL and PGA mixture at neutral pH is ~60% β-sheet, and contains PPII and extended 2.5_1-helix conformations. The β-sheet conformation shows little evidence of amide backbone hydrogen bonding to water.

We examined spatially resolved relaxation kinetics of an isotopically labeled 21-residue mainly ala peptide, AdP. The AdP penultimate ala residues were deuterated while the central residues remained hydrogenated, to allow independent monitoring of melting dynamics of the middle and the terminal peptide bonds. For 5 to 30 °C T-jumps, the central peptide bonds show a ~2-fold slower relaxation time (189±31 ns) than the exterior peptide bonds (97±15 ns). In contrast, for a 20 to 40 ºC T-jump, the central peptide bonds relaxation appears to be faster (56±6 ns) than that of the penultimate peptide bonds (131±46 ns). We explained the unusual temperature dependence of the relaxation rates of the interior and exterior peptide bonds by the different contribution of 3_{10}-helices, α-helices and π-bulges/helices which populate the conformational ensemble of the AdP terminal and internal PBs.

7.0 FURURE DIRECTIONS

The development of UV resonance Raman spectroscopy as powerful technique for elucidation of the conformational preferences of solution polypeptides, examining peptide and protein excited states, and monitoring fast protein folding events shall be continued. The full potential of the Raman technique is not completely uncovered.

7.1.1 Instrumentation development

Due to the intrinsic weakness of Raman scattering and despite all of the recent advances in spectroscopic instrumentation, the informational content of Raman spectra of biomolecules in diluted solutions often remains signal-to-noise limited. This is especially true for the Raman spectra of high molecular weight biopolymers, like proteins, due to the massive overlap of spectral features from similar molecular units. Often biologically significant events, like drug binding, or change in local hydrogen bonding strength result in comparatively small changes in protein structure or tiny variations in bondlength. Observation of such events requires instrumentation capable of recording high signal-to-noise Raman spectra in short periods of time to avoid any sample degradation. The main factors which determines signal-to-noise ratio in modern Raman spectrometers are:

1) Power of the excitation source

2) Quantum yield of the detector

3) Throughput of the monochromator

Modern deep UV laser provide more power than is required for investigation of biologically-related systems. High power excitation sources can bring about undesirable photochemical and photothermal processes which degrade the sample. This is especially true for UV resonance Raman of polypeptides. Modern detectors equipped with liquid nitrogen cooled back-thinned CCD detectors are shot-noise-limited over short accumulation times and generally do not limit the Raman spectrometer signal-to-noise ratio. Thus the main limiting factor in contemporary UV Raman spectrometers is the monochromator throughput, which is affected by inevitable losses of light at the monochromator mirrors and dispersive elements due to absorption and scattering.

We are currently developing a new spectrometer which will allows us to increase it throughput ~ 10 times compared to ones currently being used. This spectrometer will be optimized specifically for investigation of peptides and proteins secondary structure and dynamics. We hope that this advance in Raman instrumentation will allow us to monitor changes in conformation of individual PB bonds.

Our T-jump setup was recently upgraded with two Photonic Industries laser systems. A completely tunable in the DUV range (193-240nm) with ~1.5 mJ pulse energy, 1 kHz repetition rate quadrupled Ti:Sapphire laser which is time-synchronized with Nd:YAF laser coupled to OPO producing 1.9 μm IR pulses which effectively absorbed by H_2O. Both these lasers produce more stable output than Stokes/anti-Stokes Raman shifted Nd:YAG systems. These two lasers were specifically designed for the time resolved UVRR measurements and should significantly increase Raman spectra signal-to-noise due to much higher repetition rates. But the principal

advantage of these lasers is in combination of time-resolved measurements with wavelength tunability. The application of this unique combination is described in chapter 2.5

7.1.2 Glycine and proline amide bands frequency conformational dependence

Extensive studies of the dependence of the amide III frequency on the Ramachandran ψ angle and hydrogen bonding resulted in development of a family of relationships to directly estimate the Ψ Ramachandran angle from the measured UVR $AmIII_3$ frequencies for peptide bonds with known hydrogen bonding. But these relationships are only valid for "standard", α-carbon-branched, non-cyclic amino acid residues which form *trans*- peptide bonds within polypeptide chain. Other amino acids residues, like gly or pro, have different structures which change their normal modes, as well as the frequency-structure dependencies of the amide bands. For complete description of protein structure it is important to have spectra-structure correlations for all types of amino acids which can be found in natural proteins.

We will extend our investigations of amide band frequency – structure correlations to gly and pro residues. We will start from normal mode calculations (DFT level of theory, short peptides) to model the amide band frequency-φ, ψ dependences for gly and φ-dependence for pro. Then we verify obtained relationships using peptide crystals with known structures. The ultimate goal of this study is the ability of complete prediction of polypeptide conformation knowing its UVRR spectrum.

7.1.3 Search for new conformational markers

CαH stretching as a Ramachandran Φ angle markers. Extensive work done during the past several years in our group has allowed for direct determination of the Ramachandran ψ angle the amide III frequencies. As a result of this extensive work, ψ angle distributions were determined for many polypeptides in solution. For a complete description of the peptide bond conformation, however, information about φ is necessary. In chapter 3 of this thesis we experimentally and theoretically examined the dependence of the $C_\alpha H_2$ stretching frequencies on Ramachandran φ, ψ angles. Our data demonstrate that upon φ angle rotation the frequencies of the symmetric ($\nu_s CH_2$) and asymmetric ($\nu_{as} CH_2$) stretching bands can shift up to 60 cm^{-1}. Thus, Ramachandran φ angle sensitivity of the $C_\alpha H_2$ stretching vibrations is comparable in magnitude to the ψ angle sensitivity of the amide III band. In contrast to the complex nature of the amide III band, the $C_\alpha H_2$ stretching vibrations are localized and uncoupled; their frequencies are only determined by C-H bondlengths which are determined by mutual orientation of the C-Hs and peptide bond. The C-H bond is not polar and thus is significantly less sensitive to environmental conditions, like changes in hydrogen bonding strength, physical state, etc. Selective deuteration of the C_α-H bond can be used in order to separate spectral contributions from different residues.

Amide IV as a prospective conformational marker. Another Raman active vibration which has a great potential to serve as a sensitive marker of a polypeptide backbone conformation is the amide IV. This vibration is mainly in-plain PB C=O bending with some contributions from C_α-C stretching and C-N-C_α, and is usually observed around 600 – 750 cm^{-1}. Our preliminary normal mode calculations show a significant dependence of the amide IV frequencies on Ramachandran φ angle in short ala-based peptides. We will experimentally

investigate the amide IV frequency conformational dependence by observing AP peptide α-helix to PPII temperature induced malting in D_2O. The AP peptide is a convenient model system for this study since its temperature induced conformational transition is well studied.

7.1.4 Excitationally resolved secondary structure motifs of solution polypeptides for T-jump kinetics studies

Investigation of the folding/unfolding dynamics of individual secondary structures is extremely useful for understanding folding pathways of large proteins. Today, α-helix melting dynamics is the most extensively studied both experimentally and theoretically and comparatively well understood. But even the α-helix melting mechanism still needs to be clarified since it is not clear how a right-handed α-helix can melt into a left-handed PPII extended helix.

We will used a laser induced T-jump methodology developed in our group and now perfected with tunable excitation source to investigate the relaxation dynamics of π-helices, π-bulges, 3_1-helicies, β-turns etc. Excitation profiles studies done in our group have shown that the wavelength of the maxima of PB amide $\pi \rightarrow \pi^*$ absorption depends on the polypeptide backbone secondary structure. This gives us the advantage of selective enhancement of the spectral contributions from different secondary structures of interest. We will use our knowledge of excitation profiles to resolve the melting dynamics of different secondary structure motifs within the heterogeneous conformational ensemble of solution polypeptides.